Carbon Cycling and Ocean Acidification studies in Baffin Bay and Nares Strait

by

Tonya Melissa Burgers

A thesis submitted to the Faculty of Graduate Studies of
The University of Manitoba
in partial fulfillment of the degree of

Doctor of Philosophy

Department of Environment and Geography
C.H.R. Faculty of Environment, Earth, and Resources
University of Manitoba
Winnipeg, Manitoba, Canada

Supervised by

Dr. Tim Papakyriakou
Professor
Centre for Earth Observation Science
Department of Environment and Geography
University of Manitoba
Winnipeg, MB, Canada

Advisory Committee

Dr. Lisa Miller
Research Scientist
Institute for Ocean Sciences
Fisheries and Oceans Canada
Sidney, BC, Canada
and
Adjunct Professor
Department of Environment and Geography
University of Manitoba
Winnipeg, MB, Canada

Dr. Brent Else
Associate Professor
Department of Geography
University of Calgary
Calgary, AB, Canada
and
Adjunct Professor
Department of Environment and Geography
University of Manitoba
Winnipeg, MB, Canada

Dr. Mostafa Fayek
Professor
Centre for Earth Observation Science
Department of Earth Sciences
University of Manitoba
Winnipeg, MB, Canada

External Examiner

Dr. Elizabeth Shadwick
Principal Research Scientist
Commonwealth Scientific and Industrial
Research Organisation (CSIRO)
Hobart, TAS, Australia

for my parents,
for fostering my sense of adventure
and curiosity of the world

Abstract

The marine carbon cycle in Canadian Arctic waters, particularly in Nares Strait and Baffin Bay, is undergoing rapid change due to a shifting climate. Despite this, there's been a paucity of research into the carbonate chemistry and biogeochemical processes in these regions. This thesis addresses this gap by investigating the complex carbon dynamics in these waters, critical for understanding their role in the global carbon cycle.

The first research chapter evaluates the strength of the biological carbon pump during the spring ice-edge bloom in Baffin Bay. We found stark differences in springtime net community production (NCP) between Arctic and Atlantic water domains, in western and eastern Baffin Bay, respectively. Arctic outflow waters exhibited low spring NCP (< 1 mol C m^{-2}) due to persistent sea-ice cover and strong stratification of the upper water column, whereas the Atlantic water domain displayed high NCP rates (up to 5.7 mol C m^{-2}).

The first comprehensive examination of the marine carbon dynamics in Nares Strait is also presented. Using a multi-tracer linear mixing model, we distinguished the role of physical and biological processes on the distribution of dissolved inorganic carbon in Nares Strait. We identified water mass mixing as the dominant control on marine carbon dynamics, with primary production also playing an important role in decreasing surface pCO_2. Importantly, this investigation also provided the first documented evidence of Siberian river waters arriving in Nares Strait.

The final research chapter of this thesis investigates the biogeochemical processes affecting aragonite saturation states (Ω_{Ar}), and the state of ocean acidification in Baffin Bay, with a focus on the west Greenland continental shelf region, which has remained under-studied in terms of its marine biogeochemistry. We identify two main depth-dependent processes shaping the Ω_{Ar} distribution throughout Baffin Bay; within the upper 200 metres, lower Ω_{Ar} coincides with increasing fractions of Arctic-outflow waters, while below 200 metres organic matter respiration is responsible for decreasing Ω_{Ar}. Surprisingly, substantial Arctic-outflow waters were identified on the west Greenland shelf, challenging what is currently known of circulation patterns in the bay, and underscoring the need for further research.

Acknowledgements

I owe my gratitude to many people for their assistance and support throughout this PhD process. First and foremost, I would like to start by thanking my supervisor Dr. Tim Papakyriakou. I am lucky to have had a supervisor who supported my ambitions, gave me the freedom to chase my own ideas, believed in my capabilities, and gave me incredible opportunities. A big thank you also to my advisory committee, Dr. Brent Else, Dr. Lisa Miller, and Dr. Mostafa Fayek for their help, constructive feedback, and encouragement throughout this process. Special thanks to the Captains and crew of the CCGS *Amundsen*, and the Amundsen Science technicians for their hard work and support during my fieldwork. Thank you to Cara Manning, Shawn Marriott, Sarah Prestie, Mohamed Ahmed, Brian Butterworth, Monica Nelson, Alexis Beaupré-Laperrière, and Charel Wohl for their help collecting field data.

I would like to thank the many staff, faculty, and students at the Centre for Earth Observation Science (CEOS) at the University of Manitoba for their assistance, guidance, and support throughout my PhD studies. A special thank you to the late Dr. David Barber, for without your ambition and drive to create CEOS, I would not have had the incredible opportunities afforded to me throughout my graduate studies. I feel very privileged to have been part of a research centre specializing in Arctic systems science. I'd like to thank Drs. Søren Rysgaard, C.J Mundy, Jens Ehn, Zou Zou Kuzyk, Igor Dmitrenko, John Iacozza, Feiyue Wang, Karen Alley, and Kristina Brown (to name a few) from the faculty of CEOS for assistance with many questions that arose outside of my specific area of expertise. Thank you to the staff members who assisted me with many things from administrative tasks, travel bookings, and logistical support for field seasons including Linda Chow, Karen Wiens, Sebastian Luque, Emmelia Stainton, Ashley Soloway, and Debbie Armstrong. I also greatly appreciate the support and encouragement of my fellow graduate students, especially members of our "carbon group" meetings for helpful discussions. Special thanks to Dr. David Capelle, Kate Yezhova, Rachel Mandryk, Esdoorn Willcox, Alessia Guzzi, Inge Deschepper, Samantha Hugyue, and Madison Stocking.

This work also required a tremendous amount of financial support. I personally received an NSERC PGS-D scholarship, and logistical support from the Northern Scientific Training Program. I also benefitted greatly from membership in ArcticNet, a Network of Centres of Excellence of Canada. I am especially grateful to Dr. Dorthe Dahl-Jensen for her financial support in the final stretch of my PhD.

Finally, this work required a great deal of personal support, much of which came from my family, especially my mother. I'd like to thank my father for encouraging me to pursue the highest level of

education. An incredible amount of support also came from the friendships I have made here in Winnipeg. I will be eternally thankful for the friendships of Dr. Lisa Matthes, Chris Peck, Heather Stark, Dr. Nora Casson, Alexis Burt, Claire Hornby, Marc Cadieux, Alex Wall, Dr. John Iacozza, and Patricia and Montalvo-Rodriguez.

Land Acknowledgement

This research was conducted at the University of Manitoba, which is located on the original lands of Anishinaabeg, Cree, Ojibwe-Cree, Dakota, and Dene peoples and on the homeland of the Metis Nation. This research is focused on the marine environments of Baffin Bay and Nares Strait, which are part of the Qikiqtaaluk Region of the territory of Nunavut, Canada and part of Kalaallit Nunaat (Greenland). The Inuit people of Inuit Nunangat (Canada) and Kalaallit Nunaat (Greenland) have inhabited these lands since time immemorial and have an intimate connection with the land, ice, and marine environment.

Table of Contents

List of Tables

List of Figures

Chapter 1 Introduction

1.1 Motivation

Since the onset of the Industrial Revolution circa 1750, human activities have released approximately 2.5 trillion tons of carbon dioxide (CO_2) into the atmosphere (Friedlingstein et al., 2023; Gruber et al., 2023; Sabine et al., 2004). This substantial increase has led to a marked rise in atmospheric CO_2 concentrations. As of the 2023 annual average, atmospheric CO_2 concentrations stand at around 421 parts per million (ppm)(Tans & Keeling, 2024), compared to the pre-industrial average of approximately 277 in 1750 (Meinshausen et al., 2020). This large concentration change represents a significant shift from historical norms, and is unprecedented in both rate and scale. Historical records from Antarctic ice cores dating back hundreds of thousands of years show natural fluctuations in atmospheric CO_2 concentrations typically ranged between 180 and 300 ppm during glacial and interglacial periods, respectively (Lüthi et al., 2008; Petit et al., 1999). The modern spike in CO_2 concentrations far surpasses this historical range, and highlights the impact of human activities on the Earth system.

Amidst growing concerns about climate change and its ramifications, understanding the complex dynamics of the global carbon cycle has become imperative. The global ocean, covering more than 70% of the Earth's surface, plays a pivotal role in this cycle, acting as a major carbon sink through physical, chemical, and biological processes. As a carbon reservoir, the ocean contains the majority (roughly 95%) of the active pool of inorganic carbon on Earth, totaling approximately 38,000 gigatons, which is 50 times more than the atmosphere (DeVries, 2022; Falkowski et al., 2000). Currently, it is estimated that the global ocean removes 2.9 ± 0.4 Gt C yr^{-1} from the atmosphere, equivalent to roughly 26% of annual anthropogenic CO_2 emissions (Friedlingstein et al., 2023).

Despite its relatively small size compared to other oceanic regions (3% of the world ocean by surface area, and 1% by volume), the Arctic Ocean has been estimated to take up 90 to 180 Tg C yr^{-1}, accounting for approximately 5-10% of the global ocean CO_2 sink (Bates & Mathis, 2009; MacGilchrist et al., 2014; Yasunaka et al., 2018). A number of processes that occur within the Arctic Ocean drive this net CO_2 uptake. The cooling of Atlantic and Pacific-source waters as they transit into the Arctic region increases CO_2 solubility. Strong primary production over extensive continental shelf seas promotes CO_2 uptake, and the exported organic matter from this production sequesters carbon at depth (Arrigo & van Dijken, 2015; Lalande et al., 2009; Pipko et al., 2017). Sea-ice dynamics also play a large role in Arctic marine carbon dynamics, with sea-ice formation and associated brine rejection exporting CO_2 absorbed at the surface to greater depths (Anderson et al., 2010; Grimm et al., 2016; Rysgaard et al., 2011), and sea-ice

melt in spring providing a surface freshwater lens of low CO_2 water (Ahmed et al., 2019; Yamamoto-Kawai et al., 2009; Yang et al., 2024), further enhancing CO_2 uptake.

Although this oceanic uptake of CO_2 reduces the magnitude of the greenhouse effect in the atmosphere, it also leads to significant alterations in seawater chemistry. Specifically, increases in dissolved CO_2 concentrations lead to decreases in seawater pH, and hence the process name “ocean acidification”. Ocean acidification refers to both the reduction of seawater pH, and the related increase in the solubility of calcium carbonate minerals, predominantly due to the uptake of CO_2 from the atmosphere (AMAP, 2018; Doney et al., 2009). Declining pH in the world's oceans is of concern as it has the potential to exert large changes on marine biological and geochemical processes, and potentially disrupt marine ecosystems. This is especially true within the Arctic Ocean, which has been shown to be more sensitive to ocean acidification compared to other regions of the world's oceans. Low seawater temperatures, increased freshwater supply, and decreasing sea ice coverage are some of the many processes contributing to enhanced ocean acidification in Arctic waters (AMAP, 2013, 2018). Modeling studies have predicted that the Arctic Ocean will experience ocean acidification more rapidly than any other ocean, and will undergo the greatest reductions in seawater pH (AMAP, 2013; Denman et al., 2011; Steinacher et al., 2009; Steiner et al., 2014). Observational studies have already documented accelerated rates of ocean acidification in the Arctic (AMAP, 2018; Luo et al., 2016; Yamamoto-Kawai et al., 2009; Zhang et al., 2020).

These alarming trends are intricately linked to the fast pace of environmental change in the Arctic region due to climate change. Surface air temperatures in the Arctic are increasing at four times the global average (Rantanen et al., 2022). Sea-ice coverage, its thickness, and duration continue to decrease (Notz & Stroeve, 2018; Stroeve et al., 2012), affecting the seasonality of phytoplankton blooms (Ardyna & Arrigo, 2020; Leu et al., 2015). Regional warming has also led to an increased hydrological cycle (Carmack et al., 2016; White et al., 2007), increasing freshwater inputs to the Arctic Ocean from river runoff (Feng et al., 2021; McClelland et al., 2006) and glacial ice melt (Bamber et al., 2018; Mouginot et al., 2019) in addition to sea-ice melt. Each of these processes (and others) affects the seawater inorganic carbon system and ocean acidification in different ways, and will be reviewed briefly in Chapter 2.

The research presented here is motivated by the need to understand the drivers currently controlling the marine carbon cycle in Canadian Arctic waters, specifically in the waterbodies of Nares Strait and Baffin Bay. Relatively little research has been conducted to date concerning the carbonate chemistry and biogeochemical processes occurring within Baffin Bay and Nares Strait, and the region is known to be

rapidly changing due to climate change. In this thesis, I will investigate the various biogeochemical processes that impact the marine carbon cycle in these waters. This research contributes to the important need to understand the complex dynamics of the marine carbon cycle in Canadian Arctic waters, how these dynamics may be changing with ongoing climate change, and the role of these waters in the global carbon cycle.

1.2 Thesis Objectives

The overarching goal of this research is to improve our understanding of the physical and biogeochemical processes that control the flow and distribution of inorganic carbon within the waterbodies of Baffin Bay and Nares Strait. Each of the objectives of this thesis aims to quantify the role of specific processes (either physical or biological) in affecting the distribution of inorganic carbon, and also the state of ocean acidification in these water bodies. Specific processes to be investigated include: primary production and respiration, the advection and mixing of Pacific and Atlantic-source water masses, the addition of various freshwater inputs, sea-ice dynamics, and air-sea CO_2 exchange. This broad research goal will be achieved through the investigation of four proposed objectives:

1. Quantify springtime rates of net community production associated with the spring ice-edge bloom in Baffin Bay, and identify the key environmental drivers controlling its variability.
2. Investigate the origins and interactions of the water masses in Nares Strait, and describe their current carbonate chemistry and nutrient concentrations.
3. Distinguish and quantify the roles of physical and biological processes in governing the distribution of dissolved inorganic carbon in Nares Strait.
4. Provide an update on the state of ocean acidification in Baffin Bay, and investigate the influence of biogeochemical processes on the west Greenland continental shelf in affecting aragonite saturation states in these waters.

1.3 Thesis Outline

This thesis is composed of six chapters. In Chapter 2 I provide a thorough literature review of the inorganic carbon system in seawater, and the various processes known to influence the seawater inorganic carbon system in Arctic waters. Chapters 3, 4, and 5 each contain an original peer-reviewed research paper that has been published. The first research paper (Chapter 3) quantifies springtime rates of net community production in Baffin Bay associated with an ice-edge bloom, and identifies the main environmental factors controlling the magnitude and timing of the bloom. This work addresses objective 1, and it has been peer-reviewed and published in *Elementa: Science of the Anthropocene*:

Burgers, T. M., Tremblay, J.-É., Else, B. G. T., & Papakyriakou, T. N. (2020). Estimates of net community production from multiple approaches surrounding the spring ice-edge bloom in Baffin Bay. *Elementa: Science of the Anthropocene*, 8(1):013. https://doi.org/10.1525/elementa.013

The second research paper (Chapter 4) is a comprehensive investigation of the physical and biogeochemical processes influencing the marine carbon dynamics in Nares Strait. This work addresses objectives 2 and 3, and has been peer-reviewed and published in *Journal of Geophysical Research: Oceans:*

Burgers, T. M., Miller, L. A., Rysgaard, S., Mortensen, J., Else, B., Tremblay, J.-É., & Papakyriakou, T. (2023). Distinguishing Physical and Biological Controls on the Carbon Dynamics in a High-Arctic Outlet Strait. *Journal of Geophysical Research: Oceans*, *128*, e2022JC019393. https://doi.org/10.1029/2022JC019393

The final research paper (Chapter 5) investigates the current biogeochemical drivers of aragonite saturation states in Baffin Bay, including important insights from the previously undersampled west Greenland continental shelf. This research paper also reports on how the state of ocean acidification in Baffin Bay has changed since the first baseline measurements of aragonite and calcite saturation states were made between 2003 and 2005 (Azetsu-Scott et al., 2010). This work addresses objective 4, and has been peer-reviewed and published in *Journal of Geophysical Research: Oceans:*

Burgers, T. M., Azetsu-Scott, K., Myers, P. G., Else, B. G. T., Miller, L. A., Rysgaard, S., Chan, W., Tremblay, J.-É., Papakyriakou, T. (2024). Unraveling the biogeochemical drivers of aragonite saturation state in Baffin Bay: Insights from the west Greenland continental shelf. *Journal of Geophysical Research: Oceans*, 129, e2024JC021122. https://doi.org/10.1029/2024JC021122

Chapter 6 provides a summary of the main results and important scientific contributions of the research presented in Chapters 3 through 5, as well as a discussion of the limitations of this work and recommendations for future research. Contributions of all co-authors to each research paper are stated in Appendix A of this thesis.

Literature Cited

Ahmed, M., Else, B. G. T., Burgers, T. M., & Papakyriakou, T. (2019). Variability of Surface Water pCO_2 in the Canadian Arctic Archipelago From 2010 to 2016. *Journal of Geophysical Research: Oceans*, *124*, 1876–1896. https://doi.org/10.1029/2018JC014639

AMAP. (2013). *AMAP Assessment 2013: Arctic Ocean Acidification*. Oslo, Norway: Arctic Monitoring and Assessment Programme (AMAP).

AMAP. (2018). *AMAP Assessment 2018: Arctic Ocean Acidification*. Tromsø, Norway: Arctic Monitoring and Assessment Programme (AMAP).

Anderson, L. G., Tanhua, T., Björk, G., Hjalmarsson, S., Jones, E. P., Jutterström, S., et al. (2010). Arctic ocean shelf-basin interaction: An active continental shelf CO_2 pump and its impact on the degree of calcium carbonate solubility. *Deep-Sea Research Part I*, *57*, 869–879. https://doi.org/10.1016/j.dsr.2010.03.012

Ardyna, M., & Arrigo, K. R. (2020). Phytoplankton dynamics in a changing Arctic Ocean. *Nature Climate Change*, *10*, 892–903. https://doi.org/10.1038/s41558-020-0905-y

Arrigo, K. R., & van Dijken, G. L. (2015). Continued increases in Arctic Ocean primary production. *Progress in Oceanography*, *136*, 60–70. https://doi.org/10.1016/j.pocean.2015.05.002

Azetsu-Scott, K., Clarke, A., Falkner, K., Hamilton, J., Jones, E. P., Lee, C., et al. (2010). Calcium carbonate saturation states in the waters of the Canadian Arctic Archipelago and the Labrador Sea. *Journal of Geophysical Research: Oceans*, *115*, C11021. https://doi.org/10.1029/2009JC005917

Bamber, J. L., Tedstone, A. J., King, M. D., Howat, I. M., Enderlin, E. M., van der Broeke, M. R., & Noel, B. (2018). Land Ice Freshwater Budget of the Arctic and North Atlantic Oceans: 1. Data, Methods and Results. *Journal of Geophysical Research: Oceans*, *123*, 1827–1837. https://doi.org/10.1002/2017JC013605

Bates, N., & Mathis, J. (2009). The Arctic Ocean marine carbon cycle: evaluation of air-sea CO_2 exchanges, ocean acidification impacts and potential feedbacks. *Biogeosciences*, *6*, 2433–2459.

Carmack, E. C., Yamamoto-Kawai, M., Haine, T. W. N., Bacon, S., Bluhm, B. A., Lique, C., et al. (2016). Freshwater and its role in the Arctic Marine System: Sources, disposition, storage, export, and physical and biogeochemical consequences in the Arctic and global oceans. *Journal of Geophysical Research: Biogeosciences*, *121*, 675–717. https://doi.org/10.1002/2015JG003140

Denman, K., Christian, J. R., Steiner, N., Portner, H.-O., & Nojiri, Y. (2011). Potential impacts of future ocean acidification on marine ecosystems and fisheries: current knowledge and recommendations for future research. *ICES Journal of Marine Science*, *68*(6), 1019–1029. https://doi.org/10.1093/icesjms/fsr074

DeVries, T. (2022). The Ocean Carbon Cycle. *Annual Review of Environment and Resources*, *47*, 317–341. https://doi.org/10.1146/annurev-environ-120920-111307

Doney, S. C., Fabry, V. J., Feely, R. A., & Kleypas, J. A. (2009). Ocean Acidification : The Other CO_2 Problem. *Annual Review of Marine Science*, *1*, 169–194. https://doi.org/10.1146/annurev.marine.010908.163834

Falkowski, P., Scholes, R. J., Boyle, E., Canadell, J., Canfield, D., Elser, J., et al. (2000). The global carbon cycle: A test of our knowledge of earth as a system. *Science*, *290*(5490), 291–296. https://doi.org/10.1126/science.290.5490.291

Feng, D., Gleason, C. J., Lin, P., Yang, X., Pan, M., & Ishitsuka, Y. (2021). Recent changes to Arctic river

discharge. *Nature Communications*, *12*(6917). https://doi.org/10.1038/s41467-021-27228-1

Friedlingstein, P., O'Sullivan, M., Jones, M. W., Andrew, R. M., Bakker, D. C. E., Hauck, J., et al. (2023). Global Carbon Budget 2023. *Earth System Science Data*, *15*, 5301–5369. https://doi.org/10.5194/essd-15-5301-2023

Grimm, R., Notz, D., Glud, R. N., Rysgaard, S., & Six, K. D. (2016). Assessment of the sea-ice carbon pump: Insights from a three-dimensional ocean-sea-ice-biogeochemical model (MPIOM/HAMOCC). *Elementa: Science of the Anthropocene*, *4*, 000136. https://doi.org/10.12952/journal.elementa.000136

Gruber, N., Bakker, D. C. E., DeVries, T., Gregor, L., Hauck, J., Landschützer, P., et al. (2023). Trends and variability in the ocean carbon sink. *Nature Reviews Earth and Environment*, *4*(2), 119–134. https://doi.org/10.1038/s43017-022-00381-x

Lalande, C., Forest, A., Barber, D. G., Gratton, Y., & Fortier, L. (2009). Variability in the annual cycle of vertical particulate organic carbon export on Arctic shelves: contrasting the Laptev Sea, Northern Baffin Bay and the Beaufort sea. *Continental Shelf Research*, *29*(17), 2157–2165. https://doi.org/10.1016/j.csr.2009.08.009

Leu, E., Mundy, C. J., Assmy, P., Campbell, K., Gabrielsen, T. M., Gosselin, M., et al. (2015). Arctic spring awakening - Steering principles behind the phenology of vernal ice algal blooms. *Progress in Oceanography*, *139*, 151–170. https://doi.org/10.1016/j.pocean.2015.07.012

Luo, Y., Boudreau, B. P., & Mucci, A. (2016). Disparate acidification and calcium carbonate desaturation of deep and shallow waters of the Arctic Ocean. *Nature Communications*, *7*(12821). https://doi.org/10.1038/ncomms12821

Lüthi, D., Le Floch, M., Bereiter, B., Blunier, T., Barnola, J.-M., Siegenthaler, U., et al. (2008). High-resolution carbon dioxide concentration record 650,000-800,000 years before present. *Nature*, *453*, 379–382. https://doi.org/10.1038/nature06949

MacGilchrist, G. A., Garabato, A. C. N., Tsubouchi, T., Bacon, S., Torres-Valdés, S., & Azetsu-Scott, K. (2014). The Arctic Ocean carbon sink. *Deep-Sea Research Part I*, *86*, 39–55. https://doi.org/10.1016/j.dsr.2014.01.002

McClelland, J. W., Déry, S. J., Peterson, B. J., Holmes, R. M., & Wood, E. F. (2006). A pan-arctic evaluation of changes in river discharge during the latter half of the 20th century. *Geophysical Research Letters*, *33*, L06715. https://doi.org/10.1029/2006GL025753

Meinshausen, M., Nicholls, Z. R. J., Lewis, J., Gidden, M. J., Vogel, E., Freund, M., et al. (2020). The shared socio-economic pathway (SSP) greenhouse gas concentrations and their extensions to 2500. *Geoscientific Model Development*, *13*(8), 3571–3605. https://doi.org/10.5194/gmd-13-3571-2020

Mouginot, J., Rignot, E., Bjørk, A. A., van den Broeke, M., Millan, R., Morlighem, M., et al. (2019). Forty-six years of Greenland Ice Sheet mass balance from 1972 to 2018. *Proceedings of the National Academy of Sciences of the United States of America*, *116*(19), 9239–9244. https://doi.org/10.1073/pnas.1904242116

Notz, D., & Stroeve, J. (2018). The Trajectory Towards a Seasonally Ice-Free Arctic Ocean. *Current Climate Change Reports*, *4*, 407–416. https://doi.org/10.1007/s40641-018-0113-2

Petit, J. R., Jouzel, J., Raynaud, D., Barnola, J.-M., Basile, I., Bender, M., et al. (1999). Climate and atmospheric history of the past 420,000 years from the Vostok ice core, Antarctica. *Nature*, *399*, 429–436. https://doi.org/10.1038/20859

Pipko, I. I., Pugach, S. P., Semiletov, I. P., Anderson, L. G., Shakhova, N. E., Gustafsson, Ö., et al. (2017). The spatial and interannual dynamics of the surface water carbonate system and air-sea CO2 fluxes in the outer shelf and slope of the Eurasian Arctic Ocean. *Ocean Science*, *13*, 997–1016. https://doi.org/10.5194/os-13-997-2017

Rysgaard, S., Bendtsen, J., Delille, B., Dieckmann, G. S., Glud, R. N., Kennedy, H., et al. (2011). Sea ice contribution to the air-sea CO_2 exchange in the Arctic and Southern Oceans. *Tellus B*, *63B*(5), 823–830. https://doi.org/10.1111/j.1600-0889.2011.00571.x

Sabine, C. L., Feely, R. A., Gruber, N., Key, R. M., Lee, K., Bullister, J. L., et al. (2004). The oceanic sink for anthropogenic CO_2. *Science*, *305*, 367–71. https://doi.org/10.1126/science.1097403

Steinacher, M., Joos, F., Frölicher, T. L., Plattner, G.-K., & Doney, S. C. (2009). Imminent ocean acidification projected with the NCAR global coupled carbon cycle-climate model. *Biogeosciences*, *6*, 515–533.

Steiner, N. S., Christian, J. R., Six, K. D., Yamamoto, A., & Yamamoto-Kawai, M. (2014). Future ocean acidification in the Canada Basin and surrounding Arctic Ocean from CMIP5 earth system models. *Journal of Geophysical Research: Oceans*, *119*, 332–347. https://doi.org/10.1002/2013JC009069

Stroeve, J. C., Serreze, M. C., Holland, M. M., Kay, J. E., Malanik, J., & Barrett, A. P. (2012). The Arctic's rapidly shrinking sea ice cover: A research synthesis. *Climatic Change*, *110*, 1005–1027. https://doi.org/10.1007/s10584-011-0101-1

Tans, P., & Keeling, R. (2024). Trends in atmospheric carbon dioxide. Retrieved from https://gml.noaa.gov/ccgg/trends/

White, D., Hinzman, L., Alessa, L., Cassano, J., Chambers, M., Falkner, K., et al. (2007). The arctic freshwater system: Changes and impacts. *Journal of Geophysical Research: Biogeosciences*, *112*, G04S54. https://doi.org/10.1029/2006JGO00353

Yamamoto-Kawai, M., McLaughlin, F. A., Carmack, E. C., Nishino, S., & Shimada, K. (2009). Aragonite undersaturation in the Arctic Ocean: Effects of ocean acidification and sea ice melt. *Science*, *326*, 1098–1100.

Yang, W., Zhao, Y., Wu, Y., Chen, Z., Gao, X., Lin, H., et al. (2024). The impact of sea ice melt on the evolution of surface pCO_2 in a polar ocean basin. *Frontiers in Marine Science*, *11*(1307295). https://doi.org/10.3389/fmars.2024.1307295

Yasunaka, S., Siswanto, E., Olsen, A., Hoppema, M., Watanabe, E., Fransson, A., et al. (2018). Arctic Ocean CO_2 uptake: An improved multiyear estimate of the air-sea CO_2 flux incorporating chlorophyll a concentrations. *Biogeosciences*, *15*(6), 1643–1661. https://doi.org/10.5194/bg-15-1643-2018

Zhang, Y., Yamamoto-Kawai, M., & Williams, W. J. (2020). Two Decades of Ocean Acidification in the Surface Waters of the Beaufort Gyre, Arctic Ocean: Effects of Sea Ice Melt and Retreat From 1997–2016. *Geophysical Research Letters*, *47*(3), 1–10. https://doi.org/10.1029/2019GL086421

Chapter 2 Background

2.1 The Marine CO_2 system

A good understanding of the seawater carbonate system is an essential foundation for the research presented in this thesis. Carbon dioxide does not simply dissolve in water like other gases such as nitrogen and oxygen, instead CO_2 subsequently reacts with water and is partitioned among four different chemical species; aqueous carbon dioxide [$CO_{2\ (aq)}$], carbonic acid [H_2CO_3], bicarbonate [HCO_3^-], and carbonate [CO_3^{2-}]. It is difficult to distinguish analytically between the two species [$CO_{2\ (aq)}$] and [H_2CO_3], and therefore the sum of these two species is commonly denoted as CO_2 or $H_2CO_3^*$ in the literature (Zeebe & Wolf-Gladrow, 2001), herein the former of these two notations will be used.

The air-sea exchange of CO_2 represents the first equilibrium equation governing the seawater carbonate system:

$$CO_{2\ (g)} \overset{K_0}{\leftrightarrow} CO_{2\ (aq)} \tag{2.1}$$

where the concentration of dissolved CO_2 is given by Henry's Law, with the equilibrium constant K_0 being the solubility coefficient of CO_2 in seawater (Weiss, 1974; Zeebe & Wolf-Gladrow, 2001). The remainder of the seawater carbonate system is represented by the following equilibria:

$$CO_2 + H_2O \overset{K_1}{\leftrightarrow} HCO_3^- + H^+ \overset{K_2}{\leftrightarrow} CO_3^{2-} + 2H^+ \tag{2.2}$$

where the equilibrium constants K_1 and K_2 are referred to as the first and second dissociation constant of carbonic acid, respectively. All aforementioned equilibrium constants (K_0, K_1, and K_2) are dependent on the temperature and salinity of seawater. Therefore, any changes to these physical properties of seawater will alter the equilibrium state of the carbonate system, and the relative proportions of the carbonate species.

Chemical oceanographers generally utilize four measurable parameters to characterize the seawater carbonate system: dissolved inorganic carbon (DIC), total alkalinity (TA), pH, and the partial pressure of CO_2 in seawater (pCO_2). In practice, only two of these parameters need to be measured in order to quantitatively determine the carbonate system (for a given temperature, salinity, and pressure)(Sarmiento & Gruber, 2006; Zeebe & Wolf-Gladrow, 2001). Each of these four parameters provides a measure of the chemical species that are a part of the carbonate equilibria shown in equation (2.2), either individually or in combination. We can see this in the definitions of these four parameters, which are respectively:

$$DIC = \Sigma CO_2 = [CO_2] + [HCO_3^-] + [CO_3^{2-}] \quad (2.3)$$

$$TA = [HCO_3^-] + 2[CO_3^{2-}] + [B(OH)_4^-] + [OH^-] - [H^+] + minor\ components \quad (2.4)$$

$$pH = -\log [H^+] \quad (2.5)$$

$$pCO_2 = \frac{[CO_2]}{K_0} \quad (2.6)$$

DIC is a measure of the total inorganic carbon present in seawater, and is defined as the sum of all inorganic carbon species. TA represents the excess of proton acceptors (bases) over proton donors (acids) relative to the pH of carbonic acid, and therefore accurately represents the buffering capacity of seawater in terms of dissolved CO_2 (Wolf-Gladrow et al., 2007; Zeebe & Wolf-Gladrow, 2001). Both the parameters DIC and TA are expressed in units of μmol kg^{-1}, and are conservative with respect to changes in state (e.g., temperature, salinity, pressure), whereas measurements of pH and pCO_2 are not. Figure 1.1 in the following section will further illustrate this.

2.1.1 Ocean Acidification

Ocean acidification refers to both the reduction of seawater pH, and the related increase in the solubility of calcium carbonate minerals, due to the uptake of CO_2 from the atmosphere (AMAP, 2013, 2018; Doney et al., 2009). From the carbonate equilibria shown in equations (2.1 and 2.2) we can see that as more CO_2 is dissolved in seawater the equilibrium reactions will shift to the right, releasing more protons, and therefore decreasing the pH of the seawater. However, when CO_2 dissolves in seawater it does not fully dissociate into carbonate ions and protons, and therefore the pH drop is not as drastic as one might expect. This is due to the buffering capacity of the carbonate system, which can be represented by the reaction:

$$CO_2 + CO_3^{2-} + H_2O \rightarrow 2HCO_3^- \quad (2.7)$$

where CO_2 is essentially neutralized by carbonate ions, producing bicarbonate ions. These bicarbonate ions then partially dissociate according to the carbonate equilibrium reactions, decreasing the pH and contributing to ocean acidification. The resulting pH drop is much smaller than it would be in the case of an un-buffered system.

The pH of seawater is dependent upon the relative concentrations of $[CO_2]$, $[HCO_3^-]$, and $[CO_3^{2-}]$ in solution. This is better illustrated by Figure 2.1, which shows the relative abundances of these species

at different pH values, while maintaining a constant DIC. The vertical black line in Figure 2.1 represents the average global surface ocean conditions of today, with a pH of roughly 8.1 (Jiang et al., 2019).

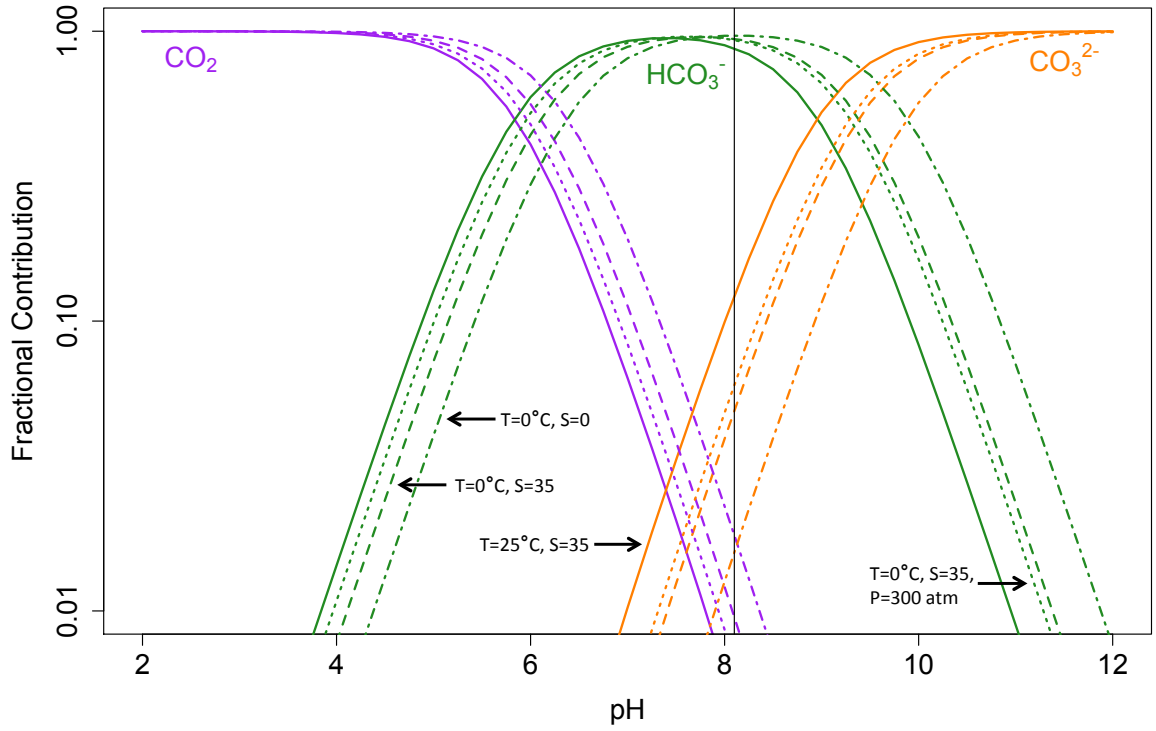

Figure 2.1: Bjerrum plot illustrating changes in carbonate species concentration with changing seawater pH. The vertical black line represents present average surface seawater conditions (AMAP, 2013). Dashed lines represent the effects of temperature, salinity, and pressure on the carbonate system. The reference case, represented by a solid line is T = 25°C, S = 35, and P = 1 atm. DIC = 2100 µmol kg^{-1} in all cases.

From Figure 2.1 it is evident that as more CO_2 is dissolved in seawater the pH will decrease. It can also be seen that with increasing [CO_2] the buffering capacity of seawater is diminished due to coincident decreases in [HCO_3^-] and [CO_3^{2-}]. Figure 2.1 also demonstrates that seawater temperature, salinity, and pressure conditions all play a role in the proportion of DIC that is present as [CO_2], with decreasing temperature and salinity leading to increased [CO_2]. This is a major reason why the cold and fresh surface waters of the Arctic Ocean are especailly susceptible to ocean acidification.

Another equilibrium reaction related to the seawater inorganic carbon system, which has not yet been discussed is the solubility of calcium carbonate ($CaCO_3$) minerals:

$$CaCO_{3\,(s)} \overset{K^*_{sp}}{\longleftrightarrow} Ca^{2+} + CO_3^{2-} \tag{2.8}$$

Where K_{sp}^{*} is the solubility product (or equilibrium constant; also dependent on temperature, salinity, and pressure conditions), which describes the saturation condition of seawater with respect to $CaCO_3$. The saturation state (Ω) of $CaCO_3$ minerals is a measure of the mineral's tendency to dissolve under certain chemical conditions, and is defined as:

$$\Omega = \frac{[Ca^{2+}]\,[CO_3^{2-}]}{K_{sp}^{*}} \tag{2.9}$$

If $\Omega > 1$ then the seawater is considered "supersaturated" with respect to $CaCO_3$, and the mineral is stable, however if $\Omega < 1$ the seawater is "undersaturated" and $CaCO_3$ minerals will tend to dissolve. From the definition of Ω it is clear that as $[CO_3^{2-}]$ decreases (with decreasing pH) seawater will tend towards undersaturation. There are two common polymorphs of $CaCO_3$ that are produced by marine calcifying organisms; calcite and aragonite, with their saturation states denoted as Ω_{Ca} and Ω_{Ar}, respectively. Both of these minerals chemically consist of $CaCO_3$, however their crystal structures are different leading to different chemical properties. Aragonite has a higher solubility product than calcite (Mucci, 1983), meaning that aragonite will dissolve at higher pH conditions relative to calcite. However, some forms of calcite in which Ca^{2+} has been switched for Mg^{2+} (called Mg-calcite) have an even higher solubility product than aragonite (AMAP, 2013).

2.2 Key processes affecting the marine CO_2 system of Arctic waters

There are a number of physical and biogeochemical processes that affect the marine carbon cycle. Ultimately any process that affects either the equilibrium constants (K_0, K_1, K_2), or the concentrations of DIC or TA will alter the seawater carbonate system. A number of the processes are termed "pumps" because they act to pull seawater pCO_2 away from achieving equilibrium with the atmosphere (Sarmiento & Gruber, 2006). Figure 2.2 shows a schematic illustrating a number of such processes acting within the Arctic marine system, divided between those processes that are dominant during the spring/summer and fall/winter seasons.

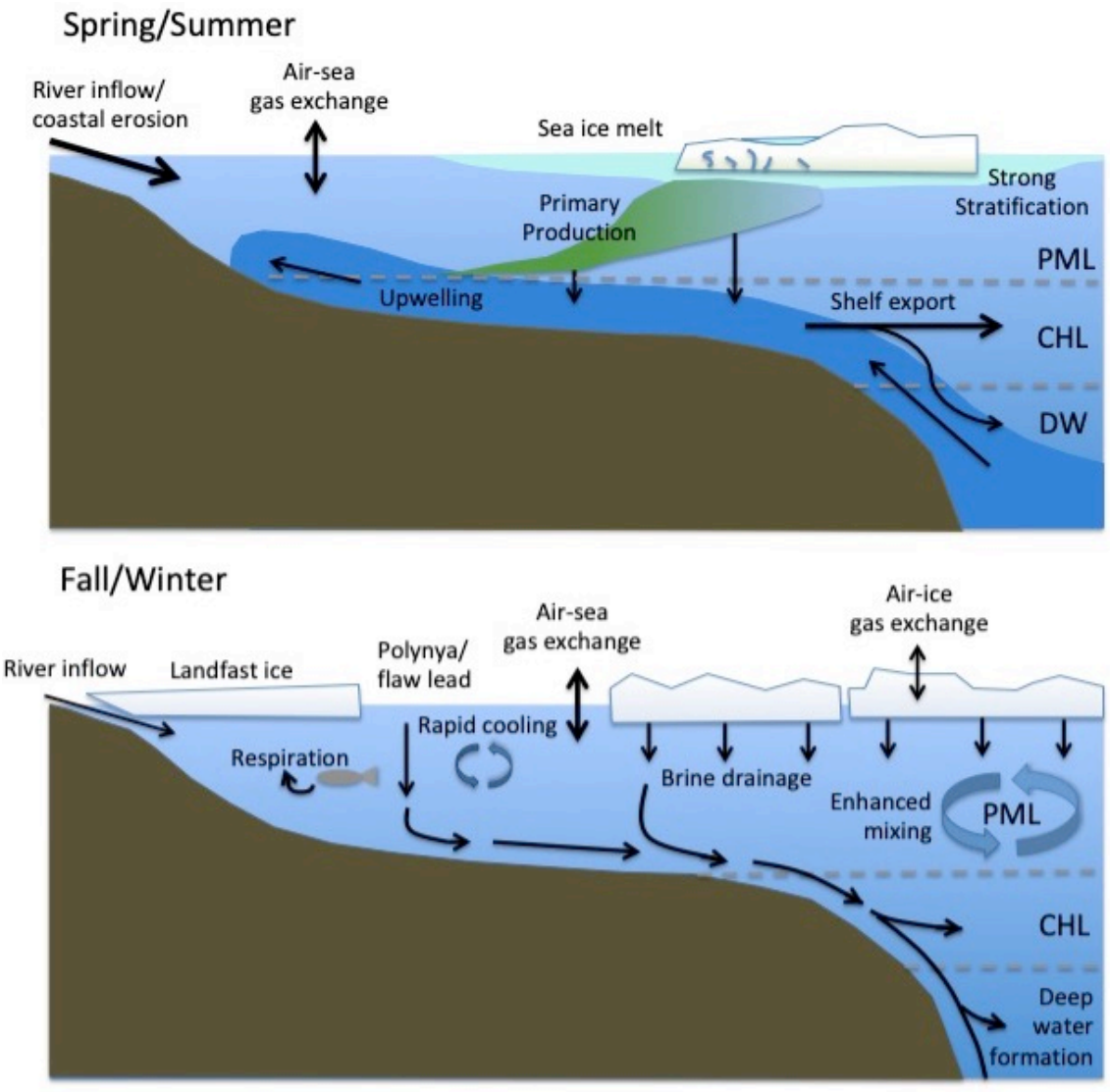

Figure 2.2: Schematic diagrams representing the main processes controlling the flow of carbon in the Arctic Ocean water column. Note that although these diagrams show these processes occurring over a continental shelf, most of the processes depicted also occur over the deep basins (with the exception of direct river inflows/coastal erosion and upwelling at the shelf break). The different water mass layers of the water column are generally denoted here as the polar mixed layer (PML), a cold halocline layer (CHL), and deep waters.

2.2.1 The effect of temperature and the Solubility Pump

It has been previously mentioned that the equilibrium constants governing the seawater carbonate system are sensitive to changes in temperature. Figure 2.1 demonstrates the effects of changing temperature on K_1 and K_2. The solubility of CO_2 in seawater (or K_0) is also impacted by changes in the temperature, affecting the pCO_2 of seawater, and the air-sea exchange of CO_2. The solubility of CO_2 increases with decreasing seawater temperature (Weiss, 1974), shifting the partitioning of the carbonate species to have relatively less $[CO_2]$, and relatively more $[HCO_3^-]$, and $[CO_3^{2-}]$. This allows colder seawater

to take in more CO_2 from the atmosphere relative to warmer seawater. On a local scale, temperature changes of surface waters can alter the source/sink behavior of a region within the Arctic Ocean (Ahmed et al., 2019; Burgers et al., 2017; Nickoloff et al., 2024). On a global scale, this temperature effect combined with the global thermohaline circulation, is referred to as the "solubility pump". Warm waters transiting northwards along the Gulf Stream and into the North Atlantic Drift will undergo a cooling of approximately 20 °C. This more than doubles the solubility of CO_2 in these waters, driving the transfer of atmospheric CO_2 into the surface ocean. In addition, as these waters cool they become more dense and begin to sink in the water column, a process called deep water formation. The combination of these two processes represents the solubility pump, and transports atmospheric CO_2 into the deep ocean, where it can be sequestered for centuries.

Although the solubility pump is strongest in the North Atlantic, it also operates to a smaller extent within the Arctic Ocean itself. Cooling of surface waters during winter, and brine release from sea ice formation create dense waters, which then sink into the halocline layer or deeper (Anderson et al., 2010). Polynyas and flaw leads also represent important sites of deep water formation in the Arctic Ocean, as these areas are devoid of sea ice cover and therefore surface waters continuously lose heat to the atmosphere and generate dense waters (Bâcle et al., 2002; Lobb, 2004; Melling et al., 2001).

Because the solubility pump relies on surface temperature gradients and deep-water formation, it is sensitive to changes in regional heat budgets and freshwater inputs, both of which impact near-surface density gradients. Therefore, the continued trends of warming surface air temperatures and increased freshwater inputs to the surface Arctic Ocean may contribute to a less effective solubility pump in the future.

2.2.2 The Biological Pump

The biological pump describes the net effect of biologically driven processes to decrease DIC in surface waters, and increase DIC at depth. Photosynthesis is the main mechanism through which CO_2 is consumed in surface waters. Photosynthesis is carried out by autotrophic organisms (such as phytoplankton and algae), which utilize dissolved nutrients (such as nitrate and phosphate) and CO_2 in seawater to produce organic matter following the reaction:

$$106\ CO_2 + 16\ HNO_3 + H_3PO_4 + 122\ H_2O \leftrightarrow C_{106}H_{263}O_{110}N_{16}P + 138\ O_{2(g)} \quad (2.10)$$

The coefficients in this chemical equation represent average values first proposed by Alfred Redfield based on measurements from marine organic matter in the North Atlantic (Redfield et al., 1963). These coefficients are commonly referred to as "Redfield Ratios", and represent the average ratios of P:N:C:O_2

(1:16:106:-138) utilization during marine metabolism. Overall, throughout the world ocean the Redfield ratio remains remarkably consistent, although slight variations do exist between different ocean basins based on their unique marine ecosystems and dominant phytoplankton species (Frigstad et al., 2014; Sterner et al., 2008; Tremblay et al., 2002, 2015). “Primary production” refers to the creation of organic matter from inorganic components, which occurs though photosynthesis. The reaction of photosynthesis is limited by the availability of light and nutrients. The requirement for light limits photosynthesis to a region of the upper water column called the euphotic zone, where large phytoplankton blooms often deplete nutrients if there is no local source to replenish the supply. The major sources of nutrients to surface waters are either horizontal advection or upwelling of deep, nutrient-rich waters. River runoff also represents a source of nutrients to the Arctic Ocean, however it is a minor source, only contributing a small fraction of the total nutrients supplied to the Arctic Ocean (Macdonald et al., 2010).

Respiration (also called remineralization) is essentially the reverse reaction of photosynthesis, whereby heterotrophic organisms (including zooplankton, fish, or bacteria) break down organic matter, releasing CO_2 and nutrients back into the water column. This process can occur both within the surface layer and the deep ocean, as heterotrophic organisms do not require light. The balance between primary production and respiration is referred to as net community production (NCP), and is used to approximate the export of carbon out of the surface layer. Any respiration occurring within the surface layer can directly contribute CO_2 and nutrients to be used again through photosynthesis. This process is termed “regenerated production”, whereas photosynthesis utilizing nutrients that have been externally added to surface waters is termed “new production”. The fraction of the total primary production (new + regenerated) that eventually exits the surface ocean (the export production) is what ultimately contributes to the biological pump. This export may be the result of sinking particulate organic matter (defined as particles larger than 0.5 µm), or by the vertical mixing of dissolved organic matter (classified as particles < 0.5 µm; (Emerson & Hedges, 2011)). Much of this exported organic matter will be remineralized in the water column, with less than 1% making it all the way to the bottom sediments (Sarmiento & Gruber, 2006). The overall effect of this vertical transport and remineralization of organic matter is to increase the DIC and lower the pH of deep waters, whereas primary production in the surface ocean will have the opposite effect, decreasing DIC and increasing pH.

Primary production is a highly seasonal process in the Arctic Ocean. This is due to the high-latitude location of this ocean, which results in a polar winter with 24-hr darkness, and a summer with 24-hr sunlight. During winter the production of sea ice brine mixes the surface water column, replenishing it with nutrients from deeper waters. Excess respiration in the water column during winter also contributes

to the stock of nutrients that will be available in spring. However, once spring begins sea ice cover still limits light transmission into the surface waters, holding back the beginning of primary production until sufficient light can penetrate through the ice cover. Microscopic algae living in the sea ice are often the first organisms to start primary production in spring, however a recent study indicates that they may not contribute significantly to the uptake of CO_2 from surface seawaters (Else et al., 2019). Often it is the formation of melt-ponds that allows sufficient light transmission into the surface ocean for primary production by phytoplankton (Matthes et al., 2020). Inputs of sea ice meltwater also support phytoplankton bloom growth by enhancing surface stratification and providing a stable habitat. Under-ice phytoplankton blooms have been found to be a common occurrence in the Arctic Ocean (Arrigo et al., 2012; Horvat et al., 2017; Mundy et al., 2009, 2014). However, the highest rates of primary production have been found associated with receding sea ice edges. These ice-edge blooms have been found to account for up to 50-65% of annual primary production over the Barents and Bering Sea shelves (Perrette et al., 2011; Sakshaug, 2004). These intense blooms are often short-lived as they quickly deplete the stock of nutrients available in the surface waters, and stratification prevents replenishment from deeper waters (Tremblay & Gagnon, 2009; Tremblay et al., 2008). At this point some primary production may continue in deeper waters, if light is able to penetrate deep enough. These so-called sub-surface chlorophyll maxima (SCMs) often occur in association with the nitracline, and have been found to contribute substantially to primary production during the summer season (Brown et al., 2015; Martin et al., 2010). However, the question of how much SCMs contribute to the total annual primary production in the Arctic Ocean still remains an open question.

2.2.3 The Sea Ice Pump

The chemical processes occurring during sea ice formation and melt also help export CO_2 to depth, representing a “sea ice pump”. There are two related processes that control the sea ice pump; (1) the rejection of DIC-rich brine during sea ice formation, and (2) the formation and dissolution of ikaite. When sea ice forms from seawater, impurities such as salts, gases, and particles are expelled as much as possible from the sea ice matrix. DIC is similarly treated as an impurity and is rejected from the sea ice matrix through brine channels. As dense brines drain from sea ice and sink in the water column they carry with them significant amounts of DIC (Brown et al., 2015; Miller et al., 2011). Within the sea ice, $CaCO_3$ can precipitate from the cold salty brine in the form of ikaite crystals (Rysgaard et al., 2011). Ikaite formation leads to decreases in both the DIC and TA of the brine solution, with TA decreasing by twice as much as DIC (because of the loss of two negative charges associated with the CO_3^{2-} ion). If the ikaite crystals remain within the ice as brine drainage occurs, this would enrich the sea ice in TA relative to

DIC. Then, in spring, when the sea ice begins to melt and the ikaite crystals dissolve, there would be an excess of TA over DIC within the sea-ice meltwater that would lower the pCO_2 of surface waters and encourage atmospheric CO_2 uptake. The uptake of CO_2 into surface waters would then feed more carbon export to depth the following winter when sea ice forms again. However, research on the carbonate chemistry of sea ice and the formation of ikaite has found both to be spatially and temporally variable, and therefore it remains uncertain how big of a role ikaite formation plays in influencing brine carbonate chemistry and CO_2 fluxes (Geilfus et al., 2016; Grimm et al., 2016).

2.2.4 Freshwater Inputs

The Arctic Ocean is disproportionally impacted by freshwater inputs compared to other oceans, as it receives 11% of global river runoff despite only accounting for 1% of global seawater volume, or 2.8% of the area (Carmack et al., 2016; Shiklomanov, 2000). Freshwater is also transported indirectly into the Arctic Ocean via the inflow of Pacific water, which is fresher than its Atlantic counterpart. This contributes to the Pacific-influenced sectors of the Arctic Ocean having an overall lower buffering capacity (lower TA), and being more sensitive to ocean acidification. These large inputs of freshwater result in widespread stratification of the top hundred meters of the water column, and affects biogeochemical processes by inhibiting exchange between the surface mixed layer and deeper waters.

In recent decades climate change has led to further increases in freshwater inputs to the Arctic Ocean, from riverine sources (McClelland et al., 2006), sea-ice melt (Yamamoto-Kawai et al., 2009), and also glacial ice melt (Bamber et al., 2018; Rignot et al., 2011). All aforementioned freshwater sources are characterized by lower salinity and TA in comparison to seawater, and therefore act to reduce the buffering capacity when mixed with seawater, leading to greater decreases in pH and Ω with added CO_2 (Carmack et al., 2016). Additionally, these freshwater sources have lower dissolved [Ca^{2+}] in comparison to seawater, and this combined with low TA further contributes to lowering Ω. Figure 2.3 depicts how Ω_{Ar} is affected by dilution by various freshwater sources. In making Figure 2.3 it was assumed that $TA_{glacial}$ and $DIC_{glacial}$ = 50 µmol kg^{-1} based on the field measurements of icebergs presented in Meire et al. [2015]. The TA and DIC of sea-ice melt has been well characterized and is also quite low (TA_{SIM} and DIC_{SIM} = 300 µmol kg^{-1}) (Yamamoto-Kawai et al., 2009), whereas river runoff exhibits the highest TA and DIC of these freshwater sources (TA_{river} and DIC_{river} = 800 µmol kg^{-1}) (Azetsu-Scott et al., 2010), however is still relatively low when compared to seawater (TA_{sea} and DIC_{sea} = ~2000 µmol kg^{-1}). Observational studies in the Arctic Ocean have already detected areas impacted by sea ice melt water and/or riverine inputs which are sufficiently corrosive to dissolve aragonite ($\Omega_{Ar} < 1$) (Bates et al., 2009; Yamamoto-Kawai et al., 2009).

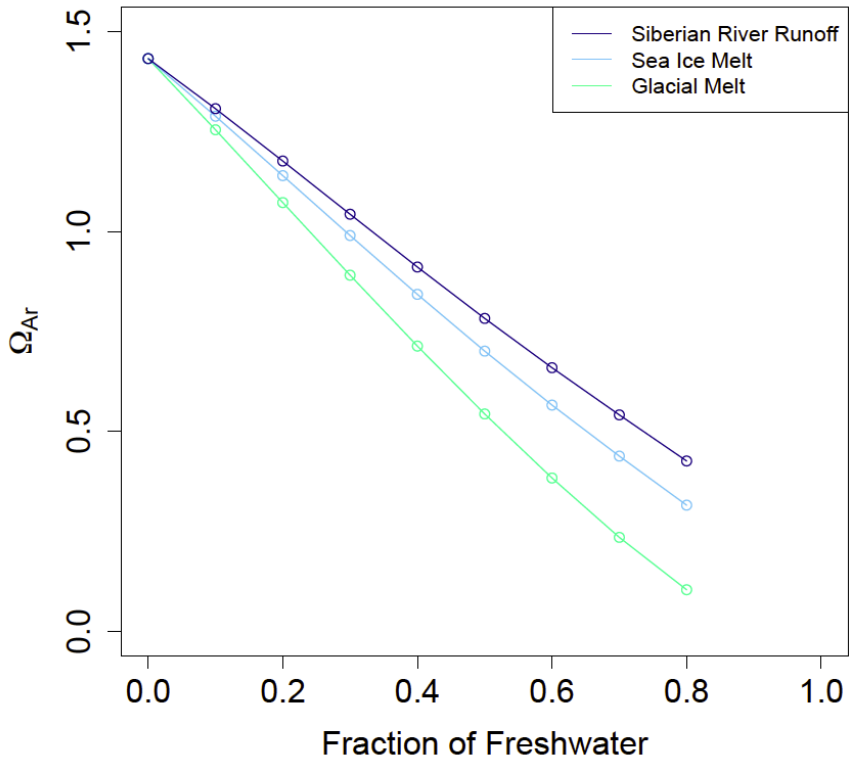

Figure 2.3: Effect of freshwater inputs on the saturation state of aragonite (Ω_{Ar}) in the Arctic Ocean.

2.2.5 Gas Exchange

Air-sea gas exchange is the process constantly trying to achieve equilibrium between the pCO_2 in both the surface seawater and the overlying atmosphere. Therefore, many of the other processes discussed previously contribute to promoting the transfer of atmospheric CO_2 into the surface ocean (if their net effect is to decrease the pCO_2 of surface waters). Since the average pCO_2 of surface waters in the Arctic Ocean is lower than that of the atmosphere, the Arctic Ocean represents a net sink of CO_2 (Yasunaka et al., 2018). The timescale that is needed for surface water pCO_2 to equilibrate with the atmosphere turns out to be much longer than the equilibration timescale of other gases. This is because added atmospheric CO_2 needs to equilibrate with the entire DIC pool in the surface waters. This results in the equilibration timescale for CO_2 in the surface ocean being on the order of 6 months, compared to that of O_2, which is approximately 14 days (Sarmiento & Gruber, 2006).

Air-sea gas exchange is the primary driver of ocean acidification in the surface waters of the Arctic Ocean (AMAP, 2013, 2018). This process when combined with a decreasing summer sea-ice extent, and the low buffering capacity of increased freshwater inputs is likely to drive considerable acidification of

surface waters in the future. This may be detrimental for certain species with calcium carbonate shells that inhabit surface waters, such as coccolithophores, foraminifera and pteropods (AMAP, 2013; Comeau et al., 2012; Niemi et al., 2021). As climate change progresses, increased stratification from freshwater inputs may limit the CO_2 uptake capacity of certain region, by limiting the volume of water available in the surface mixed layer for interaction with the atmosphere.

Literature Cited

Ahmed, M., Else, B. G. T., Burgers, T. M., & Papakyriakou, T. (2019). Variability of Surface Water pCO_2 in the Canadian Arctic Archipelago From 2010 to 2016. *Journal of Geophysical Research: Oceans*, *124*, 1876–1896. https://doi.org/10.1029/2018JC014639

AMAP. (2013). *AMAP Assessment 2013: Arctic Ocean Acidification*. Oslo, Norway: Arctic Monitoring and Assessment Programme (AMAP).

AMAP. (2018). *AMAP Assessment 2018: Arctic Ocean Acidification*. Tromsø, Norway: Arctic Monitoring and Assessment Programme (AMAP).

Anderson, L. G., Tanhua, T., Björk, G., Hjalmarsson, S., Jones, E. P., Jutterström, S., et al. (2010). Arctic ocean shelf-basin interaction: An active continental shelf CO_2 pump and its impact on the degree of calcium carbonate solubility. *Deep-Sea Research Part I*, *57*, 869–879. https://doi.org/10.1016/j.dsr.2010.03.012

Arrigo, K. R., Perovich, D. K., Pickart, R. S., Brown, Z. W., Van Dijken, G. L., Lowry, K. E., et al. (2012). Massive phytoplankton blooms under arctic sea ice. *Science*, *336*(6087), 1408. https://doi.org/10.1126/science.1215065

Azetsu-Scott, K., Clarke, A., Falkner, K., Hamilton, J., Jones, E. P., Lee, C., et al. (2010). Calcium carbonate saturation states in the waters of the Canadian Arctic Archipelago and the Labrador Sea. *Journal of Geophysical Research: Oceans*, *115*, C11021. https://doi.org/10.1029/2009JC005917

Bâcle, J., Carmack, E. C., & Ingram, R. G. (2002). Water column structure and circulation under the North Water during spring transition: April-July 1998. *Deep-Sea Research Part II: Topical Studies in Oceanography*, *49*, 4907–4925. https://doi.org/10.1016/S0967-0645(02)00170-4

Bamber, J. L., Tedstone, A. J., King, M. D., Howat, I. M., Enderlin, E. M., van der Broeke, M. R., & Noel, B. (2018). Land Ice Freshwater Budget of the Arctic and North Atlantic Oceans: 1. Data, Methods and Results. *Journal of Geophysical Research: Oceans*, *123*, 1827–1837. https://doi.org/10.1002/2017JC013605

Bates, N. R., Mathis, J. T., & Cooper, L. W. (2009). Ocean acidification and biologically induced seasonality of carbonate mineral saturation states in the western Arctic Ocean. *Journal of Geophysical Research*, *114*, C11007. https://doi.org/10.1029/2008JC004862

Brown, K. A., Miller, L. A., Mundy, C. J., Papakyriakou, T., Francois, R., Gosselin, M., et al. (2015). Inorganic carbon system dynamics in landfast Arctic sea ice during the early-melt period. *Journal of Geophysical Research: Oceans*, *120*. https://doi.org/10.1002/2014JC010620

Brown, Z. W., Lowry, K. E., Palmer, M. A., van Dijken, G. L., Mills, M. M., Pickart, R. S., & Arrigo, K. R. (2015). Characterizing the subsurface chlorophyll a maximum in the Chukchi Sea and Canada Basin. *Deep-Sea Research Part II: Topical Studies in Oceanography*, *118*, 88–104. https://doi.org/10.1016/j.dsr2.2015.02.010

Burgers, T. M., Miller, L. A., Thomas, H., Else, B. G. T., Gosselin, M., & Papakyriakou, T. (2017). Surface water pCO_2 variations and sea-air CO_2 fluxes during summer in the eastern Canadian Arctic. *Journal of Geophysical Research: Oceans*, *122*(12), 9663–9678. https://doi.org/10.1002/2017JC013250

Carmack, E. C., Yamamoto-Kawai, M., Haine, T. W. N., Bacon, S., Bluhm, B. A., Lique, C., et al. (2016). Freshwater and its role in the Arctic Marine System: Sources, disposition, storage, export, and physical and biogeochemical consequences in the Arctic and global oceans. *Journal of Geophysical Research: Biogeosciences*, *121*, 675–717. https://doi.org/10.1002/2015JG003140

Comeau, S., Gattuso, J.-P., Nisumaa, A.-M., & Orr, J. (2012). Impact of aragonite saturation state changes on migratory pteropods. *Proceedings of the Royal Society B*, *279*(1729), 732–738. https://doi.org/10.1098/rspb.2011.0910

Doney, S. C., Fabry, V. J., Feely, R. A., & Kleypas, J. A. (2009). Ocean Acidification : The Other CO_2 Problem. *Annual Review of Marine Science*, *1*, 169–194. https://doi.org/10.1146/annurev.marine.010908.163834

Else, B. G. T., Whitehead, J. J., Galindo, V., Ferland, J., Mundy, C. J., Gonski, S. F., et al. (2019). Response of the Arctic marine inorganic carbon system to ice algae and under-ice phytoplankton blooms: A case study along the fast-ice edge of Baffin Bay. *Journal of Geophysical Research: Oceans*. https://doi.org/10.1029/2018JC013899

Emerson, S. R., & Hedges, J. I. (2011). *Chemical Oceanography and the Marine Carbon Cycle*. New York: Cambridge University Press.

Frigstad, H., Andersen, T., Bellerby, R. G. J., Silyakova, A., & Hessen, D. O. (2014). Variation in the seston C:N ratio of the Arctic Ocean and pan-Arctic shelves. *Journal of Marine Systems*, *129*, 214–223. https://doi.org/10.1016/j.jmarsys.2013.06.004

Geilfus, N. X., Galley, R. J., Else, B. G. T., Campbell, K., Papakyriakou, T., Crabeck, O., et al. (2016). Estimates of ikaite export from sea ice to the underlying seawater in a sea ice-seawater mesocosm. *Cryosphere*, *10*, 2173–2189. https://doi.org/10.5194/tc-10-2173-2016

Grimm, R., Notz, D., Glud, R. N., Rysgaard, S., & Six, K. D. (2016). Assessment of the sea-ice carbon pump: Insights from a three-dimensional ocean-sea-ice-biogeochemical model (MPIOM/HAMOCC). *Elementa: Science of the Anthropocene*, *4*, 000136. https://doi.org/10.12952/journal.elementa.000136

Horvat, C., Jones, D. R., Iams, S., Schroeder, D., Flocco, D., & Feltham, D. (2017). The frequency and extent of sub-ice phytoplankton blooms in the Arctic Ocean. *Science Advances*, *3*(e1601191). https://doi.org/10.1126/sciadv.1601191

Jiang, L. Q., Carter, B. R., Feely, R. A., Lauvset, S. K., & Olsen, A. (2019). Surface ocean pH and buffer capacity: past, present and future. *Scientific Reports*, *9*(18624). https://doi.org/10.1038/s41598-019-55039-4

Lobb, J. (2004). *On Arctic and Atlantic halocline interactions in the Baffin Bay*. University of Victoria.

Macdonald, R. W., Anderson, L. G., Christensen, J. P., Miller, L. A., Semiletov, I. P., & Stein, R. (2010). The Arctic Ocean. In K.-K. Lui, L. Atkinson, R. Quinones, & L. Talaue-McManus (Eds.), *Carbon and nutrient fluxes in continental margins* (pp. 291–303). Heidelberg: Springer.

Martin, J., Tremblay, J. É., Gagnon, J., Tremblay, G., Lapoussière, A., Jose, C., et al. (2010). Prevalence, structure and properties of subsurface chlorophyll maxima in Canadian Arctic waters. *Marine Ecology Progress Series*, *412*, 69–84. https://doi.org/10.3354/meps08666

Matthes, L. C., Mundy, C. J., L.-Girard, S., Babin, M., Verin, G., & Ehn, J. K. (2020). Spatial Heterogeneity as a Key Variable Influencing Spring-Summer Progression in UVR and PAR Transmission Through Arctic Sea Ice. *Frontiers in Marine Science*, *7*(183). https://doi.org/10.3389/fmars.2020.00183

McClelland, J. W., Déry, S. J., Peterson, B. J., Holmes, R. M., & Wood, E. F. (2006). A pan-arctic evaluation of changes in river discharge during the latter half of the 20th century. *Geophysical Research Letters*, *33*, L06715. https://doi.org/10.1029/2006GL025753

Meire, L., Søgaard, D. H., Mortensen, J., Meysman, F. J. R., Soetaert, K., Arendt, K. E., et al. (2015).

Glacial meltwater and primary production are drivers of strong CO_2 uptake in fjord and coastal waters adjacent to the Greenland Ice Sheet. *Biogeosciences*, *12*, 2347–2363. https://doi.org/10.5194/bg-12-2347-2015

Melling, H., Gratton, Y., & Ingram, G. (2001). Ocean circulation within the North Water polynya of Baffin Bay. *Atmosphere - Ocean*, *39*(3), 301–325. https://doi.org/10.1080/07055900.2001.9649683

Miller, L. A., Carnat, G., Else, B. G. T., Sutherland, N., & Papakyriakou, T. N. (2011). Carbonate system evolution at the Arctic Ocean surface during autumn freeze-up. *Journal of Geophysical Research*, *116*, C00G04. https://doi.org/10.1029/2011JC007143

Mucci, A. (1983). The solubility of calcite and aragonite in seawater at various salinities, temperatures, and one atmosphere total pressure. *American Journal of Science*, *283*(7), 780–799. https://doi.org/10.2475/ajs.283.7.780

Mundy, C. J., Gosselin, M., Ehn, J., Gratton, Y., Rossnagel, A., Barber, D. G., et al. (2009). Contribution of under-ice primary production to an ice-edge upwelling phytoplankton bloom in the Canadian Beaufort Sea. *Geophysical Research Letters*, *36*, L17601. https://doi.org/10.1029/2009GL038837

Mundy, C. J., Gosselin, M., Gratton, Y., Brown, K., Galindo, V., Campbell, K., et al. (2014). Role of environmental factors on phytoplankton bloom initiation under landfast sea ice in Resolute Passage, Canada. *Marine Ecology Progress Series*, *497*, 39–49. https://doi.org/10.3354/meps10587

Niemi, A., Bednaršek, N., Michel, C., Feely, R. A., Williams, W., Azetsu-Scott, K., et al. (2021). Biological Impact of Ocean Acidification in the Canadian Arctic: Widespread Severe Pteropod Shell Dissolution in Amundsen Gulf. *Frontiers in Marine Science*, *8*(March), 1–16. https://doi.org/10.3389/fmars.2021.600184

Perrette, M., Yool, A., Quartly, G. D., & Popova, E. E. (2011). Near-ubiquity of ice-edge blooms in the Arctic. *Biogeosciences*, *8*, 515–524. https://doi.org/10.5194/bg-8-515-2011

Redfield, A. C., Ketchum, B. H., & Richards, F. A. (1963). The Influence of Organisms on the Composition of Sea-water. In M. Hill (Ed.), *The Sea* (pp. 26–77). New York: Wiley Interscience.

Rignot, E., Velicogna, I., van den Broeke, M. R., Monaghan, A., & Lenaerts, J. (2011). Acceleration of the contribution of the Greenland and Antarctic ice sheets to sea level rise. *Geophysical Research Letters*, *38*, L05503. https://doi.org/10.1029/2011GL046583

Rysgaard, S., Bendtsen, J., Delille, B., Dieckmann, G. S., Glud, R. N., Kennedy, H., et al. (2011). Sea ice contribution to the air-sea CO_2 exchange in the Arctic and Southern Oceans. *Tellus B*, *63B*(5), 823–830. https://doi.org/10.1111/j.1600-0889.2011.00571.x

Sakshaug, E. (2004). Primary and Secondary Production in the Arctic Seas. In R. W. Macdonald & R. Stein (Eds.), *The Organic Carbon Cycle in the Arctic Ocean* (4th ed., pp. 57–81). Heidelberg: Springer.

Sarmiento, J. L., & Gruber, N. (2006). Carbon Cycle. In *Ocean Biogeochemical Dynamics* (pp. 318–349). Princeton: Princeton University Press. https://doi.org/10.1063/1.2754608

Shiklomanov, I. A. (2000). Appraisal and Assessment of World Water Resources. *Water International*, *25*(1), 11–32. https://doi.org/10.1080/02508060008686794

Sterner, R. W., Andersen, T., Elser, J. J., Hessen, D. O., Hood, J. M., McCauley, E., & Urabe, J. (2008). Scale-dependent carbon:nitrogen:phosphorus seston stoichimetry in marine and freshwaters. *Limnology and Oceanography*, *53*(3), 1169–1180.

Tremblay, J.-É., & Gagnon, J. (2009). The effects of irradiance and nutrient supply on the productivity of

Arctic waters: a perspective on climate change. In J. C. J. Nihoul & A. G. Kostianoy (Eds.), *Influence of Climate Change on the Changing Arctic and Sub-Arctic Conditions* (pp. 73–92). Berlin: Springer Science. https://doi.org/10.1007/978-1-4020-9460-6_7

Tremblay, J.-É., Gratton, Y., Carmack, E. C., Payne, C. D., & Price, N. M. (2002). Impact of the large-scale Arctic circulation and the North Water Polynya on nutrient inventories in Baffin Bay. *Journal of Geophysical Research*, *107*(C8), 3112. https://doi.org/10.1029/2000JC000595

Tremblay, J.-É., Anderson, L. G., Matrai, P., Coupel, P., Bélanger, S., Michel, C., & Reigstad, M. (2015). Global and regional drivers of nutrient supply, primary production and CO_2 drawdown in the changing Arctic Ocean. *Progress in Oceanography*, *139*, 171–196. https://doi.org/10.1016/j.pocean.2015.08.009

Tremblay, J. É., Simpson, K., Martin, J., Miller, L., Gratton, Y., Barber, D., & Price, N. M. (2008). Vertical stability and the annual dynamics of nutrients and chlorophyll fluorescence in the coastal, southeast Beaufort Sea. *Journal of Geophysical Research: Oceans*, *113*, C07S90. https://doi.org/10.1029/2007JC004547

Weiss, R. F. (1974). Carbon dioxide in water and seawater: the solubility of a non-ideal gas. *Marine Chemistry*, *2*(3), 203–215. https://doi.org/10.1016/0304-4203(74)90015-2

Wolf-Gladrow, D. A., Zeebe, R. E., Klaas, C., Körtzinger, A., & Dickson, A. G. (2007). Total alkalinity: The explicit conservative expression and its application to biogeochemical processes. *Marine Chemistry*, *106*, 287–300. https://doi.org/10.1016/j.marchem.2007.01.006

Yamamoto-Kawai, M., McLaughlin, F. A., Carmack, E. C., Nishino, S., & Shimada, K. (2009). Aragonite undersaturation in the Arctic Ocean: Effects of ocean acidification and sea ice melt. *Science*, *326*, 1098–1100.

Yasunaka, S., Siswanto, E., Olsen, A., Hoppema, M., Watanabe, E., Fransson, A., et al. (2018). Arctic Ocean CO_2 uptake: An improved multiyear estimate of the air-sea CO_2 flux incorporating chlorophyll a concentrations. *Biogeosciences*, *15*(6), 1643–1661. https://doi.org/10.5194/bg-15-1643-2018

Zeebe, R., & Wolf-Gladrow, D. (2001). *CO_2 in Seawater: Equilibrium, Kinetics, Isotopes*. *Elsevier Oceanography Series* (Vol. 65). Elsevier.

Chapter 3 Estimates of net community production from multiple approaches surrounding the spring ice-edge bloom in Baffin Bay

This chapter was published in the journal *Elementa: Science of the Anthropocene*.

Burgers, T. M., Tremblay, J.-É., Else, B. G. T., & Papakyriakou, T. N. (2020). Estimates of net community production from multiple approaches surrounding the spring ice-edge bloom in Baffin Bay. *Elementa: Science of the Anthropocene*, 8(1):013. https://doi.org/10.1525/elementa.013

Please see Appendix A for the contributions of each collaborating author to this peer-reviewed paper.

Abstract

Measurements of net community production (NCP) provide an upper constraint on the strength of the oceanic biological pump, the dominant mechanism removing CO_2 from the surface ocean and sequestering it at depth. In this investigation our objectives are to describe the spatial and temporal variability of NCP associated with the spring ice-edge bloom in Baffin Bay, and identify the key environmental drivers controlling its variability. Using data collected between 9 June and 10 July 2016, we estimated NCP based on: (1) underway measurements of surface water oxygen to argon ratios (O_2/Ar), (2) underway measurements of the partial pressure of CO_2 (pCO_2), and (3) seasonal nitrate drawdown from discrete samples. These multiple approaches all displayed high NCP (up to 5.7 mol C m^{-2}) in eastern Baffin Bay, associated with modified Atlantic waters, and low NCP (< 1 mol C m^{-2}) in the presence of Arctic outflow waters in western Baffin Bay. Arctic outflow waters were characterized by low surface salinities and nitrate concentrations, suggesting that high freshwater content may have limited the nutrient availability of these waters. Different integration depths and timescales associated with each NCP approach were exploited to understand the temporal progression and succession of the bloom, revealing that the bloom was initiated under-ice up to 15 days prior to ice retreat, and that a large portion of NCP in eastern Baffin Bay (potentially up to 70%) was driven by primary production occurring below the surface mixed layer.

3.1 Introduction

Like other Arctic Seas, the waters of Baffin Bay are currently transforming under the influence of anthropogenic climate change. Sea-ice cover in Baffin Bay continues to decline in thickness and longevity, with the ice-free season growing longer (Bliss et al., 2019; Landy et al., 2017; Tang et al., 2004). This change is resulting in warmer sea surface temperatures, especially in eastern Baffin Bay (Timmermans & Ladd, 2018), and earlier commencement of spring phytoplankton blooms (Bélanger et al., 2013; Kahru et al., 2011). Additionally, freshwater inputs to Baffin Bay continue to increase from various sources, including increasingly fresh surface waters exported from the central Arctic Ocean (Carmack et al., 2016; Haine et al., 2015), and increasing glacial meltwater inputs from the Greenland ice sheet (Bamber et al., 2018; Dahl-Jensen et al., 2011). Combined, these changes will no doubt affect the primary production regime in Baffin Bay, and have consequent effects for marine ecosystems and the marine carbon cycle in this region.

Observations indicate that the Arctic Ocean represents a net sink of atmospheric CO_2 (both natural and anthropogenic), absorbing approximately 166 –180 Tg C yr^{-1} (MacGilchrist et al., 2014; Yasunaka et al., 2018). Primary production and the biological pump are key processes driving this net CO_2 uptake through the production and subsequent export of organic carbon from the surface into the deep ocean, where it can be sequestered from interaction with the atmosphere. Autotrophic organisms such as algae and phytoplankton utilize dissolved inorganic carbon and light to produce organic carbon, a portion of which may then be consumed and respired by heterotrophic organisms, converting organic carbon back into inorganic carbon. Net community production (NCP) is defined as the difference between gross primary production and ecosystem respiration. As such, NCP represents an upper constraint on the amount of organic carbon exported to depth (the biological pump), assuming that the storage of organic carbon in the surface mixed layer is modest over large spatial and temporal scales (Falkowski et al., 2003).

Primary production is a highly seasonal process in the Arctic Ocean and its adjacent seas, due to the requirements for sufficient light and nutrients. The retreat and melting of sea ice in the spring drives strong primary production due to the enhanced light availability and stratification from sea-ice meltwater in the marginal ice zone (Barber et al., 2015; Leu et al., 2015). Enhanced stratification surrounding the ice-edge limits the depth of vertical mixing, allowing phytoplankton to remain near the surface with sufficient light for photosynthesis. Ice-edge blooms are a common occurrence throughout the Arctic Ocean (Perrette et al., 2011), and are generally intense and short-lived features that quickly deplete the nutrient stock within the shallow surface mixed layer (Niebauer, 1991; Sakshaug, 2004; Tremblay et al.,

2008). Much still remains unknown, however, about the conditions required to trigger the phytoplankton spring bloom in the presence of sea ice cover. In the case of ice-edge blooms, increased light availability and stratification are occurring simultaneously, creating an ideal setting for bloom initiation. However, many instances of under-ice blooms have now been observed throughout the Arctic Ocean (Arrigo et al., 2012; Assmy et al., 2017; Fortier et al., 2002; Mundy et al., 2009), demonstrating that cracks, leads, melt ponds, or thin ice without snow cover can allow for sufficient light transmission to initiate under-ice pelagic blooms. It is now estimated that nearly 30% of the ice-covered Arctic Ocean permits under-ice blooms in July (Horvat et al., 2017). This raises the question of whether enhanced stratification is a necessity to initiate a bloom, or whether sufficient light availability is enough.

In the post-bloom phase, after the surface bloom has depleted the nutrient stock of the surface mixed layer, primary production may continue in deeper waters as subsurface chlorophyll maxima (SCM's). These features are quite common in the post-bloom Arctic Ocean (Ardyna et al., 2013; Brown et al., 2015; Martin et al., 2010; Tremblay et al., 2008) and will cause the nitracline to deepen as they continue to consume nutrients at greater depths. Ultimately, the SCM will settle at a depth between the nitracline and the bottom of the euphotic zone, balancing the requirements for light and nutrients. Despite the known ubiquity of SCM's, much remains to be understood about their ecological significance, and their contribution to NCP.

Recent investigations focused in northern Baffin Bay (in the historical location of the North Water Polynya) have documented decreases in annual NCP and phytoplankton biomass, attributing this decrease to freshening and increased water column stratification (Bergeron & Tremblay, 2014; Blais et al., 2017). However, these results may not be widely applicable to all of Baffin Bay, as water mass characteristics and sea ice conditions vary widely from east to west. In fact, using a satellite-based model to assess primary production trends from 1998 to 2010, Bélanger et al. (2013) showed positive trends in primary production rates in southeastern Baffin Bay, despite negative trends in northern Baffin Bay. The synthesis study of Codispoti et al. (2013) was the last investigation to specifically present estimates of NCP in southern Baffin Bay. However, the results of that synthesis study were calculated using data from relatively few sampling stations averaged over large spatial scales, and winter nutrient concentrations used as a baseline to estimate NCP over the West Greenland shelf were collected between the years of 1962 and 1987. Therefore, we predict the NCP estimates of Codispoti et al. (2013) will differ greatly from those calculated with more recent measurements. Further, the unique set of methods we employ in this investigation allows us to provide additional information on the temporal progression of the bloom across Baffin Bay, and to distinguish NCP contributions from the surface mixed layer and SCM.

In this study we present springtime estimates of NCP across southern Baffin Bay, associated with a receding ice cover and a transient ice-edge bloom. The main objectives of this study are to describe spatial and temporal variability of NCP in Baffin Bay, and to provide insight into the environmental factors driving this variability. In order to infer information about the spatial and temporal progression of the bloom, we make use of three different approaches of estimating NCP that integrate over different time and depth scales. Our three approaches to estimating NCP rely on; (1) sea surface measurements of the oxygen to argon ratio (O_2/Ar), (2) sea surface measurements of the partial pressure of CO_2 (pCO_2), and (3) discrete water column measurements of nitrate concentrations.

3.2 Oceanographic Setting

The oceanographic setting of Baffin Bay plays a critical role in determining the amount of primary production that is able to occur, as sea ice conditions and water mass circulation patterns dictate the availability of light and nutrients in the surface ocean. Within Baffin Bay there is an overall cyclonic circulation comprised of two main currents: the southward flowing Baffin Island Current (BIC), which exports cold Arctic outflow waters southwards to the Labrador Sea, and the northward flowing West Greenland Current (WGC), which mainly advects warm modified-Atlantic waters northwards along the West Greenland shelf (see Figure 3.1). These two current systems lead to an east-west divide in the water mass assemblies of Baffin Bay (Bâcle et al., 2002b; Münchow et al., 2015; Randelhoff et al., 2019; Tang et al., 2004). Sea ice retreat in Baffin Bay typically progresses from east to west, due to the temperature gradient between the WGC and BIC current systems, and features an ice-edge bloom that tracks the westward moving ice-edge (Perrette et al., 2011). Randelhoff et al. (2019) recently provided a detailed summary of the spring sea ice retreat and water masses present in Baffin Bay. Here we briefly review the major water masses of Baffin Bay (although Baffin Bay Deep waters at depths below 800 m are not discussed here), and we refer the reader to Randelhoff et al. (2019) and references therein for more detail.

In eastern Baffin Bay the water column is divided into three main water masses: (1) Warm surface waters, characterized by $T > 0°C$ and $S < 33.5$, which are only present during the ice-free season when solar insolation heats the upper mixed layer; (2) Winter Atlantic water (WAW), with $T < -1$ °C and $33.5 < S < 34$ located at depths of approximately 40 – 100 m, and (3) Atlantic waters (AW), characterized by $T > 1$ °C and $S > 34$ and concentrated at depths between 150 –500 m over the continental slope.

In western Baffin Bay, AW and WAW are still present but are located at greater depths in the water column. AW is generally located at depths greater than 250 m, and WAW between depths of 150

to 250 m. Above this sits Arctic water with T < −1°C and S < 33.5 which arrives in Baffin Bay from the channels of the Canadian Arctic Archipelago (CAA) and is transported southwards by the BIC. Due to the presence of multiple shallow sills in the CAA, Arctic water entering Baffin Bay is primarily of Pacific origin, as deeper Atlantic-origin waters from the central Arctic Ocean basins are held back. Similarly, the deep Atlantic waters in Baffin Bay (WAW and AW) cannot pass over these sills, and so they are recirculated southwards within Baffin Bay, being subducted underneath the Arctic water.

Nitrate delivery has been shown to vary between the two major surface currents in Baffin Bay. Arctic water entering via the BIC was reported to deliver between 5 – 12 μmol kg^{-1} of nitrate, whereas WGC waters entering from the southeast contained approximately 14.5 μmol kg^{-1} nitrate in winter (J.-É. Tremblay et al., 2002).

3.3 Methods

3.3.1 Sampling

Data presented here were collected between 9 June and 10 July 2016 onboard the *CCGS Amundsen* as part of the Green Edge expedition (Randelhoff et al., 2019). A series of seven longitudinal transects were sampled across the retreating ice-edge. Each transect was numbered 100 to 700 in the order of sampling (see Figure 3.1), and traversed between modified Atlantic waters in eastern Baffin Bay and Arctic outflow waters in the west. Mid-way through the research cruise (between transects 300 and 400) the ship travelled south to the hamlet of Qikiqtarjuaq, NU for a personnel swap with the associated Green Edge ice camp (Oziel et al., 2019). Throughout the cruise the ship's CTD/Rosette system, consisting of 24 × 12L Niskin-type bottles (OceanTest Equipment) with a Sea-Bird 911plus CTD, was deployed at a total of 135 unique station locations. The CTD was also equipped with a fluorometer for the detection of chlorophyll *a* (SeaPoint). Nutrient samples (for analysis of nitrite, nitrate, ammonium, phosphate, and silicate) were collected at 92 of these stations, while discrete samples for salinity, stable oxygen isotope ($\delta^{18}O$), and the inorganic carbon system (for analysis of total alkalinity (TA) and dissolved inorganic carbon (DIC)) were only collected at 11 stations in the 100 and 300 transects. Underway surface water measurements of O_2/Ar and pCO_2 were collected through two separate seawater intake lines, sampling at depths of approximately 5 m and 7 m below the waterline, respectively. Underway measurements of surface pCO_2 and O_2 concentrations showed good correlation with surface measurements from the CTD/Rosette (see Figure S3.1) and therefore we do not anticipate that biofouling within the seawater intake lines had any significant effect on our measurements.

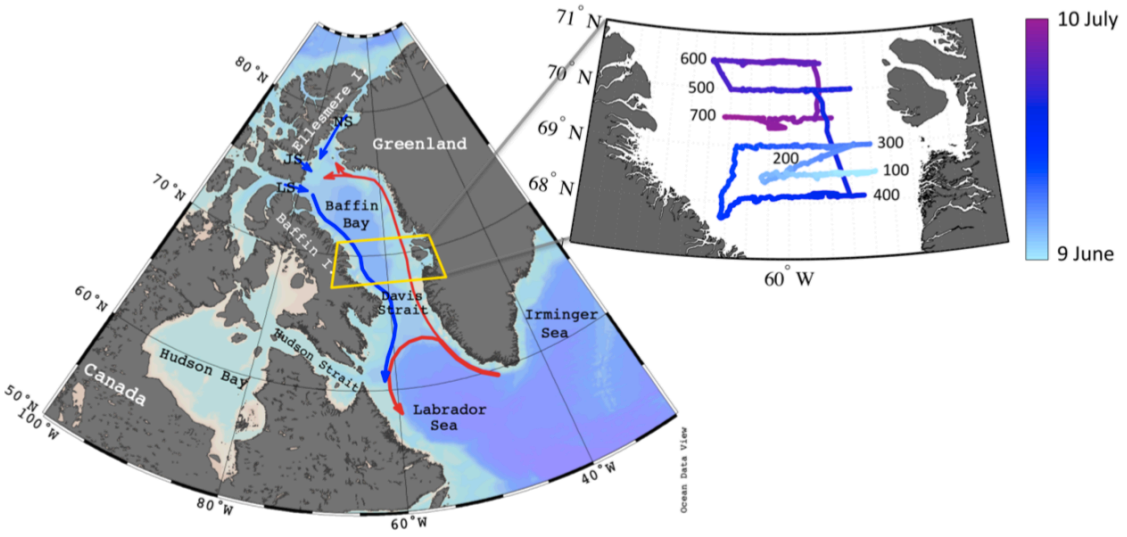

Figure 3.1: Map of the study area. Leftmost map shows the general surface circulation patterns of Baffin Bay, with the West Greenland Current shown in red, and the Baffin Island Current shown in blue. The inset map to the right shows the cruise track colored according to sampling date, with east-west transects named sequentially in the order of sampling from 100 to 700.

3.3.2 Analytical Procedures

Continuous underway $\Delta O_2/Ar$ measurements were made using Equilibrator Inlet Mass Spectrometry (EIMS) (Cassar et al., 2009). Briefly, seawater from the ship's seawater intake line (sampling from a nominal depth of 5 m) is pumped through a gas-permeable membrane cartridge, allowing the gas in the headspace of the cartridge to equilibrate with the gases in seawater. The O_2/Ar ratio is then measured from the headspace gas using a quadrupole mass spectrometer (Pfeiffer Prisma model QMG 220 M1). The system is calibrated against the atmospheric O_2/Ar ratio every four hours, and the instrument precision is ± 0.3% or better (Cassar et al., 2009). Here we present 2-minute averages of $\Delta O_2/Ar$ measurements collected every 8 seconds, following (Eveleth et al., 2017).

Continuous measurements of sea surface pCO_2 were also made underway using an infrared based showerhead equilibrator system (General Oceanics model 8050; (Pierrot et al., 2009)) using a different clean seawater intake line into the ship's engine room, at 7 m depth. The infrared gas analyzer (LI-COR model LI-7000) was calibrated twice daily against four certified gas standards (CO_2 concentrations of 0.0, 254.5, 431.3, and 554.2 ppm) traceable to World Meteorological Organization (WMO) standards. The underway system also houses a flow-through CTD (Idronaut model Ocean Seven 315) which provided coincident salinity measurements. Due to the dependency of the pCO_2 measurement on temperature, a separate temperature measurement was made by a thermocouple located directly in the seawater intake line (accurate to 0.5 °C). These "*in-situ*" temperature measurements were used to

correct for any warming that may have occurred during transport of water to the pCO_2 system's equilibrator using the method of Takahashi et al. (1993). The overall relative uncertainty of the temperature-corrected pCO_2 values is estimated to be 2 %.

Carbon system seawater samples were collected following standard protocols (Dickson et al., 2007), with replicates collected from at least one Niskin bottle per rosette cast. Samples were collected in 250-mL glass bottles, preserved with 100 µL of saturated mercuric chloride solution, capped with ground glass stoppers greased with Apiezon-M, and sealed with electrical tape. Samples were then stored in the dark at 4 °C until arrival at the Institute of Ocean Sciences in Sidney, British Columbia where analysis for total alkalinity (TA) and dissolved inorganic carbon (DIC) was conducted. The coulometric DIC analysis utilized either a SOMMA (Johnson et al., 1993) or VINDTA 3D (MARIANDA) extraction system. Measurements of TA were determined using an open-cell potentiometric titration with non-linear least squares end-point determination (Dickson et al., 2007). Both of these measurements were calibrated against certified reference materials (CRM Batch #106) provided by Andrew Dickson (Scripps Institute of Oceanography). Determination of duplicate DIC samples indicates a precision of ±1 µmol/kg, and duplicate TA samples show a precision of ± 3 µmol/kg.

Samples for the determination of $\delta^{18}O$ were analyzed at the GEOTOP stable isotope laboratory at the Université du Québec à Montréal. Measurements were made using the CO_2 equilibration method, where 200 µL of sample water was equilibrated with CO_2 for 7 hours at 40 °C. The CO_2 was then analyzed on a Micromass Isoprime™ universal triple collector mass spectrometer in dual inlet mode with an AquaPrep™ system (Isoprime Ltd., Cheadle, UK). Results are expressed in the δ notation in ‰ versus Vienna Standard Mean Ocean Water (VSMOW). For each analytical sequence, two internal reference water samples were used to normalize the sample data ($\delta^{18}O$ = –6.71 ‰ and –20.31 ‰). Uncertainties in replicate measurements were ± 0.05 ‰ (1σ).

Vertically-resolved subsamples for nutrient determination were collected directly from the Niskin bottles with syringes and filtered through a GF/F filter inserted in a Swinnex. The concentrations of phosphate and nitrate (obtained by difference between nitrite and nitrate+nitrite) were measured fresh on an Autoanalyser 3 (Bran and Luebbe) and used to estimate the fraction of Pacific water (FPW) at each sampling depth. Here we used the N-P regression lines from Jones et al. (1998), as Tremblay et al. (2015) showed the N-P relationships in northern Baffin Bay closely follow those derived by Jones et al. (1998). In order to estimate surface FPW along the ship track, average mixed layer FPW values were calculated at each sampling (as the average of all FPW values within the defined mixed layer depth).

These mixed layer average values were then linearly interpolated between sampling station locations. Surface mixed layer depths were defined following Shaw et al. (2009).

3.3.3 NCP from O_2/Ar

Rates of NCP calculated from O_2/Ar measurements exploit the similar physical properties but different biological behavior of oxygen and argon (Craig & Hayward, 1987). Since physical processes affecting oxygen concentrations (e.g. bubble entrainment, temperature changes) similarly affect argon (Ar), the biological oxygen saturation anomaly (ΔO_2/Ar) can be calculated as:

$$\Delta\, O_2/Ar = \left[\frac{([O_2]/[Ar])}{([O_2]/[Ar])_{sat}} - 1\right] \tag{3.1}$$

where $([O_2]/[Ar])$ is the measured O_2/Ar ratio from the EIMS, and $([O_2]/[Ar])_{sat}$ is the ratio of equilibrium concentrations of O_2 (Garcia & Gordon, 1992) and Ar (Hamme & Emerson, 2004). ΔO_2/Ar represents the percent deviation in seawater O_2/Ar from atmospheric equilibrium, with Ar normalization used to remove physical effects on O_2 saturation (Craig & Hayward, 1987). Assuming that the surface mixed layer is isolated from the deeper water column, NCP can be calculated as the sea-to-air flux of biologically-produced oxygen:

$$NCP_{O2/Ar}\ (mmol\ C\ m^{-2}\ day^{-1}) \approx\ k_{O_2} \cdot [O_2]_{sat} \cdot \Delta(O_2/Ar) \cdot \frac{1}{O_2{:}\,C} \tag{3.2}$$

where k_{O_2} is the gas transfer velocity for O_2 (m day^{-1}), $[O_2]_{sat}$ is the equilibrium concentration (mmol O_2 m^{-3}), and $O_2{:}\,C$ is the stoichiometric ratio of 1.4 from Laws (1991). Within equation 3.2 the term $[O_2]_{sat} \cdot \Delta(O_2/Ar)$ represents the sea-to-air gradient of biologically derived oxygen. The transfer velocity (k_{O_2}) is calculated from the wind speed parameterization of Wanninkhof (2014) using 4-times daily wind components from NCEP/NCAR reanalysis data (Kalnay et al., 1996) and is weighted to account for wind speed history over the 60 days prior to sampling following the weighting scheme of Reuer et al. (2007) as modified by Teeter et al. (2018). k_{O_2} was also linearly corrected for sea ice cover using sea ice concentrations from AMSR2 (Spreen et al., 2008) matched to the ship's sampling time and location. We chose to apply a linear scaling of k_{O_2} by sea ice cover, as this approach is supported by the recent findings of Butterworth and Miller (2016) and Prytherch et al. (2017) during the summer season in partially ice covered waters, although we do acknowledge that large uncertainty remains around transfer velocity estimates in partially ice-covered waters (more on this uncertainty below).

The recent study of Teeter et al. (2018) demonstrated that $NCP_{O2/Ar}$ calculated by this technique accurately represents the exponentially weighted NCP over the past several residence times of oxygen

in the surface mixed layer. By calculating the O_2 residence time (τ_{O2} = MLD/k_{O_2}) at each location using the associated 60-day weighted and ice corrected transfer velocity (k_{O_2}), we approximate the weighted residence time of our $NCP_{O2/Ar}$ estimates. Our daily $NCP_{O2/Ar}$ (mmol C m^{-2} day^{-1}) rates are multiplied by their associated residence times for comparison to other seasonally integrated approaches (mol C m^{-2}; see below), which are described in subsequent sections. Table 3.1 provides a summary of the relevant integration depths and timescales of each NCP approach presented.

Table 3.1: Summary of relevant integration timescales and depths of each NCP approach

NCP approach	Integration timescale (residence time of tracer)	Integration depth
$NCP_{O2/Ar}$	~20 days[a] in open water (σ = 6 days,; ranges between 8 to 32 days) ~60 days[a] under ice (σ = 45 days; ranges between 12 to 193 days)	Surface mixed layer
NCP_{pCO2}	Months to years	Surface mixed layer
NCP_N	Months to years	Euphotic zone

[a] average values for open water (SIC=0) and ice covered (SIC>0) conditions

Using this methodology of estimating $NCP_{O2/Ar}$ we employ a number of assumptions that introduce potential error. First, we assume that $[Ar]/[Ar]_{sat}$ = 1, which introduces an error equal to the actual Ar saturation of surface waters. Eveleth et al. (2014) reported that surface waters in the central Arctic Ocean can have Ar supersaturation ranging between –7% to +3%. We also assume that the surface mixed layer is isolated from deeper waters, but vertical mixing may transport oxygen-depleted waters from depth into the surface layer. In areas where vertical mixing occurs, $NCP_{O2/Ar}$ will represent a lower bound on true NCP. However, we found no evidence of doming isopycnals along our longitudinal transects, so we do not anticipate vertical mixing to have a significant impact within this particular dataset. Our greatest source of error is that associated with our estimates of transfer velocity, which Bender et al. (2011) estimate to be ~40% in open water, but are much higher when taking sea ice cover into account. Loose et al. (2009) estimate the standard error of the transfer velocity in partial sea ice cover can be up to 80%. Other studies show similarly large uncertainties in estimated transfer velocities in the presence of partial sea ice cover (Butterworth & Miller, 2016; Prytherch et al., 2017; Rutgers van der Loeff et al., 2014). Taking this into consideration, and acknowledging that this large uncertainty is again applied by our

residence time multiplier to report seasonal NCP in units of mol C m^{-2}, the relative uncertainty of our $NCP_{O2/Ar}$ estimates may be over 100% (especially in ice-covered waters). These estimates represent the best approximations we can currently make using the O_2/Ar technique in partially ice-covered waters.

3.3.4 NCP from pCO_2

Calculated values of NCP_{pCO2} utilize the seasonal drawdown of DIC in the surface mixed layer to estimate the total growing season NCP (mol C m^{-2}). NCP_{pCO2} is calculated as:

$$NCP_{pCO2} = MLD(DIC_W \cdot \rho_W - nDIC_S \cdot \rho_S) + F_{CO2} \quad (3.3)$$

where MLD is the mixed layer depth, DIC_W is the winter water DIC concentration, $nDIC_S$ is the salinity-normalized surface DIC concentration (normalized to the winter water salinity) derived from pCO_2, and ρ_W and ρ_S are the winter and surface surface water densities, respectively. The F_{CO2} term represents a correction for the air-sea exchange of CO_2 over the days of open water (DOW; see methods section on sea ice cover) prior to the sampling date. MLD values were estimated from CTD profiles and were defined as the depth at which the density increases from its surface value to 20% of the difference between 100 m and the surface following Shaw et al. (2009). MLD values were then linearly interpolated along the ship track between stations, and were assumed to remain constant seasonally.

Surface measurements of pCO_2, temperature, salinity, and salinity-based TA estimates were used to calculate surface water DIC concentrations (DIC_S) using CO2SYS (van Heuven et al., 2011) with the carbonic acid dissociation constants of Lueker et al. (2000) and those of Dickson (1990) for bisulfate. Two separate linear salinity-TA relationships were defined, one for Arctic outflow waters in western Baffin Bay ($TA_{ARC} = 43.69 * Sal + 816.98$, R^2 = 0.67, RMSE = 11.2 µmol/kg), and a separate relationship for modified-Atlantic waters in eastern Baffin Bay ($TA_{ATL} = 58.27 * Sal + 287.82$, R^2 = 0.86, RMSE =7.3 µmol/kg). All samples used to define the Arctic outflow salinity-TA relationship coincided with fractions of Pacific water (FPW) greater than or equal to 0.3, whereas all samples used to define the Atlantic-modified water relationship had FPW = 0 (see Figures S3.2 and S3.3). Following this, when estimating surface TA at any point along the ship track, interpolated MLD-average FPW values (FPW_{MLD}) were used to determine which linear salinity-TA relationship to employ. For FPW_{MLD} >= 0.3 the TA_{ARC} equation was used; for FPW_{MLD}= 0 the TA_{ATL} equation was used; and for 0.3 > FPW_{MLD} > 0 TA was determined as a weighted average, as follows:

$$TA = (FPW_{MLD}/0.30)TA_{ARC} + (1 - (FPW_{MLD}/0.30))TA_{ATL} \quad (3.4)$$

Winter surface DIC concentrations (DIC_W) were estimated from the DIC concentration at the temperature minimum (T_{min}) of each station where carbon system samples were collected (100 and 300

transects only). The T_{min} is assumed to represent the convection depth of the previous winter's mixed layer (Rudels et al., 1996), however as Randelhoff et al. (2019) pointed out, the absolute T_{min} in western Baffin Bay (found at 100 – 150 m) likely does not represent the true depth of winter convection, but is a remnant of winter convection in eastern Baffin Bay that was subsequently subducted underneath Arctic waters (this is also evidenced by the low FPW values of this layer). Therefore, we follow the adapted method proposed by Randelhoff et al. (2019) to identify the winter convection depth as the shallowest local temperature minima. It is important to note that this method is somewhat arbitrary, and leads to a range of winter mixed layer depths in western Baffin Bay from 15 to 40 m, and DIC_W of 2104.6 to 2136.8 µmol/kg. This method represents the best approximation we can make with the available data.

Due to the lower number of stations where discrete DIC samples were collected, we could not simply interpolate DIC_W between stations along the ship track. Therefore, we first determined average DIC_W and ρ_W values for the Atlantic and Arctic domains, which were averaged from DIC values with FPW = 0 and FPW > 0.3 at the identified winter convection depth, respectively. Calculated average DIC_W values for the Atlantic and Arctic domains were 2111.5 $\pm$ 11 µmol/kg and 2127.2 $\pm$ 13 µmol/kg, respectively. Then, interpolated values of FPW_{MLD} were used to determine DIC_W and ρ_W at all points along the ship track, in the same manner as TA above. We were able to use interpolated FPW_{MLD} values as a proxy for winter mixed layer conditions, as we found only small differences in FPW existed between the MLD and depth of winter convection (average difference of 0.04 $\pm$ 0.03), and these differences did not result in a change of classification between Atlantic or Arctic domains at any stations.

To account for the dilution of surface water DIC by freshwater inputs, DIC_S values were salinity-normalized to the salinity of the winter mixed layer (the salinity associated with DIC_W). We performed the salinity normalization following Friis (2003), such that:

$$nDIC_s = \frac{(DIC_s - DIC_0)}{S_s} S_w + DIC_0 \quad (3.5)$$

where DIC_s is the surface DIC derived from surface pCO_2 measurements, S_s is the surface salinity, S_w is the salinity of the winter mixed layer, and DIC_0 is the estimated DIC concentration at a salinity of zero. DIC_0 values were determined for Arctic outflow waters (DIC_{0_ARC} = 914 µmol/kg, RMSE = 13.0) and Atlantic modified waters (DIC_{0_ATL} = 0 µmol/kg, RMSE = 35.1) from linear DIC-S relationships (see Figure S3.4). The appropriate DIC_0 value to employ at each point along the ship track was determined by FPW_{MLD} in the same manner as TA and DIC_W.

The flux correction term (F_{CO2} in equation 3.3) integrates daily air-to-sea CO_2 flux estimates over the days of open water (DOW) prior to sampling. Daily fluxes were calculated as:

$$F_{daily} = \alpha k(pCO_{2sw} - pCO_{2atm}) \quad (3.6)$$

where k is the transfer velocity, estimated using the parameterization of Wanninkhof (2014) and daily wind speeds from NCEP/NCAR reanalysis data (Kalnay et al., 1996); α is the solubility of CO_2 in seawater (Weiss, 1974); and pCO_{2sw} and pCO_{2atm} are the partial pressure of CO_2 in the surface seawater and atmosphere, respectively. pCO_{2atm} is assigned a constant value of 404 μatm; the average value recorded at Alert, Nunavut between June 7th and July 14th, 2016 (World Data Centre for Greenhouse Gases). Since we do not have measurements of surface pCO_{2sw} previous to our date of sampling, we make the assumption that surface pCO_{2sw} would not have changed significantly between the day of retreat (DOR) and our sampling date (i.e. we hold the observed pCO_{2sw} values constant over DOW). This assumption is supported by the results of previous investigations in Canadian Arctic waters (Else et al., 2012; Else et al., 2019; Shadwick, Thomas, Chierici, et al., 2011), which show that surface pCO_{2sw} generally undergoes a rapid decrease associated with an under-ice or ice-edge bloom, quickly reaching its annual minimum value before beginning a slow increase throughout the open water season. The results of Else et al. (2019) demonstrate this trend occurring within our study region, showing a rapid drop in surface pCO_{2sw} and nitrate concentrations associated with the onset of an under-ice bloom in early July.

We estimate the relative uncertainty of our calculated NCP_{pCO2} values to be ±20%, based on recalculating NCP_{pCO2} with variations in TA, DIC_W, and DIC_0 within their stated limits of variability. This does not take into account the uncertainty associated with the flux correction (F_{CO2}), however the relative increase in NCP_{pCO2} due to the correction was very small (maximum of 8%), and therefore has only a small impact on the uncertainty of NCP_{pCO2}. Additionally, the sensitivity of F_{CO2} to a different definition of DOW, using a 50% sea ice cover threshold instead of 15% (as described in sea ice cover section below) was found to be very small, altering F_{CO2} by a maximum of only 0.01 mol C m^{-2}, or a maximum relative change of 0.8%. This is likely the case because of the relatively small geographical area occupied by the marginal ice zone in comparison to open water of heavily ice-covered areas (see Figure S3.5).

3.3.5 NCP from nitrate drawdown

Calculated values of NCP_N (mol C m^{-2}) correspond to the cumulated water-column drawdown of nitrate since the onset of the growing season, multiplied by the molar Redfield C:N ratio of 6.7. The nitrate drawdown is estimated from the difference between observed nitrate inventories (N_{obs}) at the time of sampling and a reconstruction of pre-bloom inventories (N_w) based on the salinity-nutrient approach

introduced by Bergeron and Tremblay (2014). These authors observed that linear salinity-nutrient relationships extend through the upper 200 m during late-winter in northern Baffin Bay and pre-bloom nutrient concentrations at each depth can be estimated from the salinity values at the time of sampling, with a correction for conservative dilution when salinity is lower than the winter minimum at the surface. See Bergeron and Tremblay (2014) and the associated supporting information for details.

3.3.6 Freshwater Fractions from $\delta^{18}O$

In order to classify low salinity waters as being affected by sea ice melt or meteoric waters, $\delta^{18}O$ and salinity measurements were used in a simple 3-endmember mass balance whereby each water sample is assumed to be a mixture of Atlantic water ($S_{AW} = 34.9$, $\delta^{18}O_{AW} = 0.3$ ‰), sea ice melt ($S_{SIM} = 4$, $\delta^{18}O_{SIM} = 0.5$ ‰), and meteoric water ($S_{MW} = 0$, $\delta^{18}O_{MW} = -20$ ‰). End-member values for sea ice melt and meteoric water are based on those of Östlund and Hut (1984) and Fairbanks (1982), respectively, whereas the Atlantic water end-members follow Dodd et al. (2012). Here it is important to remember that we cannot distinguish low-salinity Pacific water from the mixture of Atlantic water and meteoric waters. As stated by Yamamoto-Kawai et al. (2005), this is because the salinity-$\delta^{18}O$ properties of Pacific water lie on the mixing line of Atlantic water with Arctic meteoric water. Therefore, in our results the presence of Pacific water will appear in the meteoric water signal.

3.3.7 Sea ice cover

Using AMSR2 sea ice concentration data (Spreen et al., 2008) on a 6.250 km grid, we identified the day of ice retreat (DOR) for each sampling location. We defined DOR as the last day that sea ice concentration dropped below 15% and remained below that threshold for the rest of the season. Defining DOR in this way is a commonly employed climate metric in studies characterizing variability in sea ice extent, and the length of the open water season using passive microwave measurements such as AMSR2 (Peng et al., 2018; Bliss et al., 2019; and references therein). We then also calculated the days of open water (DOW) at each location at the time of sampling by subtracting DOR from our sampling date (both expressed as yearday). This resulted in positive and negative values of DOW, in locations that had become ice-free or remained ice-covered at the time of sampling, respectively.

3.4 Results

3.4.1 Sea Surface Properties

Figure 3.2 shows sea surface properties throughout the study area, with all measurements displaying both spatial (east-west) and temporal variations. Figure 3.2A shows the east-to-west retreat of the ice-edge across southern Baffin Bay (shown as DOR contours). At the beginning of the cruise (day 160) the ice-edge was located approximately along the West Greenland shelf break and by the end of the cruise (day 190) was quickly receding towards the Baffin Island shelf break. It was not until July 28th (day 210), that the entire study area became ice-free (not shown).

Surface waters in western Baffin Bay were generally colder and fresher than those in the east (Figure 3.2E,F). This is consistent with the presence of cold, less saline Arctic outflow waters in the west, and warmer, more saline modified Atlantic waters in the east. Henceforth we will refer to these two water masses as “Arctic” and “Atlantic” waters, respectively. Observed patterns in sea surface temperature and salinity are also consistent with observed sea ice concentrations along the ship track (Figure 3.2C), with ice-covered waters displaying colder temperatures. As the cruise progressed from early-June into July (DOY 160 – 190; Figure 3.2B), sea surface temperatures in the east progressively became warmer due to solar insolation, while surface salinities in the west continued to decrease as sea ice melt progressed.

Underway measurements of surface pCO_2 ranged from 124 to 389 µatm (Figure 3.2G), and also displayed an east-to-west gradient with generally lower pCO_2 observed in the east (~124 –250 µatm), and higher pCO_2 in the west (~ 250 –389 µatm). The range of this east-to-west gradient decreased over time, mainly due to decreasing surface pCO_2 in the west. The first four (southernmost) transects to be sampled displayed the greatest range in pCO_2 measurements compared to the latter three (northernmost) transects of the cruise. All underway pCO_2 measurements were consistently undersaturated with respect to the atmosphere (pCO_{2atm} =~404 uatm; average recorded value at Alert, Nunavut between June 7th and July 14th, 2016 (World Data Centre for Greenhouse Gases)).

Surface measurements of biological oxygen supersaturation ($\Delta O_2/Ar$) ranged from –5.6% to 25.4% across the region (Figure 3.2H), and generally showed a negative correlation with surface pCO_2 measurements (n=5374, R^2=0.64, p=<0.001), suggesting biological processes largely drove pCO_2 variations. In the open waters of eastern Baffin Bay $\Delta O_2/Ar$ was consistently positive (ranging between 1.2 – 25.4%) signaling that surface waters were net autotrophic. In the western ice-covered waters we observed some negative $\Delta O_2/Ar$ values, with values ranging between -5.6% to 12.8%, implying that some

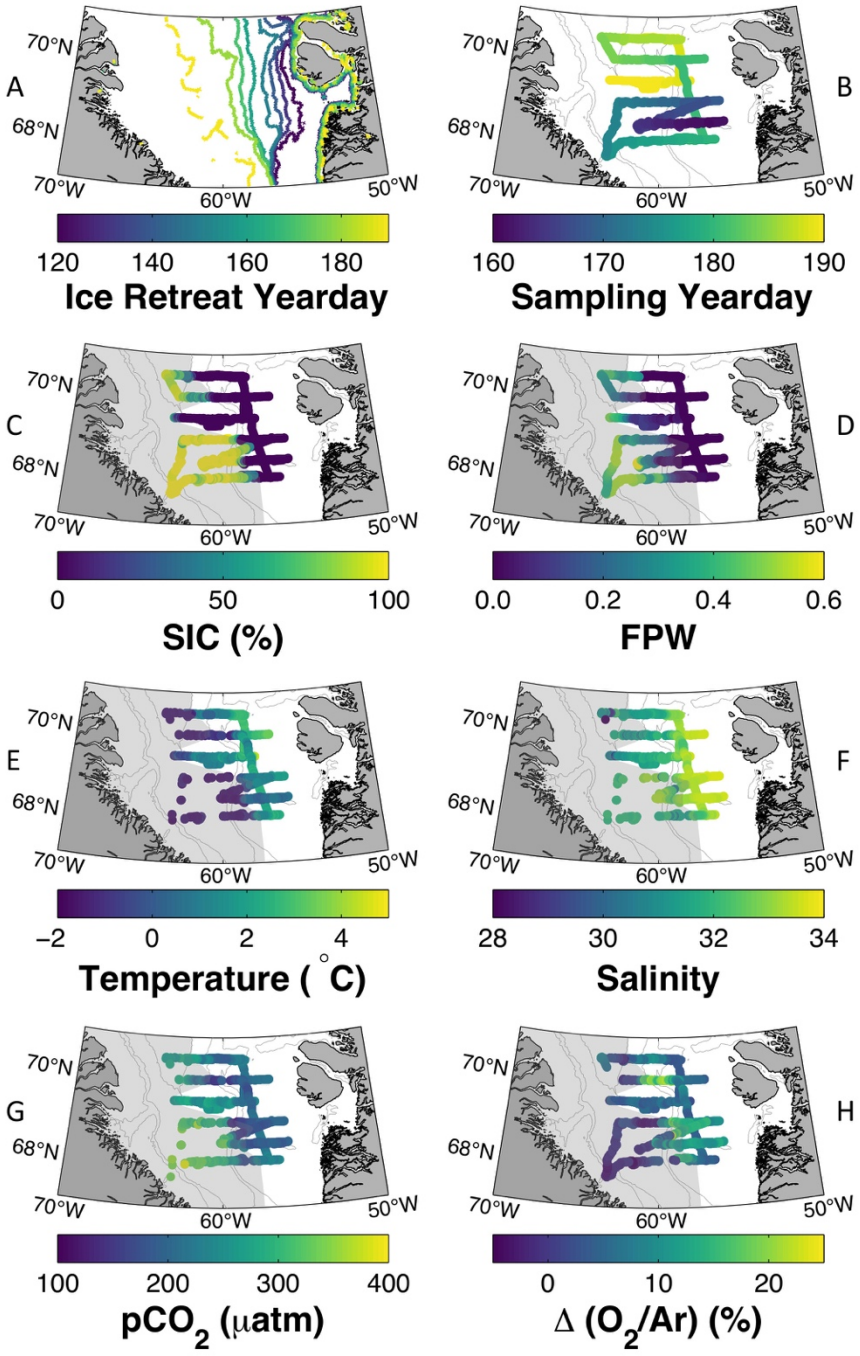

Figure 3.2: Maps of sea surface properties. Maps show: A. contours of the yearday of ice retreat (DOR) across the study region; B. the yearday of sampling (DOY) along the cruise track; C. surface measurements of sea ice cover (SIC); D. fraction of Pacific water (FPW) of the surface mixed layer; E. sea surface temperature; F. sea surface salinity (practical salinity); G. surface pCO2; and H. surface $\Delta O_2/Ar$. The research cruise took place between yearday 160 and 190. SIC measurements are from AMSR2 (Spreen et al., 2008) matched to the ship's location at the time of sampling. The grey masked area represents locations that remained ice-covered (negative DOW) at the time of sampling.

ice-covered areas may have either been net heterotrophic at the time of sampling, or impacted by upwelling.

3.4.2 Water column characteristics

Figure 3.3 shows water column properties over the upper 100 meters of the 100-transect. East-west trends shown in this transect are generally representative of all seven longitudinal transects discussed in this study.

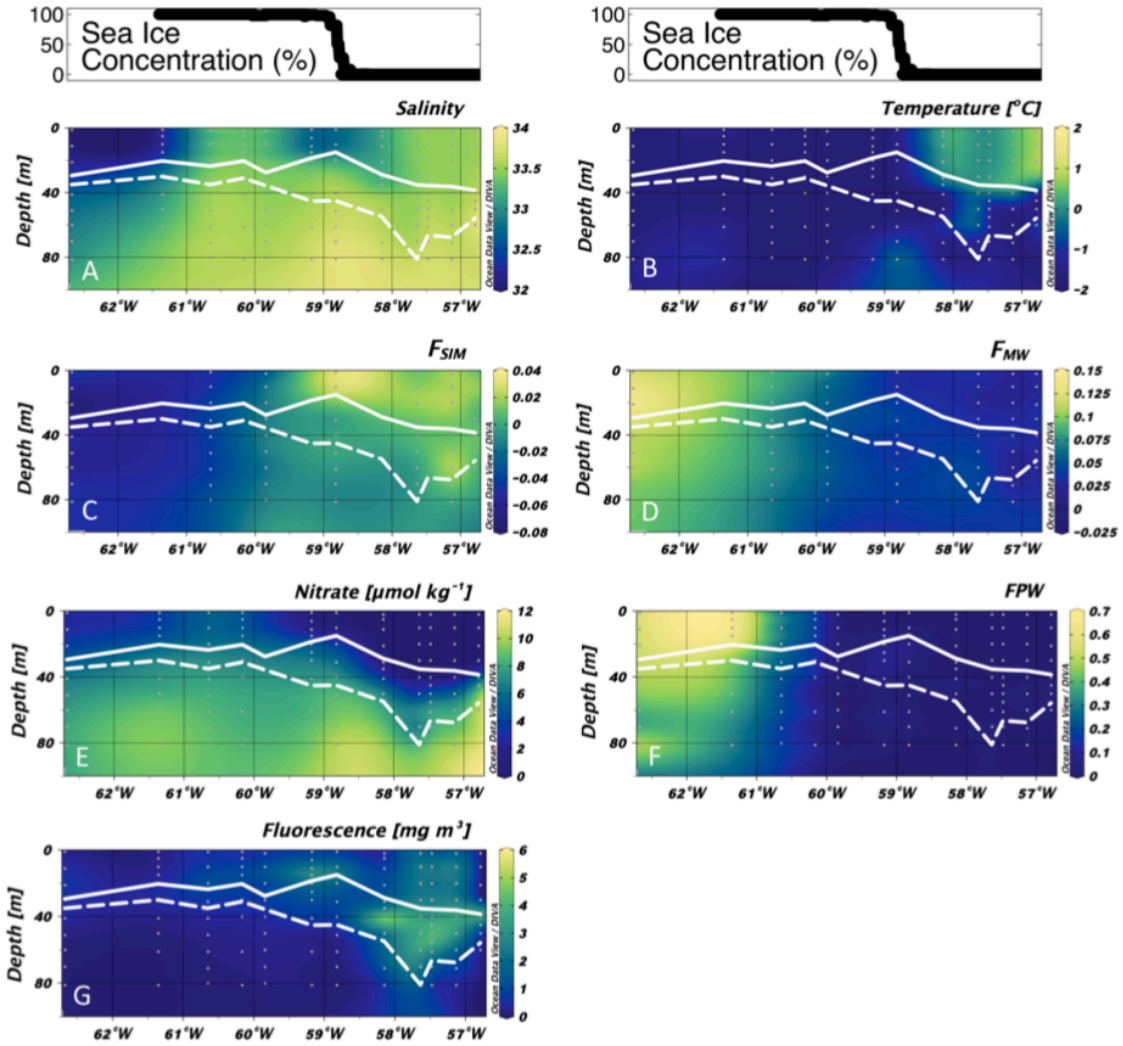

Figure 3.3: Section plots of the upper water column. Each panel displays properties over the upper 100 m of the 100-transect. The white solid line indicates the surface mixed layer depth (MLD), and the white dashed line represents the estimated depth of winter convection based on the location of the temperature minimum. Sea ice concentrations along the cruise track are shown above (A) and (B). East-west patterns were similar along the other transects.

The east-west divide between Atlantic and Arctic waters was evidenced by more saline (S > 33.5) Atlantic water extending to the surface in the east, whereas lower salinity Arctic waters were present in the upper water column west of 61 °W (Figure 3.3A). Atlantic waters were relatively warm (T > –1 °C) over the upper ~40 m in areas that had already become ice-free, with colder winter waters below (Figure 3.3B). Atlantic waters generally displayed deeper mixed layers and greater depths of winter convection, compared to Arctic waters. Within the Atlantic domain we observed a pocket of lower salinity surface waters at the ice-edge (centered at 59 °W), which was shown to be due to sea ice melt (Figure 3.3C), and coincided with a decrease in surface mixed layer depths. Arctic waters showed a predominant brine signal (negative F_{SIM}) with positive fractions of meteoric water extending below the upper 100 m (Figure 3.3D). This meteoric water signal was closely aligned with the location of Pacific waters (Figure 3.3F), suggesting it primarily results from the presence of low-salinity Pacific waters.

The distribution of nitrate (Figure 3.3E) was influenced both by water mass distribution and biogeochemical processes. A strong imprint of primary production was observed in the upper water column of the easternmost stations, where nitrate concentrations had been depleted to depths of 40 m. The observed fluorescence signal also demonstrated the downward migration of the surface bloom at the easternmost stations, becoming an SCM located at depths below 40 m (Figure 3.3G). The depth range of the SCM was found to be perched between the nitracline depth and the 0.415 mol m^{-2} day^{-2} isolume (see Figure 9 of Randelhoff et al. (2019)), balancing the need for sufficient nutrients and light. Closer to the ice-edge the fluorescence signal only indicated near-surface primary production. Surface nutrients in the west had not yet been depleted, and the fluorescence signal showed little primary production there at the time of sampling. As expected, nitrate concentrations at depth were higher in Atlantic waters (~ 10 – 12 μmol/kg) than in Arctic waters (~8 μmol/kg).

3.4.3 NCP estimates

Figure 3.4 shows spatial trends in NCP estimated by our three different approaches. Generally, all three approaches showed higher rates of NCP in eastern Baffin Bay than in the west, with the westernmost sampling locations displaying the lowest NCP estimates. The range of values estimated by each approach varied greatly (note different scales in Figure 3.4). NCP_N displayed the greatest range from 0 to 5.7 mol C m^{-2}, NCP_{pCO2} ranged from –0.7 to 3.3 mol C m^{-2}, and $NCP_{O2/Ar}$ ranged from –0.3 to 1.2 mol C m^{-2}.

Values of NCP_{pCO2} and NCP_N generally increased from west to east across each transect with one exception seen in the 100 transect (see Figure 3.1 for transect identifications), where both NCP_{pCO2} and

NCP_N decreased slightly at their easternmost sampling locations. Values of $NCP_{O2/Ar}$ did not follow the same increasing trend from west to east. Instead, $NCP_{O2/Ar}$ generally peaked near the West Greenland Shelf break.

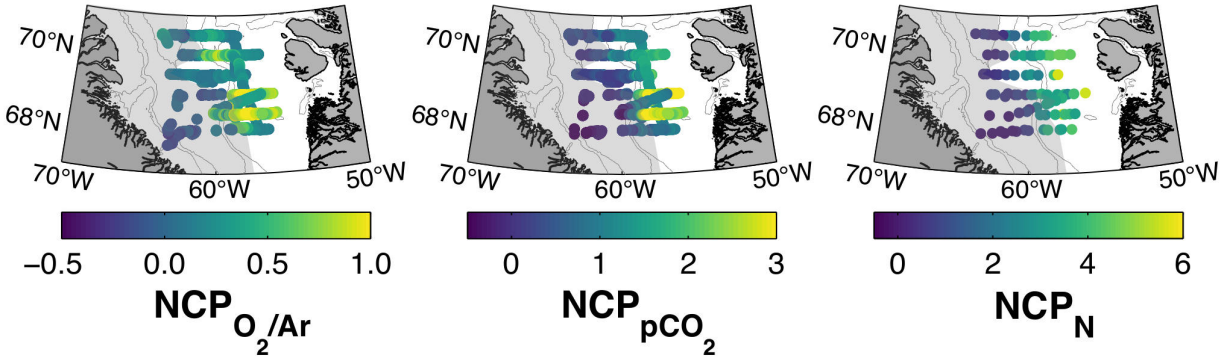

Figure 3.4: Estimates of net community production from three approaches. All NCP rates are shown in units of mol C m^{-2}. Shaded regions represent areas that remained ice-covered at the time of sampling (negative DOW).

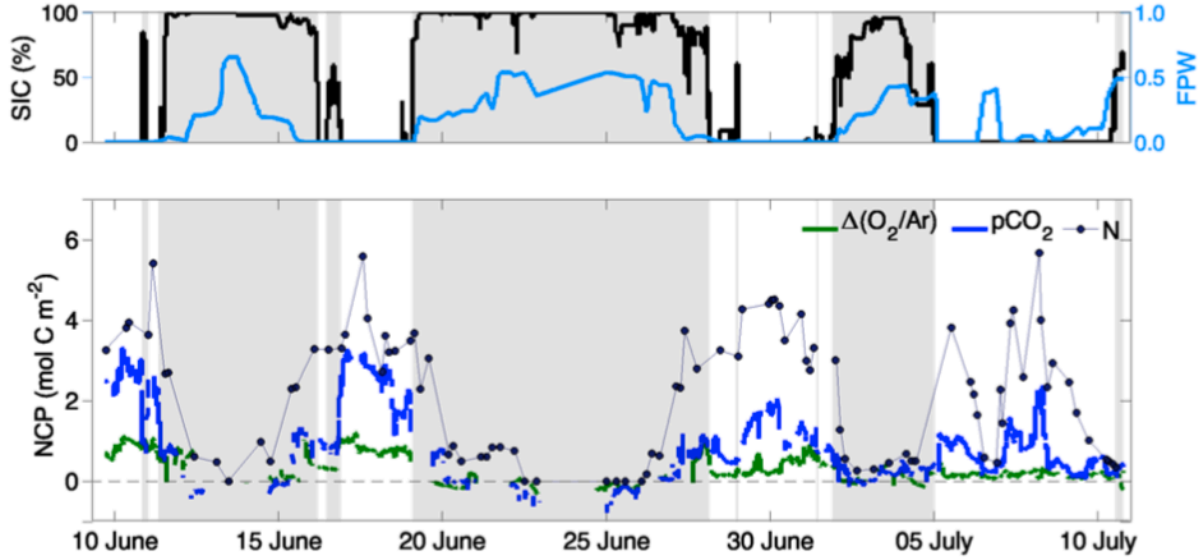

Figure 3.5: Time series of NCP estimates from each approach along the cruise track. Sea ice cover (SIC) and the average fraction of Pacific water (FPW) of the surface mixed layer are shown in the top panel. NCP estimates from our three approaches are shown in the bottom panel. Time periods shaded in grey represent areas that remained ice-covered at the time of sampling (negative DOW).

Figure 3.5 presents a time series view of NCP estimates with coinciding measurements of sea ice coverage (SIC), and surface fractions of Pacific water (FPW). All NCP estimates were generally highest in open water conditions with low FPW, and decreased under high SIC, which often also

coincided with high FPW. $NCP_{O2/Ar}$ consistently showed lower values compared to other approaches, except under high SIC, where $NCP_{O2/Ar}$ values showed good agreement with NCP_{pCO2}. Throughout the first three transects of the cruise (100 to 300) NCP_{pCO2} values dramatically changed at the ice-edge, increasing from lower values in close agreement with $NCP_{O2/Ar}$ under-ice, to higher values nearing NCP_N estimates in ice-free waters. During the later transects (400 to 700) NCP_{pCO2} estimates in open water remained well below NCP_N values. Throughout the cruise NCP_N estimates displayed a strong inverse relationship to FPW. Along the 600 and 700 transects, under lower overall SIC conditions, NCP_{pCO2} values also demonstrated an inverse relationship with FPW.

3.5 Discussion

3.5.1 Comparison of estimates from various NCP approaches

As shown in Figures 3.4 and 3.5, the ranges of the NCP estimates from each approach differed. This makes sense when considering the different integration timescales and depths of each approach (see Table 3.1). Of our three approaches, $NCP_{O2/Ar}$ integrates over both the shortest timescale and depth, meaning that the O_2/Ar approach is representative of NCP in surface waters over a relatively short window (~ 20 days in open water; longer under-ice) prior to the time of sampling. $NCP_{O2/Ar}$ displayed its highest values in open water in proximity to the receding ice-edge (Figures 3.4 and 3.5), capturing the signal of the transient ice-edge bloom as it progressed westwards. In many transects $NCP_{O2/Ar}$ showed lower rates eastwards of the ice-edge (into higher DOW), likely signaling that the surface bloom was declining after using up the available stock of nutrients in the surface mixed layer.

NCP_{pCO2} and NCP_N represent seasonally integrated NCP estimates, throughout the surface mixed layer and total euphotic zone, respectively. By “seasonally integrated” we are referring to the fact that the residence times of these tracers (nitrate and DIC) are long enough to capture all NCP that has occurred since the end of winter. Therefore, we would expect both of these NCP estimates to continually increase as the bloom continues, with NCP_N being greater than NCP_{pCO2} in areas where net primary production is also occurring below the surface mixed layer. For the most part, NCP_{pCO2} and NCP_N increase from west to east, following the trend of increasing DOW, with one exception in transect 100 where both these approaches show lower NCP estimates at the easternmost sampling station. Figure 3.3 also reveals a shallowing of the nitracline at the easternmost station of the 100 transect, along with increasing surface temperatures and a weaker fluorescence signal throughout the surface mixed layer. This is perhaps signaling a transition to a different water mass regime over the West Greenland continental shelf.

3.5.2 Controls on the timing and magnitude of NCP

Since positive rates of NCP (net autotrophy) cannot occur in the absence of net primary production, it follows that the timing and succession of the spring phytoplankton bloom will play a major role in determining the observed temporal and spatial trends in NCP. In order to gain insight into the impacts of bloom timing and succession, we can exploit the different integration timescales and depths of our NCP approaches. As we have established, $NCP_{O2/Ar}$ estimates are representative of production over a relatively short window prior to sampling (~ 20 days in open water; greater under-ice) within the surface mixed layer, whereas NCP_{pCO2} and NCP_N represent seasonal NCP integrated over the surface mixed layer and total euphotic zone, respectively. Based on this, if $NCP_{O2/Ar} \approx NCP_{pCO2}$ we can assume net autotrophic conditions began roughly around the time of sampling, whereas if $NCP_{pCO2} > NCP_{O2/Ar}$, net autotrophy had already begun previous to the time of sampling. Both the $NCP_{O2/Ar}$ and NCP_{pCO2} approaches integrate over the surface mixed layer and therefore will not capture any deeper production by the SCM. However, the NCP_N approach does capture the SCM by integrating over the total euphotic zone. Therefore, comparing NCP_{pCO2} and NCP_N estimates can provide insight into how much of the total NCP has occurred within the surface mixed layer, or deeper in the water column. If $NCP_{pCO2} \approx NCP_N$ it suggests that all NCP has occurred within the surface mixed layer, whereas if $NCP_N > NCP_{pCO2}$ the portion of NCP occurring below the surface mixed layer can be approximated by $1 - NCP_{pCO2}/NCP_N$.

Figure 3.6 directly compares the $NCP_{O2/Ar}$ estimates with those from seasonally integrated approaches. Figure 3.6A shows a strong inverse relationship between days of open water (DOW) and the slope of the $NCP_{O2/Ar}/NCP_{pCO2}$ relationship. Most $NCP_{O2/Ar}$ values that fall along the 1:1 line with NCP_{pCO2} are associated with negative DOW, indicating that net autotrophic conditions were initiated by an under-ice bloom. Based on the range of DOW values near the 1:1 line, net autotrophy began anywhere between 2 to 15 days prior to ice retreat (not considering locations that remained net heterotrophic, i.e. $NCP < 0$). We do observe some diverging bands of data points with negative DOW and $NCP_{pCO2} > NCP_{O2/Ar}$. We hypothesize that these bands may be due to the coarse resolution of the AMSR2 sea ice concentration data that was used to calculate DOW. We find a sharper relationship between *in-situ* sea surface temperature and the slope of $NCP_{O2/Ar}/NCP_{pCO2}$ (Figure S3.6), suggesting that gridded satellite data is unable to capture small scale decreases in sea ice cover that would lead to warmer sea surface temperatures by solar insolation. The coarse resolution of our sea ice concentration data would also impact our estimates of air-sea gas exchange in partially ice-covered waters, which may lead to slight underestimates in both $NCP_{O2/Ar}$ and NCP_{pCO2} within the marginal ice zone.

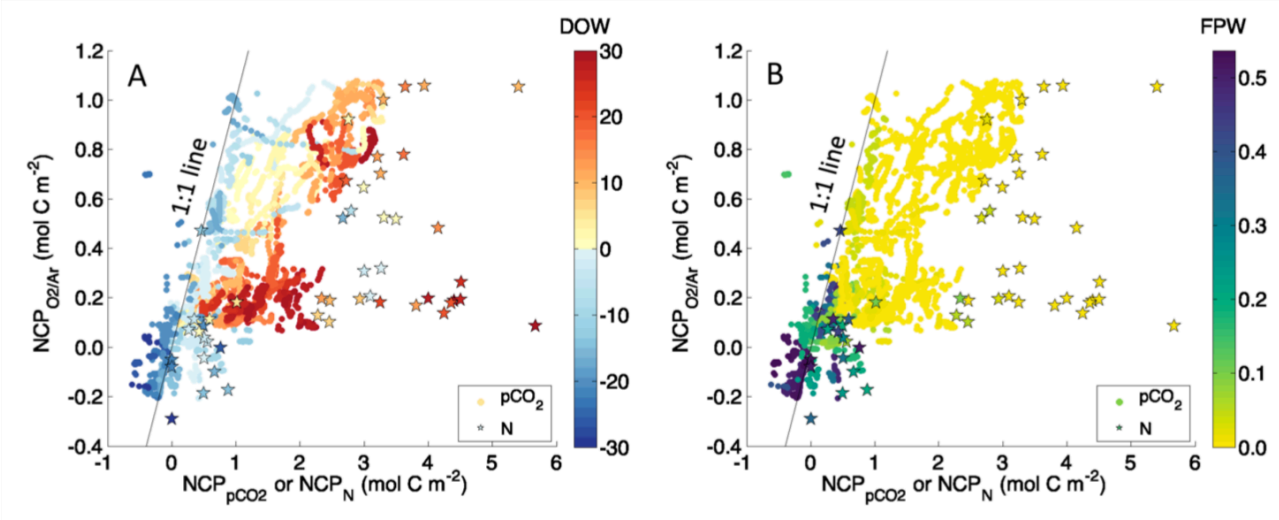

Figure 3.6: Scatterplots of $NCP_{O2/Ar}$ estimates plotted against seasonal NCP estimates (NCP_{pCO2} and NCP_N). NCP_{pCO2} values are plotted as dots, whereas NCP_N values are plotted as stars. Panel (A) shows NCP estimates colored according to the days of open water (DOW) at each sample location, and panel (B) similarly shows values colored according to the average fraction of Pacific water (FPW) within the surface mixed layer.

Under open water conditions (DOW>0), NCP_{pCO2} continued to increase while $NCP_{O2/Ar}$ either remained approximately constant or decreased. This is consistent with the short-lived ice-edge bloom commonly observed in satellite chlorophyll *a* observations, which quickly depletes the nutrient availability of the shallow, sea-ice meltwater stratified surface layer (Perrette et al., 2011). High $NCP_{O2/Ar}$ values coinciding with open water conditions were mainly observed at earlier sampling dates (yearday 160 – 175; transects 100 –300) when the ice-edge remained in the center of our study region, whereas locations sampled later in the season (yearday 185 –190) displayed $NCP_{O2/Ar}$ values near zero in open water (Figure S3.7) likely due to post-bloom nutrient-depleted surface waters.

As DOW increased, NCP_N estimates generally became increasingly greater than NCP_{pCO2}, indicating the continuation of primary production below the surface mixed layer, in sub-surface chlorophyll maxima (SCMs). During the first three transects of the cruise (100 – 300), NCP_N values were on average 1.3 mol C m^{-2} greater than NCP_{pCO2} (σ =0.7), and in later transects NCP_N values averaged 1.6 mol C m^{-2} greater than NCP_{pCO2} (σ = 1.1). This is consistent with the pattern of bloom succession described in the literature (Martin et al., 2010; Sakshaug, 2004). The fluorescence signal in Figure 3.3G also showed this progression from surface bloom to SCM in Atlantic waters, coinciding with a deepening nitracline. Based on differences between NCP_N and NCP_{pCO2} estimates in Atlantic waters, we estimate that SCMs may have contributed up to 70% of total NCP in the latter half of our study period (transects 400 – 700; see Figure S3.8).

Figure 3.6B shows a scatterplot of our NCP estimates, with data points colored according to the fraction of Pacific water (FPW), demonstrating that seasonal NCP was consistently lower in the Arctic waters in western Baffin Bay than in the Atlantic waters in eastern Baffin Bay. All seasonal NCP estimates in locations with FPW > 0.2 were lower than 1 mol C m^{-2}, with NCP_N estimates not differing greatly from NCP_{pCO2} (average difference of 0.3 mol C m^{-2}, $\sigma = 0.2$). This suggests that the majority of NCP that had occurred in this region was located near the surface. It is important to note that most sampling locations in Arctic outflow waters remained ice-covered at the time of sampling, so it is likely that given more time NCP would increase. However, the water column characteristics observed in western Baffin Bay suggest that future primary production will likely be limited compared to that in eastern Baffin Bay. Arctic waters displayed higher freshwater content over the upper ~80 m of the water column (Figure 3.3A), and displayed lower pre-bloom nitrate concentrations in comparison to Atlantic waters (Figure 3.3E; (Randelhoff et al., 2019)). Nitrate concentrations were especially low (< 3 μmol/kg) in Arctic waters over the upper 20 – 30 m of the water column, with strong stratification inhibiting the replenishment of nutrients from below. Based on these characteristics, it is likely that seasonal NCP rates in Arctic waters will remain below those observed in the east.

3.5.3 Comparison with previous studies

A number of previous studies utilizing multi-year observations in northern Baffin Bay have revealed declining trends in primary production and/or NCP (Bélanger et al., 2013; Bergeron & Tremblay, 2014; Blais et al., 2017; Marchese et al., 2017). Bergeron and Tremblay (2014) and Blais et al. (2017) reported declining rates of NCP and phytoplankton biomass, respectively, to coincide with decreasing salinity in the upper water column. Both investigations also noted the strongest declining trends occurred at western stations in Arctic outflow waters. These reported trends align well with our observations of low NCP associated with Arctic outflow waters in western Baffin Bay. Using a satellite-based model to assess primary production trends from 1998 to 2010, Bélanger et al. (2013) also found decreasing trends in primary production along major exit routes of Arctic waters, such as the outflow shelves of East Greenland, the Canadian Arctic Archipelago (CAA), and northwestern Baffin Bay.

A limited number of studies have previously published estimates of NCP in Baffin Bay. The synthesis study of Codispoti et al. (2013) reported average NCP values over large sub-regions of the Arctic Ocean, utilizing nutrient data collected between 1970 and 2007. These authors found a higher average NCP value of 32 g C m^{-2} (2.7 mol C m^{-2}) for their “Canadian Archipelago” region, which included western Baffin Bay and the channels of the CAA, compared to 10 g C m^{-2} (0.8 mol C m^{-2}) over their “Greenland Shelf” region, which encompassed both the East and West Greenland shelves. Interestingly,

this is opposite to the east-west NCP gradient we report in Baffin Bay. Codispoti et al. (2013) found surface waters in the CAA to have higher pre-bloom nitrate concentrations (~10 μM) compared to those over the Greenland shelves (< 5 μM), and reported lower surface salinities and stronger stratification over the Greenland shelves. We again find the opposite trend, with our results in western Baffin Bay displaying lower pre-bloom nitrate concentrations and stronger stratification (Figure 3.3). It is likely that this disparity of results is simply a manifestation of comparing multi-annual averaged values over immense areas, with those calculated over smaller spatial and temporal scales (this study). Therefore, perhaps meaningful comparisons cannot be made between these two studies. However, it is also possible that inter-annual changes in the freshwater inventory of both the BIC and WGC systems contributed somewhat to this disparity.

We find better agreement between our NCP_N estimates in western Baffin Bay and those reported by Bergeron and Tremblay (2014) near the end of their roughly decadal study (1997 –2011) in northern Baffin Bay. These authors reported a minimum annual NCP value of 214 mmol NO_3 m^{-2} (or 1.42 mol C m^{-2}) from the year 2009. Our NCP_N values, calculated using the same approach, produce a mean value of 0.4 mol C m^{-2} (σ = 0.3) in Arctic waters (surface FPW > 0.2), which is still significantly lower than the 2009 value of Bergeron and Tremblay (2014), but perhaps this is to be expected considering the earlier sampling dates of our study, and the declining NCP trend reported by Bergeron and Tremblay (2014).

Finally, the study of Tremblay et al. (2006) reported NCP estimates in the eastern North Water Polynya (NOW) region during June and July 1998 (comparable with our Atlantic domain in eastern Baffin Bay). These authors calculated seasonal NCP rates based on nitrate and DIC drawdown over the upper 150 m of the water column, and reported values of ~9.5 mol C m^{-2} in June, and ~10.5 mol C m^{-2} in July. These are much higher than our maximum NCP rate in eastern Baffin Bay of 5.7 mol C m^{-2}, however given the declining NCP and primary production trends over the past decade within the NOW region (Bélanger et al., 2013; Bergeron & Tremblay, 2014; Blais et al., 2017; Marchese et al., 2017), such high rates of NCP are no longer occurring within the NOW region. Our reported seasonal NCP rates within the Atlantic sector of Baffin Bay (1.4 –5.7 mol C m^{-2}) fall in the same approximate range as those reported more recently in the productive Barents Sea (2.3 –4.2 mol C m^{-2}) (Chierici et al., 2019; Codispoti et al., 2013; Fransson et al., 2001).

3.5.4 Caveats of inferring pre-bloom conditions from the temperature minimum

Due to the fact that winter measurements are scarce within the Arctic region, former studies of nutrient or DIC drawdown have inferred winter surface concentrations from summer profiles (Randelhoff

et al., 2019; Ulfsbo et al., 2014). Following Rudels et al. (1996) the temperature minimum located below the summer mixed layer is assumed to indicate the depth of winter convection during the previous winter, and therefore, it is generally assumed that nutrient concentrations at the temperature minimum are representative of the previous winter's surface mixed layer. However, depending on the water mass assembly of certain Arctic Seas it can be very challenging to accurately identify the depth of winter convection using the temperature minimum. We found this to be the case in western Baffin Bay (Figure 3.3), where the upper 100 – 150 m of the water column remains near the freezing point temperature with several temperature minima, suggesting advection from neighboring areas with slightly different convection depths and salinities. Even in eastern Baffin Bay, where the location of the temperature minimum layer is more easily identifiable, linearly interpolating between sparse sample depths may lead to significant uncertainty in defining winter surface water nutrient concentrations.

Using our nitrate measurements we performed a comparison of NCP_N estimates from two different approaches: (1) using the salinity-nutrient relationship approach of Bergeron and Tremblay (2014), which is the same as the NCP_N method used in this work, but will be referred to in this section as the “BT14” method, and (2) using the temperature minimum (T_{min}) characteristics of each station to represent the previous winter’s surface water conditions. The T_{min} approach integrates nitrate drawdown over the winter MLD (all depths above the T_{min}), and assumes that winter surface nitrate concentrations remained constant throughout this layer, unless diluted by freshwater inputs (see Text S3.1 for details on T_{min} method). It was immediately apparent from comparing these two methods that the BT14 method produced much greater NCP estimates (up to a factor of 2) than the T_{min} approach (see Figure 3.7A). In many cases, NCP values from the BT14 approach were double those produced using T_{min} characteristics. The greatest discrepancies were found at sampling locations in eastern Baffin Bay, suggesting that biological nutrient drawdown may have already occurred below the T_{min} depth at these locations. This is also supported by the pre-bloom (or winter) surface nitrate concentrations predicted by each method (Figure 3.7B), with the T_{min} approach underestimating pre-bloom surface nitrate concentrations in eastern Baffin Bay compared to the BT14 estimates. Additionally, fluorescence measurements clearly showed the downward migration of the bloom in eastern Baffin Bay to the T_{min} depth (see Figure 3.3G). It follows that the T_{min} approach may lead to underestimations of NCP and/or new production in situations where nutrient drawdown occurs at or below the T_{min} depth.

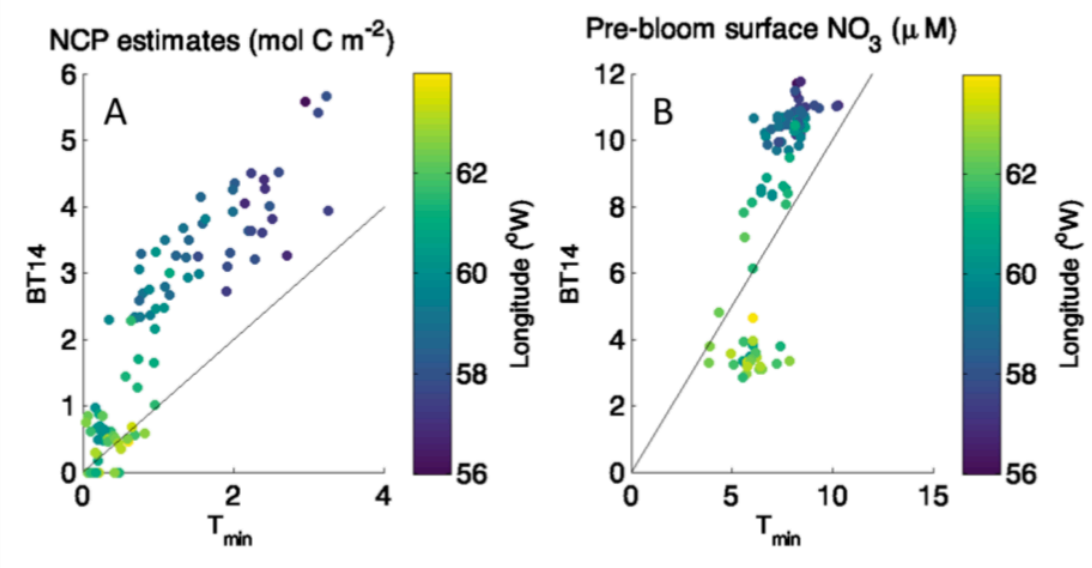

Figure 3.7: Comparison of T_{min} and BT14 approaches of estimating NCP. Panel A compares NCP estimates from both approaches. Panel B compares estimated pre-bloom surface nitrate concentrations (in μM). Points are colored according to the longitude (°W) of each sampling site, and 1:1 lines are shown in black.

Our NCP_{pCO2} approach also relies on T_{min} characteristics to define pre-bloom DIC concentrations in the Atlantic and Arctic domains of Baffin Bay. Interestingly, our NCP_{pCO2} estimates agree well with the BT14 method integrated over the surface mixed layer (see Figure S3.9). However, it is possible that this good agreement is largely due to the relatively shallow integration depth. We expect that if our NCP_{pCO2} approach were applied over a greater depth range (e.g. to the depth of winter convection estimated by T_{min}), it would also underestimate the true seasonal NCP.

3.5.5 Implications for marine ecosystems and carbon cycling

Our results highlight a strong contrast in spring NCP between the Arctic and Atlantic water domains of Baffin Bay. Arctic outflow waters displayed relatively low spring NCP (< 1 mol C m^{-2}) associated with persistent sea ice cover, high freshwater content, and strong stratification of the upper water column. Meanwhile, modified Atlantic waters in eastern Baffin Bay were largely ice-free, with comparatively deep surface mixed layers, and displayed relatively high NCP (up to 5.7 mol C m^{-2}).

The low NCP rates of Arctic outflow waters will also have secondary effects on the marine ecosystem and the cycling of carbon in this region. Lower spring NCP decreases food export to higher trophic levels, with potential adverse consequences for pelagic and benthic organisms. Blais et al. (2017) also observed decreasing phytoplankton cell sizes associated with Arctic outflow waters in northern Baffin Bay. Smaller cell sizes have lower sinking velocities and are therefore more likely to be recycled in the upper water column, feeding the microbial food web instead of passing organic material to the pelagic

and/or benthic food webs (Legendre & Rassoulzadegan, 1995). Assuming this same trend is affecting all Arctic outflow waters in western Baffin Bay, we are likely to observe decreasing biodiversity of pelagic and benthic organisms in this region.

Low NCP also has implications for the marine carbon cycle in western Baffin Bay, limiting the ability of these waters to act as an atmospheric CO_2 sink (Burgers et al., 2017). At the same time, high freshwater content will lower the buffering capacity (alkalinity) of these waters against ocean acidification, likely leading to lower pH in surface waters. Due to the cyclonic circulation within Baffin Bay, deeper Atlantic waters will be re-circulated through western Baffin Bay, transporting respiration products with them. With this combination of factors, we anticipate a build-up of high CO_2 and low pH waters in western Baffin Bay. Azetsu-Scott et al. (2010) have already shown that increasingly fresh Arctic outflow waters are prone to low seawater pH and calcium carbonate saturations states. On the other hand, high rates of NCP in eastern Baffin Bay will maintain the ability of this region to act as an atmospheric CO_2 sink throughout the productive season, and the associated export of organic material to depth will sustain populations of other pelagic and benthic organisms.

3.6 Conclusions and Future Recommendations

Based on our NCP_N estimates, we found average spring NCP of 3.7 and 0.4 mol C m^{-2} in the Atlantic and Arctic water domains of Baffin Bay, respectively. These results illustrate a strong dichotomy in the potential strength of the biological pump between eastern and western Baffin Bay. Low NCP in western Baffin Bay was likely caused by the high freshwater content of Arctic outflow waters and resultant strong stratification, which simultaneously decreased surface nitrate concentrations and restricted nutrient replenishment from below. These low rates of NCP may have adverse consequences for the pelagic and benthic food webs in this region, and decrease the ability of these waters to act as an atmospheric CO_2 sink. With the continuation of increasing glacial meltwater runoff into Baffin Bay (Bamber et al., 2018; Dahl-Jensen et al., 2011; Sharp et al., 2011), it is likely that this trend will continue and perhaps also begin to strengthen surface stratification in eastern Baffin Bay in the future (Castro de la Guardia et al., 2015), potentially also decreasing NCP rates on the West Greenland shelf in the future.

By comparing multiple NCP approaches with different integration depths and timescales we were able to track the spatial and temporal evolution of the spring bloom in southern Baffin Bay. We found the surface bloom was initiated under-ice, up to 15 days prior to ice retreat. Once the bloom progressed into open water, it quickly depleted surface nutrients and progressed deeper into the water column, becoming an SCM. We estimate that SCMs may have contributed up to 70% of the seasonal NCP within the Atlantic

domain, further establishing the importance of these features to the marine carbon cycle in Arctic Seas. We have also demonstrated that nutrient drawdown in the depth range of the SCM may coincide with, or surpass, the depth of the temperature minimum, a feature that has generally been considered a remnant of winter surface conditions. We hope this finding will serve to caution future investigations that conditions at the temperature minimum may not accurately represent the previous winter's surface conditions. Additionally, periodic sample collection in late-winter would greatly improve the accuracy of seasonal NCP estimates.

Literature Cited

Ardyna M, Babin M, Gosselin M, Devred E, Bélanger S, Matsuoka A, Tremblay J-É. 2013. Parameterization of vertical chlorophyll a in the Arctic Ocean: Impact of the subsurface chlorophyll maximum on regional, seasonal, and annual primary production estimates. *Biogeosciences* **10**(6): 4383–4404. doi: 10.5194/bg-10-4383-2013

Arrigo KR, Perovich DK, Pickart RS, Brown ZW, Van Dijken GL, Lowry KE, Mills MM, Palmer MA, Balch WM, Bahr F, et al. 2012. Massive phytoplankton blooms under arctic sea ice. *Science* **336**(6087): 1408. doi: 10.1126/science.1215065

Assmy P, Fernández-Méndez M, Duarte P, Meyer A, Randelhoff A, Mundy CJ, Olsen LM, Kauko HM, Bailey A, Chierici M, et al. 2017. Leads in Arctic pack ice enable early phytoplankton blooms below snow-covered sea ice. *Sci Rep* **7**(40850). doi: 10.1038/srep40850

Azetsu-Scott K, Clarke A, Falkner K, Hamilton J, Jones EP, Lee C, Petrie B, Prinsenberg S, Starr M, Yeats P. 2010. Calcium carbonate saturation states in the waters of the Canadian Arctic Archipelago and the Labrador Sea. *J Geophys Res Ocean* **115**(C11021). doi: 10.1029/2009JC005917

Bâcle J, Carmack EC, Ingram RG. 2002. Water column structure and circulation under the North Water during spring transition: April-July 1998. *Deep Res Part II* **49**(22–23): 4907–4925. doi: 10.1016/S0967-0645(02)00170-4

Bamber JL, Tedstone AJ, King MD, Howat IM, Enderlin EM, van der Broeke MR, Noel B. 2018. Land Ice Freshwater Budget of the Arctic and North Atlantic Oceans: 1. Data, Methods and Results. *J Geophys Res Ocean* **123**: 1827–1837. doi: 10.1002/2017JC013605

Barber DG, Hop H, Mundy CJ, Else B, Dmitrenko IA, Tremblay JE, Ehn JK, Assmy P, Daase M, Candlish LM, et al. 2015. Selected physical, biological and biogeochemical implications of a rapidly changing Arctic Marginal Ice Zone. *Prog Oceanogr* **139**: 122–150. Elsevier Ltd. doi: 10.1016/j.pocean.2015.09.003

Bélanger S, Babin M, Tremblay J-É. 2013. Increasing cloudiness in Arctic damps the increase in phytoplankton primary production due to sea ice receding. *Biogeosciences* **10**: 4087–4101. doi: 10.5194/bg-10-4087-2013

Bergeron M, Tremblay J-É. 2014. Shifts in biological productivity inferred from nutrient drawdown in the southern Beaufort Sea (2003-2011) and northern Baffin Bay (1997-2011), Canadian Arctic. *Geophys Res Lett* **41**: 3979–3987. doi: 10.1002/2014GL059649

Blais M, Ardyna M, Gosselin M, Dumont D, Bélanger S, Tremblay J-É, Gratton Y, Marchese C, Poulin M. 2017. Contrasting interannual changes in phytoplankton productivity and community structure in the coastal Canadian Arctic Ocean. *Limnol Oceanogr* **62**(6): 2480–2497. doi: 10.1002/lno.10581

Bliss AC, Steele M, Peng G, Meier WN, Dickinson S. 2019. Regional variability of Arctic sea ice seasonal change climate indicators from a passive microwave climate data record. *Environ Res Lett* **14**(045003). IOP Publishing. doi: 10.1088/1748-9326/aafb84

Brown ZW, Lowry KE, Palmer MA, van Dijken GL, Mills MM, Pickart RS, Arrigo KR. 2015. Characterizing the subsurface chlorophyll a maximum in the Chukchi Sea and Canada Basin. *Deep Res Part II Top Stud Oceanogr* **118**: 88–104. Elsevier. doi: 10.1016/j.dsr2.2015.02.010

Burgers TM, Miller LA, Thomas H, Else BGT, Gosselin M, Papakyriakou T. 2017. Surface Water pCO_2 variations and sea-air CO_2 fluxes during summer in the eastern Canadian Arctic. *J Geophys Res Ocean* **122**. doi: 10.1002/2017JC013250

Butterworth BJ, Miller SD. 2016. Air-sea exchange of carbon dioxide in the Southern Ocean and Antarctic marginal ice zone. *Geophys Res Lett* **43**: 7223–7230. doi: 10.1002/2016GL069581

Carmack EC, Yamamoto-Kawai M, Haine TWN, Bacon S, Bluhm BA, Lique C, Melling H, Polyakov I V., Straneo F, Timmermans ML, et al. 2016. Freshwater and its role in the Arctic Marine System: Sources, disposition, storage, export, and physical and biogeochemical consequences in the Arctic and global oceans. *J Geophys Res Biogeosciences* **121**: 675–717. doi: 10.1002/2015JG003140

Cassar N, Barnett BA, Bender ML, Kaiser J, Hamme RC, Tilbrook B. 2009. Continuous High-Frequency Dissolved O_2/Ar Measurements by Equilibrator Inlet Mass Spectrometry. *Anal Chem* **81**(5): 1855–1864. doi: 10.1021/ac802300u

Castro de la Guardia L, Hu X, Myers PG. 2015. Potential positive feedback between Greenland Ice Sheet melt and Baffin Bay heat content on the west Greenland shelf. *Geophys Res Lett* **42**: 4922–4930. doi: 10.1002/2015GL064626

Chierici M, Vernet M, Fransson A, Børsheim KY. 2019. Net Community Production and Carbon Exchange From Winter to Summer in the Atlantic Water Inflow to the Arctic Ocean. *Front Mar Sci* **6**(528). doi: 10.3389/fmars.2019.00528

Codispoti LA, Kelly V, Thessen A, Matrai P, Suttles S, Hill V, Steele M, Light B. 2013. Synthesis of primary production in the Arctic Ocean: III. Nitrate and phosphate based estimates of net community production. *Prog Oceanogr* **110**: 126–150. doi: 10.1016/j.pocean.2012.11.006

Craig H, Hayward T. 1987. Oxygen Supersaturation in the Ocean : Biological Versus Physical Contributions. *Science* **235**(4785): 199–202.

Dahl-Jensen D, Bamber J, Bøggild CE, van den Broeke M, Buck E, Christensen J, Dethloff K, Fahnestock M, Marshall S, Rosing M, et al. 2011. Chapter 8: The Greenland Ice Sheet in a Changing Climate. In: *Snow, Water, Ice and Permafrost in the Arctic (SWIPA): Climate Change and the Cryosphere*. Oslo, Norway: Arctic Monitoring and Assessment Programme (AMAP). p. xii + 538 pp.

Dickson AG. 1990. Standard potential of the reaction: AgCl(s) + 12H_2(g) = Ag(s) + HCl(aq), and and the standard acidity constant of the ion HSO_4^- in synthetic sea water from 273.15 to 318.15 K. *Chem Thermodyn* **22**: 113–127. https://doi.org/10.1016/0021-9614(90)90074-Z

Dickson AG, Sabine CL, Christian JR. 2007. Guide to best practices for ocean CO_2 measurements. *PICES Spec Publ* **3**: p191. doi: 10.1159/000331784

Dodd PA, Rabe B, Hansen E, Falck E, MacKensen A, Rohling E, Stedmon C, Kristiansen S. 2012. The freshwater composition of the Fram Strait outflow derived from a decade of tracer measurements. *J Geophys Res Ocean* **117**(11): 1–26. doi: 10.1029/2012JC008011

Else BGT, Papakyriakou TN, Galley RJ, Mucci A, Gosselin M, Miller LA, Shadwick EH, Thomas H. 2012. Annual cycles of pCO_{2sw} in the southeastern Beaufort Sea: New understandings of air-sea CO_2 exchange in arctic polynya regions. *J Geophys Res Ocean* **117**: C00G13. doi: 10.1029/2011JC007346

Else BGT, Whitehead JJ, Galindo V, Ferland J, Mundy CJ, Gonski SF, Ehn JK, Rysgaard S, Babin M. 2019. Response of the Arctic marine inorganic carbon system to ice algae and under-ice phytoplankton blooms: A case study along the fast-ice edge of Baffin Bay. *J Geophys Res Ocean*, in press. doi: 10.1029/2018JC013899

Eveleth R, Cassar N, Doney SC, Munro DR, Sweeney C. 2017. Biological and physical controls on O_2/Ar, Ar and pCO_2 variability at the Western Antarctic Peninsula and in the Drake Passage. *Deep Res II* **139**: 77–88. doi: 10.1016/j.dsr2.2016.05.002

Eveleth R, Timmermans M-L, Cassar N. 2014. Physical and biological controls on oxygen saturation variability in the upper Arctic Ocean. *J Geophys Res Ocean* **119**: 7420–7432. doi: 10.1002/2014JC009816

Fairbanks R. 1982. The Origin of Continental Shelf and Slope Water in the New York Bight and Gulf of Maine: Evidence from $H_2{}^{18}O/ H_2{}^{16}O$ Ratio Measurements. *J Geophys Res* **87**(C8): 5796–5808.

Falkowski P, Laws E, Barber R, Murray J. 2003. Phytoplankton and their role in primary, new, and export production. In: Fasham MR, editor. *Ocean Biogeochemistry*. Berlin, Heidelberg: Springer. p. 99–121.

Fortier M, Fortier L, Michel C, Legendre L. 2002. Climatic and biological forcing of the vertical flux of biogenic particles under seasonal Arctic sea ice. *Mar Ecol Prog Ser* **225**: 1–16. doi: 10.3354/meps225001

Fransson A, Chierici M, Anderson LG, Bussmann I, Kattner G, Peter Jones E, Swift JH. 2001. The importance of shelf processes for the modification of chemical constituents in the waters of the Eurasian Arctic Ocean: Implication for carbon fluxes. *Cont Shelf Res* **21**: 225–242. doi: 10.1016/S0278-4343(00)00088-1

Friis K. 2003. The salinity normalization of marine inorganic carbon chemistry data. *Geophys Res Lett* **30**(2). doi: 10.1029/2002GL015898

Garcia HE, Gordon LI. 1992. Oxygen solubility in seawater : Better fitting equations. *Limnol Oceanogr* **37**(6): 1307–1312.

Haine TWN, Curry B, Gerdes R, Hansen E, Karcher M, Lee C, Rudels B, Spreen G, de Steur L, Stewart KD, et al. 2015. Arctic freshwater export: Status, mechanisms, and prospects. Global and Planetary Change. doi: 10.1016/j.gloplacha.2014.11.013

Hamme RC, Emerson SR. 2004. The solubility of neon, nitrogen and argon in distilled water and seawater. *Deep Sea Res Pt I* **51**: 1517–1528. doi: 10.1016/j.dsr.2004.06.009

van Heuven S, Pierrot D, Rae JWB, Lewis E, Wallace DW. 2011. MATLAB program developed for CO_2 system calculations. Oak Ridge: US Department of Energy: ORML/CDIAC-105b. Carbon Dioxide Information Analysis Center.

Horvat C, Jones DR, Iams S, Schroeder D, Flocco D, Feltham D. 2017. The frequency and extent of sub-ice phytoplankton blooms in the Arctic Ocean. *Sci Adv* **3**(e1601191). doi: 10.1126/sciadv.1601191

Johnson KM, Wills KD, Butler DB, Johnson WK, Wong CS. 1993. Coulometric total carbon dioxide analysis for marine studies : maximizing the performance of an automated gas extraction system and coulometric detector. *Mar Chem* **44**(1993): 167–187. doi: 10.1016/0304-4203(93)90201-X

Jones EP, Anderson LG, Swift JH. 1998. Distribution of Atlantic and Pacific waters in the upper Arctic Ocean : Implications for circulation. *Geophys Res Lett* **25**(6): 765–768. doi: 10.1029/98gl00464

Kahru M, Brotas V, Manzano-Sarabia M, Mitchell BG. 2011. Are phytoplankton blooms occurring earlier in the Arctic? *Glob Chang Biol* **17**(4): 1733–1739. doi: 10.1111/j.1365-2486.2010.02312.x

Kalnay E, Kanamitsu M, Kistler R, Collins W, Deaven D, Gandin L, Iredell M, Saha S, White G, Woollen J, et al. 1996. The NCEP / NCAR 40-Year Reanalysis Project. *Bull Am Meteorol Soc* **77**(3): 437–471.

Landy JC, Ehn JK, Babb DG, Thériault N, Barber DG. 2017. Sea ice thickness in the Eastern Canadian Arctic: Hudson Bay Complex & Baffin Bay. *Remote Sens Environ* **200**: 281–294. doi: 10.1016/j.rse.2017.08.019

Laws EA. 1991. Photosynthetic quotients, new production and net community production in the open ocean. *Deep Sea Res* **38**(1): 143–167. doi: 10.1016/0198-0149(91)90059-O

Legendre L, Rassoulzadegan F. 1995. Plankton and nutrient dynamics in marine waters. *Ophelia* **41**(1): 153–172. doi: 10.1080/00785236.1995.10422042

Leu E, Mundy CJ, Assmy P, Campbell K, Gabrielsen TM, Gosselin M, Juul-Pedersen T, Gradinger R. 2015. Arctic spring awakening - Steering principles behind the phenology of vernal ice algal blooms. *Prog Oceanogr* **139**: 151–170. Elsevier Ltd. doi: 10.1016/j.pocean.2015.07.012

Lueker TJ, Dickson AG, Keeling CD. 2000. Ocean pCO_2 calculated from dissolved inorganic carbon, alkalinity, and equations for K1 and K2: validation based on laboratory measurements of CO_2 in gas and seawater at equilibrium. *Mar Chem* **70**: 105–119.

MacGilchrist GA, Garabato ACN, Tsubouchi T, Bacon S, Torres-Valdés S, Azetsu-Scott K. 2014. The Arctic Ocean carbon sink. *Deep Res Part I* **86**: 39–55. Elsevier. doi: 10.1016/j.dsr.2014.01.002

Marchese C, Albouy C, Tremblay J-É, Dumont D, D'Ortenzio F, Vissault S, Bélanger S. 2017. Changes in phytoplankton bloom phenology over the North Water (NOW) polynya: a response to changing environmental conditions. *Polar Biol* **40**: 1721–1737. doi: 10.1007/s00300-017-2095-2

Martin J, Tremblay JÉ, Gagnon J, Tremblay G, Lapoussière A, Jose C, Poulin M, Gosselin M, Gratton Y, Michel C. 2010. Prevalence, structure and properties of subsurface chlorophyll maxima in Canadian Arctic waters. *Mar Ecol Prog Ser* **412**: 69–84. doi: 10.3354/meps08666

Münchow A, Falkner KK, Melling H. 2014. Baffin Island and West Greenland Current Systems in northern Baffin Bay. *Prog Oceanogr* **132**: 305–317. doi: 10.1016/j.pocean.2014.04.001

Mundy CJ, Gosselin M, Ehn J, Gratton Y, Rossnagel A, Barber DG, Martin J, Tremblay J-E, Palmer M, Arrigo KR, et al. 2009. Contribution of under-ice primary production to an ice-edge upwelling phytoplankton bloom in the Canadian Beaufort Sea. *Geophys Res Lett* **36**: L17601. doi: 10.1029/2009GL038837

Niebauer HJ. 1991. Bio-physical oceanographic interactions at the edge of the Arctic ice pack. *J Mar Syst* **2**: 209–232. doi: 10.1016/0924-7963(91)90025-P

Östlund HG, Hut G. 1984. Arctic Ocean water mass balance from isotope data. *J Geophys Res Ocean* **89**(C4): 6373–6381. doi: 10.1029/JC089iC04p06373

Oziel L, Massicotte P, Randelhoff A, Ferland J, Vladoiu A, Lacour L, Galindo V, Lambert-Girard S, Dumont D, Cuypers Y, et al. 2019. Environmental factors influencing the seasonal dynamics of spring algal blooms in and beneath sea ice in western Baffin Bay. *Elem Sci Anth* **7**(1): 34. doi: 10.1525/elementa.372

Peng G, Steele M, Bliss AC, Meier WN, Dickinson S. 2018. Temporal means and variability of Arctic sea ice melt and freeze season climate indicators using a satellite climate data record. *Remote Sens* **10**(1328). doi: 10.3390/rs10091328

Perrette M, Yool A, Quartly GD, Popova EE. 2011. Near-ubiquity of ice-edge blooms in the Arctic. *Biogeosciences* **8**: 515–524. doi: 10.5194/bg-8-515-2011

Pierrot D, Neill C, Sullivan K, Castle R, Wanninkhof R, Lüger H, Johannessen T, Olsen A, Feely RA, Cosca CE. 2009. Recommendations for autonomous underway pCO_2 measuring systems and data-reduction routines. *Deep Res Part II* **56**: 512–522. doi: 10.1016/j.dsr2.2008.12.005

Prytherch J, Brooks IM, Crill PM, Thornton BF, Salisbury DJ, Tjernström M, Anderson LG, Geibel MC, Humborg C. 2017. Direct determination of the air-sea CO_2 gas transfer velocity in Arctic sea ice

regions. *Geophys Res Lett* **44**: 3770–3778. doi: 10.1002/2017GL073593

Randelhoff A, Oziel L, Massicotte P, Bécu G, Galí M, Lacour L, Dumont D, Vladoiu A, Marec C, Bruyant F, et al. 2019. The evolution of light and vertical mixing across a phytoplankton ice-edge bloom. *Elem Sci Anthr* **7**: 20. doi: 10.1525/elementa.357

Reuer MK, Barnett BA, Bender ML, Falkowski PG, Hendricks MB. 2007. New estimates of Southern Ocean biological production rates from O_2/Ar ratios and the triple isotope composition of O_2. *Deep Res Part I* **54**(6): 951–974. doi: 10.1016/j.dsr.2007.02.007

Rudels B, Anderson LG, Jones EP. 1996. Formation and evolution of the surface mixed layer and halocline of the Arctic Ocean. *J Geophys Res* **101**(C4): 8807–8821. doi: 10.1029/96JC00143

Rutgers van der Loeff MM, Cassar N, Nicolaus M, Rabe B, Stimac I. 2014. The influence of sea ice cover on air-sea gas exchange estimated with radon-222 profiles. *J Geophys Res Ocean* **119**: 2735–2751. doi: 10.1002/2013JC009321

Sakshaug E. 2004. Primary and Secondary Production in the Arctic Seas. In: Macdonald RW, Stein R, editors. *The Organic Carbon Cycle in the Arctic Ocean*4th ed. Heidelberg: Springer. p. 57–81.

Shadwick EH, Thomas H, Chierici M, Else B, Fransson A, Michel C, Miller LA, Mucci A, Niemi A, Papakyriakou TN, et al. 2011. Seasonal variability of the inorganic carbon system in the Amundsen Gulf region of the southeastern Beaufort Sea. *Limnol Oceanogr* **56**(1): 303–322. doi: 10.4319/lo.2011.56.1.0303

Sharp M, Ananicheva M, Arendt A, Hagen J-O, Hock R, Josberger E, Moore D, Pfeffer WT, Wolken GJ. 2011. Chapter 7: Mountain Glaciers and Ice Caps. In: *Snow, Water, Ice and Permafrost in the Arctic (SWIPA): Climate Change and the Cryosphere*. Oslo, Norway: Arctic Monitoring and Assessment Programme (AMAP). p. xii + 538 pp.

Shaw WJ, Stanton TP, McPhee MG, Morison JH, Martinson DG. 2009. Role of the upper ocean in the energy budget of Arctic sea ice during SHEBA. *J Geophys Res* **114**: C06012. doi: 10.1029/2008JC004991

Spreen G, Kaleschke L, Heygster G. 2008. Sea ice remote sensing using AMSR-E 89-GHz channels. *J Geophys Res Ocean* **113**(2). doi: 10.1029/2005JC003384

Takahashi T, Olafsson J, Goddard JG, Chipman DW, Sutherland SC. 1993. Seasonal variation of CO_2 and nutrients in the high-latitude surface oceans: A comparative study. *Global Biogeochem Cycles* **7**(4): 843–878. doi: 10.1029/93GB02263

Tang CCL, Ross CK, Yao T, Petrie B, DeTracey BM, Dunlap E. 2004. The circulation, water masses and sea-ice of Baffin Bay. *Prog Oceanogr* **63**: 183–228. doi: 10.1016/j.pocean.2004.09.005

Teeter L, Hamme RC, Ianson D, Bianucci L. 2018. Accurate Estimation of Net Community Production From O2/Ar Measurements. *Global Biogeochem Cycles* **32**: 1163–1181. doi: 10.1029/2017GB005874

Timmermans M-L, Ladd C. 2018. Sea surface temperature. In: *Arctic Report Card 2018*. p. 33–35.

Tremblay J-É, Anderson LG, Matrai P, Coupel P, Bélanger S, Michel C, Reigstad M. 2015. Global and regional drivers of nutrient supply, primary production and CO_2 drawdown in the changing Arctic Ocean. *Prog Oceanogr* **139**: 171–196. doi: 10.1016/j.pocean.2015.08.009

Tremblay J-É, Gratton Y, Carmack EC, Payne CD, Price NM. 2002. Impact of the large-scale Arctic circulation and the North Water Polynya on nutrient inventories in Baffin Bay. *J Geophys Res* **107**(C8): 1–15. doi: 10.1029/2000JC000595

Tremblay JÉ, Hattori H, Michel C, Ringuette M, Mei Z-P, Lovejoy C, Fortier L, Hobson KA, Amiel D, Cochran K. 2006. Trophic structure and pathways of biogenic carbon flow in the eastern North Water Polynya. *Prog Oceanogr* **71**: 402–425. doi: 10.1016/j.pocean.2006.10.006

Tremblay JÉ, Simpson K, Martin J, Miller L, Gratton Y, Barber D, Price NM. 2008. Vertical stability and the annual dynamics of nutrients and chlorophyll fluorescence in the coastal, southeast Beaufort Sea. *J Geophys Res Ocean* **113**: C07S90. doi: 10.1029/2007JC004547

Ulfsbo A, Cassar N, Korhonen M, Heuven S Van, Hoppema M, Kattner G, Anderson L. 2014. Late summer net community production in the central Arctic Ocean using multiple approaches. *Global Biogeochem Cycles* **28**: 1129–1148. doi: 10.1002/2014GB004833

Wanninkhof R. 2014. Relationship between wind speed and gas exchange over the ocean revisited. *Limnol Oceanogr Methods* **12**: 351–362. doi: 10.1029/92JC00188

Weiss RF. 1974. Carbon dioxide in water and seawater: the solubility of a non-ideal gas. *Mar Chem* **2**(3): 203–215. doi: 10.1016/0304-4203(74)90015-2

Yamamoto-Kawai M, Tanaka N, Pivovarov S. 2005. Freshwater and brine behaviors in the Arctic ocean deduced from historical data of $\delta^{18}O$ and alkalinity (1929-2002 A.D.). *J Geophys Res Ocean* **110**(C10003). doi: 10.1029/2004JC002793

Yasunaka S, Siswanto E, Olsen A, Hoppema M, Watanabe E, Fransson A, Chierici M, Murata A, Lauvset SK, Wanninkhof R, et al. 2018. Arctic Ocean CO_2 uptake: An improved multiyear estimate of the air-sea CO_2 flux incorporating chlorophyll a concentrations. *Biogeosciences* **15**(6): 1643–1661. doi: 10.5194/bg-15-1643-2018

Supplemental Material

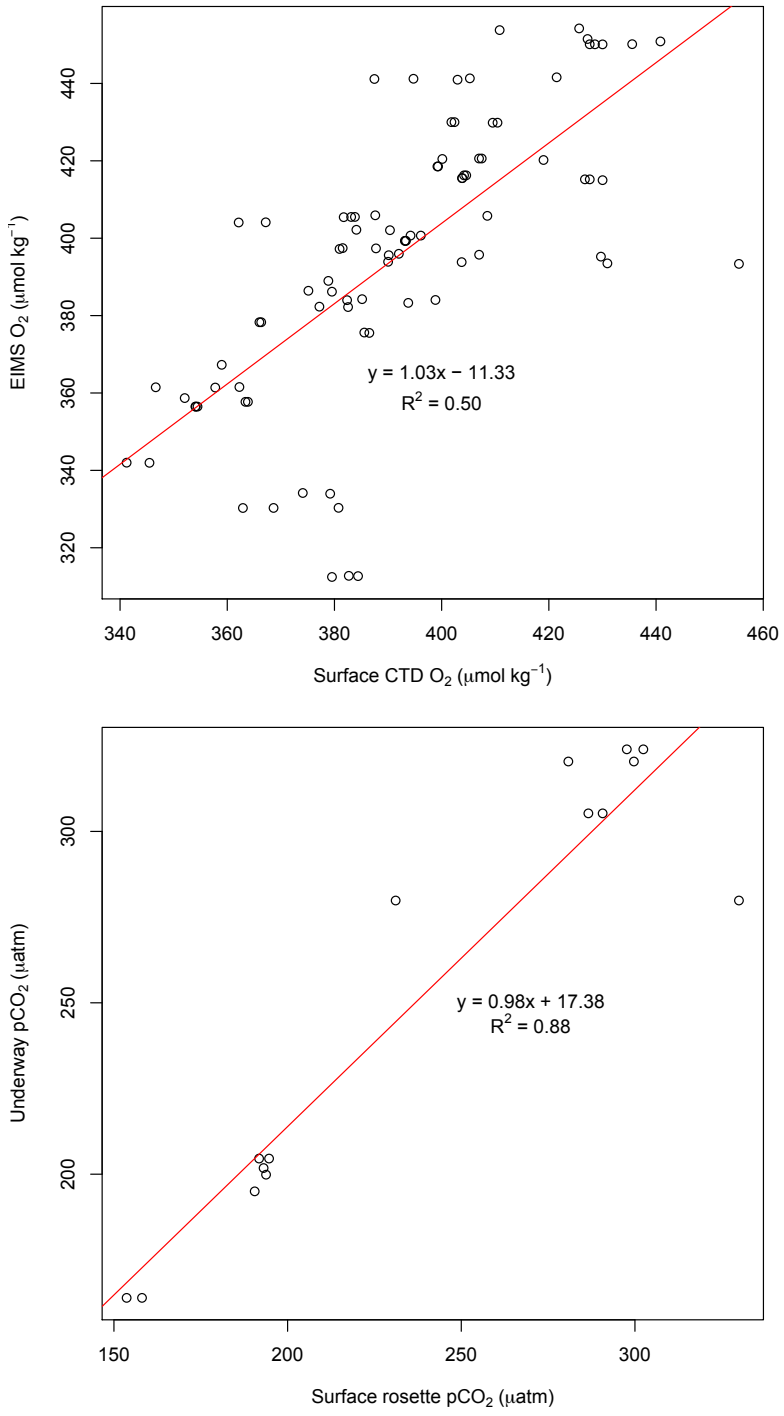

Figure S3.1: Comparison of underway measurements with surface measurements from the CTD/Rosette. Underway O_2 concentrations from the EIMS system were compared with surface values from an SBE43 sensor on the CTD/Rosette system. Underway pCO_2 measurements were compared with calculated pCO_2 values from surface bottle samples (for dissolved inorganic carbon and total alkalinity) collected within the upper 2 meters. Surface pCO_2 from bottle measurements were calculated using the carbonic acid dissociation constants from Lueker et al. (2000) and those of Dickson (1990) for bisulphate.

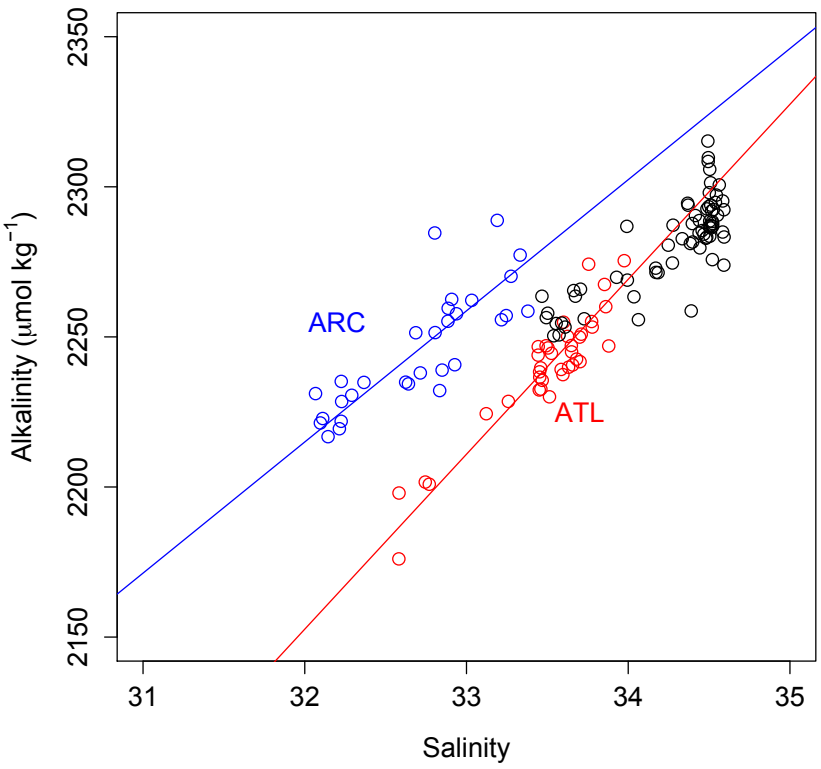

Figure S3.2: Defined salinity-alkalinity relationships for Arctic outflow (ARC) and modified-Atlantic waters (ATL). Blue dots represent sample data from ARC waters in the upper water column (salinity < 33.5) of western Baffin Bay, whereas red samples represent ATL waters in the upper water column (salinity < 34) of eastern Baffin Bay. The salinity constraints applied to isolate the upper water column were chosen to encompass all water masses above and including Arctic waters (ArW) in western Baffin Bay and Winter Atlantic water (WAW) in eastern Baffin Bay. All samples located at depths below these water masses are plotted as black dots and were not considered when defining the upper water column salinity-alkalinity relationships (red and blue lines).

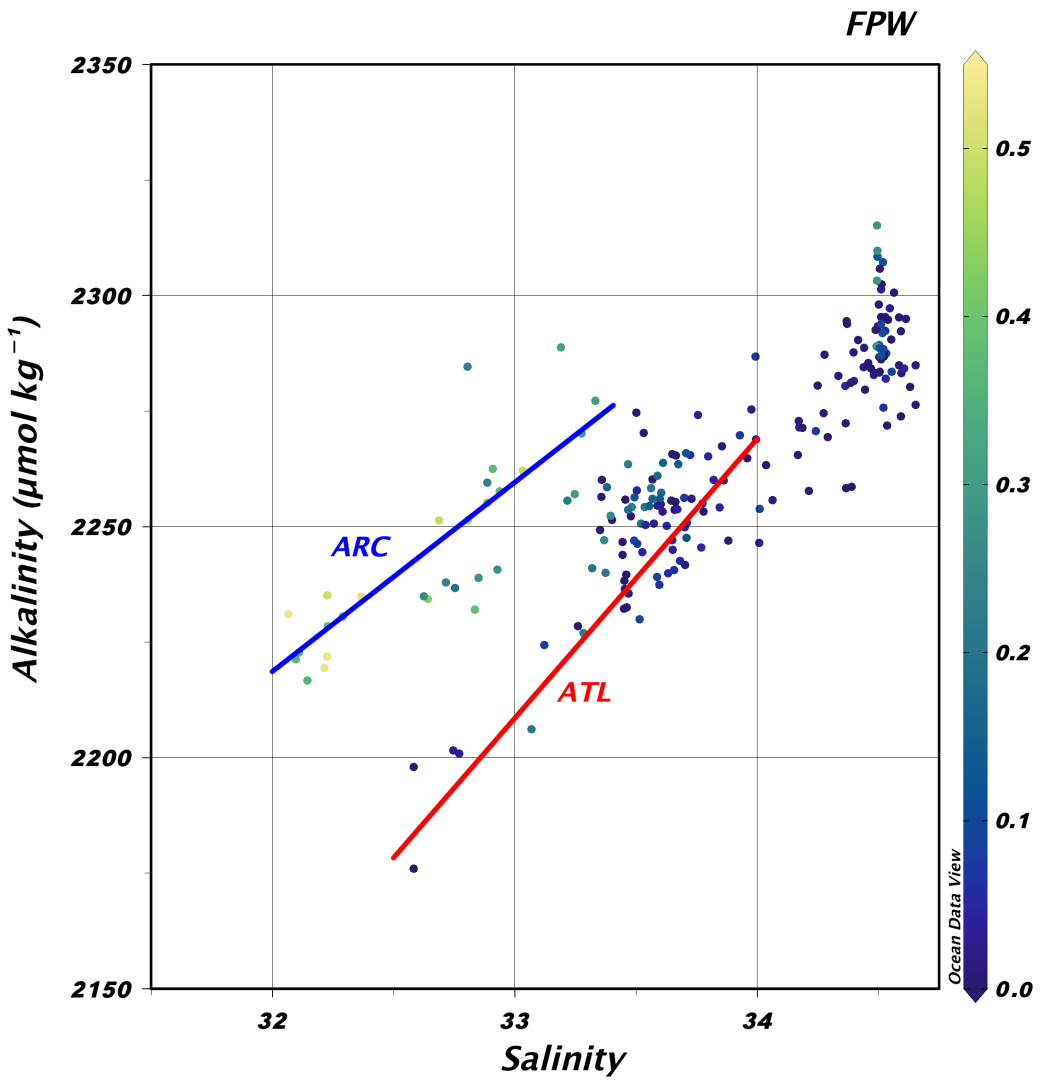

Figure S3.3: Salinity-alkalinity relationships for Arctic outflow (ARC) and modified-Atlantic waters (ATL). Same linear relationships (red and blue lines) as shown in Figure S2.2, with data points colored according to the fraction of Pacific water (FPW) at each sampling location.

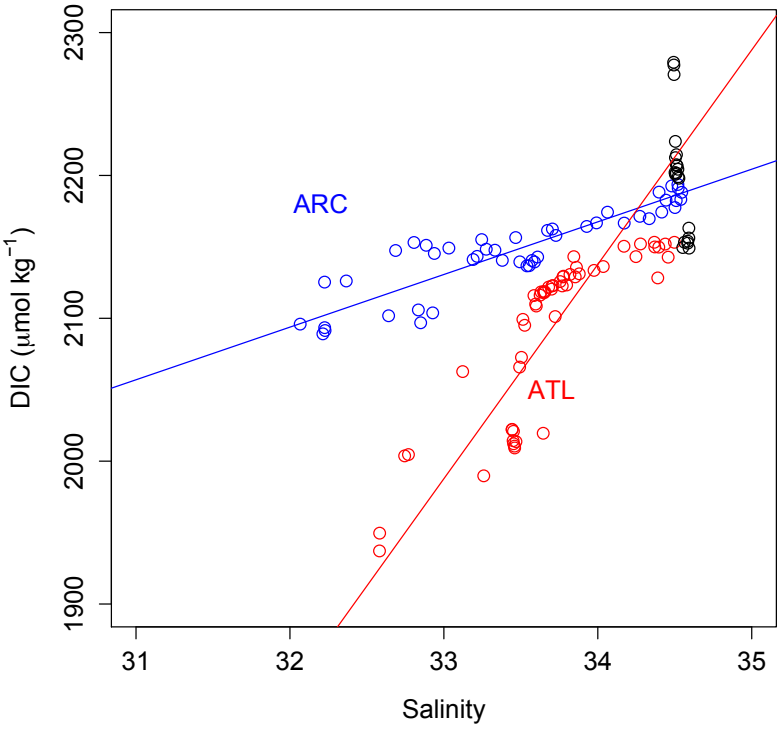

Figure S3.4: Defined salinity-DIC relationships for Arctic outflow (ARC) and modified-Atlantic waters (ATL). Blue dots represent sample data from ARC waters in the upper water column (salinity < 33.5) of western Baffin Bay, whereas red samples represent ATL waters in the upper water column (salinity < 34) of eastern Baffin Bay. The salinity constraints applied to isolate the upper water column were chosen to encompass all water masses above and including Arctic waters (ArW) in western Baffin Bay and Winter Atlantic water (WAW) in eastern Baffin Bay. All samples located at depths below these water masses are plotted as black dots and were not considered when defining the upper water column salinity-alkalinity relationships (red and blue lines).

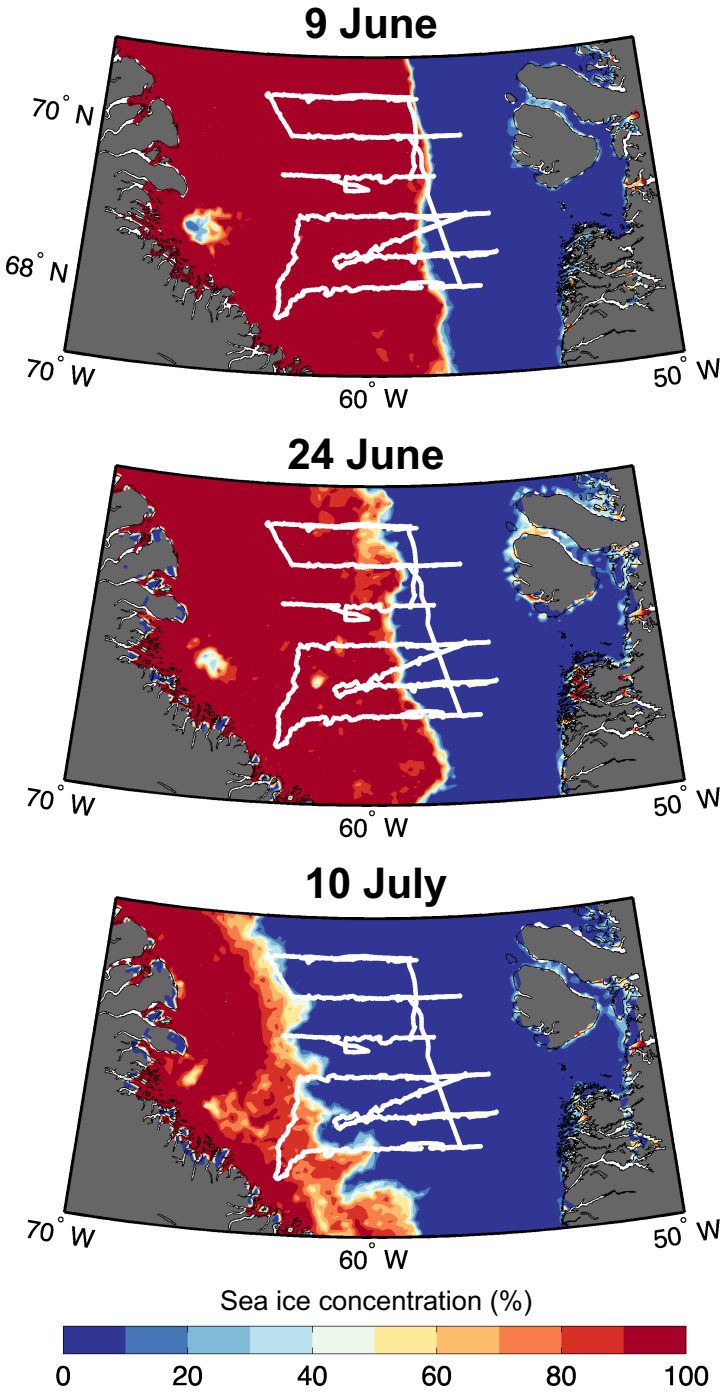

Figure S3.5: Daily sea ice concentration maps. Three daily maps of sea ice concentration (%) measurements from AMSR2 at the beginning (9 June 2016), middle (24 June 2016), and end (10 July 2016) dates of our research cruise.

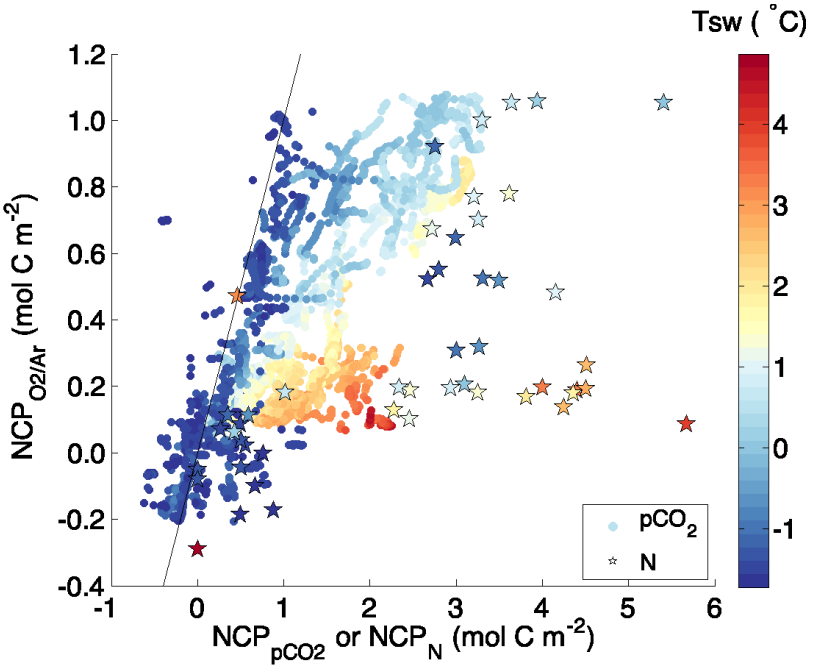

Figure S3.6: $NCP_{O2/Ar}$ vs. seasonal NCP estimates (NCP_{pCO2} and NCP_N). NCP_{pCO2} values are plotted as dots, whereas NCP_N values are plotted as stars. All plotted symbols are colored according to in-situ measurements of surface seawater temperature (Tsw).

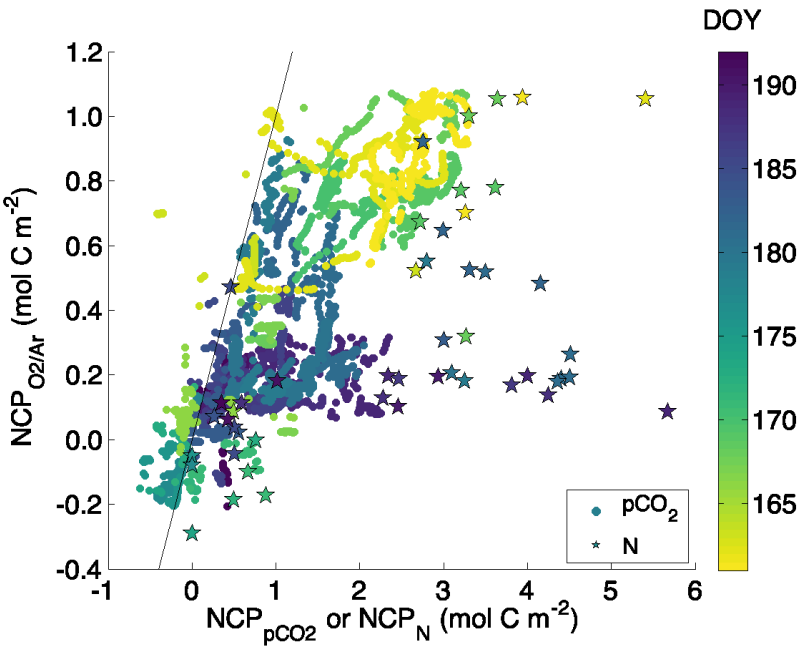

Figure S3.7: $NCP_{O2/Ar}$ vs. seasonal NCP estimates (NCP_{pCO2} and NCP_N). NCP_{pCO2} values are plotted as dots, whereas NCP_N values are plotted as stars. All plotted symbols are colored according to the sampling date, expressed as the numerical day of year (DOY).

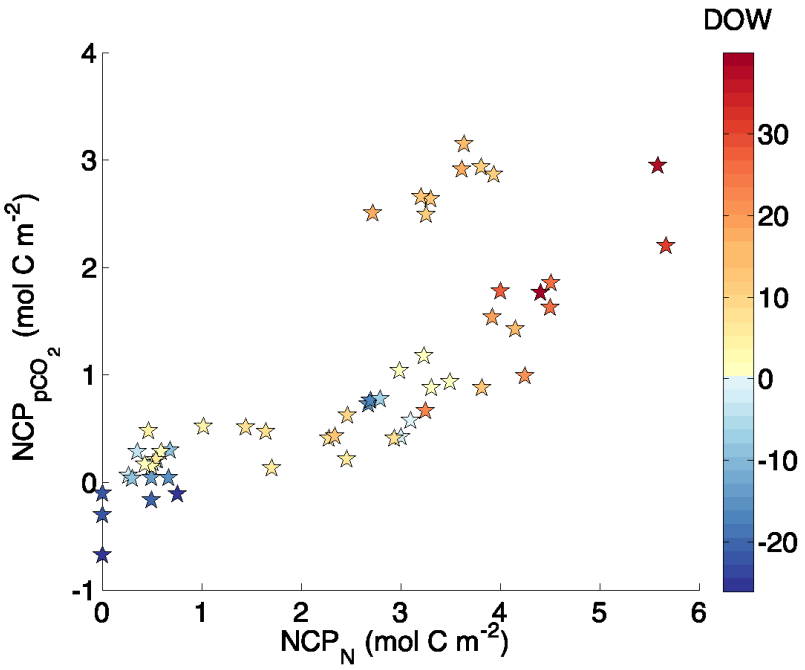

Figure S3.8: Comparison of seasonal NCP approaches. The NCP_{pCO2} approach integrates dissolved inorganic carbon drawdown within the surface mixed layer, whereas the NCP_N approach integrates nitrate drawdown over the total euphotic zone. All plotted NCP estimates are colored according to the days of open water (DOW) at each sampling location.

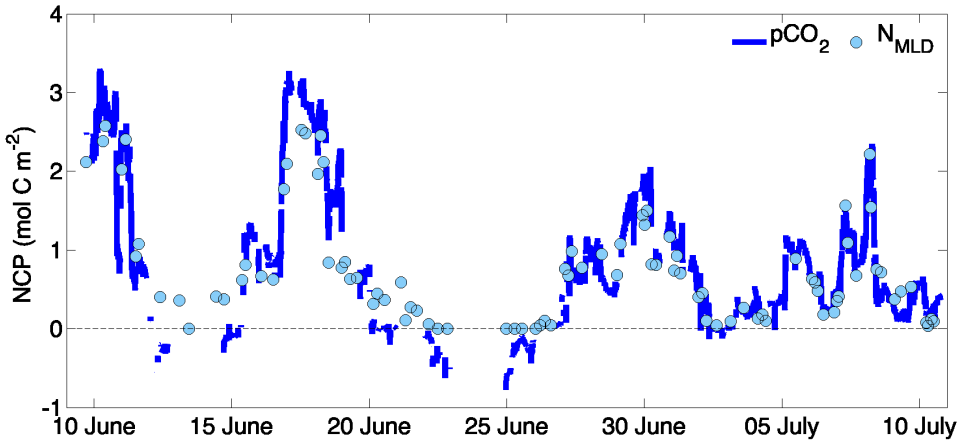

Figure S3.9: Timeseries of seasonal NCP approaches integrated over the surface mixed layer. NCP estimates from: (1) the pCO_2 approach, and (2) the nitrate drawdown approach of Bergeron and Tremblay (2014) integrated over the surface mixed layer (N_{MLD}).

Text S3.1: Estimating NCP based on temperature minimum (T_{min}) characteristics

NCP is estimated from the difference between observed spring nitrate concentrations (N_{obs}) and the assumed winter surface water nitrate concentration (N_w). The temperature minimum of each station profile is assumed to represent the characteristics of the previous winter's surface mixed layer; thus, N_w

is estimated from linear interpolation of the nearest neighboring sample depths. In order to account for the dilution of nutrients by freshwater inputs, N_w is linearly scaled by salinity at each depth following:

$$N_{wdil} = N_w(S_{obs}/S_w)$$

where S_w is the salinity at the temperature minimum, S_{obs} are observed salinities at each sample depth, and N_{wdil} represents the "expected" nitrate concentrations if there was no biological activity since the end of winter. We then calculate NCP_N as the depth-integrated nitrate deficit between the "expected" N_{wdil} concentrations and the observed concentrations, N_{obs} :

$$NCP_{Tmin}\ (\mathrm{mol\ C\ m^{-2}}) = \int_0^{MLD_W} (N_{wdil} - N_{obs})\,dz \cdot (R_{C:N})$$

where MLD_W is the depth of the winter mixed layer (the depth of the temperature minimum), and $R_{C:N}$ denotes the Redfield ratio of 106C:16N (Redfield et al., 1963). Values of NCP_N represent estimates of the time-integrated net community production since the end of winter up until the point of sampling.

References

Redfield AC, Ketchum BH, Richards FA. 1963. The Influence of Organisms on the Composition of Sea-water. In: Hill M, editor. *The Sea*. New York: Wiley Interscience. p. 26–77.

Chapter 4 Distinguishing physical and biological controls on the carbon dynamics in a high-Arctic outlet strait

This chapter was published in *Journal of Geophysical Research: Oceans.*

Burgers, T. M., Miller, L. A., Rysgaard, S., Mortensen, J., Else, B., Tremblay, J.-É., & Papakyriakou, T. (2023). Distinguishing Physical and Biological Controls on the Carbon Dynamics in a High-Arctic Outlet Strait. *Journal of Geophysical Research: Oceans*, *128*, e2022JC019393. https://doi.org/10.1029/2022JC019393

Please see Appendix A for the contributions of each collaborating author to this peer-reviewed paper.

Abstract

The water mass assembly of Nares Strait is variable, owing to fluctuating wind forcings over the central Arctic Basin, and irregular northward flows from the West Greenland Current (WGC) in Baffin Bay. Here we characterize the physico-chemical properties of the water masses entering Nares Strait in August 2014. We employ an extended optimum multi-parameter (OMP) analysis to estimate the mixing fractions of predefined source water masses, and to distinguish the role of physical and biological processes in governing the distribution of dissolved inorganic carbon (DIC) in Nares Strait. We show the first documented evidence of Siberian shelf waters arriving in Nares Strait, along with a diluted upper halocline layer of partial Pacific-origin. These mixed-origin water masses appear to play an important role in driving a modest phytoplankton bloom in Kane Basin, leading to decreased surface pCO_2 concentrations in Nares Strait. Although inorganic nitrogen was already limited near the surface in northern Nares Strait, the rather shallow upper halocline layer and the shoaling bathymetry in Kane Basin facilitated upwelling of nutrients to the surface. Our observations suggest that the positioning of the Transpolar Drift, and hence the balance of Atlantic and Pacific water delivered to Nares Strait, may play an important role in regional biological productivity and carbon uptake from the atmosphere. We also observed water masses from the WGC transported as far north as Kane Basin, contributing to relatively high pCO_2 and low pH in the intermediate and deep water column of southern Nares Strait and northern Baffin Bay.

4.1 Introduction

The many channels of the Canadian Arctic Archipelago (CAA) represent an important export pathway for Arctic outflow waters and the transport of freshwater to the North Atlantic (Carmack et al., 2016). Located between Ellesmere Island and Greenland, Nares Strait is the northernmost outflow gateway of the Arctic Ocean, and one of two main passages through the CAA (Figure 4.1). Nares Strait connects the Lincoln Sea, an ice-covered continental shelf sea, with northern Baffin Bay, which harbors the ecologically significant North Water (NOW) polynya, or *Pikialasorsuaq* in Greenlandic (Eegeesiak et al., 2017). Nares Strait is largely a flow-through system, transporting Arctic waters southwards through a series of channels and basins, which from north to south are: Robeson Channel, Hall Basin, Kennedy Channel, Kane Basin, and finally Smith Sound (Figure 4.1a). The net southward volume transport through Nares Strait is estimated to be 0.8 ± 0.3 Sv, approximately equal to the net volume flux of Pacific water into the Arctic Ocean via Bering Strait (Münchow et al., 2006). In Kane Basin the seafloor shoals to a minimum sill depth of 220 m, allowing only a portion of deep Atlantic-origin waters to be exported from the Arctic Ocean.

Previous studies have shown that the region north of the Lincoln Sea acts as a switchyard, directing either Pacific- or Atlantic-origin surface waters towards the Lincoln Sea and Nares Strait depending on the predominant atmospheric circulation patterns and the location of the Transpolar Drift (TPD; Jackson et al., 2014; Newton & Sotirin, 1997; Steele et al., 2004; de Steur et al., 2013). The TPD is a surface current of water and sea ice that forms at the intersection of two gyres in the central Arctic Ocean: the anticyclonic Beaufort Gyre that dominates the surface circulation of the Amerasian Basin; and the cyclonic circulation over the Eurasian Basin (Figure 4.1b). The position of the TPD has been found to vary, from being roughly aligned with the Lomonosov Ridge during periods of predominantly anticyclonic circulation (an expanded Beaufort Gyre; negative Arctic Oscillation index), to beginning closer to the Chukchi shelf, spreading along the Mendeleyev Ridge during periods of predominantly cyclonic circulation (a contracted Beaufort Gyre; positive Arctic Oscillation index) (Morison et al., 2012; Steele et al., 2004). The spread of Pacific waters into the central Arctic Ocean is dependent on the expansion versus the contraction of the Beaufort Gyre, and thus the orientation of the TPD also largely determines the location of the Pacific/Atlantic front (Alkire et al., 2021). Steele et al. (2004) reported a connection between the onset of a positive Arctic Oscillation (AO) index in the early 1990's and the arrival of relatively warm (temperature of −1.2 °C) summer Pacific waters in the Lincoln Sea, following an approximately 3-year time lag. Later deSteur et al. (2013) reinforced these findings, also noting large freshwater anomalies in the Lincoln Sea coinciding with the arrival of summer Pacific waters, but found

the time lag could vary from zero to 3 years. Other recent studies in the Lincoln Sea and Nares Strait have documented significant interannual variability in the water mass assembly, with inputs from both the Amerasian (Pacific-influenced) and Eurasian (Atlantic-influenced) basins (Alkire et al., 2010; Hamilton et al., 2021; Jackson et al., 2014; Münchow et al., 2007). Depending on the configuration of the TPD, in any particular year the Lincoln Sea (and Nares Strait) may receive surface waters from the west Siberian shelves (Atlantic-origin) or the Chukchi shelf (Pacific-origin). The influence of this "switchyard effect" (the changing positioning of the TPD) on the waters transported through Nares Strait has not been studied, and may have implications for the export budgets of freshwater and carbon from the Arctic Ocean.

The Lincoln Sea is also the location of the Last Ice Area, the region where multiyear sea ice is expected to persist longest in the face of climate change (Moore et al., 2019). Historically, the formation of an ice arch at Smith Sound has contributed to both the longevity of the Last Ice Area and the formation of the NOW polynya. However, since the 1990s the timing and location of the ice arch has become increasingly variable, with the ice arch forming later, breaking up earlier, and occasionally forming farther north, at the boundary between Nares Strait and the Lincoln Sea (Figure 4.1a; Vincent, 2019). When the ice arch is not present the southerly flow of sea ice through Nares Strait can substantially decrease downstream salinity in the Labrador Sea (Barber et al., 2018; Kwok et al., 2010) and increases the export of multiyear sea ice from the Last Ice Area (Moore et al., 2019; Ryan & Münchow, 2017). This can also have negative consequences for annual primary production in the NOW polynya region, as thick multiyear sea-ice floes shade the upper water column, limiting light availability for phytoplankton (Blais et al., 2017; Marchese et al., 2017).

The NOW polynya region in northern Baffin Bay has its own unique water column characteristics, governed by the convergence of Arctic outflow waters from Nares Strait with a separate water mass assembly transported northwards by the West Greenland Current (WGC) from the subpolar North Atlantic (Bâcle et al., 2002; Lobb et al., 2003; Melling et al., 2001; Mortensen et al., 2022; Rysgaard et al., 2020). At the front where these two water mass assemblies meet, cross-frontal gradients in temperature and salinity have been found to be largely density compensating, leading to a high degree of isopycnal interleaving (Lobb et al., 2003). The complex bathymetry of the NOW region plays a key role in directing the interaction of these water mass assemblies, as the majority of WGC waters follow the 600 m isobath westwards across northern Baffin Bay without entering the NOW polynya region. A smaller portion of the WGC follows the 400 m isobath entering the NOW region from the southeast, and has been observed as far north as Smith Sound where it is forced southwards again by the shoaling bathymetry (Melling et al., 2001). Sporadic net northerly flows have been documented across Smith Sound, but the frequency of

these events is not regular and the forcings that drive them are only just beginning to be understood (Melling et al., 2001; Münchow et al., 2015; Myers et al., 2021). For example, Myers et al. (2021) recently linked a month-long net transport reversal in Baffin Bay and Nares Strait to an anomalous wind pattern along the West Greenland coast.

Variability in the water mass assembly and sea-ice cover in Nares Strait has implications for freshwater and nutrient budgets, and for biogeochemical processes such as air-sea CO_2 exchange, primary production, and ocean acidification. This water mass variability impacts not only the biogeochemistry of Nares Strait, but also that of ecologically important downstream regions such as the NOW polynya. Despite the importance of Nares Strait as a conduit connecting the greater Arctic Ocean to northern Baffin Bay and ultimately the North Atlantic, very little is known about the biogeochemical processes occurring within these waters, nor about the transport and distribution of dissolved carbon. A former study, using a portion of the data presented here, identified relatively high surface CO_2 partial pressure (pCO_2) coinciding with a strong riverine signal in Nares Strait in August 2014 (Burgers et al., 2017). The present study builds on those initial findings by investigating the water mass assembly that was present in Nares Strait at that time. We employ an extended optimum multi-parameter (eOMP) analysis to characterize and trace the various water masses transiting through Nares Strait, and to distinguish the impacts of physical (water mass transport) and biological processes on the observed distribution of dissolved inorganic carbon (DIC). The objectives of this study were to investigate: (1) the origins of the water masses observed in Nares Strait, (2) the carbonate chemistry and nutrient concentrations of these water masses, and (3) the biogeochemical processes occurring within Nares Strait that affect the observed water column distribution of DIC. Finally, we will put our results in context by describing the possible variability in the water mass assembly of Nares Strait that may affect the future carbon dynamics and primary production in this region.

4.2 Data and Methods

4.2.1 Setting

Sampling for this study was conducted during the 2014 ArcticNet scientific cruise onboard the Canadian icebreaker CCGS *Amundsen,* starting with an east-to-west transect of stations across the NOW region from 30 July to 1 August (stations 115 to 101, Figure 4.1a). The *Amundsen* then transited north in Nares Strait before completing a north-to-south series of stations from the northern end of Kennedy Channel (station Ken1) on 3 August back into the NOW region of northern Baffin Bay (station 120) on 6 August (see Table S4.1 for sampling times and exact locations). At the time of sampling the NOW polynya ice arch remained present at the northern end of Kennedy Channel, causing sea ice

concentrations to remain above 90% north of 81.5 °N, with mainly open waters southwards where our sampling was conducted (Figure 4.1a).

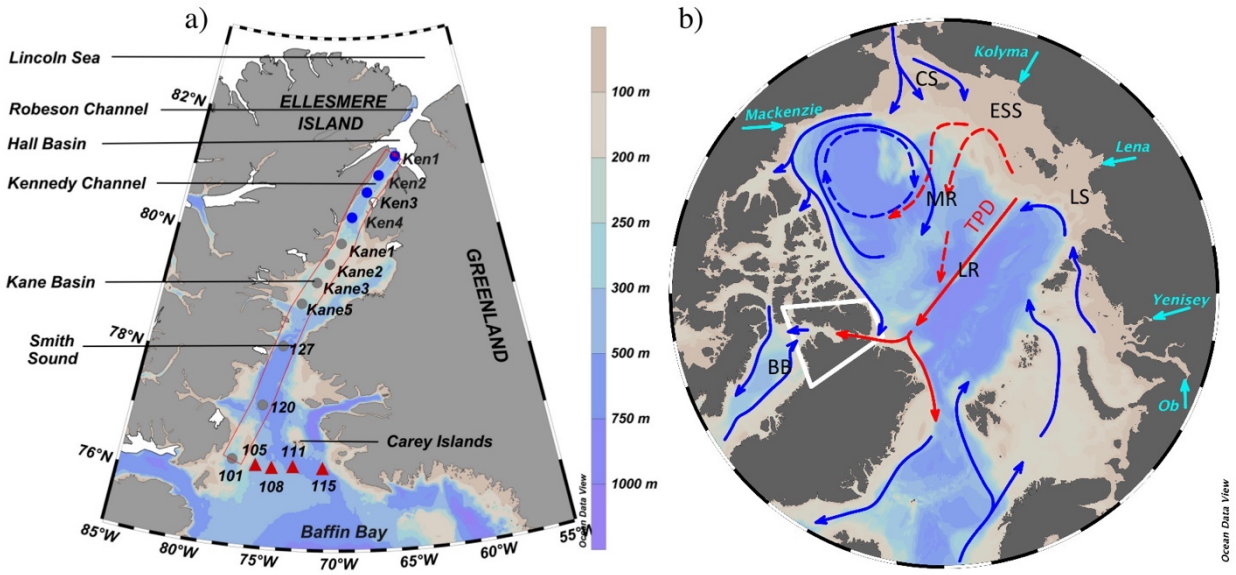

Figure 4.1: (a) Map of the study area, with water column sampling stations indicated as coloured dots, and the Nares Strait transect referred to throughout the text indicated by a red outline. Stations plotted as blue dots indicate the northern source region, while stations plotted as red triangles indicate the southern source region, relevant to our eOMP analysis (see section 2.4), stations plotted as grey dots represent the mixing region between the two source regions. Areas where sea-ice concentrations were >90% at the time of sampling are shaded white, based on weekly ice charts from the Canadian Ice Service. (b) Map of the Arctic Ocean with major surface circulation features (arrows), including the Transpolar Drift (TPD; red arrows). Solid and dotted lines indicate the position of these features during a negative and positive Arctic Oscillation index, respectively. Outflow locations of major Arctic rivers are shown in cyan, with the current study area outlined in white. Abbreviations: Baffin Bay (BB), Laptev Sea (LS), East Siberian Sea (ESS), Chukchi Sea (CS), Lomonosov Ridge (LR), Mendeleyev Ridge (MR), Transpolar Drift (TPD). Maps created using Ocean Data View software (Schlitzer, 2020) with bathymetry contours from IBCAO version 3 (Jakobsson et al., 2012).

4.2.2 Sampling and sample analyses

At each sampling station seawater was collected with 12L Niskin-type bottles mounted on a rosette system equipped with a SeaBird 911plus CTD, as well as sensors for chlorophyll *a* fluorescence (SeaPoint), dissolved oxygen (Seabird SBE-43), and dissolved organic matter fluorescence (FDOM, WetLabs ECO). Salinity is reported using the practical salinity scale 1978. The oxygen sensor was calibrated against Winkler titrations from discrete samples (as described by Grasshoff et al., 1999) using a Mettler Toledo titrator. Residuals between Winkler samples and sensor concentrations indicated a precision better than 1 μmol kg^{-1} (n=15). Chlorophyll *a* (chl *a*) concentrations from the fluorescence probe were calibrated from extracted chl *a* (Amundsen Science Data Collection, 2018). The FDOM units are relative from factory calibrations. Discrete water samples were collected for the determination of nutrients (including nitrate, nitrite, ammonium, phosphate, and silicate), and the marine CO_2 system (dissolved inorganic carbon [DIC] and total alkalinity [TA]). Discrete samples were collected at standard depths of:

2, 10, 20, 30, 40, 50, 60, 70, 80, 100, 125, 150, 175, 200, 250, and 300 m with any depths greater than 300 m being sampled at 100 m intervals to a maximum depth of 10 m above the sea floor. If required an additional sampling depth was added at the chl *a* maximum. At some stations DIC/TA samples were only collected at the surface and 10 m depth. Stations with full DIC/TA profiles are indicated in Table S4.1.

Nutrient samples were collected directly from the Niskin-type bottles with syringes, filtered in-line (Swinnex-mounted, Whatman GF/F), and captured in acid-cleaned polyethylene tubes. Nutrient concentrations for nitrate+nitrite, ammonium, phosphate, and silicate were measured colorimetrically with a Bran and Luebbe AutoAnalyzer III (Hansen & Koroleff, 1999) onboard the ship within a few hours of collection. Working standards were prepared at each station and checked against certified reference material (KANSO CRM) inserted into the sample runs. Analytical detection limits were 0.03 μM for nitrate, 0.02 μM for nitrite, 0.05 μM for phosphate, and 0.1 μM for silicate. Ammonium concentrations were measured using the method of Holmes et al. (1999) with a detection limit of 0.02 µM. The precision of triplicate nutrient measurements under the range of concentrations observed was the same as or better than the detection limit for each nutrient.

Seawater samples for the determination of DIC and TA were collected and analyzed following standard protocols (Dickson et al., 2007). Samples were collected in 250-mL glass bottles, preserved with 100 μL of saturated mercuric chloride solution, capped with ground glass stoppers greased with Apiezon M, and sealed with electrical tape. Replicates were collected from at least one Niskin-type bottle per rosette cast. Samples were then stored in the dark at 4°C until analysis at the Institute for Ocean Sciences in Sidney, British Columbia, within 10 months of collection. The coulometric DIC analysis utilized either a SOMMA or VINDTA 3D (MARIANDA) extraction system. Measurements of TA used open-cell potentiometric titrations with nonlinear least squares end-point determination. Both of these measurements were calibrated against certified reference materials (CRM batches 88, 115, and 133, provided by Andrew Dickson, Scripps Institute of Oceanography). Analyses of duplicate DIC and TA samples indicated a precision of ± 1 μmol kg^{-1} (n=27) and ± 3 μmol kg^{-1} (n=23), respectively. Following the determination of DIC and TA, we calculated in-situ pH on the total scale (pH_T), the partial pressure of CO_2 (pCO_2), aragonite saturation state (Ω_{Ar}), and calcite saturation state (Ω_{Ca}) using the MATLAB CO_2Sys program of van Heuven et al. (2011) (based on the original CO_2Sys by Lewis & Wallace, 1998). Uncertainties in calculated CO_2 system variables were determined with the uncertainty propagation routine of Orr et al. (2018). Within CO_2Sys we applied the carbonic acid dissociation constants of Lueker et al. (2000), the HSO_4^- dissociation constants of Dickson (1990), and the total boron concentration from Lee et al. (2010). The Lueker et al. (2000) constants were selected as they have been shown to produce

good agreement between measured and calculated values in Arctic waters (Chen et al., 2015; Woosley et al., 2017).

Additionally, continuous sea surface measurements of pCO_2 were collected using an underway system (General Oceanics model 8050; Pierrot et al., 2009), which sampled from a seawater intake line at a nominal depth of 7 m. The system's infrared gas analyzer (LI-COR LI-7000) was calibrated twice daily against three certified gas standards traceable to World Meteorological Organization (WMO) standards. The relative uncertainty of the resulting pCO_2 measurements is estimated to be 2%; see Burgers et al. (2017) for further information about the underway pCO_2 system and data processing.

4.2.3 Geochemical tracers

Due to active sedimentary denitrification over the Chukchi shelf, inflowing Pacific-source waters to the Arctic Ocean exhibit a lower nitrogen-phosphate (N-P) ratio compared to inflowing Atlantic waters from Fram Strait and the Barents Sea. Following Newton et al. (2013), we calculated the "Arctic N-P" tracer (ANP) which exploits this difference in N-P ratio to estimate the amount of Pacific-source water contained in a sample. In calculating ANP we applied the N-P regression lines of Pacific and Atlantic waters from Yamamoto-Kawai et al. (2008) to our measurements of total inorganic nitrogen (TIN = NO_3^- + NO_2^- + NH_4^+) and phosphate (PO_4^{3-}). The regression lines of Yamamoto-Kawai et al. were defined using measurements of TIN, like ours, instead of solely nitrate concentrations (e.g. Jones et al., 1998). If ANP=0, the TIN-P pair falls along the Atlantic water regression line, whereas if ANP=1, the TIN-P pair falls along the Pacific water line.

The Chukchi shelf is not the only shelf sea of the Arctic Ocean where denitrification can occur. Denitrification has also been documented in the shelf sediments of the East Siberian and Laptev Seas (Bauch et al., 2011; Nitishinsky et al., 2007). Hence, ANP values greater than 0 do not exclusively indicate Pacific source waters, as Atlantic source waters may also undergo denitrification in the Siberian shelf seas. Alkire et al. (2019, 2021) have proposed using the NO parameter as a qualitative tracer for distinguishing waters from the Chukchi and Siberian shelf seas. NO is a quasi-conservative tracer, defined as: $NO = 9[NO_3^-] + [O_2]$ (Broecker, 1974), that can be used to trace water masses at depths below the surface mixed layer. Since nitrate and oxygen concentrations are generally higher in the Chukchi Sea compared to the Siberian shelf seas, NO is generally higher in waters originating from the Chukchi (> 400 μmol kg^{-1}) compared to the Siberian shelf seas (< 400 μmol kg^{-1}; Alkire et al., 2021). Hence, NO can be a useful tool in distinguishing these two shelf waters, both of which may ventilate the upper halocline layer within the Amerasian basin of the Arctic Ocean.

4.2.4 eOMP analysis

In this investigation we utilize the extended optimum multiparameter (eOMP) analysis of Dinauer & Mucci (2018), which estimates both the mixing fractions of predefined source water masses, and the impact of biological processes (photosynthesis/respiration) that best reproduce the observed tracer measurements. The base MATLAB code for the eOMP analysis was provided by Ashley Dinauer (Woods Hole Oceanographic Institution), and is described in detail in Dinauer & Mucci (2018). We have also made some modifications to the method of Dinauer & Mucci, which will be outlined later in this section. Briefly, OMP analysis is a weighted, non-negative, linear inverse mixing model that optimizes the information contained in a hydrographic dataset. OMP analysis calculates the best fitting fractions (*f*) of (*n*+1) source water masses that contribute to the (*n*) observed tracer measurements in a parcel of water by solving an over-determined system of linear equations that minimizes residual error (Tomczak & Large, 1989; Tomczak, 1981). The *extended* OMP (eOMP) method employed here also includes a biological term which estimates tracer concentration changes due to the impact of net photosynthesis or net respiration within the water column. The eOMP method of Dinauer & Mucci employs the measure of apparent oxygen utilization (AOU) to predict the biogeochemical regime (either net photosynthesis or net respiration), at any given measurement point. When AOU > 0 we assume that community respiration exceeds photosynthesis (net respiration), releasing DIC and nutrients into the water column while consuming oxygen. When AOU < 0 we assume that the rate of photosynthesis exceeds community respiration, with phytoplankton consuming DIC and nutrients while releasing oxygen. Therefore, whether AOU is positive or negative at any given measurement point determines the sign of the Redfield ratios in equation 4.1 (below).

We employ the eOMP framework with nine physicochemical tracers: potential temperature (θ), salinity (*S*), dissolved oxygen (DO), phosphate (P), total inorganic nitrogen (TIN), silicate (Si), total alkalinity (TA), dissolved inorganic carbon (DIC), and dissolved organic matter fluorescence (FDOM). The equations applied in this eOMP framework are:

$$
\begin{aligned}
&f_1\theta_1 + \cdots + f_n\theta_n + 0 = \theta_{obs} + R_\theta \\
&f_1 S_1 + \cdots + f_n S_n + 0 = S_{obs} + R_S \\
&f_1 DO_1 + \cdots + f_n DO_n \pm r_{DO/P}\Delta P = DO_{obs} + R_{DO} \\
&f_1 P_1 + \cdots + f_n P_n \pm r_{P/P}\Delta P = P_{obs} + R_P
\end{aligned}
\qquad (4.1)
$$

$$f_1 TIN_1 + \cdots + f_n TIN_n \pm r_{N/P}\Delta P = TIN_{obs} + R_{TIN}$$

$$f_1 Si_1 + \cdots + f_n Si_n \pm r_{Si/P}\Delta P = Si_{obs} + R_{Si}$$

$$f_1 TA_1 + \cdots + f_n TA_n \pm r_{N/P}\Delta P = TA_{obs} + R_{TA}$$

$$f_1 DIC_1 + \cdots + f_n DIC_n \pm r_{C/P}\Delta P = DIC_{obs} + R_{DIC}$$

$$f_1 FDOM_1 + \cdots + f_n FDOM_n + 0 = FDOM_{obs} + R_{FDOM}$$

$$f_1 + \cdots + f_n + 0 = 1 + R_{mass}$$

where *f* indicates the calculated mixing fractions of *n* source water masses, which compose the observed tracer fields through conservative mixing. Subscripts on variable names (e.g., S_n, TIN_n, etc.) indicate the defined source water mass concentrations (see Table 4.1). On the right-hand side of the equations, *obs* terms represent observed tracer concentrations, and *R* are residual terms of each tracer.

For the biological change term we employ Redfield-type ratios relative to phosphate ($r_{tracer/P}$). The eOMP model calculates the term ΔP, representing the change in phosphate concentration due to biological processes, which is calculated from deviations in observed phosphate concentrations relative to a preformed phosphate concentration (i.e., the concentration due solely to water mass mixing). The multiplication of ΔP by the appropriate Redfield ratio for each tracer estimates the concentration change of that tracer due to biological activity. Following Dinauer & Mucci (2018) we applied the traditional C:-O_2 Redfield ratio of 106:-138, whereas we estimated the local TIN:P and Si:P ratios for Nares Strait. To do this we utilized linear regressions of nutrient data throughout the upper water column (S ≤ 33.2) at our two most northerly stations, where surface waters had just emerged from under thick ice cover, and measurements of chl *a* fluorescence were less than 1 mg m^{-3} (see Figure S4.1 for linear regressions). The TIN:P ratio from this analysis was 11:1, which is somewhat lower than the classical Redfield ratio, but this is typical of Arctic surface waters (Tremblay et al., 2015), and the Si:P ratio was 20:1, which also agrees well with ratios previously reported in Canadian Arctic waters (Tremblay et al., 2002, 2015).

The first step in our eOMP analysis is to define the source water masses that contribute to the water mass assembly in Nares Strait and the NOW region. For biogeochemical OMP studies it is important that each source water mass be defined at the location where it enters the region of interest. This allows for the assumption that observed tracer concentrations “downstream” result from the mixing and biological processes occurring within the study region. Nares Strait and the NOW region are influenced by two water mass assemblies, one arriving from the Arctic Ocean and flowing southwards

through Nares Strait, and a second entering from the southeast NOW region and flowing northwards with a branch of the WGC. Following this, two "source regions" were designated where water masses may enter the study region: (1) the northern source region which encompasses our four most northerly stations in Kennedy Channel (represented by the blue stations in Figure 4.1a); and (2) the southern source region, which includes the four easternmost stations across the NOW region of northern Baffin Bay (red stations in Figure 4.1a). Water masses in each source region were identified by their unique physicochemical characteristics (e.g., temperature minimum, nutrient maximum). We identified three water masses arriving from the northern source region: Polar Mode water (PMW), Upper Halocline water (UHW), and Canada Basin Atlantic water (CBAW); and another two source water masses arriving from the southern source region: Baffin Bay Polar water (BBPW) and Subpolar Mode water (SPMW) (Mortensen et al., 2022; Rysgaard et al., 2020). The specific properties and origins of each source water mass is described in section 4.3.1. We additionally included two freshwater sources in our eOMP analysis, river runoff (RR) and sea ice melt (SIM), with their definitions derived from literature values (see Table 4.1 for all source water mass definitions).

Table 4.2: Defined properties of source water masses employed in eOMP analysis[a]. Source water masses include Polar Mode water (PMW), Upper Halocline water (UHW), Canada Basin Atlantic water (CBAW), Baffin Bay Polar Water (BBPW), and Subpolar Mode water (SPMW). Freshwater sources include sea-ice melt (SIM) and river runoff (RR).

	Source water masses					Freshwater sources	
Property	**PMW**	**UHW**	**CBAW**	**BBPW**	**SPMW[b]**	**SIM**	**RR**
Temp (°C)	-1.6 ± 0.04	-1.3 ± 0.02	0.36 ± 0.03	-1.2 ± 0.2	2.0	0 to 3	0 to 3
Salinity	31.4 ± 0.3	33.2 ± 0.1	34.8 ± 0.1	33.5 ± 0.1	34.3	4 ± 1[c]	0
DO (μmol kg^{-1})	360 ± 2	290 ± 2	270 ± 5	310 ± 23	220	100 ± 30[d]	380 ± 20[i]
P (μmol kg^{-1})	0.70 ± 0.04	1.10 ± 0.05	0.88 ± 0.01	0.78 ± 0.07	1.10	0[e]	0.69 ± 0.05[h]
TIN (μmol kg^{-1})	3.5 ± 0.3	9.6 ± 0.3	13 ± 1	7.9 ± 0.6	14	0[e]	0.04 ± 0.4[h]
Si (μmol kg^{-1})	9.2 ± 0.7	17 ± 1	8.0 ± 0.2	7.7 ± 0.9	17	0[e]	12 ± 1[h]
DIC (μmol kg^{-1})	2130 ± 6	2190 ± 9	2170 ± 10	2130 ± 6	2190	330 ± 30[f]	1100 ± 100[g]
TA (μmol kg^{-1})	2230 ± 10	2260 ± 10	2300 ± 6	2230 ± 20	2260	420 ± 40[f]	1000 ± 100[g]
FDOM (rel. units)	11 ± 0.3	8.2 ± 0.2	4.5 ± 0.1	4.4 ± 0.4	4.9	0	17 ± 1

[a] The defined properties of each source water mass (average ± one standard deviation) were derived from our dataset, and freshwater properties were defined from literature values, see the following footnotes.
[b] SPMW properties are defined at the subsurface temperature maximum of station 115 (Figure 4.1a)
[c] Östlund & Hut (1984)
[d] Rysgaard et al. (2008)
[e] Mundy et al. (2011)
[f] Rysgaard et al. (2007); Miller et al. (2011)
[g] Concentrations extrapolated to 100% meteoric water from Charette et al. (2020)
[h] Concentrations at 20% meteoric water in the surface TPD from Charette et al. (2020)
[i] Estimated from the average SML concentration in the northern source region

Tracer concentrations for the RR definition were taken from Charette et al. (2020), who reported linear regression relationships between meteoric water fractions and tracer concentrations in the surface waters of the TPD. Since the major Siberian rivers exert a stronger influence on the TPD than North American rivers (Bauch et al., 2011; Morison et al., 2012), our RR definition is representative of discharge weighted average concentrations from Siberian rivers (Charette et al., 2020). In some cases where tracer concentrations could not be extrapolated to 100% meteoric water without high uncertainty, we utilized tracer concentrations at 20% meteoric water, representing an effective shelf end-member concentration at the point of origin to the TPD (Charette et al. 2020). In the case of FDOM, our measurements could not be compared with those of Charette et al., which were given in raw volts. To estimate an FDOM RR end-member we employed a linear regression of the observed salinity vs. FDOM measurements in the northern source region, at salinities between 31.4 and 33.2 (between the PMW and UHW layers; Figure S4.2). FDOM measurements at salinities lower than 31.4 were excluded from the linear regression because they showed decreasing FDOM values, likely due to dilution by other freshwater inputs such as sea-ice melt. FDOM measurements from deeper (S>33.2) waters were excluded because there was a slight change in the slope of the salinity vs. FDOM relationship in these layers. The FDOM RR end-member was obtained by extrapolating this linear relationship to a salinity of 27.7, which was the average salinity of TPD surface waters with meteoric water fractions greater than 20% from Charette et al. (2020). This end-member is assumed to represent the riverine FDOM signal that enters the TPD from the Siberian shelves.

Within the eOMP framework the applied tracers are normalized and weighted to allow comparison of otherwise incommensurable parameters, and to account for environmental variability and measurement errors. In this study we have chosen to apply separate weighting schemes in the upper ($S < 33.2$) and deep ($S \geq 33.2$) water column, following Lansard et al. (2012). This allows the flexibility to apply lower weights to temperature-sensitive or non-conservative tracers (e.g., θ, DO, TIN) within the upper water column, where they may be affected by non-conservative processes such as primary production and atmospheric interaction, but increase their weighting at depth where these tracers approach more conservative behaviour. Weights were chosen for the upper and lower water column somewhat subjectively, with consideration of the range and precision of each tracer, as well as how conservatively they behave (see Table 4.2 for assigned weights). In surface waters *S* was assigned the highest weighting because it is both conservative and precise. The lowest weightings were applied to θ and DO as they are influenced by large changes in temperature due to solar insolation near the surface, as well as influences by biological processes for DO. TIN and P were also assigned low weightings due

to their biologically-influenced non-conservative behavior. DIC, Si, and FDOM were assigned intermediate weights, as they are non-conservative in surface waters (FDOM photochemically degrades, and DIC and Si are biologically impacted), but they have a high range-to-precision ratio and are powerful tracers for distinguishing water masses in the upper water column. TA was also assigned an intermediate weighting in surface waters as it is a near-conservative parameter, but is a less precise measurement compared to our other tracers. Weightings applied in the deep water column increased for θ, DO, Si, DIC, TA, and FDOM, as these tracers approach more conservative behaviour away from the atmosphere-ocean interface.

The base MATLAB code of Dinauer and Mucci (2018) was also modified to perform separate eOMP runs for the surface and deep water column, only considering certain source water masses in each domain. This was necessary since not all tracers were sampled at all depths, leading to constraints on the number of source water mass fractions that could be solved for at each sampling depth. Within the surface domain, deep and saline ($S > 34$) source water masses were not solved for (i.e., CBAW and SPMW in Table 4.1). In the deep domain, the freshwater inputs were not considered along with the relatively shallow and fresh PMW (Table 4.1). Taking this approach still produces realistic results because of the strong salinity stratification in this region, which limits mixing between the upper and lower water column, and water masses that are present at the interface between the two domains are solved for in all cases (UHW and BBPW).

We performed a sensitivity analysis of this eOMP framework, to assess how robust the calculated water mass fractions are with regards to: (1) the applied weightings for each tracer; and (2) the natural variability of each source water mass definition. We did this by completing multiple eOMP runs while varying the applied tracer weights by +/- 10 (up to a maximum of 25, or down to a minimum of 1), and by varying the source water mass definitions by one standard deviation (see Table 4.1 for source water mass definitions). The results of these sensitivity analyses are presented in Figures S4.3 to S4.5 in the supplemental materials and demonstrate that the results of our eOMP analysis are quite stable. Generally, changes in calculated water mass fractions were under 0.1 (or 10%). The one exception where we found higher sensitivity is in calculated fractions of PMW and BBPW (up to 0.5) within the surface domain (Figure S4.3). The eOMP framework has trouble discriminating these two water masses near the surface when certain tracer weightings are altered, specifically non-conservative tracers such as DO, P, TIN, Si, and FDOM. Therefore, we find that calculated fractions of PMW and BBPW within the surface domain are affected by the highest uncertainties. A more detailed discussion of our sensitivity analysis is included in the supplementary information (Text S4.1).

Table 4.3: Weights applied to each tracer used in the eOMP analysis, as well as the analytical precision of each tracer measurement, and the median residual term of each tracer after running the eOMP analysis.

		Weights in OMP analysis		
Parameters	Analytical precision	Surface (S < 33.2)	Deep (S ≥ 33.2)	Median eOMP residual term*
Temperature (°C)	0.01	1	25	0.08
Salinity	0.01	25	25	0.03
Oxygen (μmol kg^{-1})	1	1	2	0.5
Phosphate (μmol kg^{-1})	0.05	2	2	0.02
TIN (μmol kg^{-1})	0.03	2	2	0.5
Silicate (μmol kg^{-1})	0.1	10	20	0.3
DIC (μmol kg^{-1})	1	7	10	8.0
TA (μmol kg^{-1})	3	10	15	10.5
FDOM (rel. units)	0.09	7	10	0.1

*Values in this column represent the median residual term, R_{tracer}, for each tracer from equation (3.1)

Another indicator of the uncertainty associated with our eOMP analysis is shown by the calculated residual terms (R) of each tracer. Table 4.2 includes the median residual terms for each applied tracer. The median mass conservation residual (R_{mass} from equation (4.1)) is 0.003 (total range of 0.001 to 0.045). Since multiple sources of error exist in the application of eOMP (e.g., source water mass definition error, measurement errors), the mass conservation residual will never be zero, but the fact that our mass conservation residuals do not exceed 0.05 indicates that the source water masses considered in our model replicate the observed water mass properties well (Dinauer & Mucci, 2018).

4.2.5 Inorganic carbon budget

The combined effects of water mass mixing, biological activity, and air-sea gas exchange on the observed DIC field are summarized by the following budget:

$$DIC_{obs} = DIC_{mix} + \Delta DIC_{bio} + \Delta DIC_{gas} \quad (4.2)$$

where DIC_{obs} is the observed value, DIC_{mix} is the DIC concentration resulting from the mixing of source water masses, ΔDIC_{bio} is the change in DIC concentration due to either net photosynthesis or respiration,

and ΔDIC_{gas} represents either the addition or loss of DIC due to CO_2 gas exchange with the atmosphere. The DIC_{mix} and ΔDIC_{bio} terms in this budget are derived from our eOMP model output, as:

$$DIC_{mix} = f_1 DIC_1 + \cdots + f_n DIC_n \quad (4.3)$$

$$\Delta DIC_{bio} = \pm r_{C/P} \Delta P \quad (4.4)$$

each calculated ΔDIC_{bio} value represents the cumulative effect of net photosynthesis or net respiration in a water parcel compared to conditions entering the study region (i.e., ΔDIC_{bio} represents the cumulative "downstream" impact of biological processes).

The ΔDIC_{gas} term is not directly accounted for within the eOMP framework. This term is more difficult to accurately estimate, as biological processes and mixing are likely to have a larger influence over relatively short timescales. At the time of our sampling in Nares Strait an ice-arch remained present north of Kennedy Channel, meaning surface waters had only recently come into contact with the atmosphere after emerging from a consolidated sea ice cover. We take advantage of this unique setting to calculate the ΔDIC_{gas} term as the time-integrated flux of carbon into the surface mixed layer for each of the eleven sampling stations along the Nares Strait transect (see Figure 4.1a for transect location) since the estimated time that sampled water parcel emerged from under the ice-arch in northern Kennedy Channel. We assume that the surface flow in Nares Strait is predominantly southwards until arriving in the NOW polynya region, where surface waters from the WGC also enter the region (Melling et al., 2001; this will also be demonstrated in section 4.3.2) and would have a longer history of atmospheric interaction. Therefore, we do not calculate the ΔDIC_{gas} term for stations in our southern source region (see Figure 4.1a).

We calculate the ΔDIC_{gas} term by utilizing underway pCO_2 measurements, and wind speeds from the North American Regional Reanalysis (NARR), to calculate a time-integrated flux of carbon into the surface mixed layer for each of the sampling stations in our Nares Strait transect. We assume that the observed spatial pattern in surface water pCO_2 would remain roughly constant throughout the summer season, and that surface waters in Nares Strait travelled at an average southward speed of 15 cm s^{-1} (Münchow, 2016). Assuming this constant current speed, we can estimate the date and time at which a water parcel emerged from the northern ice arch, before arriving at its sampled station location downstream. Following this procedure, the DIC_{gas} term is calculated as:

$$\Delta DIC_{gas} = \frac{\int_{t_1}^{t_2} -F_{gas}}{\overline{MLD} \cdot \rho_{MLD}} \quad (4.5)$$

where F_{gas} is the air-sea CO_2 flux (μmol C m^{-2} day^{-1}; positive upward, from ocean to atmosphere) associated with each underway pCO_2 measurement, t_1 is the estimated time that a sampled water parcel departed the ice arch, and t_2 is the time it was sampled at each station downstream. $\overline{MLD}$ is the surface mixed layer depth at each station, and ρ_{MLD} is the mean surface mixed layer density at each station (associated with time t_2). F_{gas} was calculated as:

$$F_{gas} = \alpha k(\Delta pCO_2) \quad (4.6)$$

where the gas transfer velocity (k) was parameterized following Wanninkhof (2014) employing NARR wind speeds matched to the estimated times along the transect, α is the CO_2 solubility at in-situ temperature and salinity (Weiss, 1974), and ΔpCO_2 is the difference in the CO_2 partial pressures between the surface water and atmosphere ($pCO_{2sw} - pCO_{2atm}$). Atmospheric CO_2 measurements were collected using a closed-path infrared gas analyzer (LI-COR model LI-7000) with an intake located at a height of 13 m above sea level on a meteorological tower on the ship's foredeck.

When calculating ΔDIC_{gas} we integrated the negative of F_{gas} over time, so that positive ΔDIC_{gas} values represent oceanic uptake of CO_2 from the atmosphere, and negative ΔDIC_{gas} values indicate CO_2 loss to the atmosphere. Further details on the calculation of ΔDIC_{gas} are provided in Text S4.2. We estimate the relative uncertainty of the ΔDIC_{gas} term to be 20 – 30% based on the propagation of uncertainties associated with the gas transfer velocity (approximately 20% relative uncertainty; Wanninkhof, 2014), and the uncertainty of our underway pCO_2 measurements (approximately 2% relative uncertainty; Burgers et al., 2017).

Calculated values of ΔDIC_{bio} and ΔDIC_{gas} represent the cumulative effect of biological activity (net photosynthesis or net respiration) and air-sea gas exchange, respectively, in a water parcel since it emerged from under the ice arch in northern Kennedy Channel. Daily rates of change in ΔDIC_{bio} and ΔDIC_{gas} can also be estimated within the surface mixed layer along the Nares Strait transect by applying the same time history of water transport that was applied to calculate the ΔDIC_{gas} term (assuming surface waters travel southwards at 15 cm s^{-1}). Using this time history we can estimate the number of days it would take a surface water parcel to travel between two sequential sampling stations. We therefore calculate daily rates of change in ΔDIC_{bio} and ΔDIC_{gas} between sampling stations as:

$$Daily\ rate\ of\ change\ (\mu mol\ kg^{-1}\ day^{-1}) = \frac{(\Delta DIC_{n+1} - \Delta DIC_n)}{\Delta days} \quad (4.7)$$

where ΔDIC represents the cumulative ΔDIC_{bio} or ΔDIC_{gas} term at two sequential stations (n and n+1), and Δdays represents the time (in days) it takes a surface water parcel to transit between the two sequential stations.

4.3 Results and Discussion

4.3.1 Source water mass characteristics and origins

Vertical section plots of tracer concentrations along the Nares Strait transect are shown in Figure 4.2 (refer to Figure 4.1a for the transect location). Additionally, Figure 4.3 displays salinity-property plots for all tracers and stations employed in the eOMP analysis, with source water mass definitions shown as large symbols.

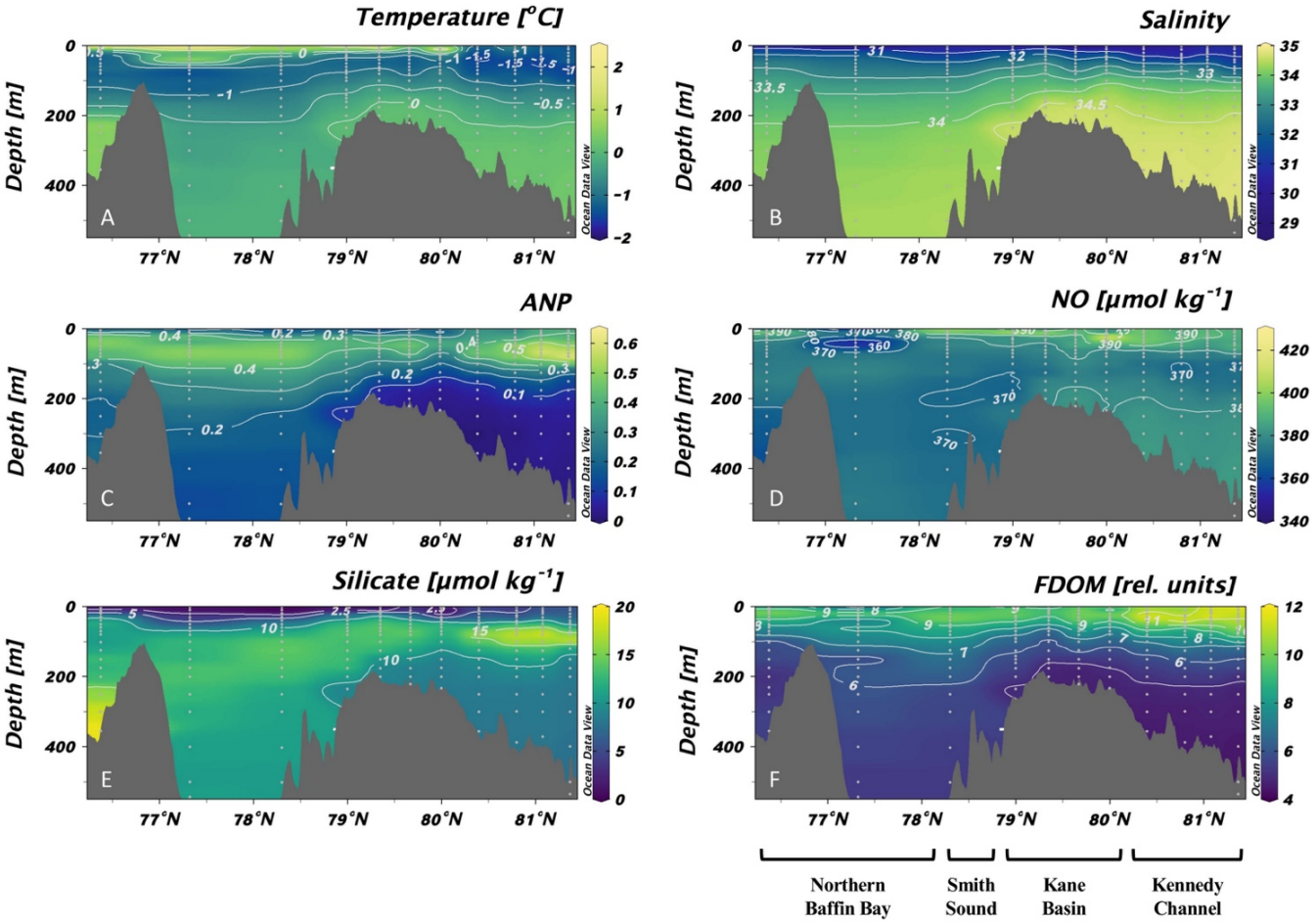

Figure 4.2: Section plots of (a) temperature, (b) salinity, the (c) ANP, and (d) NO parameters (section 4.2.3), (e) silicate, and (f) dissolved organic matter fluorescence (FDOM) in Nares Strait (see section outline plotted in red in Figure 4.1a). Approximate locations of Kennedy Channel, Kane Basin, Smith Sound, and northern Baffin Bay are shown below panel f. Figure created using Ocean Data View software (Schlitzer, 2020) with bathymetry from IBCAO version 3 (Jakobsson et al., 2012).

In the northern source region (Kennedy Channel; blue stations in Figure 4.1a) we identify three source water masses entering the study region (Figure 4.3). The shallowest of these water masses is characterized by a sub-surface temperature minimum near the freezing point (-1.7 °C) located at ~50 m depth, coinciding with a maximum in FDOM. We refer to this as Polar Mode Water (PMW), as it represents a winter mode water formed by repeated convection from cooling and brine release. PMW is also commonly referred to as the polar mixed layer in the literature of the Amerasian basin of the Arctic Ocean (Peralta-Ferriz & Woodgate, 2015; Rudels et al., 2004). In summer, PMW is altered due to the addition of freshwater from SIM or RR which re-stratifies the surface waters, forming a shallower and warmer surface mixed layer (SML) which is underlain by the temperature minimum of the previous winter's PMW. We observe this transformation beginning to occur downstream in Kane Basin (Figure 4.2a). We defined the characteristics of PMW by averaging all tracer measurements at the temperature minimum of each station in the northern source region.

Our defined properties of PMW overlap in salinity, temperature, and depth with previously described East Siberian cold shelf water (Wang et al., 2021), with the high FDOM observed in this layer also pointing to its origins on the Siberian shelves, where significant inputs of river runoff and extensive seasonal sea-ice formation in winter contribute to the near-freezing temperature and high FDOM (Bauch et al., 2011; Stedmon et al., 2021). The average ANP value of the PMW layer is 0.46, signaling that this water mass represents a mixture of Atlantic and Pacific-origin surface waters. This may be due to a mixture of surface waters from the Laptev and East Siberian shelves, as the East Siberian shelf receives a westerly flow of Pacific waters from the Chukchi sea (Alkire et al., 2021; Semiletov et al., 2005). Recent investigations of pan-Arctic trends in FDOM (Stedmon et al., 2021; Williford et al., 2022) have demonstrated its utility as a tracer of water mass origins (when combined with temperature and salinity), with FDOM trends being especially useful in distinguishing terrestrial DOM (dissolved organic matter) from the Siberian shelves, and marine DOM from the productive Chukchi shelf. The terrestrial DOM signal has been found to exhibit peak FDOM values within the upper 50 m of the water column (associated with near-freezing temperatures), and displays greater peak FDOM values compared to the marine DOM signal, which generally peaks in the intermediate water column between 100 and 200 m depth (Charette et al., 2020; Stedmon et al., 2021; Williford et al., 2022). The salinity vs. FDOM relationship found in our northern source region (see Figure 4.3b) shows a quasi-linear relationship in the sub-surface waters (negative correlation). The results of Stedmon et al. (2021) demonstrate that this type of negative linear correlation between salinity and FDOM, with the highest FDOM values within the upper 50 m, is indicative of Siberian shelf waters exported from the Laptev and East Siberian seas into the TPD. These high FDOM

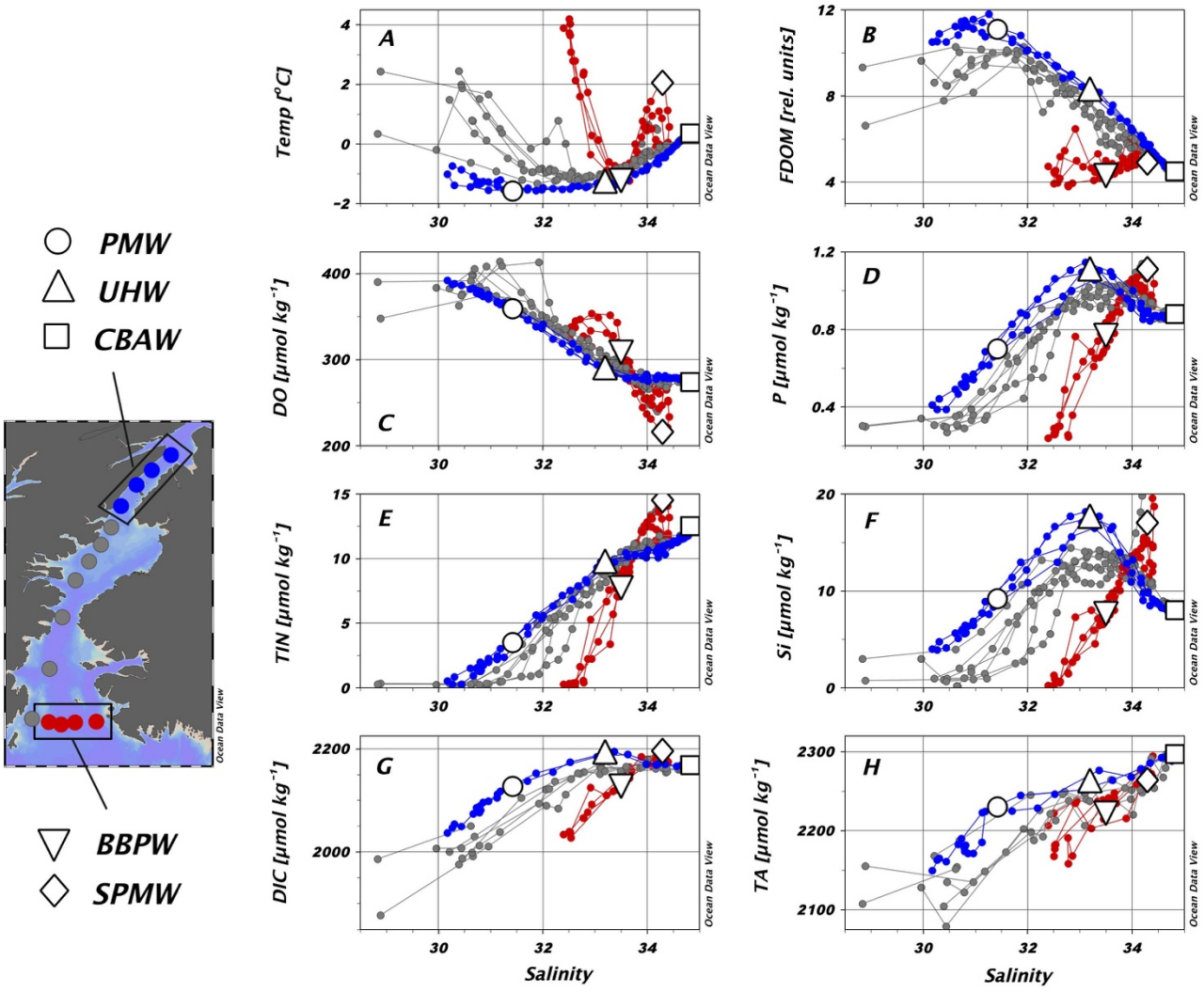

Figure 4.3: Salinity versus (a) temperature, (b) dissolved organic matter fluorescence (FDOM), (c) dissolved oxygen, (d) phosphate, (e) total inorganic nitrogen (TIN = NO_3^- + NO_2^-, + NH_4^+), (f) silicate, (g) dissolved inorganic carbon, and (h) total alkalinity for all stations in Nares Strait and the NOW polynya region of northern Baffin Bay. Data from stations designated as the northern source region are plotted in blue in each panel, stations designated as the southern source region are plotted in red, with stations in between the two source regions plotted in grey. Source water mass definitions are plotted as open symbols: circle, polar mode water (PMW); upward triangle, upper halocline water (UHW); square, Canada Basin Atlantic water (CBAW); inverted triangle, Baffin Bay Polar Water (BBPW); diamond, sub-polar mode water (SPMW). Tracer measurements from the northern source region were used to define properties of the PMW, UHW, and CBAW, whereas measurements from the southern source region were used to define BBPW and SPMW properties (see text in section 4.3.1 for details). Figure created using Ocean Data View software (Schlitzer, 2020).

surface waters carry with them a terrigenous DOM signal from Siberian river runoff (Williford et al., 2022). FDOM measurements from across the Arctic Ocean presented in Williford et al. (2022) and Charette et al. (2020) also confirm that high FDOM surface waters are uniquely found within the TPD, and originate from the Siberian shelves. We are confident that the TPD is the only possible source of such a high FDOM signal in the near-surface waters of Kennedy Channel. Organic matter release from Eurasian

rivers is approximately 5 times larger than that from North American rivers, and other local sources of organic matter from Ellesmere Island or northern Greenland can be ruled out due to the low amounts of soil organic matter present there (Martens et al., 2022). PMW with a pronounced FDOM maximum attributed to Siberian river runoff has previously been documented exiting the Arctic region via Fram Strait (Dodd et al., 2012; Gonçalves-Araujo et al., 2016; Granskog et al., 2012), but to our knowledge this dataset provides the first observational evidence of its passage through Nares Strait.

Below the PMW, a second water mass at intermediate depths (centered around 100 m, about 60 m thick) is characterized by a maximum in dissolved nutrients (e.g., Si, P, DIC; Figure 4.3). This water mass was defined by fitting a smoothing spline curve through the salinity-silicate measurements of the northern source region (blue stations and data points in Figure 4.3) and extracting the peak silicate concentration of this curve (17.4 μmol kg^{-1}) and its associated salinity (S = 33.2). For all other tracers we similarly fit a smoothing spline curve through the salinity-tracer relationship of the northern source region and extracted the tracer value corresponding to S = 33.2. We identify this source water mass as Upper Halocline Water (UHW), sometimes also referred to as Pacific Winter Water in the literature (Brown et al., 2016; Steele et al., 2004). We find the peak silicate concentration of UHW to be low compared to previous reports of UHW in the Canada Basin, where the silicate maximum has been observed to range from 35 to 45 μmol kg^{-1} (Alkire et al., 2021; Jones & Anderson, 1986; McLaughlin et al., 1996).

The average ANP value of UHW in Kennedy Channel is 0.5 (Figure 4.2c), suggesting that this water mass also represents a mixture of Pacific and Atlantic source water contributions, potentially also influenced by mixing over the Siberian shelves. Indeed, the NO parameter suggests this as well, displaying relatively low values (368 to 375 μmol kg^{-1}; Figure 4.2d) compared to those typically associated with UHW in the Chukchi Sea and Canada Basin (420 to 430 μmol kg^{-1} and S = 33.1; Alkire et al., 2021). Recent studies have documented waters in the East Siberian Sea that could ventilate the UHW of the deep Arctic basins, and are similarly characterized by a silicate maximum and denitrification signal (Anderson et al., 2013, 2017; Nishino et al., 2013; Wang et al., 2021), but can be distinguished by a decrease in the NO parameter (Alkire et al., 2021).

Modeling studies of the distribution and circulation of the upper halocline (Bertosio et al., 2022a) and other freshwaters (Bertosio et al., 2022b) showed that from 2010 to 2016 the western edge of the Beaufort Gyre had expanded over the Mendeleyev Ridge, transporting Pacific UHW westward along the East Siberian shelf before entering the deep Makarov Basin. This proposed circulation route would explain the mixed Pacific and Atlantic signal of this water mass, and the relatively low values of the NO parameter. Based on this, we hypothesize that the UHW observed in Kennedy Channel was transported

across the Makarov Basin towards Nares Strait, roughly aligned with the Pacific-Atlantic front through the central Arctic Ocean.

The deepest water mass entering Nares Strait from the north is characterized by temperatures above 0°C at depths below 200 m, with a maximum temperature of 0.36 °C observed at 500 m depth in Kennedy Channel. This is identified as Canada Basin Atlantic Water (CBAW), as the observed temperature maximum does not exceed 0.5 °C, compared to the warmer temperature maxima of Atlantic water observed in the Amundsen (approximately 1 °C) and Nansen (1.5 – 2 °C) basins (Rudels, 2009).

From the southern source region (red stations in Figure 4.1a) we identify two more source water masses entering the study region. The uppermost water mass is characterized by a temperature minimum that is observed as a characteristic “knee” in the *TS* diagram (Figure 4.3a). This is identified as Baffin Bay Polar Water (BBPW; Mortensen et al., 2022; Rysgaard et al., 2020), a winter mode water previously documented along the West Greenland continental slope from Disko Bay to the NOW region (Bâcle et al., 2002; Lobb et al., 2003; Myers et al., 2009; Rysgaard et al., 2020; Tang et al., 2004). The exact formation site of BBPW currently remains unknown (Mortensen et al., 2022). In the literature BBPW is characterized by a temperature minimum near the freezing point (around -1.8 °C) and salinity of 33.6 (Rysgaard et al., 2020). The BBPW we observe in the southeastern NOW is characterized by an average temperature minimum of -1.15 °C and a salinity of 33.5, suggesting it has been somewhat diluted from its original characteristics at its point of origin. Our defined BBPW properties were calculated by averaging all tracer measurements at the temperature minimum of each station in the southern source region.

A second relatively deep and warm water mass is observed entering the southern source region at 300 m depth. This water mass is characterized by a temperature maximum of 2 °C at a salinity of 34.3, as well as a pronounced DO minimum and maximum in nutrient concentrations of TIN, P, Si, and DIC (Figure 4.3). We identify this as Subpolar Mode Water (SPMW), which originates in the subpolar North Atlantic as a winter mode water before being transported around Cape Farewell by the Irminger Current and continuing northwards into Baffin Bay with the WGC (Rysgaard et al., 2020). This water mass has also formerly been referred to in the literature as Irminger Water, West Greenland Irminger Water, or winter Atlantic water (Azetsu-Scott et al., 2012; Curry et al., 2014; Myers et al., 2009; Randelhoff et al., 2019). Our definition of SPMW (Table 4.1) represents the properties observed at the deep temperature maximum at station 115. Rysgaard et al. (2020) distinguish between upper and deep SPMW in their classification of water masses over the West Greenland shelf and slope. Our observations represent a modified version of their deep SPMW (i.e., $T = 4$ °C, $S = 34.7$), due to cooling and mixing with relatively fresh water masses as it progresses northwards (Rysgaard et al., 2020). The high nutrient and low DO

concentrations of SPMW are likely the result of strong remineralization of organic matter, exported to depth from the highly productive surface waters of the West Greenland shelf in southeastern Baffin Bay (Burgers et al., 2020).

Many previous investigations of water mass properties in northern Baffin Bay have relied solely on temperature and salinity measurements. Our additional geochemical tracer measurements reveal that the water mass assembly from the southern source region (influenced by the WGC) can be distinguished from the northern water mass assembly (Arctic outflow waters) by very different salinity-tracer relationships (Figure 4.3).

4.3.2 Modeled source water mass distributions

Figure 4.4 shows vertical sections of the eOMP-calculated source water fractions along the Nares Strait transect. From north to south in Nares Strait the water mass assembly transitions from being dominated by PMW, UHW, and CBAW in Kennedy Channel, to being significantly influenced by intrusions of BBPW and SPMW in northern Baffin Bay. Within the upper 50 m we observe a slow north-to-south dilution of the PMW layer due to increasing fractions of RR and SIM, as well as intrusions of BBPW south of Smith Sound. At station 120 (77.3 °N) an intrusion of BBPW at 40 m depth is also associated with fractions of SIM up to 0.05. This intrusion likely represents surface waters from the WGC interleaving with Arctic outflow waters at the appropriate density horizon.

Below the upper 50 m of the Nares Strait transect, fractions of UHW and CBAW also undergo a similar north-to-south dilution due to northward intrusions of BBPW and SPMW. The complex bathymetry in the region also plays an important role in directing this interaction. As Arctic-sourced UHW and CBAW enter Kane Basin they encounter rapidly shoaling bathymetry, leading to slight upwelling of these layers. In the surface waters (upper 20 m) of Kane Basin some UHW fractions between 0.3 to 0.6 are observed, possibly due to upwelling and some upward mixing by strong tidal motions (Münchow, 2016). We suspect that these surface UHW fractions may be overestimated, as they are not supported by a matching increase in nutrient concentrations (e.g., Si, DIC, TIN) at the surface (see Figure 4.2). Within Kane Basin maximum fractions of UHW decreased to approximately 0.5, being mixed with BBPW fractions up to 0.45. A pulse of SPMW with fractions up to 0.15 also interleaves between layers of UHW and CBAW at approximately 120 m depth in Kane Basin. South of the Kane Basin sill, the remaining UHW and CBAW layers sink down to greater depths, with CBAW fractions dominating the water column below 200 m.

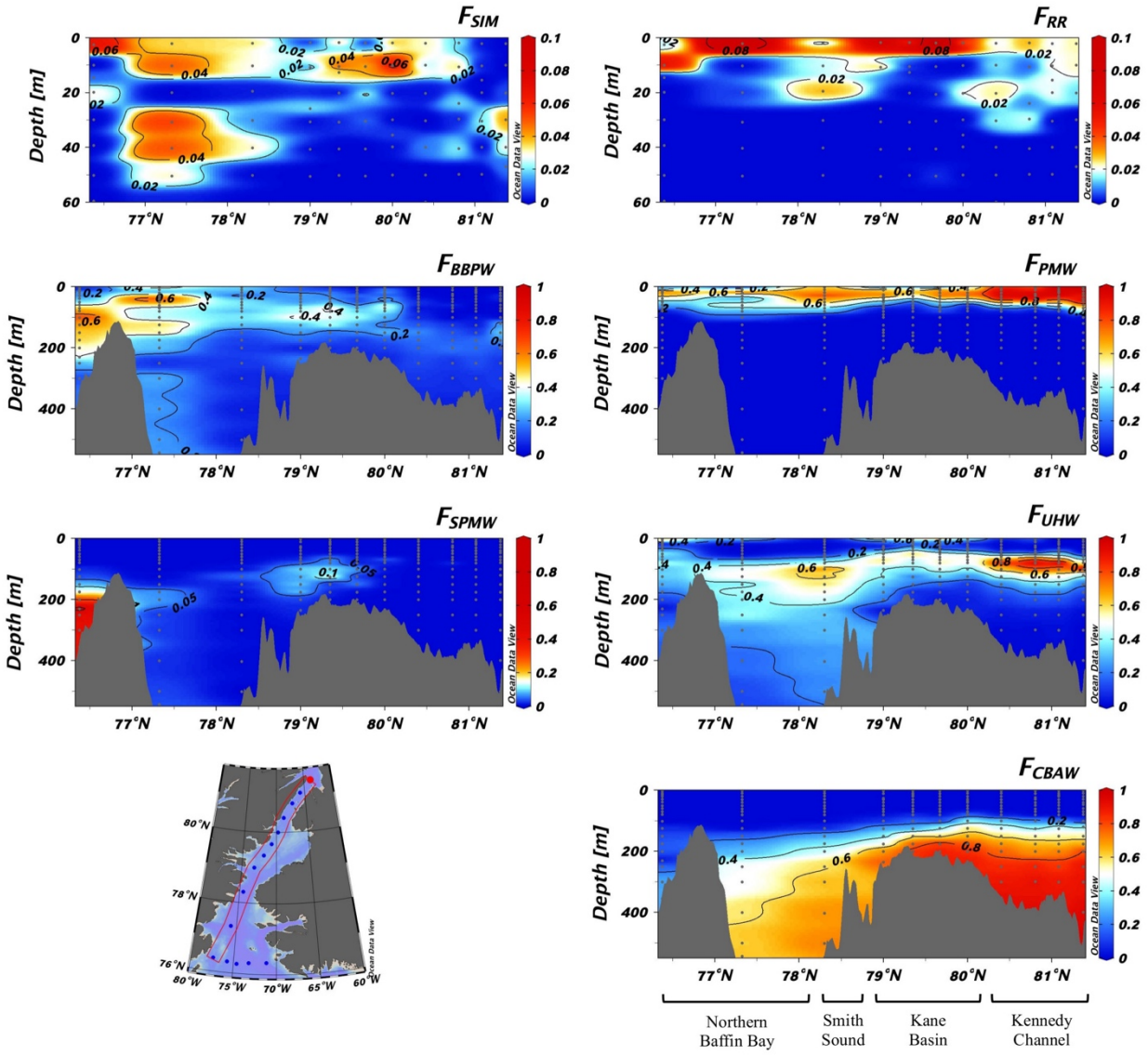

Figure 4.4: Calculated source water mass fractions along the Nares Strait transect (transect location shown in bottom left map). Freshwater sources are sea-ice melt (SIM) and river runoff (RR), note the depth scale is reduced to the upper 60 m for freshwater panels. Source water masses are: Baffin Bay Polar water (BBPW), Subpolar Mode water (SPMW), Polar Mode water (PMW), Upper Halocline water (UHW), and Canada Basin Atlantic water (CBAW). Note the different colour scales on all panels. Figure was created using Ocean Data View software (Schlitzer, 2020) with bathymetry from IBCAO version 3 (Jakobsson et al., 2012).

Station 101 (at the southern end of the Nares Strait transect) is located at the site of a large hollow in the seafloor, isolated on all sides by banks of 100 – 200 m in depth. Here we find the water column below 200 m to contain mostly SPMW (up to 0.56), mixed with BBPW above 300 m, and CBAW below 300 m. The upper water column at station 101 contains mostly PMW (up to 0.75) at depths above 60 m, with a mixture of BBPW and UHW between 60 m and 200 m depth.

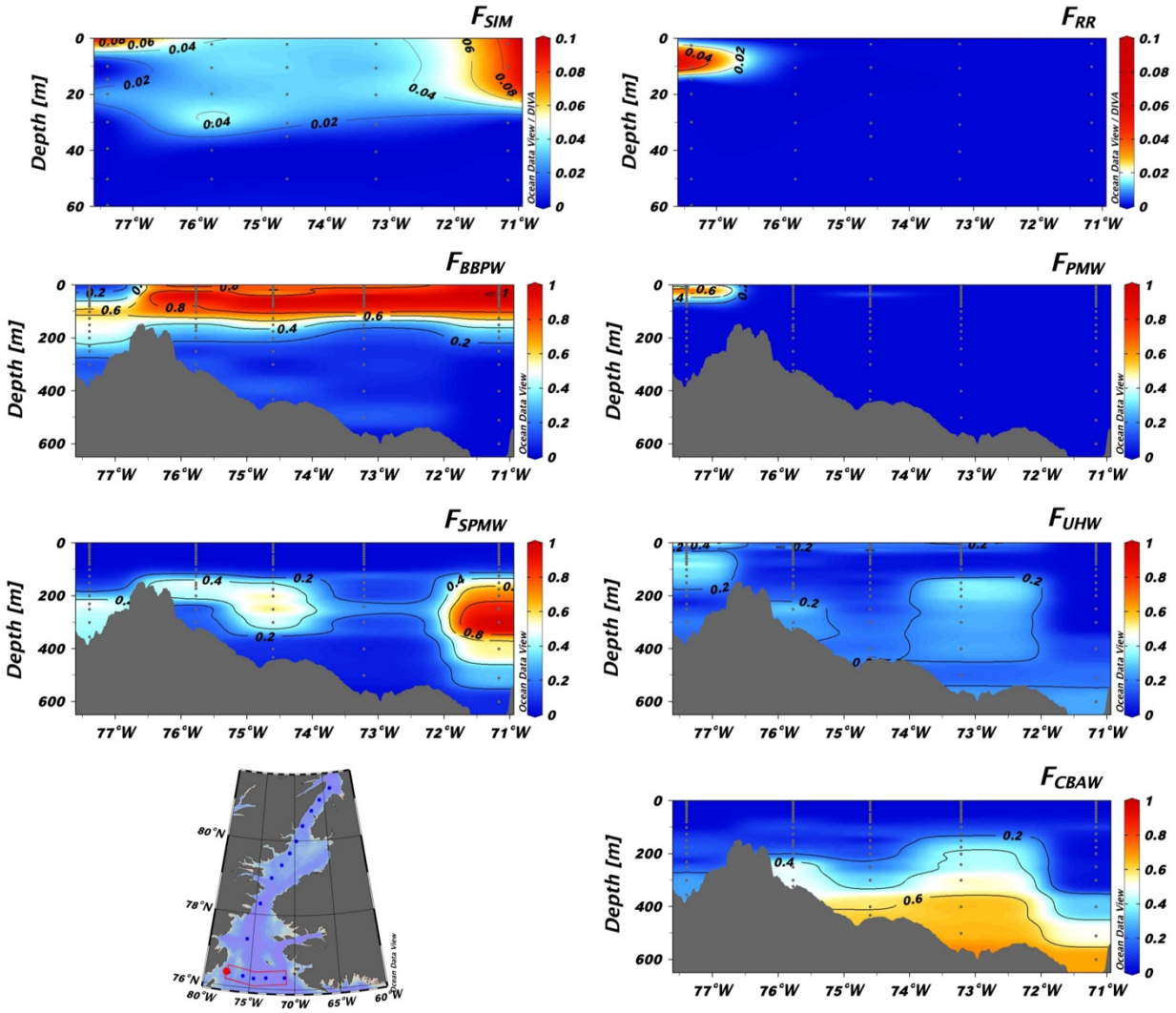

Figure 4.5: Calculated source water mass fractions across the NOW transect (transect location shown in bottom left map). Freshwater sources and source water masses are the same as shown in Figure 4.4. Note the different colour scales and shorter depth scale of the top two freshwater panels. Figure was created using Ocean Data View software (Schlitzer, 2020) with bathymetry from IBCAO version 3 (Jakobsson et al., 2012).

Figure 4.5 displays vertical sections of source water mass fractions across the east-west NOW transect in northern Baffin Bay. At station 115 (easternmost station of the transect) the surface mixed layer is composed of mainly BBPW fractions (> 0.9) with fractions of SIM from 0.07 to 0.09. This surface layer spreads from east to west across the NOW region, retaining BBPW fractions above 0.8 and low SIM fractions (above 0.02) until reaching station 101 in the east where the PMW from the Arctic dominates the surface waters along with RR fractions between 0.02 and 0.05. Also at station 115 (in the east) we can see the entrance of SPMW into the region at 300 m depth. Since low fractions of SPMW are seen at station 111 (immediately west of station 115), we assume SPMW transits northwards from station 115 following a deep (> 400 m) trough around the east side of the Carey Islands (Figure 4.1a).

This flow path might also explain why our eOMP source water mass fractions do not show significant SPMW at stations 120 and 127 in northern Baffin Bay, but do show small fractions (up to 0.15) arriving in Kane Basin (Figure 4.4). It is possible that our sampling stations 120 and 127 were located west of the northward moving SPMW fractions. Results at station 111 (immediately west of station 115) indicate that the western side of the deep trough through the NOW region plays an important role transporting a mixture of UHW and CBAW southwards into northern Baffin Bay at depths below 150 m. At the stations west of 74 °W we observe the southward return of SPMW from its northern detour to Kane Basin. At all stations across the NOW transect we observe a mixture of mostly CBAW (0.5 to 0.6) and some UHW (0.2 to 0.3) flowing southwards below the layer dominated by SPMW. These results fit well with previous observations by Lobb et al. (2003) of "a near-bottom intrusion of relatively cold water" within the WGC-dominated area of warm SPMW in the eastern NOW region. Our water mass distributions also match the results of Melling et al. (2001) who documented the cyclonic flow of warm SPMW throughout the NOW region, noting that SPMW "transits northwards following the eastern edge of a deep channel that is 600 m in depth extending northward as far as Smith Sound" before joining with the Arctic outflow flowing southwards out of Nares Strait.

4.3.3 Marine CO_2 system

Figure 4.6 shows section plots of the CO_2 system variables DIC, TA, pCO_2, pH_T, Ω_{Ar}, and Ω_{Ca} along the Nares Strait transect. Both DIC and TA display considerable variability throughout Nares Strait, with surface concentrations decreasing by roughly 200 μmol kg^{-1} and 100 μmol kg^{-1}, respectively, from north to south. Increasing freshwater inputs and biological DIC drawdown by a moderate phytoplankton bloom in Kane Basin drive these decreases (biological impacts will be further discussed in section 4.3.4). In Kennedy Channel, there is a slight DIC maximum located at a depth of 100 m, coinciding with the silicate maximum of the UHW (see Figures 4.2e and 4.3f). However, the peak DIC concentration observed in this layer (2194 μmol kg^{-1} at station Ken1) is not as high as DIC concentrations that have been observed in the UHW of the Canada Basin (2225 to 2260 μmol kg^{-1}; Brown et al., 2016; Miller et al., 2014). The UHW in Kennedy Channel also displays a maximum in pCO_2 (490 ± 20 μatm), and minima in pH_T, Ω_{Ar}, and Ω_{Ca} (7.95 ± 0.03, 1.00 ± 0.05, and 1.60 ± 0.09, respectively). Below the UHW layer in Kennedy Channel there is a modest decrease in DIC with depth, indicating transition to CBAW. Compared to the UHW layer, CBAW displays relatively lower pCO_2 (350 ± 10 μatm) and higher pH_T (8.05 ± 0.03), Ω_{Ar} (1.30 ± 0.07), and Ω_{Ca} (2.10 ± 0.12).

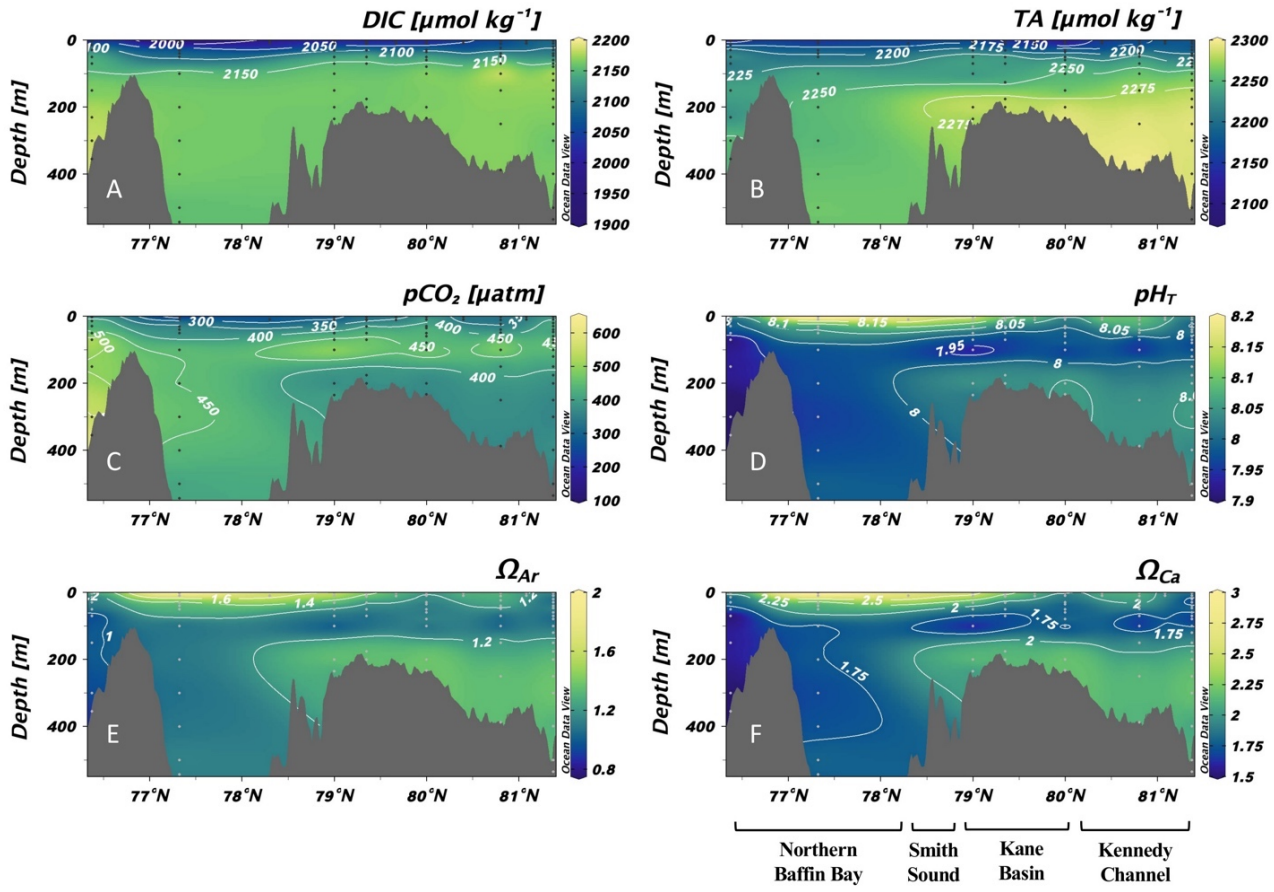

Figure 4.6: Section plots of carbonate chemistry measurements along the Nares Strait transect (transect outline shown in red in Figure 4.1a). Figure created using Ocean Data View software (Schlitzer, 2020) with bathymetry contours from IBCAO version 3 (Jakobsson et al., 2012).

In Kane Basin the subsurface DIC maximum that was observed in Kennedy Channel is eroded. At the same time TA concentrations in the intermediate water column decrease between depths of 80 and 150 m. This coincides with the location of BBPW and SPMW intrusions in Kane Basin (Figure 4.4). Both BBPW and SPMW are characterized by lower TA in comparison to UHW and CBAW of the northern water mass assembly (Table 4.1). The TA decrease observed in Kane Basin compensates for the erosion of the UHW DIC-maximum in maintaining a high pCO_2 and low pH and Ω layer throughout Kane Basin.

South of Kane Basin (at station 120; Figure 4.1a) we also note a TA decrease at depths greater than 200 m, compared to conditions farther north (Figure 4.6b). This represents the dilution of CBAW by mixing with UHW and intrusions of BBPW and SPMW (Figure 4.4), all of which are characterized by lower TA concentrations compared to CBAW (Table 4.1). This TA decrease at depth also leads to a relative decrease in pH_T, Ω_{Ar}, and Ω_{Ca}, and a relative increase in pCO_2 in the deep waters of the northern NOW region. The lowest observations of pH_T, Ω_{Ar}, and Ω_{Ca}, (and highest pCO_2) throughout the Nares Strait

transect were observed below 100 m at the southern end of the transect at station 101, coinciding with relatively high fractions of SPMW filling a deep hollow, and high BBPW fractions (up to 0.65) sitting above (Figure 4.4).

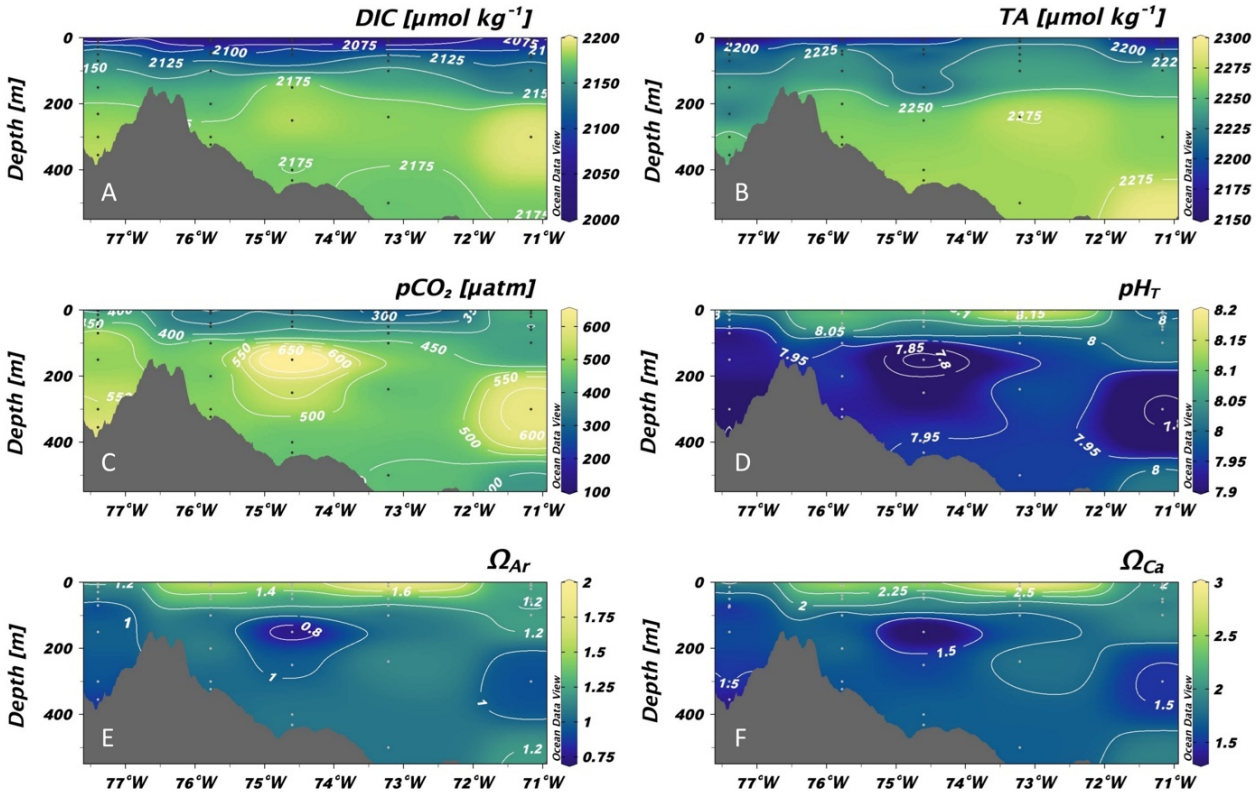

Figure 4.7: Section plots of carbonate chemistry measurements across the NOW transect (transect outline shown in inset map of Figure 4.5). Figure created using Ocean Data View software (Schlitzer, 2020) with bathymetry from IBCAO version 3 (Jakobsson et al., 2012).

Figure 4.7 displays vertical section plots of the same CO_2 system variables across the NOW transect. Here we can see SPMW entering the study region at the eastern end of the transect (station 115 at 300 m depth) is characterized by low pH_T (7.9 ± 0.4), low Ω_{Ar} (0.94 ± 0.05), and high pCO_2 (610 ± 20 μatm). In fact, high SPMW fractions (> 0.4) across the NOW transect (Figure 4.5) show the lowest observed pH_T, Ω_{Ar} and Ω_{Ca} throughout the study region. Other characteristics of SPMW, such as high nutrient concentrations (Figure 4.3) and high AOU (Figure S4.6) indicate that this water mass likely transports a strong remineralization signal due to the export of organic material from the productive West Greenland shelf (Burgers et al., 2020). BBPW entering the region at the surface at station 115 also displayed relatively low pH_T (8.0 ± 0.3), Ω_{Ar} near saturation (1.09 ± 0.06), and relatively high pCO_2 (440 ± 20). The upper 80 m of the central three stations (105, 108, and 111) of the NOW transect displayed

lower pCO_2 (below 350 μatm), and higher pH_T (> 8.05) and Ω_{Ar} (> 1.4) due to the impact of a surface bloom (Figure S4.6) and inputs of SIM (Figure 4.5).

4.3.4 Biological concentration changes (ΔDIC_{bio})

Calculated values of ΔDIC_{bio} (equation 4.4) represent the cumulative effect of biological processes since a water parcel departed from the ice arch at the northernmost station. Positive values of ΔDIC_{bio} indicate an overall DIC addition due to net respiration, while negative values represent net DIC removal due to net photosynthesis. Figure 4.8 shows section plots of ΔDIC_{bio}, AOU, chl *a* fluorescence, and TIN concentrations throughout the upper 100 m of the Nares Strait transect. We observe a clear divide between the surface and deeper waters, with negative values of ΔDIC_{bio} extending from the surface to depths of 40 m, and mostly near-zero (or slightly positive) values of ΔDIC_{bio} in deeper waters.

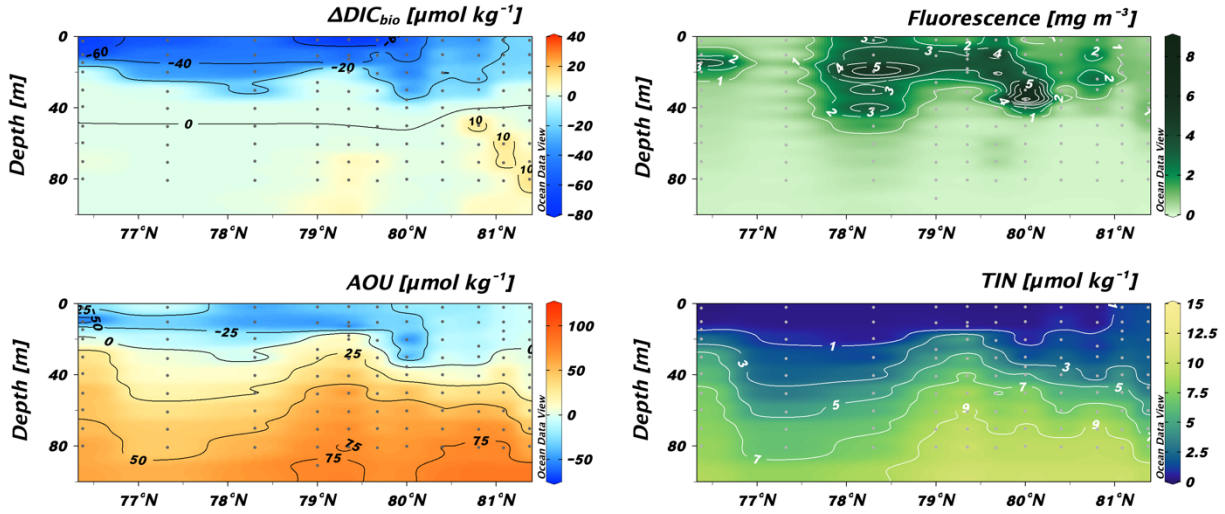

Figure 4.8: Section plots of biologically driven changes in DIC (ΔDIC_{bio}), chl a fluorescence, Apparent Oxygen Utilization (AOU), and total inorganic nitrogen (TIN) throughout the upper 100m of the Nares Strait transect (same transect as Figures 4.2, 4.4, and 4.6). Figure was created using Ocean Data View software (Schlitzer, 2020).

Within the upper 40 m of the Nares Strait transect negative values of ΔDIC_{bio} indicate a modest phytoplankton bloom, which progresses through multiple phases as waters transit southwards from Kennedy Channel. Measurements of chl *a* fluorescence and total inorganic nitrogen (TIN) concentrations (Figure 4.8) indicate the different bloom stages and nutrient limitations that drive them. The initial surface bloom in Kennedy Channel is weak, owing to the low initial concentrations of TIN available in the surface mixed layer (less than 2 μmol kg^{-1}). Due to the nutrient depleted surface waters, a subsurface chlorophyll maximum (SCM) develops at the entrance to Kane Basin (around 80 °N) at 40 m depth. Further into Kane Basin the shallowing bathymetry approaching 79 °N injects some UHW fractions (Figure 4.4) and nutrients into the surface mixed layer. This addition of nutrients spurred a second bloom in Kane Basin,

which is associated with the greatest ΔDIC_{bio} value of -73 μmol kg^{-1} at the surface (at approximately 79.5 °N). South of Kane Basin values of ΔDIC_{bio} remain fairly constant in the upper 20 m, indicating that there was not substantially more primary production and DIC drawdown past this point.

We do not observe any significant net respiration signal (positive ΔDIC_{bio}) in Nares Strait (see Figure S4.7 for a full vertical section of ΔDIC_{bio} along the Nares Strait transect). Within Kennedy Channel there are some low positive ΔDIC_{bio} values ranging from 3 to 12 μmol kg^{-1}, coinciding with the location of the UHW layer in the water column (Figure 4.8). However, these positive ΔDIC_{bio} estimates are approximately equal to the residual DIC term from the eOMP output (8 μmol kg^{-1}; Table 4.2), indicating that these small net respiration estimates may simply be the result of uncertainty within the eOMP framework. These results suggest that net respiration within the water column of Nares Strait is likely negligible. Only at the southernmost station of the transect (station 101), in the relatively isolated hollow dominated by SMPW (Figure 4.4) do we find a significant signal of net respiration (Figure S4.7).

Across the east-west transect in the NOW region we do observe some positive ΔDIC_{bio} values (> 20 μmol kg^{-1}) at depths below 300 m (Figure S4.6). We presume this is related to remineralization of organic material transported with SPMW from the WGC, seeing as the positive ΔDIC_{bio} values do not extend deeper (below 500 m depth) where significant CBAW fractions were located (Figure 4.5).

4.3.5 Gas exchange term (ΔDIC_{gas})

Table 4.3 shows cumulative ΔDIC_{gas} values at each sampling station of the Nares Strait transect, with positive values indicating that the surface ocean acts as a net sink of atmospheric CO_2. Due to the consistent undersaturation of surface water pCO_2 in Nares Strait, the whole study region was found to be an atmospheric CO_2 sink. As expected, ΔDIC_{gas} estimates start off small in Kennedy Channel, where surface waters had only recently emerged from under the ice arch. ΔDIC_{gas} estimates slightly increased in Kane Basin, where biological drawdown of DIC and increasing SIM fractions contribute to decreasing surface water pCO_2 and shallow surface mixed layer depths. ΔDIC_{gas} increases substantially in Smith Sound (station 127) and northern Baffin Bay (station 120 and 101), where wind speeds increased significantly (not shown, see Figure 5 of Burgers et al., 2017), and surface mixed layer depths remained shallow. At station 127 the ΔDIC_{gas} term becomes comparable to the maximum ΔDIC_{bio} drawdown in Kane Basin (Figure 4.8). Further south at station 120 the ΔDIC_{gas} term has surpassed the maximum ΔDIC_{bio} drawdown. This is possibly also represented in our surface underway pCO_2 measurements, which begin to fluctuate more and increase slightly south of station 127 (south of 78.3 °N, Figure 4.9a). The largest spike in underway pCO_2 around latitude 77.5 °N coincides with the highest wind speed observations in this region, suggesting that enhanced air-sea gas exchange may be responsible. This is

also potentially the reason for an increase in AOU in the surface mixed layer at station 120 in northern Baffin Bay (section 4.3.4; Figure 4.8), as gas exchange would have also led to uptake of atmospheric O_2.

Table 4.4: Summary of surface pCO_2 measurements (underway and surface rosette bottle) and ΔDIC_{gas} estimates within the surface mixed layer (SML) at each station of the Nares Strait transect.

Station	Latitude (°N)	SML (m)	Underway pCO_2 (μatm)	Surface Bottle pCO_2 (μatm)	pCO_2 difference (Underway - Bottle) (μatm)	Days since ice arch	ΔDIC_{gas}[a] (μmol kg^{-1})
Ken1	81.37	7.9	357.3	347.1	10.2	0.4	0.07± 0.02
Ken2	81.08	18.8	351.1	354.4	-3.2	2.1	1.4 ± 0.4
Ken3	80.80	14.8	312.1	320.9	-8.8	3.7	3.5 ± 0.9
Ken4	80.40	5.9	302.0	314.6	-12.7	5.8	6.5 ± 1.5
Kane1	80.00	8.9	295.6	299.4	-3.8	7.6	8.0 ± 1.8
Kane2	79.67	1.9	298.5	293.9	4.6	9.4	16 ± 4
Kane3	79.35	4.9	264.7	278.3	-13.6	11.0	20 ± 4
Kane5	79.00	9.9	251.0	243.0	8.0	12.7	18 ± 4
127	78.30	9.9	248.6	255.8	-7.2	16.0	53 ± 12
120	77.32	3.0	270.3	125.7	144.6	20.4	132 ± 28
101	76.38	7.9	273.6	318.3	-44.7	24.3	187 ± 38

[a] Uncertainty in the ΔDIC_{gas} term was calculated from the propagation of uncertainties associated with the gas transfer velocity parameterization, and underway pCO_2 measurements (see section 4.2.5).

4.3.6 DIC budget in Nares Strait

Table 4.4 presents average values of DIC_{mix}, ΔDIC_{bio}, and ΔDIC_{gas} in three sub-regions of Nares Strait: (1) Kennedy Channel, (2) Kane Basin, and (3) northern Baffin Bay. The northern Baffin Bay region includes stations 127, 120 and 101 (Figure 4.1a). The average DIC budget terms are also summarized by depth intervals, split between the surface mixed layer (see Table 4.3 for depths), intermediate depths (50 – 150 m) and the deep water column (> 200 m). As mentioned previously, values of ΔDIC_{bio} and ΔDIC_{gas} represent cumulative changes in a sampled water parcel since it emerged from under consolidated ice cover in northern Kennedy Channel. To better inform on local rates of biological activity and air-sea gas exchange, average daily rates of change in the ΔDIC_{bio} and ΔDIC_{gas} terms have been calculated for surface waters within each sub-region, and are included in parentheses in Table 4.4.

Predictably, we find that water mass mixing and transport (captured by the DIC_{mix} term) is responsible for most of the DIC variability across the region. Within the surface mixed layer DIC_{mix} estimates decreased from 2105 μmol kg^{-1} at station Ken1 to 2026 μmol kg^{-1} at station 101 in northern Baffin Bay. This decrease partially results from the intrusion of surface waters from the WGC (a mixture

of BBPW and SIM), which contain less DIC than the PMW waters exiting the Arctic Ocean, and also partially from increasing freshwater contributions (SIM and RR) in the surface mixed layer of Nares Strait (Figure 4.4). At intermediate depths we find a decrease in DIC_{mix} from Kennedy Channel towards northern Baffin Bay. This is due to the interaction of UHW with BBPW in Kane Basin, and even higher BBPW fractions present at this depth range in northern Baffin Bay (Figure 4.4). DIC_{mix} concentrations at depths below 200 m remained essentially constant across Kennedy Channel, Kane Basin, and northern Baffin Bay despite changes in source water mass fractions transitioning from mainly CBAW in the north to a mixture of CBAW with UHW and BBPW contributions in northern Baffin Bay.

Table 4.5: Regionally averaged DIC_{mix} (Eq. 4.3), ΔDIC_{bio} (Eq. 4.4), and ΔDIC_{gas} (Eq. 4.5) in the surface mixed layer, intermediate (50 – 100 m), and deep (> 150 m) layers of Kennedy Channel, Kane Basin, and northern Baffin Bay (including Smith Sound). Average daily rates of change in surface ΔDIC_{bio} and ΔDIC_{gas} are included in parentheses for each sub-region, and are indicative of local rates of biological production/respiration and air-sea gas exchange in each sub-region. All DIC budget values are in units of μmol kg^{-1}, daily rates of change (in parentheses) are in units of μmol kg^{-1} day^{-1}. Insignificant values are not included.

	Kennedy Channel	Kane Basin	Northern Baffin Bay
	Surface mixed layer		
DIC_{mix}	2086 ± 20	2057 ± 17	2040 ± 31
ΔDIC_{bio}	-23 ± 6 (-2 ± 5)	-54 ± 14 (-6 ± 6)	-56 ± 10 (1 ± 5)
ΔDIC_{gas}	3 ± 3 (0.9 ± 0.5)	16 ± 5 (2 ± 1)	123 ± 26 (14 ± 4)
	Intermediate (50 - 150 m)		
DIC_{mix}	2184 ± 4	2172 ± 4	2158 ± 8
ΔDIC_{bio}	6 ± 5	5 ± 3	-
	Deep (>200 m)		
DIC_{mix}	2174 ± 5	2170 ± 7	2172 ± 4
ΔDIC_{bio}	-	-	8 ± 9

Despite the fact that ΔDIC_{bio} represents a relatively small portion of the overall DIC pool, we find it plays an important role in determining surface pCO_2 concentrations. We investigated the contributions of water mass mixing, biology, and gas exchange to the surface pCO_2 in Nares Strait, by comparing observed pCO_2 values from discrete samples (pCO_2(obs); light blue symbols in Figure 4.9) with hypothetical values of pCO_2(mix), pCO_2(mix+bio), and pCO_2(mix+bio+gas) derived from CO_2 system calculations in CO_2Sys. The term pCO_2(mix) represents the surface pCO_2 due solely to water mass mixing and was calculated from inputs of average DIC_{mix}, TA_{mix}, in-situ *S*, and in-situ temperature *(T)* within the surface mixed layer of each station. The term pCO_2(mix+bio), represents the surface pCO_2 due

to water mass mixing and biology, and is calculated from inputs of $DIC_{mix}+\Delta DIC_{bio}$, $TA_{mix}+\Delta TA_{bio}$, in-situ *S*, and in-situ *T*. Similarly, the term pCO_2(mix+bio+gas) represents the surface pCO_2 due to all three processes and was calculated from inputs of $DIC_{mix}+\Delta DIC_{bio}+\Delta DIC_{gas,}$ $TA_{mix}+\Delta TA_{bio}$, in-situ *S*, and in-situ *T*. For all terms that consider biological changes we have factored in a slight increase in TA due to nitrate uptake during primary production, which can be estimated as $\Delta TA_{bio} = (11/106)\Delta DIC_{bio}$ by applying our local Redfield ratios (11 TIN : 106 DIC) and assuming that one unit of nitrate uptake increases TA by one unit.

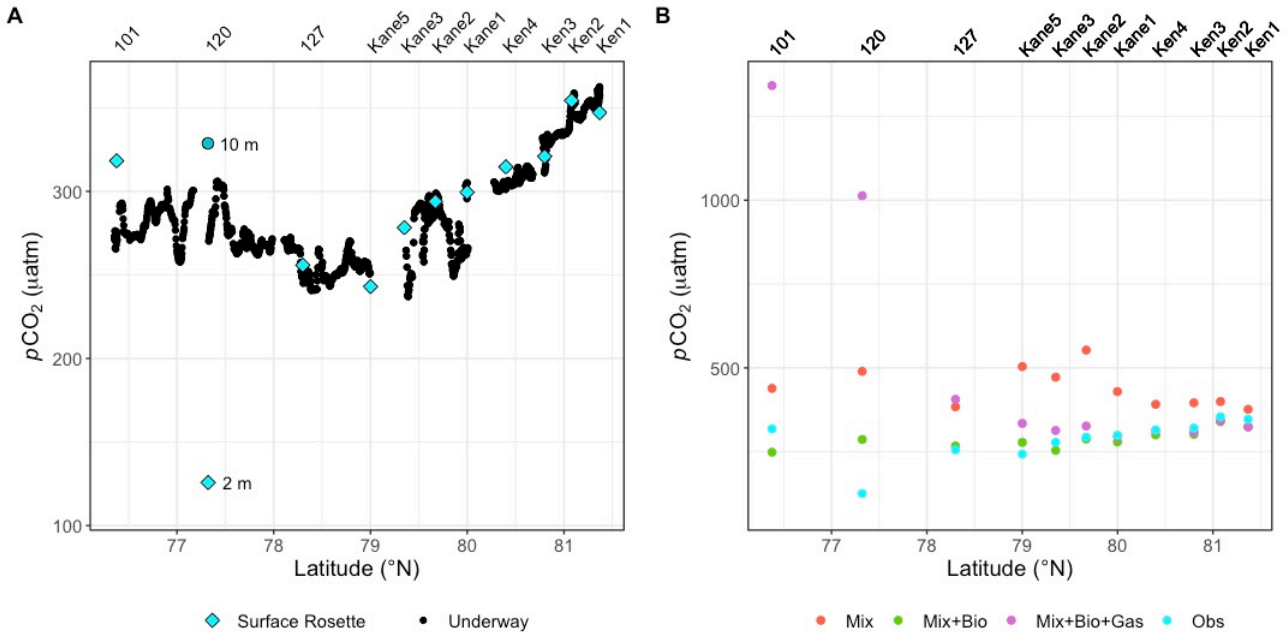

Figure 4.9: Trends in surface pCO_2 along the Nares Strait transect. (a) Surface pCO_2 measurements by the underway system, which sampled at 7 m depth (black dots), and calculated from DIC and TA measured in the shallowest rosette samples, at 2 m depth (blue diamonds). At station 120 the calculated pCO_2 is also shown for the rosette sample from 10 m depth. (b) eOMP modeled surface pCO_2 terms due to mixing (Mix, red dots), mixing and biology (Mix+Bio, green dots), mixing, biology, and gas exchange (Mix+Bio+Gas, purple dots), compared against observed pCO_2 from surface rosette samples (Obs, blue dots, same as blue diamonds in panel a).

Figure 4.9b displays the terms pCO_2(mix), pCO_2(mix+bio), pCO_2(mix+bio+gas), and pCO_2(obs) for the surface mixed layer at each station along the Nares Strait transect. Here we can see that biology plays a major role in lowering surface pCO_2 in Nares Strait, especially in Kane Basin where upwelling of UHW fractions increases the pCO_2(mix) term. The only station where biology does not fully account for the difference between pCO_2(mix) and pCO_2(obs) is station 120. The rosette samples at this station indicate a very sharp gradient in surface pCO_2 between the surface and 10 m depth (Figure 4.9a), and CTD profiles from this station similarly show steep gradients in temperature and salinity near the surface (not shown). Strong surface stratification is known to cause considerable uncertainty in the accurate

quantification of surface pCO_2, and air-sea CO_2 flux estimates in Arctic coastal waters (Ahmed et al., 2020; Dong et al., 2021; Miller et al., 2019). Our calculated freshwater fractions indicate relatively high fractions of both RR and SIM in the surface waters at station 120 (77.3 °N; Figure 4.4). However, the pCO_2(mix) term at station 120 remains high (approximately 490 μatm) despite these freshwater contributions. We also note that the observed surface TA measurement at station 120 was unusually high (at 2 m depth; TA = 2155 μmol kg^{-1}), despite very low salinity and DIC measurements at the same location (S = 28; DIC = 1877 μmol kg^{-1}). Therefore, it is also possible that a questionable surface TA measurement is responsible for the abnormally low surface pCO_2(obs) at station 120. Underway pCO_2 measurements at station 120 (270 μatm; Table 4.3; Figure 4.9a) are in closer agreement with the pCO_2(mix+bio) term.

Further factoring in the impact of air-sea gas exchange with the term pCO_2(mix+bio+gas), we find good agreement with observations until Smith Sound (station 127), where the ΔDIC_{gas} term begins to grow rapidly, surpassing the maximum ΔDIC_{bio} value in Kane Basin. This leads to large overestimates of the surface pCO_2 compared to observed values. This suggests that our ΔDIC_{gas} values likely overestimate the actual surface DIC increase due to air-sea gas exchange, especially south of Smith Sound. There is a high relative uncertainty associated with our ΔDIC_{gas} estimates (up to 30%), and our time-integrated method of calculating ΔDIC_{gas} should be considered a maximum estimate, because the CO_2 equilibration time between the atmosphere and the ocean (typically several months to a year; Sarmiento & Gruber, 2006) is much longer than the residence time of surface waters transiting through Nares Strait (20 to 40 days; Münchow, 2016).

4.3.7 The broader picture of water mass variability in Nares Strait and the North Water

In this study we observed a water mass assembly in Kennedy Channel that resembles characteristics of the TPD and the transition zone of the Pacific-Atlantic front in the central Arctic basin. It is worth exploring how the characteristics, and nutrient availability, of the waters entering Nares Strait via the Lincoln Sea might change under a different atmospheric forcing pattern (a different Arctic Oscillation Index; AO), and what implications this might have for carbon dynamics in Nares Strait in a changing climate.

To put our observations into context, during the 3 years preceding our observations on the 2014 ArcticNet cruise, the winter season (JFM) average AO was neutral to negative (NOAA Climate Prediction Center: https://www.cpc.ncep.noaa.gov/products/precip/CWlink/daily_ao_index/), and thus the TPD was likely aligned over the Lomonosov Ridge, transporting Siberian shelf waters towards the Lincoln Sea (solid red arrows, Figure 4.1b). We have considered the winter season AO because the cold season

commonly captures the largest AO variability throughout the year, and the JFM indices have been similarly employed in previous studies of surface water mass transport across the Arctic Ocean (Steele et al., 2004; de Steur et al., 2013). The modeling study of Bertosio et al. (2022b) confirms that from 2010 to 2016 the Beaufort Gyre expanded westwards over the Mendeleyev Ridge, causing the TPD to be roughly aligned with the Lomonosov Ridge. Bertosio et al. (2022b) also performed forward trajectories of water parcels released at 80 m depth in the central Makarov Basin (between the Lomonosov and Mendeleyev Ridges) in 2011, and found that they exited the Arctic Ocean via Nares Strait 1.5 to 2 years later. These findings lend support to our proposed origins and circulation of the PMW and UHW layers arriving in Nares Strait in 2014.

Under a positive AO, characterized by a less expansive Beaufort Gyre, the TPD tends to be aligned over the Mendeleyev Ridge, transporting a greater proportion of Pacific-source waters from the Chukchi Sea towards Fram Strait. Under this atmospheric forcing scenario, the Lincoln Sea and Nares Strait are located firmly in the Pacific-sector of the Arctic Ocean, to the west of the Pacific-Atlantic front (Figure 4.1b). Therefore, under this forcing scenario we would expect the water mass assembly entering Nares Strait from the north to be more representative of conditions in the Canada Basin (Newton & Sotirin, 1997; Steele et al., 2004; de Steur et al., 2013). Upper water column stratification is much stronger in the Canada Basin, due to the presence of relatively low-salinity Pacific waters (both summer and winter varieties) and due to surface flow convergence within the Beaufort Gyre which acts to retain freshwater from SIM and RR in the surface mixed layer (Brown et al., 2020; Carmack et al., 2016). The perennial stratification of the Canada Basin inhibits nutrient replenishment by convective mixing with deeper water masses during the winter season (Randelhoff et al., 2020), with the upper 50 m having nitrate concentrations below 1 μM even during winter (Brown et al., 2020). The UHW layer within the Canada Basin is generally centered around 150 m depth (Alkire et al., 2021; Brown et al., 2020), slightly deeper than the UHW layer we observed in 2014 in Kennedy Channel (centered at 100 m depth). The UHW of the Canada Basin is also characterized by higher DIC and nutrient concentrations (DIC from 2225 to 2260 μmol kg^{-1}, and Si from 35 to 45 μmol kg^{-1}) (e.g., Alkire et al., 2021; Brown et al., 2016; Miller et al., 2014) and displays lower pH and Ω_{Ar} (7.82 ± 0.03 and 0.75 ± 0.16, respectively) (Beaupré-Laperrière et al., 2020) than in the Eurasian Basin, due to the stronger remineralization signal downstream of the very productive Chukchi shelf (Yamamoto-Kawai et al., 2013). Were this water mass assembly to arrive in Nares Strait we would likely observe more nutrient-depleted surface waters with a higher freshwater content, and stronger stratification throughout the upper water column (Coupel et al., 2015; Randelhoff et al., 2020), which could inhibit the nutrient replenishment by vertical mixing, even over the Kane Basin

sill (Figure 4.2c). Under this scenario primary production in Nares Strait would be even more limited, and we could expect the waters to be more susceptible to ocean acidification, with the UHW layer likely transporting a corrosive aragonite signal ($\Omega_{Ar} < 1$) downstream into northern Baffin Bay (Azetsu-Scott et al., 2010; Yamamoto-Kawai et al., 2013).

On the other hand, under a negative AO scenario (with the TPD aligned over the Lomonosov Ridge) we expect some of the surface TPD signal to arrive in Nares Strait (as observed in this study), transporting with it high surface FDOM from Siberian river runoff (Stedmon et al., 2021) and moderate surface nutrient concentrations. Our observations in Kennedy Channel show modest nitrate concentrations entering from the north (up to 3.5 μmol kg^{-1} in PMW; Figure 4.3e). Charette et al. (2020) found that nitrate concentrations in the upper 50 m of the TPD in the central Arctic Ocean ranged from 0 to 8.4 μM during a similar period of neutral to negative AO (their observations are from 2015). Although these surface nitrate concentrations are still not high in comparison to those observed in the Eurasian Basin, which can reach up to 11 μM (Randelhoff et al., 2020; Brown et al., 2020), the fact remains that they are greater than surface nitrate concentrations that would arrive from the Canada Basin under a positive AO. Also under a negative AO forcing, the Pacific-Atlantic front would be roughly aligned with the TPD, transporting a somewhat shallower, thinner, and diluted (in terms of peak nutrient concentrations) UHW layer towards Nares Strait. Charette et al. (2020) observed UHW with peak silicate concentrations of 20 – 25 μM centered at ~80 m depth underneath the TPD in the central Arctic Ocean, whereas in this study the UHW was centered at ~100 m depth in Kennedy Channel. The relatively shallow position of the UHW layer within the Pacific-Atlantic front, compared to the Canada Basin, would make it easier for nutrients from deeper waters to be entrained into the euphotic zone by upwelling and mixing over the Kane Basin sill, providing greater nutrient supply to the surface waters in Nares Strait under a negative AO, despite likely lower peak nutrient concentrations in the UHW layer than under a positive AO.

Much remains unknown about water mass transport from the WGC and variability in the NOW region (Mortensen et al., 2022). However, a number of recent modeling studies align in predicting that the strength of the WGC, and the amount of heat it transports around Baffin Bay in the SPMW layer, will likely increase in the future (Buchart et al., 2022; Castro de la Guardia et al., 2015; Gillard et al., 2020; Grivault et al., 2017). Recent paleoclimate studies of the NOW polynya region also suggest that warm periods have historically been associated with warming SPMW temperatures, further northward penetration of SPMW, and decreased productivity (Jackson et al., 2021; Ribeiro et al., 2021). In this study we observed SPMW with a temperature of 2 °C arriving in the southeastern NOW region (at

approximately 76 °N; Table 4.1), but temperatures of SPMW contributions farther north quickly decreased to below 0 °C as SPMW mixed with UHW and CBAW (Figures 4.2 and 4.4). More observational studies are needed to understand the changing strength and heat content of the WGC and its influence on the NOW region.

4.4 Summary and Conclusions

We have described the interaction of water masses entering Nares Strait from the north (Kennedy Channel) and south (the North Water polynya region of northern Baffin Bay) using a series of chemical tracers and an extended optimum multi-parameter (eOMP) analysis. Our tracer observations in Kennedy Channel display a Polar Mode water (PMW) characterized by high FDOM, near freezing temperatures and low salinity (31.4), suggesting the arrival of Siberian shelf waters with a strong riverine signal. Underneath the PMW, we find a slightly diluted layer of Upper Halocline water (UHW) of partial Pacific origin (as indicated by ANP values of ~0.5; Newton et al., 2013), displaying silicate concentrations up to 18 μmol kg^{-1}, and centered at 100 m depth. These upper water column characteristics indicate that our sampling region in Kennedy Channel likely received waters influenced by the TPD and the Pacific-Atlantic front. The deep-water column in Kennedy Channel contains Canada Basin Atlantic water (CBAW), with a relatively warm temperature (T = 0.36 °C) compared to the other Arctic-outflow water masses.

Across the North Water polynya region of northern Baffin Bay we observe another two water masses entering Nares Strait from the southeast. The upper water column is dominated by Baffin Bay Polar water (BBPW), a winter mode water formed somewhere in eastern Baffin Bay (Mortensen et al., 2022; Rysgaard et al., 2020), characterized by a near-surface temperature minimum close to the freezing point and a salinity of approximately 33.5. Centered at 300 m depth we also observe a relatively warm (T = 2 °C) and saline (S = 34.3) Subpolar Mode Water (SPMW) layer transiting northwards. SPMW is also characterized by high nutrient and low DO concentrations, suggesting a history of organic matter remineralization, leading to the lowest observed pH_T and calcium carbonate saturation states (pH_T = 7.85, Ω_{Ca} = 1.49, Ω_{Ar} = 0.94) of any water mass in our study region.

The results of our eOMP analysis document the interaction of all these source water masses throughout Nares Strait, and the effects of water mass mixing and biological processes on the DIC budget of the region. We find a great degree of mixing in Kane Basin, driven by the presence of a shallow sill (220 m depth), which forces upwelling and vertical mixing of the UHW and CBAW layers from the north, and the BBPW and SPMW layers from the south. The role of water mass mixing clearly dominates the DIC budget of the region, although a modest phytoplankton bloom in Kane Basin is found to play a key role in decreasing surface pCO_2 concentrations throughout Nares Strait. We do not observe any

significant respiration signal at depth within Nares Strait, suggesting that there is either too little primary production occurring to generate a detectable respiration signal from sinking biomass, or the currents may be too fast in Nares Strait to allow enough time for sinking particles to accumulate and remineralize within the strait (surface waters only take 20 to 40 days to flow through Nares Strait; Münchow, 2016). We do observe a respiration signal at depth in the NOW region (DIC_{bio} as high as 30 μmol kg^{-1}), associated with high SPMW fractions, implying that the respiration signal is derived from organic matter transported with this water mass from the West Greenland shelf. Air-sea gas exchange is found to play a minor role in the surface carbon dynamics in this region, although atmospheric CO_2 uptake may be responsible for a slight increase in surface pCO_2 south of Smith Sound (at stations 120 and 101), where wind speeds were high and we observed a coincident increase in AOU, suggesting the uptake of atmospheric O_2 as well.

These results represent only one snapshot in time of the water mass characteristics in Nares Strait, a waterway that is subject to large interannual variability in water mass fluxes from the Arctic Ocean (Jackson et al., 2014; de Steur et al., 2013). As climate change affects the Arctic Ocean and Baffin Bay, it is likely that greater freshwater inputs from melting sea ice, glaciers, and rivers will further increase freshwater content in this area, leading to enhanced stratification of the water column and further limiting nutrient availability for primary production (Bergeron & Tremblay, 2014; Blais et al., 2017). Our observations in Kennedy Channel show that there is already very limited nutrient availability in surface waters from the TPD, and if a different surface water mass were to arrive from the Canada Basin, nutrient availability would likely be even more limited (Brown et al., 2020; Coupel et al., 2015; Randelhoff et al., 2020). At the same time, the northward transport of water masses from the West Greenland shelf may increase in the future with a strengthening of the WGC (Buchart et al., 2022; Castro de la Guardia et al., 2015; Jackson et al., 2021), and will perhaps become the dominant source of surface nutrients to the NOW region, despite also being influenced by increasing freshwater inputs.

Literature Cited

Ahmed, M. M. M., Else, B. G. T., Capelle, D., Miller, L. A., & Papakyriakou, T. (2020). Underestimation of surface pCO_2 and air-sea CO_2 fluxes due to freshwater stratification in an Arctic shelf sea, Hudson Bay. *Elementa*, *8(1):084*. https://doi.org/10.1525/elementa.084

Alkire, M. B., Falkner, K. K., Boyd, T., & Macdonald, R. W. (2010). Sea ice melt and meteoric water distributions in Nares Strait, Baffin Bay, and the Canadian Arctic Archipelago. *Journal of Marine Research*, *68*(6), 767–798.

Alkire, M. B., Rember, R., & Polyakov, I. (2021). The Pacific-Atlantic Front in the East Siberian Sea of the Arctic Ocean. In *The Handbook of Environmental Chemistry*. Springer, Berlin, Heidelberg. https://doi.org/10.1007/698_2021_795

Amundsen Science Data Collection. (2018). CTD data collected by the CCGS Amundsen in the Canadian Arctic. ArcticNet Inc., Québec, Canada. Processed data. Version 1, Release 2. Archived at www.polardata.ca, Canadian Cryospheric Information Network (CCIN), Waterloo, Canada. https://doi.org/10.5884/12713. Accessed January 2020.

Anderson, L. G., Andersson, P. S., Björk, G., Jones, E. P., Jutterström, S., & Wåhlström, I. (2013). Source and formation of the upper halocline of the Arctic Ocean. *Journal of Geophysical Research: Oceans*, *118*, 410–421. https://doi.org/10.1029/2012JC008291

Anderson, L. G., Björk, G., Holby, O., Jutterström, S., Magnus Mörth, C., O'Regan, M., et al. (2017). Shelf-Basin interaction along the East Siberian Sea. *Ocean Science*, *13*(2), 349–363. https://doi.org/10.5194/os-13-349-2017

Azetsu-Scott, K., Clarke, A., Falkner, K., Hamilton, J., Jones, E. P., Lee, C., et al. (2010). Calcium carbonate saturation states in the waters of the Canadian Arctic Archipelago and the Labrador Sea. *Journal of Geophysical Research: Oceans*, *115*(C11021). https://doi.org/10.1029/2009JC005917

Azetsu-Scott, K., Petrie, B., Yeats, P., & Lee, C. (2012). Composition and fluxes of freshwater through Davis Strait using multiple chemical tracers. *Journal of Geophysical Research*, *117*(C12), C12011. https://doi.org/10.1029/2012JC008172

Bâcle, J., Carmack, E. C., & Ingram, R. G. (2002). Water column structure and circulation under the North Water during spring transition: April-July 1998. *Deep-Sea Research Part II: Topical Studies in Oceanography*, *49*, 4907–4925. https://doi.org/10.1016/S0967-0645(02)00170-4

Barber, D. G., Babb, D. G., Ehn, J. K., Chan, W., Matthes, L., Dalman, L. A., et al. (2018). Increasing Mobility of High Arctic Sea Ice Increases Marine Hazards Off the East Coast of Newfoundland. *Geophysical Research Letters*, *45*, 2370–2379. https://doi.org/10.1002/2017GL076587

Bauch, D., van der Loeff, M. R., Andersen, N., Torres-Valdes, S., Bakker, K., & Abrahamsen, E. P. (2011). Origin of freshwater and polynya water in the Arctic Ocean halocline in summer 2007. *Progress in Oceanography*, *91*, 482–495. https://doi.org/10.1016/j.pocean.2011.07.017

Beaupré-Laperrière, A., Mucci, A., & Thomas, H. (2020). The recent state and variability of the carbonate system of the Canadian Arctic Archipelago and adjacent basins in the context of ocean acidification. *Biogeosciences*, *17*, 3923–3942. https://doi.org/10.5194/bg-17-3923-2020

Bergeron, M., & Tremblay, J.-É. (2014). Shifts in biological productivity inferred from nutrient drawdown in the southern Beaufort Sea (2003-2011) and northern Baffin Bay (1997-2011), Canadian Arctic. *Geophysical Research Letters*, *41*, 3979–3987. https://doi.org/10.1002/2014GL059649

Bertosio, C., Provost, C., Athanase, M., Sennéchael, N., Garric, G., Lellouche, J. M., Kim, J. H., et al.

(2022a). Changes in Arctic Halocline Waters Along the East Siberian Slope and in the Makarov Basin From 2007 to 2020. *Journal of Geophysical Research: Oceans*, *127*(9), 1–21. https://doi.org/10.1029/2021JC018082

Bertosio, C., Provost, C., Athanase, M., Sennéchael, N., Garric, G., Lellouche, J.-M., Bricaud, C., et al. (2022b). Changes in Freshwater Distribution and Pathways in the Arctic Ocean Since 2007 in the Mercator Ocean Global Operational System. *Journal of Geophysical Research: Oceans*, *127*, e2021JC017701. https://doi.org/10.1029/2021JC017701

Blais, M., Ardyna, M., Gosselin, M., Dumont, D., Bélanger, S., Tremblay, J.-É., et al. (2017). Contrasting interannual changes in phytoplankton productivity and community structure in the coastal Canadian Arctic Ocean. *Limnology and Oceanography*, *62*(6), 2480–2497. https://doi.org/10.1002/lno.10581

Broecker, W. S. (1974). "NO", a conservative water-mass tracer. *Earth and Planetary Science Letters*, *23*(1), 100–107. https://doi.org/10.1016/0012-821X(74)90036-3

Brown, K. A., McLaughlin, F., Tortell, P. D., Yamamoto-Kawai, M., & Francois, R. (2016). Sources of dissolved inorganic carbon to the Canada Basin halocline: A multitracer study. *Journal of Geophysical Research: Oceans*, *121*. https://doi.org/10.1002/2015JC011535

Brown, K. A., Holding, J. M., & Carmack, E. C. (2020). Understanding Regional and Seasonal Variability Is Key to Gaining a Pan-Arctic Perspective on Arctic Ocean Freshening. *Frontiers in Marine Science*, *7:606*. https://doi.org/10.3389/fmars.2020.00606

Buchart, L., Castro de la Guardia, L., Xu, Y., Ridenour, N., Marson, J. M., Deschepper, I., et al. (2022). Future Climate Scenarios for Northern Baffin Bay and the Pikialasorsuaq (North Water Polynya) Region. *Atmosphere-Ocean*, *60*(2), 102–123. https://doi.org/10.1080/07055900.2022.2067028

Burgers, T. M., Miller, L. A., Thomas, H., Else, B. G. T., Gosselin, M., & Papakyriakou, T. (2017). Surface Water pCO_2 variations and sea-air CO_2 fluxes during summer in the eastern Canadian Arctic. *Journal of Geophysical Research: Oceans*, *122*, 9663–9678. https://doi.org/10.1002/2017JC013250

Burgers, T. M., Tremblay, J.-É., Else, B. G. T., & Papakyriakou, T. N. (2020). Estimates of net community production from multiple approaches surrounding the spring ice-edge bloom in Baffin Bay. *Elementa: Science of the Anthropocene*, *8(1):013*. https://doi.org/10.1525/elementa.013

Carmack, E. C., Yamamoto-Kawai, M., Haine, T. W. N., Bacon, S., Bluhm, B. A., Lique, C., et al. (2016). Freshwater and its role in the Arctic Marine System: Sources, disposition, storage, export, and physical and biogeochemical consequences in the Arctic and global oceans. *Journal of Geophysical Research: Biogeosciences*, *121*, 675–717. https://doi.org/10.1002/2015JG003140

Castro de la Guardia, L., Hu, X., & Myers, P. G. (2015). Potential positive feedback between Greenland Ice Sheet melt and Baffin Bay heat content on the west Greenland shelf. *Geophysical Research Letters*, *42*, 4922–4930. https://doi.org/10.1002/2015GL064626

Charette, M. A., Kipp, L. E., Jensen, L. T., Dabrowski, J. S., Whitmore, L. M., Fitzsimmons, J. N., et al. (2020). The Transpolar Drift as a Source of Riverine and Shelf-Derived Trace Elements to the Central Arctic Ocean. *Journal of Geophysical Research: Oceans*, *125*(5). https://doi.org/10.1029/2019JC015920

Chen, B., Cai, W.-J., & Chen, L. (2015). The marine carbonate system of the Arctic Ocean: Assessment of internal consistency and sampling considerations, summer 2010. *Marine Chemistry*, *176*, 174–188. https://doi.org/10.1016/j.marchem.2015.09.007

Coupel, P., Ruiz-Pino, D., Sicre, M. A., Chen, J. F., Lee, S. H., Schiffrine, N., et al. (2015). The impact of freshening on phytoplankton production in the Pacific Arctic Ocean. *Progress in Oceanography*, *131*,

113–125. https://doi.org/10.1016/j.pocean.2014.12.003

Curry, B., Lee, C. M., Petrie, B., Moritz, R. E., & Kwok, R. (2014). Multiyear Volume, Liquid Freshwater, and Sea Ice Transports through Davis Strait, 2004–10. *Journal of Physical Oceanography*, *44*(4), 1244–1266. https://doi.org/10.1175/JPO-D-13-0177.1

Dickson, A. G. (1990). Standard potential of the reaction: AgCl(s) + $12H_2$(g) = Ag(s) + HCl(aq), and the standard acidity constant of the ion HSO_4- in synthetic sea water from 273.15 to 318.15 K. *The Journal of Chemical Thermodynamics*, *22*(2), 113–127. https://doi.org/10.1016/0021-9614(90)90074-Z

Dickson, A. G., Sabine, C. L., & Christian, J. R. (2007). Guide to best practices for ocean CO_2 measurements. *PICES Special Publication*, *3*, 191 p. https://doi.org/10.1159/000331784

Dinauer, A., & Mucci, A. (2018). Distinguishing between physical and biological controls on the spatial variability of pCO_2: A novel approach using OMP water mass analysis (St. Lawrence, Canada). *Marine Chemistry*, *204*, 107–120. https://doi.org/10.1016/j.marchem.2018.03.007

Dodd, P. A., Rabe, B., Hansen, E., Falck, E., MacKensen, A., Rohling, E., et al. (2012). The freshwater composition of the Fram Strait outflow derived from a decade of tracer measurements. *Journal of Geophysical Research: Oceans*, *117*, C11005. https://doi.org/10.1029/2012JC008011

Dong, Y., Yang, M., Bakker, D. C. E., Liss, P. S., Kitidis, V., Brown, I., et al. (2021). Near-Surface Stratification Due to Ice Melt Biases Arctic Air-Sea CO_2 Flux Estimates. *Geophysical Research Letters*, *48*, e2021GL095266. https://doi.org/10.1029/2021GL095266

Eegeesiak, O., Aariak, E., & Kleist, K. V. (2017). *People of the Ice Bridge: The Future of the Pikialasorsuaq*. *Pikialasorsuaq Commission*. Ottawa.

Gillard, L. C., Hu, X., Myers, P. G., Ribergaard, M. H., & Lee, C. M. (2020). Drivers for Atlantic-origin waters abutting Greenland. *Cryosphere*, *14*, 2729–2753. https://doi.org/10.5194/tc-14-2729-2020

Gonçalves-Araujo, R., Granskog, M. A., Bracher, A., Azetsu-Scott, K., Dodd, P. A., & Stedmon, C. A. (2016). Using fluorescent dissolved organic matter to trace and distinguish the origin of Arctic surface waters. *Scientific Reports*, *6*, 33978. https://doi.org/10.1038/srep33978

Granskog, M. A., Stedmon, C. A., Dodd, P. A., Amon, R. M. W., Pavlov, A. K., De Steur, L., & Hansen, E. (2012). Characteristics of colored dissolved organic matter (CDOM) in the Arctic outflow in the Fram Strait: Assessing the changes and fate of terrigenous CDOM in the Arctic Ocean. *Journal of Geophysical Research*, *117*, C12021. https://doi.org/10.1029/2012JC008075

Grasshoff, Klaus, Kremling, K., & Ehrhardt, M. (Eds.). (1999). *Methods of Seawater Analysis* (3rd ed.). Wiley-VCH. https://doi.org/10.1002/9783527613984

Grivault, N., Hu, X., & Myers, P. G. (2017). Evolution of Baffin Bay Water Masses and Transports in a Numerical Sensitivity Experiment under Enhanced Greenland Melt. *Atmosphere - Ocean*, *55*(3), 169–194. https://doi.org/10.1080/07055900.2017.1333950

Hamilton, A. K., Mueller, D., & Laval, B. E. (2021). Ocean Modification and Seasonality in a Northern Ellesmere Island Glacial Fjord Prior to Ice Shelf Breakup: Milne Fiord. *Journal of Geophysical Research: Oceans*, *126*. https://doi.org/10.1029/2020jc016975

Hansen, H. P., & Koroleff, F. (1999). *Determination of nutrients*. (K. Grasshoff, K. Kremling, & M. Ehrhardt, Eds.), *Methods of seawater analysis* (3rd ed.). Weinheim, Germany: Wiley-VCH. https://doi.org/10.1002/9783527613984.ch10

van Heuven, S., Pierrot, D., Rae, J. W. B., Lewis, E., & Wallace, D. W. R. (2011). MATLAB program

developed for CO_2 system calculations. Oak Ridge: US Department of Energy: ORML/CDIAC-105b. Carbon Dioxide Information Analysis Center. https://doi.org/doi: 10.3334/CDIAC/otg.CO2SYS_MATLAB_v1.1

Holmes, R. M., Aminot, A., Kérouel, R., Hooker, B. A., & Peterson, B. J. (1999). A simple and precise method for measuring ammonium in marine and freshwater ecosystems. *Canadian Journal of Fisheries and Aquatic Sciences*, *56*, 1801–1808. https://doi.org/10.1139/f99-128

Jackson, J. M., Lique, C., Alkire, M., Steele, M., Lee, C. M., Smethie, W. M., & Schlosser, P. (2014). On the waters upstream of Nares Strait, Arctic Ocean, from 1991 to 2012. *Continental Shelf Research*, *73*, 83–96. https://doi.org/10.1016/j.csr.2013.11.025

Jackson, R., Kvorning, A. B., Limoges, A., Georgiadis, E., Olsen, S. M., Tallberg, P., et al. (2021). Holocene polynya dynamics and their interaction with oceanic heat transport in northernmost Baffin Bay. *Scientific Reports*, *11*, 10095. https://doi.org/10.1038/s41598-021-88517-9

Jakobsson, M., Mayer, L., Coakley, B., Dowdeswell, J. A., Forbes, S., Fridman, B., et al. (2012). The International Bathymetric Chart of the Arctic Ocean (IBCAO) Version 3.0. *Geophysical Research Letters*, *39*(12), L12609. https://doi.org/10.1029/2012GL052219

Jones, E. P., & Anderson, L. G. (1986). On the origin of the chemical properties of the Arctic Ocean halocline. *Journal of Geophysical Research: Oceans*, *91*(C9), 10759–10767. https://doi.org/10.1029/jc091ic09p10759

Jones, E Peter, Anderson, L. G., & Swift, J. H. (1998). Distribution of Atlantic and Pacific waters in the upper Arctic Ocean : Implications for circulation. *Geophysical Research Letters*, *25*(6), 765–768. https://doi.org/10.1029/98gl00464

Kwok, R., Pedersen, L. T., Gudmandsen, P., & Pang, S. S. (2010). Large sea ice outflow into the Nares Strait in 2007. *Geophysical Research Letters*, *37*, L03502. https://doi.org/10.1029/2009GL041872

Lansard, B., Mucci, A., Miller, L. A., Macdonald, R. W., & Gratton, Y. (2012). Seasonal variability of water mass distribution in the southeastern Beaufort Sea determined by total alkalinity and $\delta^{18}O$. *Journal of Geophysical Research*, *117*, C03003. https://doi.org/10.1029/2011JC007299

Lee, K., Kim, T.-W., Byrne, R. H., Millero, F. J., Feely, R. A., & Liu, Y.-M. (2010). The universal ratio of boron to chlorinity for the North Pacific and North Atlantic oceans. *Geochimica et Cosmochimica Acta*, *74*(6), 1801–1811. https://doi.org/10.1016/j.gca.2009.12.027

Lewis, E., & Wallace, D. W. R. (1998). Program Developed for CO_2 System Calculations. https://doi.org/10.3334/CDIAC/otg.CO2SYS_DOS_CDIAC 105

Lobb, J., Weaver, A. J., Carmack, E. C., & Ingram, R. G. (2003). Structure and mixing across an Arctic/Atlantic front in northern Baffin Bay. *Geophysical Research Letters*, *30*(16), 1833. https://doi.org/10.1029/2003GL017755

Lueker, T. J., Dickson, A. G., & Keeling, C. D. (2000). Ocean pCO_2 calculated from dissolved inorganic carbon, alkalinity, and equations for K1 and K2: validation based on laboratory measurements of CO_2 in gas and seawater at equilibrium. *Marine Chemistry*, *70*, 105–119.

Marchese, C., Albouy, C., Tremblay, J.-É., Dumont, D., D'Ortenzio, F., Vissault, S., & Bélanger, S. (2017). Changes in phytoplankton bloom phenology over the North Water (NOW) polynya: a response to changing environmental conditions. *Polar Biology*, *40*, 1721–1737. https://doi.org/10.1007/s00300-017-2095-2

Martens, J., Wild, B., Semiletov, I., Dudarev, O. V., & Gustafsson, Ö. (2022). Circum-Arctic release of

terrestrial carbon varies between regions and sources. *Nature Communications*, *13*, 5858. https://doi.org/10.1038/s41467-022-33541-0

McLaughlin, F. A., Carmack, E. C., Macdonald, R. W., & Bishop, J. K. B. (1996). Physical and geochemical properties across the Atlantic / Pacific water mass front in the southern Canadian Basin. *Journal of Geophysical Research*, *101*(C1), 1183–1197. https://doi.org/https://doi.org/10.1029/95JC02634

Melling, H., Gratton, Y., & Ingram, G. (2001). Ocean circulation within the North Water polynya of Baffin Bay. *Atmosphere - Ocean*, *39*(3), 301–325. https://doi.org/10.1080/07055900.2001.9649683

Miller, L. A., Papakyriakou, T. N., Collins, R. E., Deming, J. W., Ehn, J. K., MacDonald, R. W., et al. (2011). Carbon dynamics in sea ice: A winter flux time series. *Journal of Geophysical Research: Oceans*, *116*, C02028. https://doi.org/10.1029/2009JC006058

Miller, L. A., Macdonald, R. W., Mclaughlin, F., Mucci, A., Yamamoto-Kawai, M., Giesbrecht, K. E., et al. (2014). Changes in the marine carbonate system of the western Arctic : patterns in a rescued data set. *Polar Research*, *33*(1), 20577. https://doi.org/10.3402/polar.v33.20577

Miller, L. A., Burgers, T. M., Burt, W. J., Granskog, M. A., & Papakyriakou, T. N. (2019). Air-Sea CO_2 Flux Estimates in Stratified Arctic Coastal Waters : How Wrong Can We Be ? *Geophysical Research Letters*, *46*, 235–243. https://doi.org/10.1029/2018GL080099

Moore, G. W. K., Schweiger, A., Zhang, J., & Steele, M. (2019). Spatiotemporal Variability of Sea Ice in the Arctic's Last Ice Area. *Geophysical Research Letters*, *46*, 11237–11243. https://doi.org/10.1029/2019GL083722

Morison, J., Kwok, R., Peralta-Ferriz, C., Alkire, M., Rigor, I., Andersen, R., & Steele, M. (2012). Changing Arctic Ocean freshwater pathways. *Nature*, *481*, 66–70. https://doi.org/10.1038/nature10705

Mortensen, J., Rysgaard, S., Winding, M. H. S., Arendt, K. E., Lund, H., Stuart-Lee, A. E., & Meire, L. (2022). Multidecadal Water Mass Dynamics on the West Greenland Shelf. *Journal of Geophysical Research: Oceans*, *127*. https://doi.org/10.1029/2022JC018724

Münchow, A. (2016). Volume and freshwater flux observations from Nares Strait to the west of Greenland at daily time scales from 2003 to 2009. *Journal of Physical Oceanography*, *46*(1), 141–157. https://doi.org/10.1175/JPO-D-15-0093.1

Münchow, A., Melling, H., & Falkner, K. K. (2006). An observational estimate of volume and freshwater flux leaving the Arctic Ocean through Nares Strait. *Journal of Physical Oceanography*, *36*(11), 2025–2041. https://doi.org/10.1175/JPO2962.1

Münchow, A., Falkner, K. K., & Melling, H. (2007). Spatial continuity of measured seawater and tracer fluxes through Nares Strait, a dynamically wide channel bordering the Canadian Archipelago. *Journal of Marine Research*, *65*, 759–788. https://doi.org/10.1357/002224007784219048

Münchow, A., Falkner, K. K., & Melling, H. (2015). Baffin Island and West Greenland Current Systems in northern Baffin Bay. *Progress in Oceanography*, *132*, 305–317. https://doi.org/10.1016/j.pocean.2014.04.001

Mundy, C. J., Gosselin, M., Ehn, J. K., Belzile, C., Poulin, M., Alou, E., et al. (2011). Characteristics of two distinct high-light acclimated algal communities during advanced stages of sea ice melt. *Polar Biology*, *34*, 1869–1886. https://doi.org/10.1007/s00300-011-0998-x

Myers, P. G., Donnelly, C., & Ribergaard, M. H. (2009). Structure and variability of the West Greenland Current in Summer derived from 6 repeat standard sections. *Progress in Oceanography*, *80*(1–2),

93–112. https://doi.org/10.1016/j.pocean.2008.12.003

Myers, P. G., Castro de la Guardia, L., Fu, C., Gillard, L. C., Grivault, N., Hu, X., et al. (2021). Extreme High Greenland Blocking Index Leads to the Reversal of Davis and Nares Strait Net Transport Toward the Arctic Ocean. *Geophysical Research Letters*, *48*. https://doi.org/10.1029/2021GL094178

Newton, J. L., & Sotirin, B. J. (1997). Boundary undercurrent and water mass changes in the Lincoln Sea. *Journal of Geophysical Research: Oceans*, *102*(C2), 3393–3403.

Newton, R., Schlosser, P., Mortlock, R., Swift, J., & MacDonald, R. (2013). Canadian Basin freshwater sources and changes: Results from the 2005 Arctic Ocean Section. *Journal of Geophysical Research: Oceans*, *118*, 2133–2154. https://doi.org/10.1002/jgrc.20101

Nishino, S., Itoh, M., Williams, W. J., & Semiletov, I. (2013). Shoaling of the nutricline with an increase in near-freezing temperature water in the Makarov Basin. *Journal of Geophysical Research: Oceans*, *118*, 635–649. https://doi.org/10.1029/2012JC008234

Nitishinsky, M., Anderson, L. G., & Hölemann, J. A. (2007). Inorganic carbon and nutrient fluxes on the Arctic Shelf. *Continental Shelf Research*, *27*, 1584–1599. https://doi.org/10.1016/j.csr.2007.01.019

Orr, J. C., Epitalon, J.-M., Dickson, A. G., & Gattuso, J.-P. (2018). Routine uncertainty propagation for the marine carbon dioxide system. *Marine Chemistry*, *207*, 84–107. https://doi.org/10.1016/j.marchem.2018.10.006

Östlund, H. G., & Hut, G. (1984). Arctic Ocean water mass balance from isotope data. *Journal of Geophysical Research: Oceans*, *89*(C4), 6373–6381. https://doi.org/10.1029/JC089iC04p06373

Peralta-Ferriz, C., & Woodgate, R. A. (2015). Seasonal and interannual variability of pan-Arctic surface mixed layer properties from 1979 to 2012 from hydrographic data , and the dominance of stratification for multiyear mixed layer depth shoaling. *Progress in Oceanography*, *134*, 19–53. https://doi.org/10.1016/j.pocean.2014.12.005

Pierrot, D., Neill, C., Sullivan, K., Castle, R., Wanninkhof, R., Lüger, H., et al. (2009). Recommendations for autonomous underway pCO_2 measuring systems and data-reduction routines. *Deep-Sea Research Part II*, *56*, 512–522. https://doi.org/10.1016/j.dsr2.2008.12.005

Randelhoff, A., Oziel, L., Massicotte, P., Bécu, G., Galí, M., Lacour, L., et al. (2019). The evolution of light and vertical mixing across a phytoplankton ice-edge bloom. *Elementa: Science of the Anthropocene*, *7:20*. https://doi.org/10.1525/elementa.357

Randelhoff, A., Holding, J., Janout, M., Sejr, M. K., Babin, M., Tremblay, J. É., & Alkire, M. B. (2020). Pan-Arctic Ocean Primary Production Constrained by Turbulent Nitrate Fluxes. *Frontiers in Marine Science*, *7*(150). https://doi.org/10.3389/fmars.2020.00150

Ribeiro, S., Limoges, A., Massé, G., Johansen, K. L., Colgan, W., Weckström, K., et al. (2021). Vulnerability of the North Water ecosystem to climate change. *Nature Communications*, *12*, 4475. https://doi.org/10.1038/s41467-021-24742-0

Rudels, B. (2009). Arctic ocean circulation. In J. H. Steele, S. A. Thorpe, & K. K. Turekian (Eds.), *Encyclopedia of Ocean Sciences* (pp. 211–225). Academic Press. https://doi.org/https://doi.org/10.1016/B978-012374473-9.00601-9

Rudels, B., Jones, E. P., Schauer, U., & Eriksson, P. (2004). Atlantic sources of the Arctic Ocean surface and halocline waters. *Polar Research*, *23*(2), 181–208. https://doi.org/10.1029/2001JC001141.MacKinnon

Ryan, P. A., & Münchow, A. (2017). Sea ice draft observations in Nares Strait from 2003 to 2012. *Journal of Geophysical Research: Oceans*, *122*, 3057–3080. https://doi.org/10.1002/2016JC011966

Rysgaard, S., Boone, W., Carlson, D., Sejr, M. K., Bendtsen, J., Juul-Pedersen, T., et al. (2020). An updated view on water masses on the pan-West Greenland continental shelf and their link to proglacial fjords. *Journal of Geophysical Research: Oceans*, *125*. https://doi.org/10.1029/2019jc015564

Rysgaard, Søren, Glud, R. N., Sejr, M. K., Bendtsen, J., & Christensen, P. B. (2007). Inorganic carbon transport during sea ice growth and decay: A carbon pump in polar seas. *Journal of Geophysical Research*, *112*, C03016. https://doi.org/10.1029/2006JC003572

Rysgaard, Søren, Glud, R. N., Sejr, M. K., Blicher, M. E., & Stahl, H. J. (2008). Denitrification activity and oxygen dynamics in Arctic sea ice. *Polar Biology*, *31*(5), 527–537. https://doi.org/10.1007/s00300-007-0384-x

Sarmiento, J. L., & Gruber, N. (2006). *Ocean Biogeochemical Dynamics*. Princeton: Princeton University Press.

Schlitzer, R. (2020). Ocean Data View. https://doi.org/https://odv.awi.de

Semiletov, I., Dudarev, O., Luchin, V., Charkin, A., Shin, K.-H., & Tanaka, N. (2005). The East Siberian Sea as a transition zone between Pacific-derived waters and Arctic shelf waters. *Geophysical Research Letters*, *32*, L10614. https://doi.org/10.1029/2005GL022490

Stedmon, C. A., Amon, R. M. W., Bauch, D., Bracher, A., Gonçalves-Araujo, R., Hoppmann, M., et al. (2021). Insights Into Water Mass Origins in the Central Arctic Ocean From In-Situ Dissolved Organic Matter Fluorescence. *Journal of Geophysical Research: Oceans*, *126*, e2021JC017407. https://doi.org/10.1029/2021JC017407

Steele, M., Morison, J., Ermold, W., Rigor, I., & Ortmeyer, M. (2004). Circulation of summer Pacific halocline water in the Arctic Ocean. *Journal of Geophysical Research*, *109*, C02027. https://doi.org/10.1029/2003JC002009

de Steur, L., Steele, M., Hansen, E., Morison, J., Polyakov, I., Olsen, S. M., et al. (2013). Hydrographic changes in the Lincoln Sea in the Arctic Ocean with focus on an upper ocean freshwater anomaly between 2007 and 2010. *Journal of Geophysical Research: Oceans*, *118*, 4699–4715. https://doi.org/10.1002/jgrc.20341

Tang, C. C. L., Ross, C. K., Yao, T., Petrie, B., DeTracey, B. M., & Dunlap, E. (2004). The circulation, water masses and sea-ice of Baffin Bay. *Progress in Oceanography*, *63*, 183–228. https://doi.org/10.1016/j.pocean.2004.09.005

Tomczak, M, & Large, D. (1989). Optimim Multiparameter Analysis of Mixing in the Thermocline of the Eastern Indian Ocean. *Journal of Geophysical Research: Oceans*, *94*(CII), 15141–16149. https://doi.org/10.1029/JC094iC11p16141

Tomczak, Matthias. (1981). A multi-parameter extension of temperature/salinity diagram techniques for the analysis of non-isopycnal mixing. *Progress in Oceanography*, *10*, 147–171. https://doi.org/10.1016/0079-6611(81)90010-0

Tremblay, J.-É., Gratton, Y., Carmack, E. C., Payne, C. D., & Price, N. M. (2002). Impact of the large-scale Arctic circulation and the North Water Polynya on nutrient inventories in Baffin Bay. *Journal of Geophysical Research*, *107*(C8), 3112. https://doi.org/10.1029/2000JC000595

Tremblay, J.-É., Anderson, L. G., Matrai, P., Coupel, P., Bélanger, S., Michel, C., & Reigstad, M. (2015).

Global and regional drivers of nutrient supply, primary production and CO_2 drawdown in the changing Arctic Ocean. *Progress in Oceanography*, *139*, 171–196. https://doi.org/10.1016/j.pocean.2015.08.009

Vincent, R. F. (2019). A Study of the North Water Polynya Ice Arch using Four Decades of Satellite Data. *Scientific Reports*, *9*, 20278. https://doi.org/10.1038/s41598-019-56780-6

Wang, X., Zhao, J., Lobanov, V. B., Kaplunenko, D., Rudykh, Y. N., He, Y., & Chen, X. (2021). Distribution and Transport of Water Masses in the East Siberian Sea and Their Impacts on the Arctic Halocline. *Journal of Geophysical Research: Oceans*, *126*. https://doi.org/10.1029/2020JC016523

Wanninkhof, R. (2014). Relationship between wind speed and gas exchange over the ocean revisited. *Limnology and Oceanography: Methods*, *12*, 351–362. https://doi.org/https://doi.org/10.4319/lom.2014.12.351

Weiss, R. F. (1974). Carbon dioxide in water and seawater: the solubility of a non-ideal gas. *Marine Chemistry*, *2*(3), 203–215. https://doi.org/10.1016/0304-4203(74)90015-2

Williford, T., Amon, R. M. W., Kaiser, K., Benner, R., Stedmon, C., Bauch, D., et al. (2022). Spatial complexity in dissolved organic matter and trace elements driven by hydrography and freshwater input across the Arctic Ocean during 2015 Arctic GEOTRACES expeditions. *Journal of Geophysical Research: Oceans*, *127*(11), e2022JC018917. https://doi.org/10.1029/2022JC018917

Woosley, R. J., Millero, F. J., & Takahashi, T. (2017). Internal consistency of the inorganic carbon system in the Arctic Ocean. *Limnology and Oceanography: Methods*, *15*, 887–896. https://doi.org/10.1002/lom3.10208

Yamamoto-Kawai, M., McLaughlin, F. A., Carmack, E. C., Nishino, S., & Shimada, K. (2008). Freshwater budget of the Canada Basin, Arctic Ocean, from salinity, $\delta^{18}O$, and nutrients. *Journal of Geophysical Research: Oceans*, *113*, C01007. https://doi.org/10.1029/2006JC003858

Yamamoto-Kawai, Michiyo, McLaughlin, F., & Carmack, E. (2013). Ocean acidification in the three oceans surrounding northern North America. *Journal of Geophysical Research: Oceans*, *118*(11), 6274–6284. https://doi.org/10.1002/2013JC009157

Supplementary Material

Table S4.1: Station names, locations, and sample collection details during the 2014 ArcticNet cruise.

Region	Station	Date	Time (UTC)	Latitude (°N)	Longitude (°W)	Depths sampled	Full DIC/TA profile?	Bottom Depth [m]
Northern Baffin Bay	115	30-Jul	21:23	76.33	71.17	20	✓	674
	111	31-Jul	13:26	76.31	73.22	19	✓	598
	108	31-Jul	22:26	76.27	74.60	18	✓	448
	105	01-Aug	10:25	76.32	75.78	17	✓	333
	101	01-Aug	21:30	76.38	77.40	19	✓	360
Kennedy Channel	Ken 1	03-Aug	18:27	81.37	63.94	19	✓	549
	Ken 2	04-Aug	3:04	81.08	65.83	18	surface + 10 m	387
	Ken 3	04-Aug	7:56	80.80	67.30	18	✓	408
	Ken 4	04-Aug	13:01	80.40	68.81	18	surface + 10 m	369
Kane Basin	Kane 1	04-Aug	18:48	80.00	69.76	16	✓	245
	Kane 2	05-Aug	4:53	79.67	70.74	16	surface + 10 m	236
	Kane 3	05-Aug	9:07	79.35	71.87	15	✓	213
	Kane 5	06-Aug	4:17	79.00	73.20	16	✓	251
Smith Sound	127	06-Aug	10:15	78.30	74.48	18	surface + 10 m	526
Northern Baffin Bay	120	06-Aug	19:02	77.32	75.70	19	✓	560

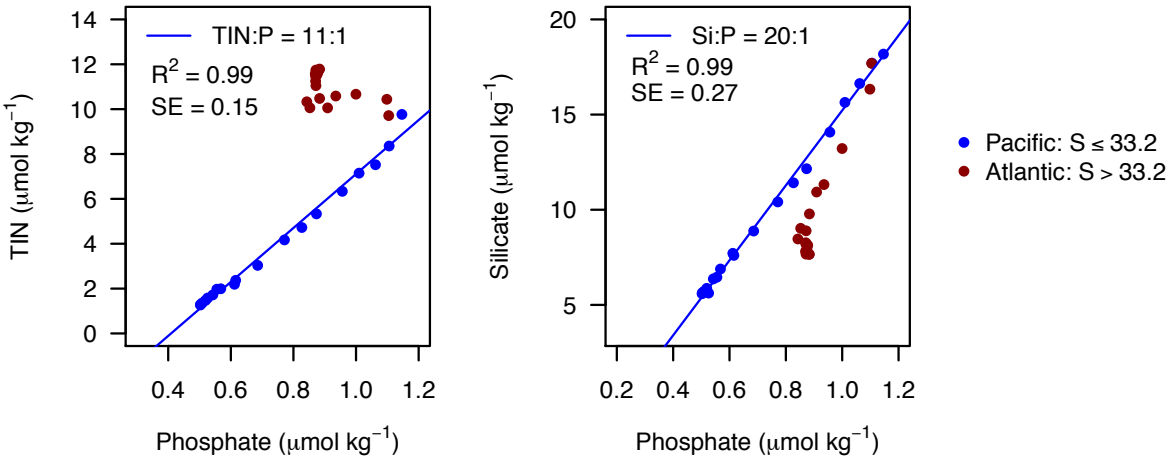

Figure S4.1: Correlations between total inorganic nitrogen (TIN) and phosphate (left panel), and between silicate and phosphate concentrations (right panel) in the upper water column of stations Ken1 and Ken2. The coefficient of determination (R^2) and standard error (SE) are shown for each correlation (each panel). We have separated the Pacific-influenced upper water column from the Atlantic-influenced deeper water column, delineating the boundary between them as the 33.2 isohaline, the defined salinity of the local upper halocline water (UHW).

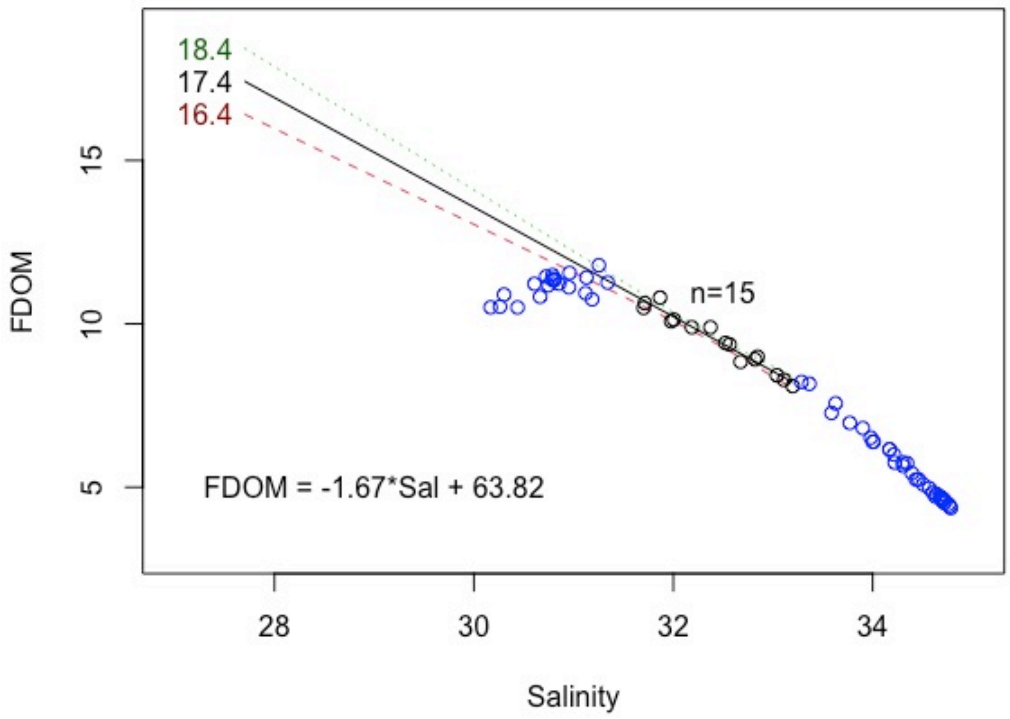

Figure S4.2: Linear regression of FDOM as a function of salinity. Data utilized in fitting the regression are restricted to the salinity range between 31.4 and 33.2 (between the PMW and UHW source water masses) in the northern source region (Kennedy Channel). Upper (green dotted) and lower (red dashed) lines indicate uncertainty bounds corresponding to 95% confidence intervals.

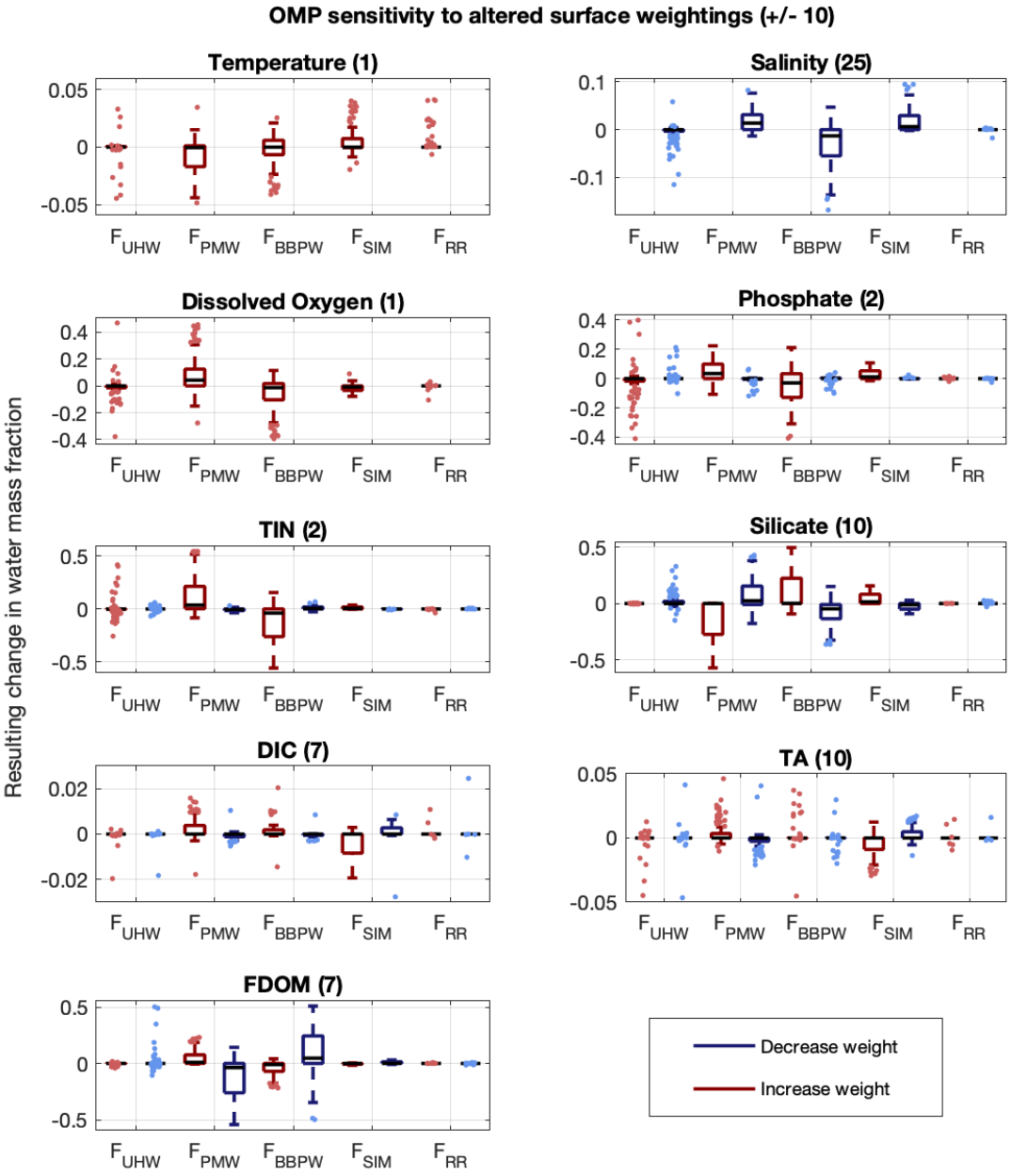

Figure S4.3: Boxplots displaying the sensitivity of eOMP-calculated water mass fractions (y-axes) to increased (red) or decreased (blue) applied weightings to each physico-chemical tracer involved in the model. The original applied weighting of each tracer is stated in the title of each sub-plot, and weightings were increased or decreased by 10, up to a maximum weighting of 25, or a minimum weighting of 1. The sensitivity analysis shown in this figure only applies to the "surface" domain, defined as all data points with a salinity less than 33.2, and therefore changes in water mass fractions are only assessed for water masses present in the surface domain (see x-axis labels; the water masses CBAW and SPMW are excluded from the surface domain). Note the different y-axis scales on each panel. Boxplots are plotted such that the median is represented by a horizontal black line, the box (representing the interquartile range (IQR)) and the whiskers (1.5×IQR) are plotted as dark coloured lines. Outliers (representing values that are 1.5×IQR away from the top or bottom of the box) are plotted as lighter coloured dots.

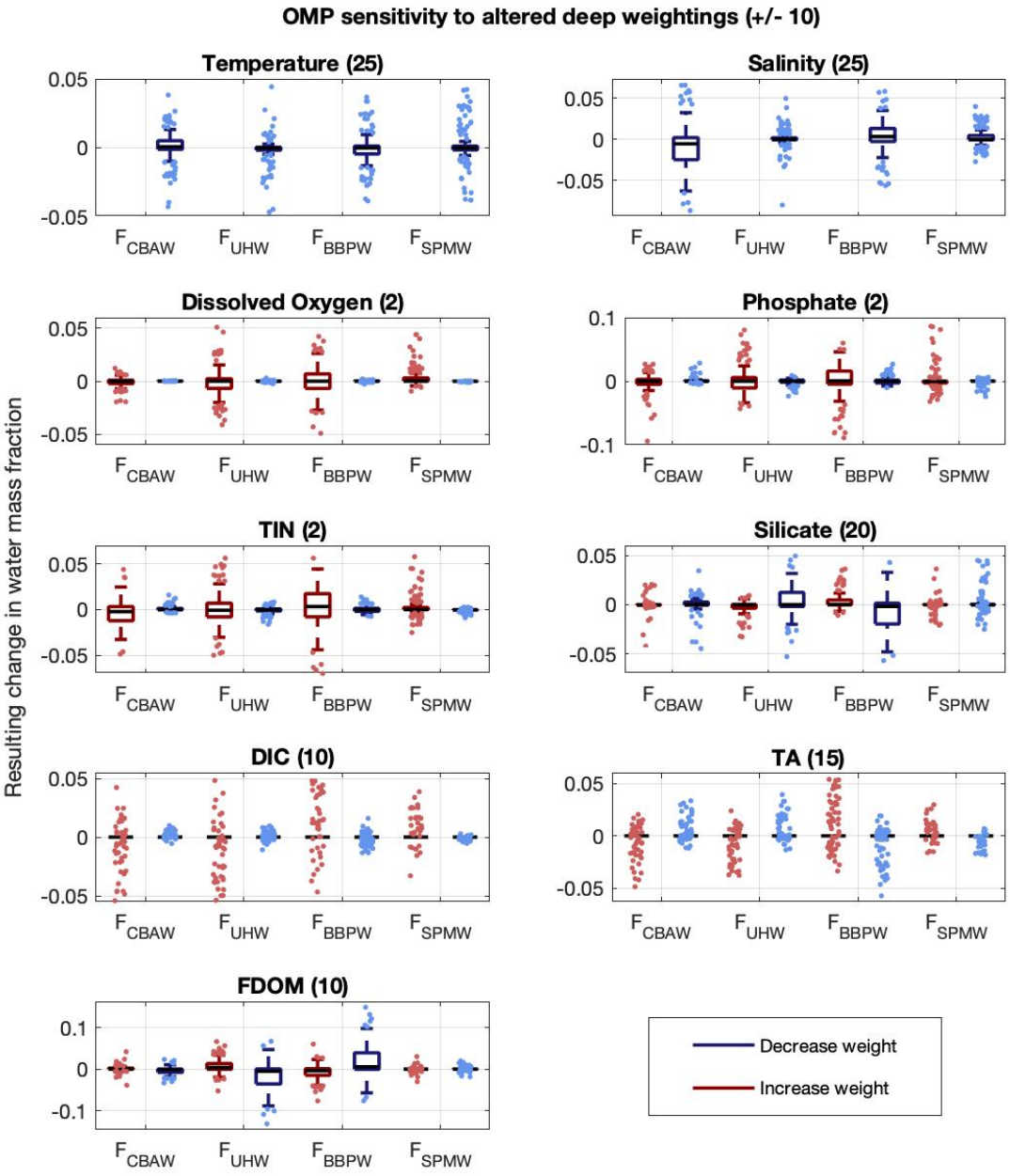

Figure S4.4: Boxplots displaying the sensitivity of eOMP-calculated water mass fractions (y-axes) to increased (red) or decreased (blue) applied weightings to each physico-chemical tracer involved in the model. The original applied weighting of each tracer is stated in the title of each sub-plot, and weightings were increased or decreased by 10, up to a maximum weighting of 25, or a minimum weighting of 1. The sensitivity analysis shown in this figure only applies to the "deep" domain, defined as all data points with a salinity greater than or equal to 33.2, and therefore changes in water mass fractions are only assessed for water masses present in the deep domain (see x-axis labels; excluded from the deep domain are freshwater sources SIM and RR, as well as PMW). Note the different y-axis scales on each panel. Boxplots are plotted such that the median is represented by a horizontal black line, the box (representing the interquartile range (IQR)) and the whiskers (1.5×IQR) are plotted as dark coloured lines. Outliers (representing values that are 1.5×IQR away from the top or bottom of the box) are plotted as lighter coloured dots.

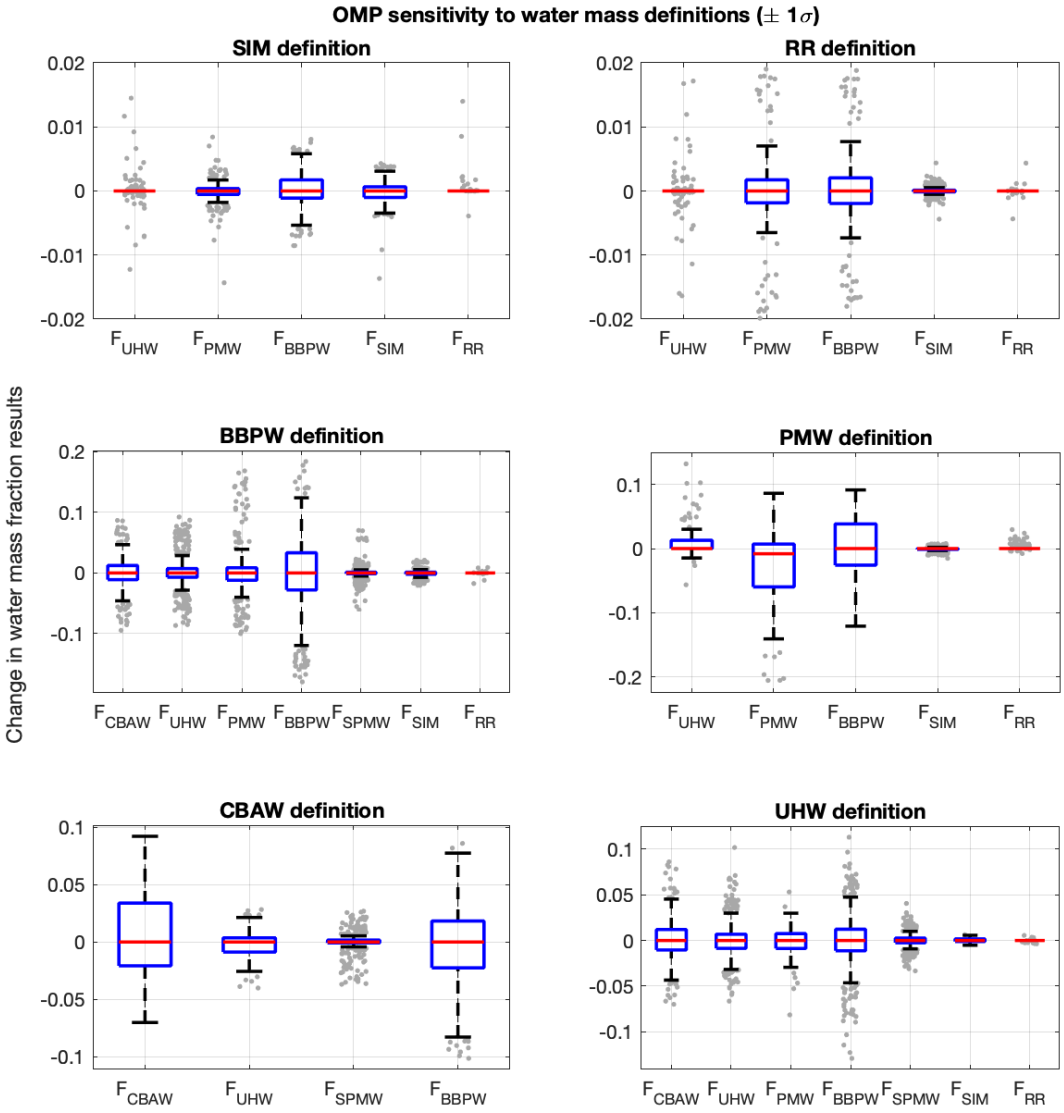

Figure S4.5: Boxplots displaying the sensitivity of eOMP-calculated water mass fractions to uncertainty in source water mass definitions (see Table 4.1 of main paper for water mass definitions and uncertainty). Each panel depicts the effect of altering one water mass definition (indicated by the title) by ± one standard deviation. We do not distinguish between the impact of increasing or decreasing the water mass definition, as the results were nearly symmetric in the majority of cases. When altering the definition of a water mass that is only present in the surface domain (i.e. SIM, RR, PMW), the change will only impact other water mass fractions in the surface domain (and vice versa for CBAW in the deep domain). The only water masses present in both the surface and deep domains are UHW and BBPW, and therefore changes in these water mass definitions may impact all other calculated water mass fractions. The uncertainty of the SPMW definition could not be assessed, since we defined this water mass only at one data point. Boxplots are plotted such that the median is represented by a horizontal red line, the box (representing the interquartile range (IQR)) is shown in blue, and the whiskers (1.5×IQR) are plotted as black dashed lines. Outliers (representing values that are 1.5×IQR away from the top or bottom of the box) are plotted as lighter grey dots.

Text S4.1: *Sensitivity of eOMP results to applied tracer weightings and source water mass definitions*

The above figures S4.3 to S4.5 demonstrate the sensitivity of the eOMP-calculated water mass fractions in this study to (1) altered tracer weightings in the "surface" and "deep" water column domains, and (2) our source water mass definitions. Values plotted in Figures S4.3 to S4.5 represent all samples that were input into the eOMP model. In this study we applied different weightings to tracers in the surface ($S < 33.2$) and deep ($S \geq 33.2$) domains of the eOMP model, and only take into account certain source water masses in each domain. To assess the sensitivity to altered tracer weightings we separately increased then decreased the chosen weightings for each tracer by 10, up to a maximum weighting of 25, or a minimum weighting of 1. Freshwater sources such as sea-ice melt (SIM) and river runoff (RR) were excluded from the deep domain, as well as polar mode water (PMW) since it is a near-surface water mass exiting the Arctic Ocean and is relatively fresh. In the surface domain we excluded Canada Basin Atlantic water (CBAW) and Subpolar Mode water (SPMW) as these water masses are very saline and dense and reside in the deep water column only.

Figures S4.3 and S4.4 display the sensitivity of eOMP-calculated water mass fractions to altered tracer weightings in the surface and deep domains, respectively. Overall, we find the results to be quite stable with most changes in water mass fractions under 0.1 (or 10%), and especially stable within the deep domain. However, some larger sensitivities are found within the surface domain associated with calculated fractions of Polar Mode water (PMW) and Baffin Bay Polar water (BBPW). Altering the weightings of dissolved oxygen, phosphate, total inorganic nitrogen (TIN), silicate, and CDOM results in large changes in fractions of PMW and BBPW (up to 0.5). Some of these tracers display high sensitivities because they are particularly useful in distinguishing PMW and BBPW, which is the case for CDOM as it displays very different average concentrations in these two water masses. However, other tracers such as silicate and phosphate have relatively similar concentrations within PMW and BBPW and may not be particularly useful in discriminating the two water masses. This sensitivity analysis shows that calculated fractions of PMW and BBPW within surface waters are associated with the largest uncertainties.

Figure S4.5 shows the sensitivity of eOMP-calculated water mass fractions to uncertainty in our source water mass definitions. Here we find that calculated fractions of BBPW are the most sensitive to changes in any water mass definition. Changes in calculated BBPW fractions are generally below 0.1 (or 10%), except in the case where the BBPW definition is altered, which results in fractional changes just over 0.1. We also find that altering the BBPW definition causes relatively high changes in all other calculated water mass fractions (but still below 0.1). This makes sense as our definition of BBPW was the most uncertain of our source water masses. The sampling stations used to define the properties of

this water mass displayed a high amount of variability, as they were located across a mixing front in the North Water polynya region. Overall, changes due to uncertainty in water mass definitions remained under 0.1, with the exception of BBPW fractions that showed a maximum change of 0.19 (outlier value).

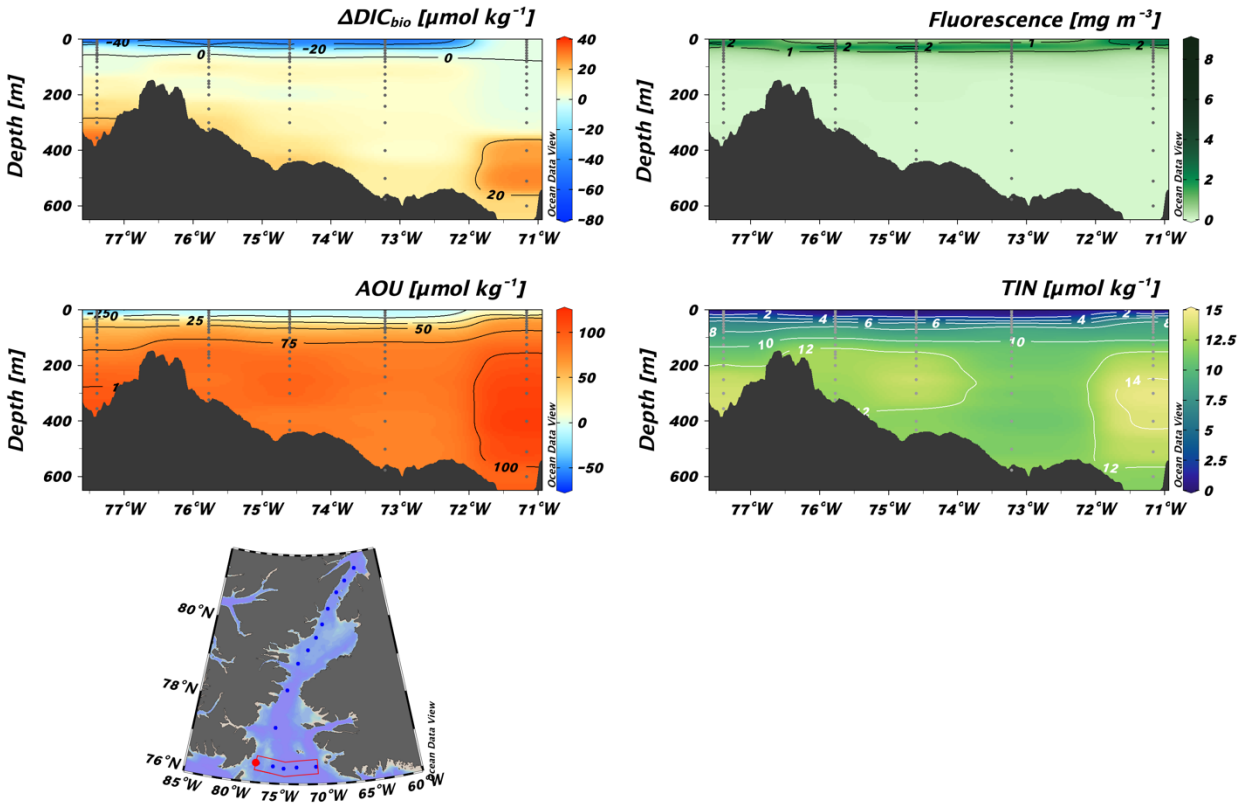

Figure S4.6: Section plots of the biologically driven changes in DIC (ΔDIC$_{bio}$), chlorophyll-a fluorescence, Apparent Oxygen Utilization (AOU), and total inorganic nitrogen (TIN) along the North Water (NOW) polynya transect (transect outline delineated in red in inset map). Figure was created using Ocean Data View software (Schlitzer, 2020).

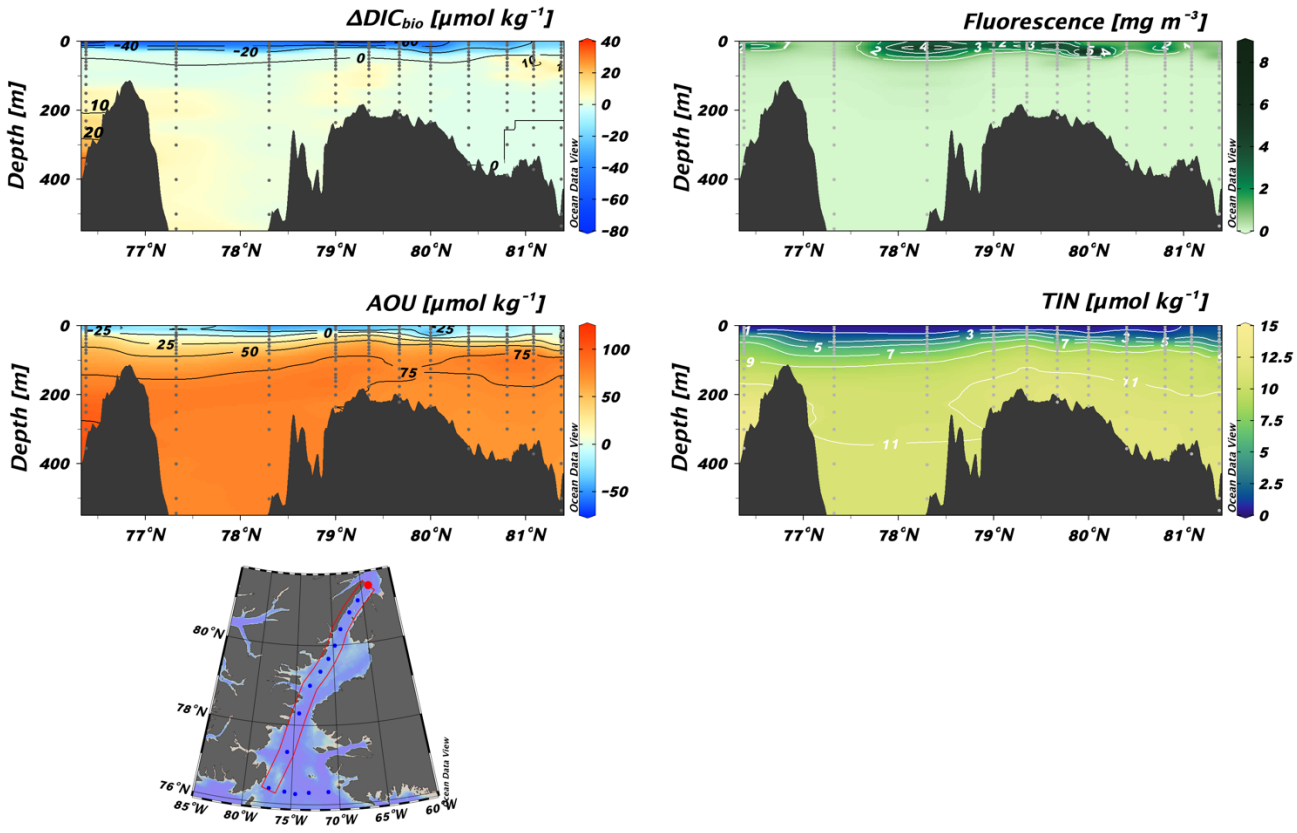

Figure S4.7: Full vertical section plots of ΔDIC_{bio}, chlorophyll-a fluorescence, Apparent Oxygen Utilization (AOU), and total inorganic nitrogen (TIN) along the Nares Strait transect. Figure was created using Ocean Data View software (Schlitzer, 2020).

Text S4.2: *Calculation of ΔDIC_{gas}*

To calculate an integrated air-sea CO_2 flux (ΔDIC_{gas}) into the surface mixed layer at each sampling station in the Nares Strait transect, we integrated a timeseries of instantaneous air-sea CO_2 flux measurements along the ship track between the ice arch (in the north) and each sampling station (southwards of the ice arch). A separate timeseries of surface pCO_2 measurements (and NARR wind speeds) was created for each station, going back in time from the time of sampling, to the time the water parcel would have emerged from under the ice-arch in northern Kennedy Channel assuming a constant surface current speed of 15 cm s^{-1}. Each surface pCO_2 measurement was assigned an "age" in days since that water parcel would have emerged from under the ice-arch, based on its distance in kilometers along the Nares Strait transect from the ice-arch. The "age" of each water parcel was also used to estimate a historical date and time associated with each underway pCO_2 measurement, and to select NARR wind speeds that most closely matched the location, date and time of each pCO_2 measurement in the timeseries.

We then performed a trapezoidal integration of the air-sea CO_2 fluxes (in units of μmol m^{-2} day^{-1}) by their "age" (in days) to calculate an integrated flux (with units of μmol m^{-2}). To convert the integrated flux (μmol m^{-2}) into a concentration change (μmol kg^{-1}) within the surface mixed layer at each station, we divided the integrated flux by the mixed layer depth (m) and by the average density (kg m^{-3}) of the surface mixed layer for each station.

Chapter 5 Unraveling the biogeochemical drivers of aragonite saturation states in Baffin Bay: Insights from the west Greenland continental shelf

This chapter has been published in *Journal of Geophysical Research: Oceans*

Burgers, T. M., Azetsu-Scott, K., Myers, P. G., Else, B. G. T., Miller, L. A., Rysgaard, S., Chan, W., Tremblay, J.-É., Papakyriakou, T. (2024) Unraveling the biogeochemical drivers of aragonite saturation state in Baffin Bay: Insights from the west Greenland continental shelf. *Journal of Geophysical Research: Oceans*, *129*, e2024JC021122. https://doi.org/10.1029/2024JC021122

Please see Appendix A for the contributions of each collaborating author to this submitted manuscript.

Abstract

This study investigates the biogeochemical drivers of aragonite saturation state (Ω_{Ar}) in Baffin Bay, with a focus on the relatively undersampled west Greenland shelf. Our findings reveal two main depth-dependant processes controlling the spatial distribution of Ω_{Ar} in Baffin Bay; within the upper 200 m, lower Ω_{Ar} coincides with increasing fractions of Arctic-outflow waters, while below 200 m organic matter respiration decreases Ω_{Ar}. A temporal analysis comparing historical measurements from 1997 and 2004 with our 2019 dataset reveals a significant decrease in the Ω_{Ar} of Arctic-outflow waters, coinciding with reduced total alkalinity (TA). However, no discernable anthropogenic ocean acidification signal is identified. Significant Arctic water fractions (20 – 40%) are found to be present on the west Greenland shelf, associated with reduced TA and Ω_{Ar}. A numerical modeling simulation incorporating a passive tracer demonstrates that periodic changes in wind direction lead to a switch from onshore to offshore Ekman transport along the Baffin Island current, transporting Arctic waters towards the west Greenland shelf. This challenges the conventional understanding of Baffin Bay's circulation and underscores the need for further research on the region's physical oceanography. Based on salinity-TA relationships, surface waters on the west Greenland shelf have a significantly lower meteoric TA end-member compared to waters of the Baffin Island Current in western Baffin Bay. The low eastern TA freshwater end-member agrees well with recent glacial meltwater TA measurements, suggesting that glacial meltwater is the main freshwater source to surface waters on the west Greenland shelf.

5.1 Introduction

With ongoing increases in atmospheric carbon dioxide (CO_2) concentrations, the surface ocean continues to absorb more CO_2 through air-sea gas exchange as it attempts to achieve equilibrium with the atmosphere. Current estimates suggest that the global surface ocean has taken up roughly one quarter of all anthropogenic CO_2 emissions over the past decade (Friedlingstein et al., 2023). Although this process is beneficial in reducing the magnitude of the greenhouse effect in the atmosphere, it also results in major changes to ocean chemistry. Specifically, increases in dissolved CO_2 concentrations cause decreases in seawater pH (leading to the process name "ocean acidification"), and simultaneous increases in the solubility of calcium carbonate ($CaCO_3$) minerals, which many marine calcifying species utilize to form their shells and skeletons (AMAP, 2013; Doney et al., 2009).

The saturation state (Ω) of $CaCO_3$ minerals is a measure of the mineral's tendency to dissolve under certain chemical conditions, and is defined as:

$$\Omega = [Ca^{2+}][CO_3^{2-}]/K_{sp}^{*} \quad (5.1)$$

where $[Ca^{2+}]$ and $[CO_3^{2-}]$ are the dissolved concentrations of calcium and carbonate ions in seawater, respectively, and K_{sp}^{*} is the conditional solubility product of $CaCO_3$ in seawater (dependent on seawater temperature, salinity, and pressure). The two most common polymorphs of $CaCO_3$ that are produced by marine calcifying organisms are calcite and aragonite, with their saturation states denoted as Ω_{Ca} and Ω_{Ar}, respectively. Aragonite is more soluble (i.e., has a higher solubility product) than calcite (Mucci, 1983), meaning that aragonite will dissolve under higher pH conditions relative to calcite. If $\Omega > 1$ then the seawater is considered "supersaturated", and the $CaCO_3$ mineral is stable, but if $\Omega < 1$ the seawater is "undersaturated" and $CaCO_3$ minerals will tend to dissolve.

The Arctic Ocean has been found to be especially vulnerable to ocean acidification, because of high freshwater inputs, cold seawater temperatures, and declining sea-ice cover (AMAP, 2018). Freshwater inputs from river runoff, sea-ice melt, and glacial meltwater are all characterized by low total alkalinity (TA) compared to seawater, and therefore reduce the seawater's buffering capacity against ocean acidification, leading to greater decreases in pH and Ω for every unit of added CO_2. Even Pacific-origin seawater, which enters the Arctic Ocean via the Bering Strait, has a lower salinity than Atlantic-origin seawater and therefore also has relatively low TA. Pacific waters also contain more dissolved inorganic carbon (DIC) due to the accumulation of respiration products along the global thermohaline circulation route. Hence, Pacific waters are predisposed towards low pH and Ω values due to their

relatively low TA:DIC ratio (Azetsu-Scott et al., 2010; Shadwick et al., 2011; Yamamoto-Kawai et al., 2013).

Baffin Bay (*Sannirutiup Imanga* in Inuktitut) is a seasonally ice-covered sea in the eastern Canadian Arctic, with a complex interplay of Atlantic and Arctic-outflow waters. Much like the greater Arctic Ocean, Baffin Bay is particularly susceptible to ocean acidification (AMAP, 2018; Azetsu-Scott et al., 2010). Arctic waters that enter Baffin Bay from the north are predominantly Pacific-source waters, which are already prone to low pH and Ω. On top of this, additional freshwater inputs may be added within Baffin Bay from melting sea ice or glacial meltwater, further decreasing TA. In fact, Bamber et al. (2018) found that Baffin Bay currently receives the largest freshwater flux anomalies (compared to the 1960-1990 mean) from land ice compared to other seas surrounding Greenland, and continues to show the steepest rates of acceleration in these fluxes. Baffin Bay is also a very biologically productive marine environment (Burgers et al., 2020; Klein et al., 2002; Krawczyk et al., 2021), contributing to organic matter export and deep respiration by heterotrophic organisms, releasing dissolved inorganic carbon (DIC) while decreasing TA, leading to decreases in Ω of the deep and bottom waters.

In light of these vulnerabilities to ocean acidification, Azetsu-Scott et al. (2010) provided the first baseline measurements of Ω_{Ca} and Ω_{Ar} throughout the outflow shelves of the eastern Canadian Arctic (including Baffin Bay) between 2003 and 2005. Their measurements showed a west-to-east deepening of the aragonite saturation horizon (Ω_{Ar} = 1) across Baffin Bay, from approximately 200 m depth in the west to 500 m in the east. This gradient was found to be due to the presence of Arctic-outflow waters in the upper water column of western Baffin Bay, with its greater Pacific water influence contributing to lower Ω_{Ar} values (Azetsu-Scott et al., 2010; Yamamoto-Kawai et al., 2013).

With rising air temperatures (Rantanen et al., 2022), declining sea-ice thickness (Landy et al., 2017), a longer open-water season (Ballinger et al., 2022), and increasing freshwater inputs both from glacial discharge (Bamber et al., 2018; Mouginot et al., 2019) and increasingly fresh surface waters exported from the Arctic Ocean (Carmack et al., 2016; Haine et al., 2015), conditions in Baffin Bay are changing rapidly. Such drastic changes will have consequences for the marine ecosystem in the bay, and for biogeochemical processes such as air-sea CO_2 exchange, primary production, and ongoing ocean acidification. It is therefore important to keep monitoring the biogeochemistry of the region, especially in light of its important ecological areas (such as the North Water polynya) and economic interests (e.g., the west Greenland shrimp fishery; AMAP, 2018). In past oceanographic studies of Baffin Bay, there have been few measurements over the west Greenland shelf (the eastern portion of Baffin Bay). Often the only location to have been sampled fully from west to east is Davis Strait in southern

Baffin Bay. The coastline of west Greenland northwards of Davis Strait houses many large and fast-flowing tidewater glaciers, and this region has been shown to display greater glacial ice discharge rates than other coastal regions of Greenland (Mouginot et al., 2019). It is therefore very important to investigate whether such large glacial ice and/or freshwater fluxes may be impacting the marine carbonate chemistry of the west Greenland shelf.

In this investigation we present recent (July and August, 2019) measurements of the marine carbonate system, along with stable oxygen isotope ratios ($\delta^{18}O$) and nutrient concentrations across Baffin Bay, including many sampling locations along the west Greenland shelf between 67°N and 76°N (Figure 5.1). The objectives of this study have been to: (1) investigate the importance of biogeochemical processes on the west Greenland shelf in controlling the distribution of Ω_{Ar} within Baffin Bay; and (2) compare our 2019 measurements with those presented in Azetsu-Scott et al. (2010) from 1997 and 2004 to identify any temporal trends in Ω_{Ar}.

5.2 Oceanographic Setting

The distribution of water masses in Baffin Bay is governed by an overall cyclonic circulation, which consists of two major currents (Figure 5.1a): the Baffin Island Current (BIC) and the West Greenland Current (WGC). The BIC transports relatively cold and fresh Arctic outflow waters from the channels of the Canadian Arctic Archipelago (CAA) southwards along the Baffin Island continental slope, and into the Labrador Sea. The northward flowing WGC advects relatively warm and saline waters from the North Atlantic into eastern Baffin Bay along the west Greenland continental shelf and slope (Curry et al., 2014; Tang et al., 2004; see Figure 5.1b). These two current systems create different water mass assemblies in eastern and western Baffin Bay, and also affect the timing of sea ice formation and retreat across Baffin Bay. Due to the relatively warm surface water temperatures of the WGC, sea ice retreats much earlier (April) in eastern Baffin Bay than to the west (July). All of Baffin Bay is generally ice free from July to October (Bi et al., 2019). When the data for this study were collected (July and August, 2019), all of Baffin Bay was essentially ice free (Figure S5.1).

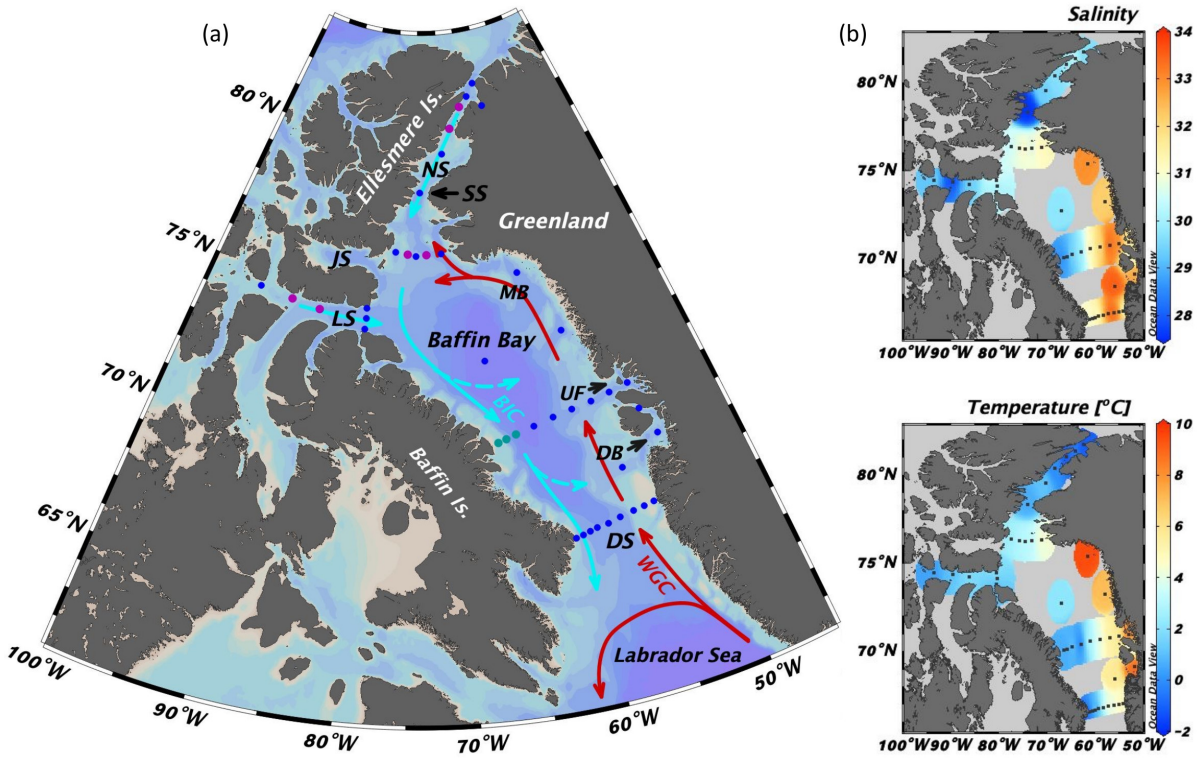

Figure 5.1: (a) Map of the study area, with water column sampling stations indicated as coloured dots. At stations plotted as blue dots samples were collected for inorganic carbon throughout the water column at standard sampling depths. At purple station locations inorganic carbon samples were only collected at the surface and 10 m depths. Alkalinity samples from the green stations were excluded from our discussion, because of an analytical malfunction (see section 5.3.1). Abbreviations: Baffin Island Current (BIC), West Greenland Current (WGC), Nares Strait (NS), Smith Sound (SS), Jones Sound (JS), Lancaster Sound (LS), Davis Strait (DS), Uummannaq Fjord (UF), Disko Bay (DB), and Melville Bay (MB). (b) Surface distributions of salinity (on the practical scale, top) and temperature in Baffin Bay.

In the water column of eastern Baffin Bay, we identify two main water masses (Figure 5.2): (1) Baffin Bay Polar Water (BBPW) with $T < -1°C$ and $33.4 < S < 33.65$, located between depths of 40 – 100 m, and (2) Subpolar Mode Water (SPMW) displaying $T > 0°C$, $S > 34.3$, and located at depths between 200 and 500 m (Rysgaard et al., 2020). BBPW is a winter mode water (i.e., formed by winter convection) that is characterized by temperatures near the freezing point, and has been commonly observed along the west Greenland shelf north of Disko Bay (Bâcle et al., 2002; Burgers et al., 2017; Rysgaard et al., 2020; Tang et al., 2004). Sporadically, BBPW has also been observed as far south as 64 °N along the west Greenland shelf (Mortensen et al., 2022). SPMW is formed as a winter mode water in the subpolar North Atlantic before flowing around southern Greenland in the Irminger Current, and continuing northwards into Baffin Bay with the WGC (Rysgaard et al., 2020). In previous literature SPMW has been referred to as either Atlantic water, Irminger water, or West Greenland Irminger water (Azetsu-Scott et al., 2012; Lin et al., 2018; Myers et al., 2009). As SPMW transits cyclonically around Baffin Bay it becomes slightly cooler and fresher as it mixes with Arctic outflow waters from the CAA.

In western Baffin Bay, BBPW and SPMW are still present but are located at greater depths in the water column and are overlain by Arctic Ocean outflow waters (ARC, Figure 5.2). Along the Baffin Island continental slope BBPW is generally found near 150 m depth, and SPMW between depths of 300 and 700 m. Arctic outflow waters are present throughout the upper 150 m in western Baffin Bay, displaying T < 0°C and S < 33.3. These Arctic waters represent a mixture composed of primarily Pacific-origin halocline waters (31 > S > 33.1), with contributions from sea-ice meltwater and meteoric waters from pan-Arctic rivers, glacial melt, and net precipitation (Carmack et al., 2016). Due to shallow sill depths within the channels of the CAA, Arctic waters entering Baffin Bay are primarily of Pacific-origin, as deeper Atlantic-origin water masses are held back by the shallow sills within the channels of the CAA. Only Nares Strait has a sill deep enough (approximately 220 m in Kane Basin; Melling et al., 2008) to allow the continuation of some modified-Atlantic waters from the Arctic Ocean to flow southwards into northern Baffin Bay (Azetsu-Scott et al., 2010).

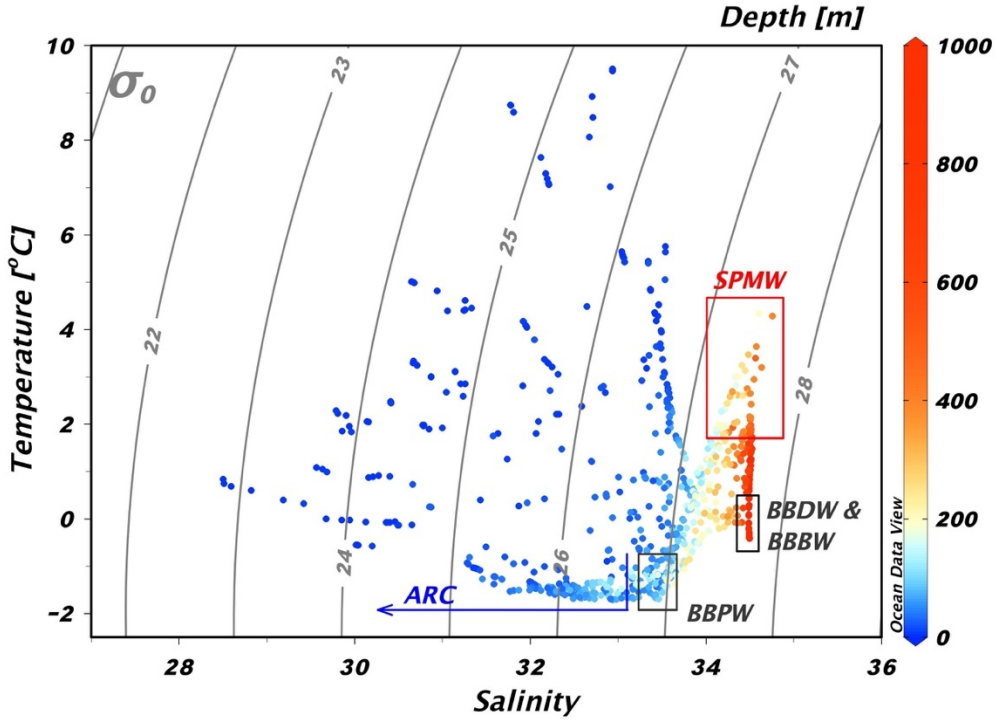

Figure 5.2: Temperature-salinity (TS) plot for the Baffin Bay region during July and August, 2019. Thin grey lines represent isopycnals. For station locations see Figure 5.1. Major water masses are identified by rectangles on the TS-diagram. Abbreviations: Arctic water (ARC), Baffin Bay Polar Water (BBPW), Subpolar Mode Water (SPMW), Baffin Bay Deep Water (BBDW), Baffin Bay Bottom Water (BBBW).

The deep basin in central Baffin Bay reaches depths of approximately 2400 m, and here the water at depth is composed of Baffin Bay Deep water (BBDW) and Baffin Bay Bottom water (BBBW). Salinity is quite stable throughout these water masses, at 34.5. BBDW has a temperature of 0 °C and is found at

depths between 1200 and 1800 m (Curry et al., 2011), whereas BBBW has a temperature of -0.4 °C, and is found at depths greater than 1800 m. A recent study by Zeidan et al. (2022) estimated the residence time of BBDW to be between 360 to 690 years based on radiocarbon ($\Delta^{14}C$) values, indicating that carbon is likely stored for centuries in deep Baffin Bay.

5.3 Methods

5.3.1 Sampling and Sample Analysis

Sampling for this study was conducted between 5 July and 15 August during Leg 2 of the 2019 ArcticNet scientific cruise aboard the CCGS *Amundsen*. At each sampling station seawater was collected with 12L Niskin-type bottles mounted on a rosette system equipped with a SeaBird 911plus CTD, and a dissolved oxygen sensor (SeaBird SBE-43). Discrete water samples were collected for the determination of salinity, stable oxygen isotope ratios ($\delta^{18}O$), nutrients (including nitrate + nitrite, ammonium, phosphate and silicate), dissolved inorganic carbon (DIC), and total alkalinity (TA). Discrete samples were collected at standard depths of: 2, 5, 10, 20, 30, 50, 70, 100, 150, 200, 250, 300, 400, 600, 800, 1000 and 1200 m. Only two stations in central Baffin Bay had bottom depths deeper than 1200 m, and were sampled at 100 m intervals between depths of 1400 and 2300 m. At a subset of stations DIC and TA samples were only collected at the surface and 10 m depth, these stations are indicated in Figure 5.1a by purple dots. Bottle salinity measurements were made onboard using a Guideline Autosal model 8400 salinometer provided by Amundsen Science, and reported using the practical salinity scale (PSU).

Nutrient samples were collected directly from the rosette bottles with syringes, filtered through a Swinnex-mounted Whatman GF/F, and captured in acid-cleaned polyethylene tubes. Concentrations of nitrate + nitrite, ammonium, phosphate, and silicate were measured colorimetrically using a Bran and Luebbe AutoAnalyzer III within a few hours of collection. Working standards were prepared at each station and checked against certified reference material (KANSO CRM) inserted in the sample runs. Analytical detection limits were 0.03 μM for nitrate (obtained by the difference between nitrite and nitrate + nitrite), 0.02 μM for nitrite, 0.05 μM for phosphate, and 0.1 μM for silicate. Ammonium concentrations were determined using the method of Holmes et al. (1999) with a detection limit of 0.02 μM. The precision of triplicate nutrient measurements under the range of concentrations observed was the same as, or better than, the detection limit for each nutrient.

Samples for $\delta^{18}O$ were analyzed at the University of Calgary using an integrated off-axis cavity absorption spectrometer (Los Gatos Research, LGR, Triple Liquid Water Isotope Analyzer, model 912-0032). The LGR analyzer was standardized every 4 samples with in-house standards that were calibrated

against VSMOW2 (Vienna Standard Mean Ocean Water 2) and SLAP2 (Standard Light Antarctic Precipitation 2) standards. For each sample, 8 replicates were sequentially measured through an auto-injector. The first 4 measurements were discarded to eliminate memory effects, and the average of the last 4 measurements was used for isotope ratio calculations. The analytical precision (2σ) of the $\delta^{18}O$ measurements was better than ± 0.2‰.

Samples for DIC and TA determination were collected and analyzed following standard protocols (Dickson et al., 2007), with duplicates collected from at least one bottle on each rosette cast. Samples were collected in 250 or 500-mL borosilicate glass bottles, preserved with 100 μL of a saturated $HgCl_2$ solution, capped with ground glass stoppers greased with Apiezon M, and sealed with clips and elastic closures or with electrical tape. Samples were stored in the dark at 4 °C until analysis at either the Bedford Institute of Oceanography (BIO) in Dartmouth, Nova Scotia or the Institute for Ocean Sciences (IOS) in Sidney, British Columbia. Both labs analyzed samples for DIC coulometrically, followed by TA determination from the same bottle using potentiometric titrations. At BIO samples were analyzed for DIC using a modified SOMMA (Johnson et al., 1993), whereas IOS measured DIC using a VINDTA 3D (MARIANDA). At both labs TA was analyzed using custom-built open-cell titration systems (see Punshon et al. (2019) for further specifics of sample analysis at BIO). Measurements from both labs were calibrated against certified reference materials provided by Andrew Dickson (Scripps Institute of Oceanography). Analysis of duplicate DIC and TA samples at IOS indicated precisions of ± 1 μmol kg^{-1} and ± 2 μmol kg^{-1}, respectively. Similarly, the DIC and TA samples analyzed at BIO had precisions of ± 1 μmol kg^{-1} and ± 3 μmol kg^{-1}, respectively. A subset of the TA measurements were affected by a clogged tube in the titration system, causing insufficient sample to be dispensed into the titration cup. These TA values have been flagged as bad, and excluded from further data analysis. The station locations without TA values due to this issue are shown in green in Figure 5.1a.

We computed the aragonite saturation state (Ω_{Ar}) from the DIC and TA measurements using the R package Seacarb (Gattuso et al., 2021) and employing the equilibrium constants (K_1 and K_2) of Sulpis et al. (2020), which are valid for seawater temperatures down to -1.7 °C, and are therefore better suited to cold high-latitude regions. Uncertainties in calculated Ω_{Ar} values due to measurement uncertainties in DIC, TA, and phosphate and silicate concentrations were assessed using the error propagation routine of Orr et al. (2018). To assess the variability in Ω_{Ar} due to the choice of equilibrium constants, we also calculated Ω_{Ar} using the constants of Lueker et al. (2000), which are generally recommended by best practices for oceanic carbonate system measurements (Dickson et al., 2007), but were found by Sulpis et al. (2020) to underestimate pK_1 and pK_2 in seawater temperatures below 8 °C. It is important to note

that differences in Ω_{Ar} values due to the choice of equilibrium constants are larger than the errors caused by the propagation of measurement precisions (Table 5.1), and based on the results of an unpaired t-test the difference is statistically significant ($p < 0.01$).

Table 5.6: Average uncertainties in calculated Ω_{Ar} values due to measurement error in temperature, salinity, phosphate (P), silicate (Si), dissolved inorganic carbon (DIC) and total alkalinity (TA). Also listed is the cumulative uncertainty due to measurement errors in the formerly listed parameters, and the average difference in calculated Ω_{Ar} due to the choice of equilibrium constants between Lueker et al. (2000) and Sulpis et al. (2020), denoted as L00 and S20, respectively. All uncertainty estimates in Ω_{Ar} were calculated using the error propagation routine of Orr et al. (2018).

	Temp (°C) (x 10^{-5})	Salinity (x 10^{-5})	P (x 10^{-5})	Si (x 10^{-6})	DIC	TA	Cumulative measurement precision error	Difference in equilibrium constants (L00 – S20)
$\Delta\Omega_{Ar}$	7.9 ± 1.6	8.8 ± 5.1	40 ± 7.5	13 ± 6.5	0.0073 ± 0.0013	0.018 ± 0.0049	0.019 ± 0.0039	0.025 ± 0.0079

5.3.2 Historical datasets

Historical datasets of the marine carbonate system in Baffin Bay were downloaded from GLODAPv2.2022 (Lauvset et al., 2022). Measurements of DIC and TA from cruises in 1997, 2003 and 2004 were accessed (expocodes 18SN19970803, 32H120030721, and 316N20040922, respectively). The dataset from 1997 was collected in August from the CCGS *Louis S. St.Laurent*, the 2003 dataset was collected in July and August from the R/V *Healy*, and the 2004 dataset was collected in September from R/V *Knorr*. Herein, we re-calculated Ω_{Ar} values from these historical datasets using the equilibrium constants of Sulpis et al. (2020) in order to compare them with Ω_{Ar} values from the 2019 cruise.

5.3.3 Freshwater Partitioning

We distinguish fractions of sea-ice meltwater (F_{SIM}), meteoric water (F_{MW}), Arctic water (F_{ARC}) and Atlantic water (F_{ATL}) using measurements of salinity, $\delta^{18}O$, dissolved inorganic nitrogen (DIN = NO_3^- + NO_2^- + NH_4^+), and phosphate (P). Our methodology closely follows that of Azetsu-Scott et al. (2012), but employs DIN:P regression relationships unique to our dataset. In Baffin Bay there are two separate types of seawater that interact: Arctic and Atlantic waters, which enter the Bay from the north through channels of the CAA, and from the south through Davis Strait, respectively. Arctic waters are mainly composed of modified Pacific waters, that were impacted by denitrification in the oxygen minimum zones of the North Pacific and in the benthos of the shallow Bering and Chukchi shelves (Cooper et al., 1997; Jones et al., 1998; Yamamoto-Kawai et al., 2008). Therefore, Arctic waters display a relatively low DIN:P ratio compared to Atlantic waters. In this study, we first determine the ratio of Arctic and Atlantic seawater in

a particular sample using the unique DIN:P relationships for each seawater type. The resulting ratio is then used to calculate a seawater end-member value for each sample, using known Arctic and Atlantic water end-member properties (Table 5.2). Finally, fractions of sea-ice meltwater, meteoric water, and seawater are determined for each sample using salinity and $\delta^{18}O$ measurements in a three end-member mixing model.

Table 5.7: End-member values and their uncertainties used in freshwater decomposition.

	Atlantic Water[a]	Arctic Water[b]	Sea-Ice Meltwater[a]	Meteoric Water[a,c]
Salinity	34.8 ± 0.1	32 ± 1	4 ± 1	0
$\delta^{18}O$ (‰)	0.19 ± 0.06	-2.0 ± 0.5	0.63 ± 0.14	-20 ± 2

[a]Azetsu-Scott et al. (2012)
[b]Calculated from the observations in this study (averages of samples with S ≤ 33.3 and T < 0°C)
[c]Fairbanks (1982)

Figure 5.3 shows the DIN:P relationships defined for Arctic and Atlantic waters in Baffin Bay using this dataset from summer 2019. The Atlantic water line was determined from samples with S > 33.3, T > 0°C, and depths less than 1000 m to eliminate BBDW and BBBW where benthic denitrification is known to occur (Lehmann et al., 2019). It is worth noting that our definition of Atlantic water within Baffin Bay represents a modified (relatively fresh) version of pure Atlantic water, with modified nutrient ratios. Therefore, our calculated water mass fractions will differ from other studies which have applied the nutrient relationship of Jones et al. (1998), defined using observations from the St. Anna Trough. The Arctic water line was determined from samples with S ≤ 33.3 and T < 0°C, representing mainly Pacific halocline waters and any additional freshwater inputs (e.g., sea-ice melt, river runoff, glacial melt) that are exiting the Arctic Ocean. The ratio of Arctic and Atlantic seawater in a particular sample is determined by the relative distance of the measured DIN:P ratio between the two regression lines:

$$P_{ARC} = (DIN_{obs} + 7.97)/14.23 \quad (5.1)$$

$$P_{ATL} = (DIN_{obs} + 1.76)/14.66 \quad (5.2)$$

$$f_{ARC} = (P_{ATL} - P_{obs})/(P_{ATL} - P_{ARC}) \quad (5.3)$$

$$f_{ATL} = 1 - f_{ARC} \quad (5.4)$$

where P_{ARC} and P_{ATL} represent the phosphate concentrations expected, based on the observed concentration of DIN, if the sample falls along the Arctic or Atlantic water line, respectively (equations 5.1 and 5.2). If the observed phosphate concentration (P_{obs}) matches that predicted by the Arctic water line (P_{ARC}), it will yield an Arctic water fraction of 1 (f_{ARC} = 1). If P_{obs} falls somewhere between the Arctic and

Atlantic water lines, it will yield a lower f_{ARC} and higher f_{ATL} (equations 5.3 and 5.4). If P_{obs} falls to the left of the Atlantic line in Figure 5.3, creating a negative f_{ARC} value, we assume there is no Arctic water and f_{ATL}=1. Similarly, if P_{obs} falls to the right of the Arctic line, we assume there is no Atlantic water and f_{ARC} = 1.

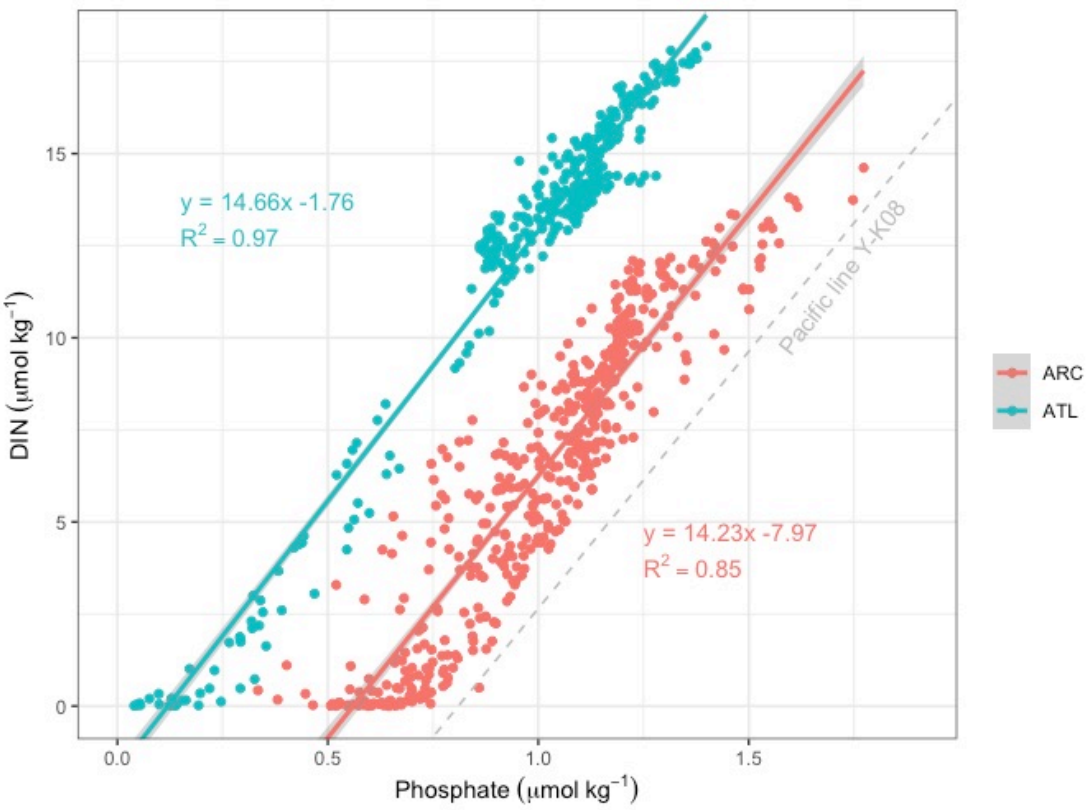

Figure 5.3: Linear regression relationships of dissolved inorganic nitrogen (DIN) versus phosphate for Atlantic waters and Arctic waters in Baffin Bay. The Atlantic water line (blue line) was determined from samples with S > 33.3 and T > 0 °C and depths < 1000m (blue dots). The Arctic water line (red line) was determined from samples with S ≤ 33.3 and T < 0 °C (red dots). The 95% confidence intervals for each regression line are shown as shaded grey bands. The Pacific line from the previous study of Yamamoto-Kawai et al. (2008) is also shown for comparison.

In this method, the slopes of the two source water lines must be equal, otherwise there is no unique solution for the ratio of the two seawater types (Azetsu-Scott et al., 2012). This fact is often overlooked in other studies using a Pacific water line based on DIN:P relationships, whose slopes are not the same as that of the Atlantic water line. The slopes of the two regression lines in this study were tested using an ANOVA and were found to be equal within statistical uncertainty. Uncertainties in the determined seawater composition of each sample arise from the errors associated with the determination of the Arctic and Atlantic lines. The 95% confidence intervals for each line are shown in Figure 4.3 (as shaded grey bands), and indicate that both lines are robust. Overall, uncertainties due to the regression estimates are very low, with mean uncertainties in f_{ARC} and f_{ATL} being less than 0.01. A maximum uncertainty of 0.04 was associated with the Arctic line at high nutrient concentrations (P > 1.3 μmol kg^{-1}).

Another key assumption made when using this approach is that the biological production and decay of organic matter also follows the same DIN:P slope as the Atlantic and Arctic lines. However, this may vary, and contributes further uncertainty to this approach.

Once preliminary fractions of Atlantic and Arctic waters are known, they are used to define the salinity and $\delta^{18}O$ of the seawater end-member (SW) in a three end-member mixing model (equations 5.5 to 5.7). Once fractions of SIM, MW and SW have been estimated, the Pacific and Atlantic water fractions are recalculated (final F_{ARC} and F_{ATL} values in equations 5.8 and 5.9). End-member values of salinity (S) and $\delta^{18}O$ and their uncertainties are summarized in Table 5.2.

$$F_{SIM}S_{SIM} + F_{MW}S_{MW} + F_{SW}[f_{ARC}S_{ARC} + f_{ATL}S_{ATL}] = S_{obs} \quad (5.5)$$

$$F_{SIM}\delta^{18}O_{SIM} + F_{MW}\delta^{18}O_{MW} + F_{SW}[f_{ARC}\delta^{18}O_{ARC} + f_{ATL}\delta^{18}O_{ATL}] = \delta^{18}O_{obs} \quad (5.6)$$

$$F_{SIM} + F_{MW} + F_{SW} = 1 \quad (5.7)$$

$$F_{ARC} = f_{ARC}F_{SW} \quad (5.8)$$

$$F_{ATL} = f_{ATL}F_{SW} \quad (5.9)$$

Sensitivity of the calculated water-type fractions to the uncertainty in end-member values (Table 5.2) was examined using a Monte Carlo simulation. Each of the end-member values in Table 5.2 (excluding S_{MW}, which is 0 ± 0) was represented by one thousand random numbers, normally-distributed according to their stated mean and standard deviation. By solving the three end-member mixing model (equations 5.5 to 5.9) for each of the randomly created end-member values, a distribution of one thousand possible water-type fractions for F_{ARC}, F_{ATL}, F_{SIM}, and F_{MW} was created. The standard deviations of these distributions are plotted in Figures S5.2 and S5.3, representing the absolute uncertainties in calculated water-type fractions. It is important to note that the absolute uncertainties are directly related to the water-type fractions, and therefore can be less important than the relative uncertainties (shown in Figure S5.4 and S5.5), represented by the coefficient of variation (CV = standard deviation/mean). For example, the largest absolute uncertainties in F_{ARC} are observed in the surface waters of western Baffin Bay, Lancaster Sound and northern Nares Strait, simply because those are the areas where F_{ARC} is highest (>0.85, see Figure 5.4c). On the other hand, the CV of F_{ARC} is still quite low (<0.05) in those areas, and therefore those F_{ARC} values are actually quite robust. In contrast, high CV (> 0.9) are associated with most positive F_{SIM} values, indicating that F_{SIM} estimates throughout the study region are less reliable.

5.3.4 Passive tracer analysis with NEMO

A passive tracer analysis of Pacific-source water transport was conducted using a coupled ocean and sea ice model based on the Nucleus for European Modeling of the Ocean (available at https://www.nemo-ocean.eu) Version 3.4 (Madec, 2008). The sea ice module used here is the Louvain-la-Neuve sea ice Model Version 2 with an elastic-viscous-plastic rheology (Hunke & Dukowicz, 1997), including both thermodynamic and dynamic components (Bouillon et al., 2009; Fichefet & Morales Maqueda, 1997). The entire model domain covers the Arctic Ocean and the Northern Hemisphere Atlantic (ANHA) with two open boundaries, one close to Bering Strait in the Pacific Ocean and the other one at 20 °S across the Atlantic Ocean, at 1/12 degree resolution. Benefiting from the tripolar grid, ANHA12 has a horizontal grid spacing of less than 4.5 km in most regions in the Arctic Ocean. In the vertical, there are 50 geopotential levels with higher resolution focused on the upper ocean. Level thickness smoothly transitions from approximately ~1 m at the surface (22 levels for the top 100 m) to 458m at the last level. Partial steps (Barnier et al., 2006) are enabled to better resolve the seafloor. Further detail on this configuration and experiment, including model evaluation, are given by Hu et al. (2019) and Courtois et al. (2020).

The simulations are integrated from 1 January 2002 to 31 December 2019. This time period was chosen to allow enough spin-up time for the Pacific water tracer to reach and build up in Baffin Bay, and the results near the end of the simulation can be compared to our observations in 2019. At the surface, the model is driven with high temporal (hourly) and spatial resolution (33 km) atmospheric forcing data from the Canadian Meteorological Centre Global Deterministic Prediction System ReForecasts data set (Smith et al., 2004). To trace Pacific water flowing into the Arctic Ocean and then Baffin Bay, a passive tracer is added along a section across Bering Strait from the beginning of the simulation, that is, 1 January 2002, using the NEMO-TOP module (Aumont et al., 2018). The passive tracer concentration (C) is assigned at T points in the Arakawa C grid (Mesinger & Arakawa, 1976) along the selected section and updated every time step with an increment ΔC proportional to the volume flux at Bering Strait. Further details on the passive tracer and its implementation can be found in Hu et al. (2019). The results are presented as an idealized thickness of Pacific water present in the upper 150 m of the water column in Baffin Bay, focusing on the period 2009 to 2019. The idealized thickness of Pacific water formally represents the fraction of Pacific water in the grid cell, times the thickness of that grid cell, integrated in the vertical (in the case of this study, integrated over the upper 150 m of the water column).

5.4 Results and Discussion

5.4.1 Surface distributions

Surface (0-5m) distributions of calculated water mass fractions (F_{SIM}, F_{MW}, and F_{ARC}) and carbonate system parameters (DIC, TA, and Ω_{Ar}) are shown in Figure 5.4. The spatial distribution of these parameters strongly reflects the regional oceanography, with clear gradients between eastern and western Baffin Bay as they are influenced by the WGC and BIC, respectively. High F_{ARC} values are observed entering Baffin Bay from Nares Strait and Lancaster Sound, and flow southwards through western Baffin Bay. Surface waters with high F_{ARC} also generally coincide with low DIC, TA, and Ω_{Ar}, which is consistent with previous studies in Baffin Bay during summer, and the fact that Arctic waters are primarily composed of Pacific halocline waters (Azetsu-Scott et al., 2012; Shadwick et al., 2011; Yamamoto-Kawai et al., 2013). In contrast, eastern Baffin Bay (along the west Greenland shelf) displays low F_{ARC} values, since this region is dominated by Atlantic waters (F_{ATL}; not shown) being transported northwards by the WGC (Figure 5.4c).

Sea-ice melt fractions (F_{SIM}) are greatest in the western and northernmost regions where sea ice is known to persist the longest into the summer season (Bi et al., 2019; Randelhoff et al., 2019; Tang et al., 2004), although we do not observe any large SIM contributions within the study area (all F_{SIM} are below 0.1, Figure 5.4a). Sea-ice melt dilutes DIC and TA in surface waters (Yamamoto-Kawai et al., 2009), and indeed areas where we observe the highest F_{SIM} coincide with very low surface DIC and TA, such as Smith Sound and western Baffin Bay along the Baffin Island coastline. The relative uncertainty associated with F_{SIM} estimates was generally quite high throughout the study area (CV > 0.9), but the high positive F_{SIM} seen in Smith Sound and western Baffin Bay was apparently robust (CV < 0.5; Figure S5.4).

Significant surface meteoric water fractions (F_{MW}) are present in Lancaster Sound and Smith Sound but also show high contributions in Disko Bay and Uummannaq Fjord along the west Greenland coast (Figure 5.4b). Meteoric water contributions entering from Lancaster Sound and Smith Sound may be due to river runoff inputs into the central Arctic Ocean, which are now exiting through the CAA channels, or could be from small rivers within the islands of the CAA (Alkire et al., 2017; Brown et al., 2020). The fact that the F_{MW} signal in Smith Sound is not also present further north in Nares Strait may point to a nearby glacial meltwater source, such as the Trinity and Wykeham glaciers, which are currently the fastest flowing glaciers in the CAA (Dalton et al., 2019, 2022). However, we also note that the high F_{MW} signal is represented by one data point and therefore might not be robust. The highest observed F_{MW}

in our study area are located in Disko Bay and Uummannaq Fjord, where many large and fast flowing tidewater glaciers expel icebergs and glacial meltwater. Disko Bay receives discharge from Sermeq Kujalleq (also known as Jakobshavn Isbræ), which has been the single largest source of mass loss from the Greenland ice sheet over the last 20 years (Mouginot et al., 2019). These large F_{MW} inputs in west Greenland fjords are also the most robust F_{MW} signal according to our Monte Carlo uncertainty analysis (Figure S5.4).

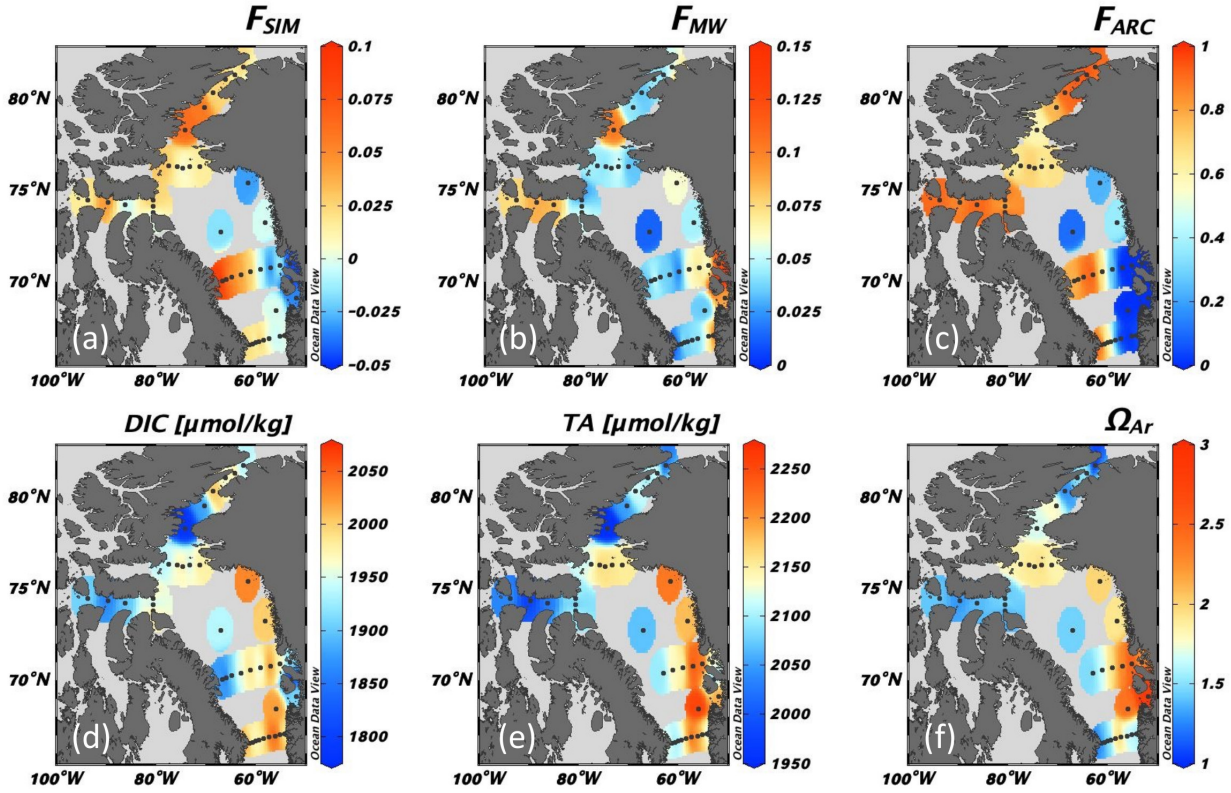

Figure 5.4: Surface distributions of water-type fractions, (a) fraction of sea-ice meltwater (F_{SIM}), (b) fraction of meteoric water (F_{MW}), (c) fraction of Arctic water (F_{ARC}), and inorganic carbon system parameters, (d) dissolved inorganic carbon concentration (DIC), (e) total alkalinity concentration (TA), and (f) aragonite saturation state (Ω_{Ar}).

Although there is high F_{MW} entering these major west Greenland fjords, we do not observe low Ω_{Ar} at the surface (Figures 5.4b,f). This is in contrast to our observations in western Baffin Bay, which display freshwater inputs mainly from Arctic waters and sea-ice melt, and have relatively low surface Ω_{Ar}. In the west Greenland fjords we observe very low surface DIC (Figure 5.4d), suggesting that biological uptake of CO_2 is exerting a more substantial influence on Ω_{Ar} compared to the TA decrease from glacial meltwater inputs. The west Greenland fjords and continental shelf are known to be very productive, with large spring phytoplankton blooms that strongly decrease surface DIC concentrations but do not alter TA

(Burgers et al., 2020; Krawczyk et al., 2021). Due to the particularly high TA:DIC ratios in this area, these waters have a high buffering capacity against decreases in saturation state.

5.4.2 Varying meteoric water characteristics

In order to investigate differences in meteoric water characteristics in eastern and western Baffin Bay we have plotted linear regression relationships of TA and $\delta^{18}O$ against salinity in the waters of the WGC and BIC (Figure 5.5). We consider measurements throughout the entire water column in these linear regression relationships. The y-intercepts of these regressions provide an estimate of freshwater end-member values for TA and $\delta^{18}O$ in these two regions of Baffin Bay. For the purpose of this investigation the BIC region shown in Figure 5.5 encompasses the channels of Lancaster Sound and Nares Strait, which both transport Arctic outflow waters into the BIC in western Baffin Bay. The stations near central Baffin Bay have been included in the BIC region as Arctic waters, defined as S ≤ 33.3 and T < 0°C, were present in the upper water column at these locations.

It is important to consider how these linear regression relationships may be altered by the presence of sea-ice melt or formation, which have an impact on salinity, TA, and $\delta^{18}O$ properties. Here, we perform a correction on salinity and TA to account for sea-ice related processes following the method of Yamamoto-Kawai et al. (2005):

$$S_0 = (S - S_{SIM}F_{SIM})/(1 - F_{SIM}) \quad (5.10)$$

$$TA_0 = (TA - TA_{SIM}F_{SIM})/(1 - F_{SIM}) \quad (5.11)$$

where S_0 and TA_0 are salinity and TA corrected for the influence of sea-ice melt or formation. Values of F_{SIM} were calculated previously for each sample using salinity and $\delta^{18}O$ observations in equations 5.5 to 5.7. We apply a value of 420 μmol kg^{-1} for TA_{SIM} (Miller et al., 2011; Rysgaard et al., 2007) and 4 for S_{SIM} (Table 5.2). We are unable to perform a similar sea-ice process correction to the $\delta^{18}O$ values, since we have already used these measurements to calculate the F_{SIM} estimates used in the correction. Performing the correction would simply reinforce our chosen meteoric water $\delta^{18}O$ end-member value of -20 ‰.

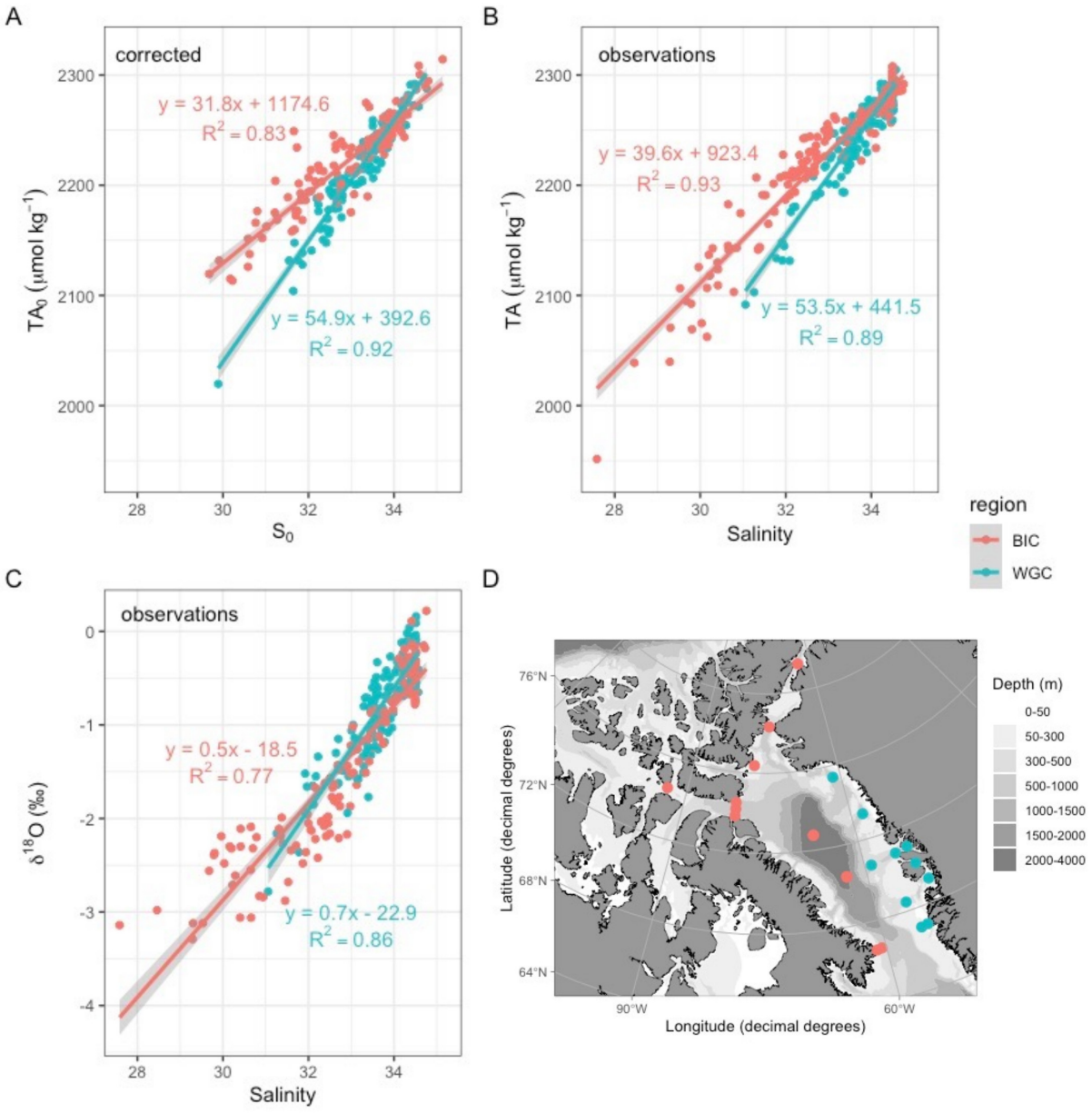

Figure 5.5: Linear regressions of salinity versus TA in the waters of the Baffin Island Current (BIC) and the West Greenland Current (WGC) within Baffin Bay, (a) corrected values (eqns. 10 and 11) for the influence of sea-ice melt or formation, (b) observed salinity-TA relationships, (c) observed salinity-$\delta^{18}O$ relationships, (d) map showing station locations for the BIC region (red) and WGC region (blue) used to determine the regression relationships in panels (a) through (c).

Based on the resulting linear regressions, the waters of the WGC display a much lower freshwater TA end-member (y-intercept) compared to the BIC in western Baffin Bay. For waters of the WGC, the y-intercept of the observed salinity-TA plot (Figure 5.5b) is 440 ± 150 μmol kg^{-1}, whereas for waters of the BIC the y-intercept of the observed salinity-TA relationship is 920 ± 76 μmol kg^{-1} (note that all stated uncertainty values are based on the 99% confidence levels of the regression relationships). This already

suggests that there is quite a large difference between the estimated meteoric TA end-member values of eastern and western Baffin Bay. After applying corrections for the impacts of sea-ice melt or formation (Figure 5.5a), the y-intercept of the salinity-TA relationships become 390 ± 140 μmol kg^{-1} for the WGC, and 1170 ± 120 μmol kg^{-1} for the BIC, further enhancing the difference in estimated meteoric TA end-member values between these two regions of Baffin Bay. It is interesting to note that the intersection points of the observed and corrected salinity-TA regressions change from being located at a salinity of 34.7 to 33.8, respectively. This presumably indicates that in the absence of sea ice related processes (melt or brine inputs) the water mass salinity and TA properties would be the same at a salinity of approximately 33.8 in both the WGC and BIC regions. Estimates of δ^{18}O meteoric end-member values using the observed salinity-δ^{18}O relationships show y-intercept values of -23 ± 3.0 ‰ for the WGC, and -18 ± 1.4 ‰ for the BIC (Figure 5.5c). These are relatively similar meteoric δ^{18}O end-member values in both regions, but applying an analysis of covariance (ANCOVA) by region found the slopes and y-intercepts of the WGC and BIC regression relationships for salinity-δ^{18}O to be statistically different (p-value <0.05).

The corrected meteoric TA end-member for the BIC region (1170 ± 120 μmol kg^{-1}; Figure 5.5a) agrees quite well with previous estimates of TA in average river runoff into the Arctic Ocean (e.g., 831 ± 100 μmol kg^{-1} from Yamamoto-Kawai et al. (2005); flow-weighted average of 1048 μmol kg^{-1} from Cooper et al. (2008); 1000 ± 100 μmol kg^{-1} in the Transpolar drift stream from Charette et al., (2020). This would be consistent with the BIC region receiving Arctic outflow waters and transporting them southwards along the Baffin Island shelf and slope into the Labrador Sea.

We hypothesize that the much lower TA end-member found in the WGC region (390 ± 140 μmol kg^{-1}; Figure 5.5a) indicates that glacial meltwater is the dominant source of fresh water on the west Greenland shelf. TA measurements of glacial discharge across the Arctic have so far revealed a range from 20 to 550 μmol kg^{-1} (Hopwood et al., 2020; Rysgaard et al., 2012), which spans our calculated TA end-member value for the WGC region. The type of bedrock below a glacier can also greatly affect the TA end-member of its meltwater (Fransson et al., 2015). If calcareous bedrock, such as limestone or marble, is present, it would be expected to increase the TA end-member of the meltwater by contributing bicarbonate or carbonate ions from weathering. Geological maps available from the Geological Survey of Denmark and Greenland (GEUS) through their Greenland Portal indicate that the bedrock along the west Greenland coast is predominantly composed of orthogneiss all the way from Kangerlussaq in the south (approximately 67 °N) to the Nussuaq Peninsula in the north (approximately 74 °N) (Escher, 1985; Garde & Marker, 2010). Orthogneiss is formed by the metamorphism of igneous rocks, is not calcareous,

and therefore would not be expected to contribute any additional TA to glacial meltwater, consistent with the low TA freshwater end-member value we have derived for this region. The highly depleted $\delta^{18}O$ meteoric end-member found in the WGC (-23 ± 3 ‰) may also be consistent with a significant contribution of glacial meltwater. Carlson et al. (2019) collected glacial ice samples from icebergs in Nuup Kangerlua (Godthåbsfjord), in early January 2019 using an ice drone, and found the icebergs to have a mean $\delta^{18}O$ value of -26.33 ± 0.08 ‰. Since our linear regressions in Baffin Bay do not include measurements of water with very low salinities, and the y-intercepts are therefore extrapolations, we cannot state conclusively that glacial meltwater is the main source of meteoric waters on the west Greenland shelf, although we surmise this is likely the case, seeing as the central west Greenland coastline houses many large and fast-flowing tidewater glaciers (Mouginot et al., 2019), coupled with the large difference in TA meteoric end-member values we derived for the WGC and BIC.

5.4.3 The west Greenland shelf

The waters of the west Greenland shelf have been relatively understudied compared to the BIC in western Baffin Bay. Figure 5.6 shows the physico-chemical characteristics of the water column from Davis Strait in the south to Melville Bay in the north (including an eastward diversion into Disko Bay). Near the surface we observe a shallow fresh and warm layer that has been heated by solar insolation (Figure 5.6a). This layer contains relatively high fractions of meteoric waters which appear in Disko Bay and Uummannaq Fjord (Figure 5.6d) and are transported northwards with the WGC. Between depths of 40 to 150 m there is a temperature minimum layer centered at a salinity of approximately 33.5, representing BBPW (Figure 5.6a,b). The coldest temperatures of the BBPW layer are observed at the northern end of the west Greenland shelf, suggesting that its formation site is located somewhere in northern Baffin Bay. The deepest water mass on the west Greenland shelf is the relatively warm and saline SPMW, which can be seen entering from the south and shows a decreasing temperature maximum towards the north (Figure 5.6a).

We find significant F_{ARC} within the upper 150 m of the West Greenland shelf transect, especially in the northernmost half of the transect (Figure 5.6c). The highest F_{ARC} value of the transect (0.57) is found at 30 m depth at the northernmost station. Along the rest of the transect, maximum F_{ARC} ranges between 0.15 and 0.4 and is generally found at depths of 60 or 70 m, coinciding with the coldest temperatures of the BBPW layer with salinity values between 33.4 and 33.6 (Figure 5.6a,b). It is surprising to see relatively high F_{ARC} on the west Greenland shelf, since Arctic waters are thought to flow predominantly southwards along the Baffin Island shelf and slope with the BIC. Since our F_{ARC} values are calculated based on DIN:P

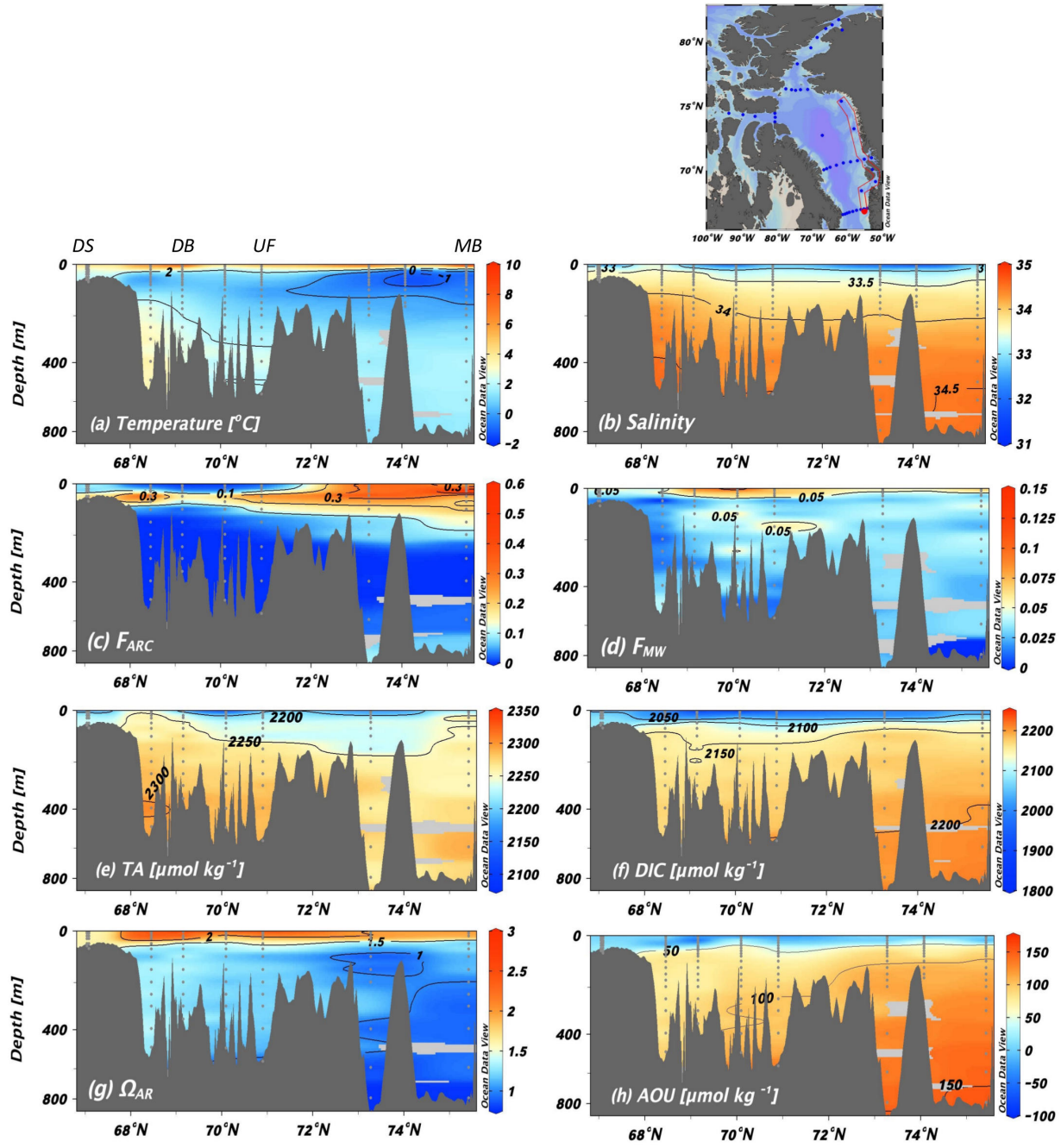

Figure 5.6: Section plots along the west Greenland shelf from Davis Strait (DS) to Melville Bay (MB). The locations of Disko Bay (DB) and Uummannaq Fjord (UF) are shown along the top of panel (a), and the transect location is outlined in red in the top-right map. Section plots show spatial distributions of various physico-chemical properties: (a) Temperature, (b) Salinity, (c) the fraction of Arctic water (F_{ARC}), (d) the fraction of meteoric water (FMW), (e) total alkalinity (TA), (f) dissolved inorganic carbon (DIC), (g) aragonite saturation state (Ω_{Ar}), and (h) Apparent Oxygen Utilization (AOU).

ratios (see Figure 5.3 and section 5.3.3), it is possible that local denitrification could alter the DIN:P ratio, leading to a false identification of Arctic-outflow waters. If denitrification were the cause of these relatively high F_{ARC} values on the West Greenland shelf, it would likely originate from the very productive and

shallow continental shelves in southeastern Baffin Bay (near Disko Bay and further south). Using the few stations in this dataset over the continental shelf in southeastern Baffin Bay, we investigated whether there was any signal of benthic denitrification that could be leading to falsely high F_{ARC} values, but found no evidence of denitrification (see Figure S5.6). In fact, we found higher dissolved oxygen concentrations, lower AOU, and lower DIC over the shallow continental shelf compared to waters offshore of the shelf break. If there were local denitrification occurring in this area, we would expect these trends to be reversed. Therefore, we do not anticipate that local denitrification is responsible for the relatively high F_{ARC} values we derived over the West Greenland shelf, and we expect that the F_{ARC} values are in fact due to the transport of Arctic-outflow waters to this region.

The presence of significant F_{ARC} in the BBPW layer suggests that this water mass may be formed in an area where surface waters contain some portion of Arctic-outflow waters. Such an area might be the North Water polynya region in northern Baffin Bay, which receives Arctic waters from the outflow of Nares Strait, and also receives comparatively more saline surface waters from the WGC. It is possible that winter convection mixes surface water contributions from both the BIC and WGC, leading to the formation of BBPW at an intermediate salinity. However, our observations show that BBPW displays lower TA concentrations compared to what would be expected from Arctic-outflow waters at the same salinity by roughly 20 μmol kg^{-1} (based on the observed TA vs. salinity regressions in Figure 5.5b). The reason for this is unclear. One hypothesis could be that glacial meltwater is also incorporated into BBPW during its formation in winter. Another hypothesis could be the expulsion of relatively low-TA brine during sea-ice formation, with TA being retained in the sea ice as ikaite crystals (Papadimitriou et al., 2007; Rysgaard et al., 2007). More research is needed into the location and formation mechanisms of BBPW in order to fully comprehend the TA characteristics of this water mass. Our observations also show a zone of undersaturated Ω_{Ar} near the bottom of the BBPW layer at approximately 73 °N (Figure 5.6g), due to the relatively low TA:DIC ratio at this location (at this depth DIC has not been lowered by surface primary production). This is notable since previously reported values of Ω_{Ar} in BBPW have not noted any undersaturation (AMAP, 2018).

Below 200m, the water column is mainly composed of SPMW, which upon entering Baffin Bay in the south contains high TA (average of 2280 ± 10 μmol kg^{-1}; Figure 5.6e) and moderate DIC (average of 2160 ± 10 μmol kg^{-1}; Figure 5.6f). As the SPMW flows northwards, its TA decreases and DIC increases, decreasing Ω_{Ar}. Increasing DIC at depths below 200m coincides with increasing Apparent Oxygen Utilization (AOU; Figure 5.6h), which represents the deviation from O_2 saturation. This suggests the respiration of organic matter is responsible for the increases in DIC at these depths. TA also decreases

slightly with organic matter respiration, although in this case respiration cannot account for the total observed decrease in TA. The average TA value in the Melville Bay region decreased to 2268 ± 5 μmol kg^{-1}, representing an average decrease of 12 μmol kg^{-1} from the SPMW entering Baffin Bay at eastern Davis Strait. Assuming traditional Redfield ratios (6 DIN: 106 DIC), organic matter respiration would account for approximately 2 μmol kg^{-1} of this TA decrease. The reason for the additional TA decrease at depth is uncertain.

5.4.4 The eastward propagation of Arctic waters

The presence of Arctic waters on the west Greenland shelf suggests that there is a significant west-to-east flow across Baffin Bay. There is limited observational support for this notion, due to the relatively small number of studies relating to the physical oceanography of Baffin Bay. Myers & Ribergaard (2013) observed cold and relatively fresh Arctic waters in Disko Bay prior to 1997, but post-1997 this layer, located at depths between 30 to 200 m, warmed by 1 to 2 °C. The authors suggested that this disappearance of the Arctic water layer in Disko Bay was related to circulation changes in Baffin Bay, and supported this using regional ocean modeling results that looked at conservation of vorticity and flow following lines of *f/H* (where *f* is the Coriolis parameter and *H* is the depth). Azetsu-Scott et al. (2012) also noted a sub-surface extension of Arctic waters propagating eastwards at Davis Strait, forced by a combination of the bottom topography along the western margin of Davis Strait, and the tendency of currents to follow *f/H* contours. At the time of our observations in 2019, some F_{ARC} was present in a narrow layer between 30 to 80 m in Disko Bay (Figure 5.6c), although we observed a much larger volume of Arctic waters towards the north, in Melville Bay (from the surface to 150 m depth).

Following on the modeling study of Wu et al. (2012), which examined circulation patterns in the upper water column (depths < 200 m) and showed an extension of the BIC towards the center of Baffin Bay, we use a passive tracer, run online as part of a high resolution numerical model simulation, to assess the circulation of Pacific-source Arctic waters in Baffin Bay. The model simulation correctly shows the entrance of Pacific water into Baffin Bay from the passages of the CAA and its predominant southward flow along the Baffin Island shelf and slope. At certain times, the simulation shows a pulse of Pacific water moving eastwards, towards the west Greenland shelf (such an instance is shown in Figure 5.7).

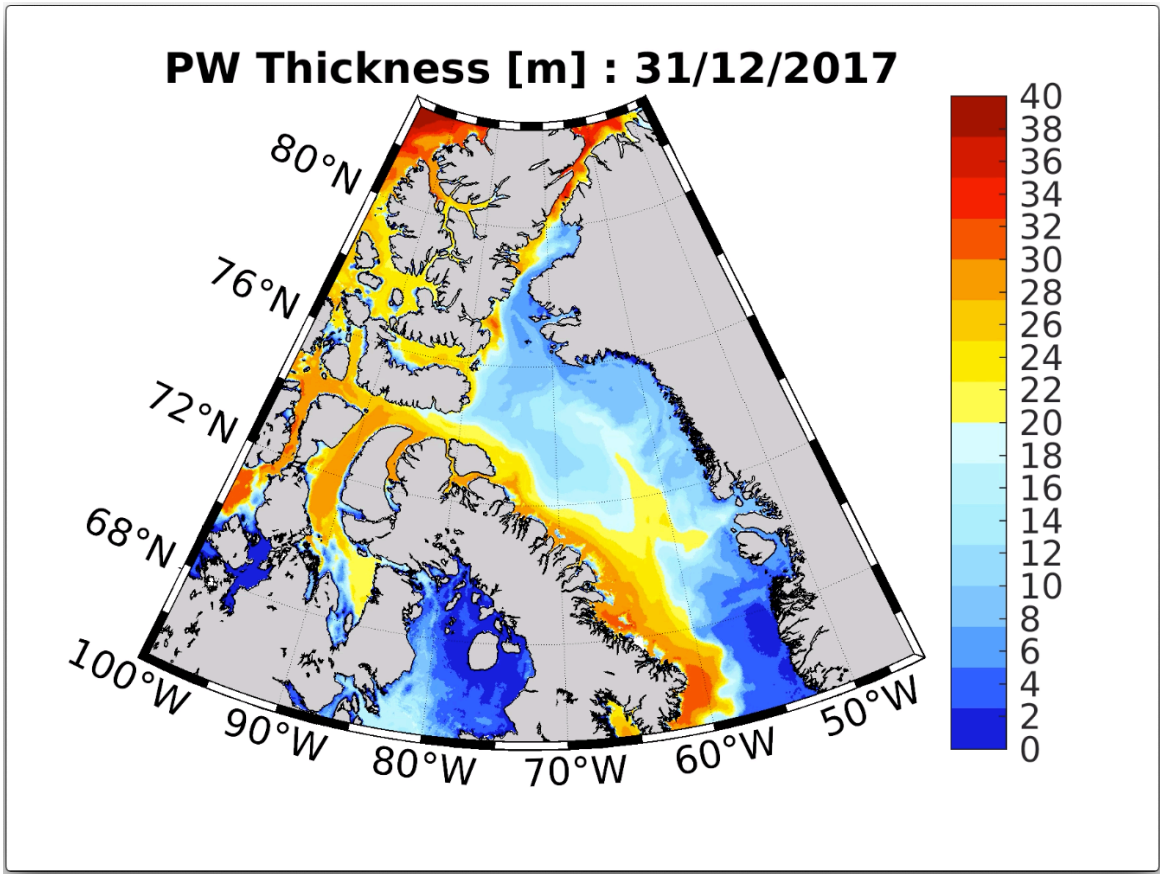

Figure 5.7: Snapshot of the Pacific water thickness throughout the upper 150 m of Baffin Bay, in meters, based upon a passive tracer in a 1/12 degree NEMO model simulation of the Arctic and North Atlantic. Pacific water thickness values are calculated as the fraction of the Pacific water tracer, times the thickness of the grid cell, integrated in the vertical (in this case over the upper 150 m of the water column). The figure shows a snapshot of the 5 day average ending on 31 December 2017, to show an example of an instance where a pulse of Pacific waters is propagated eastwards from the Baffin Island Current into central Baffin Bay, and ultimately onto the west Greenland shelf.

A full movie of the passive tracer simulation is provided by (Myers, 2023). Instances when the model simulation shows an eastward propagation of Pacific waters were found to coincide with a change in wind direction and associated Ekman transports. Most of the year the Ekman transport in western Baffin Bay is directed onshore constraining Pacific waters on the Baffin Island shelf. When the wind direction reverses, Ekman transport is then offshore, towards the center of the Bay, and ultimately over onto the west Greenland shelf. At the end of the passive tracer simulation, the highest Pacific water tracer concentrations over the West Greenland shelf were centered at approximately 40 m depth (± 10 m), with Pacific water fractions greater than 0.1 being present at depths between 10 m to 130 m depending on the location. This aligns fairly well with the depths of our highest calculated F_{ARC} values from observations along the West Greenland shelf, which ranged from being more shallow in the north (30 m) to deeper in the south (60 to 70 m) of the transect (Figure 5.6c).

5.4.5 Bay-wide drivers of Ω_{Ar}

We now consider a bay-wide perspective of Ω_{Ar} values to examine the main biogeochemical processes controlling its distribution. Figure 5.8a shows Ω_{Ar} values plotted in DIC-TA space. Generally, low values of TA and DIC are located in the upper water column, and high values at depth. Two main trends can be seen in Ω_{Ar}. Firstly, an east-west trend can be seen with relatively high Ω_{Ar} values located in the surface waters of the major fjord systems of central west Greenland, and relatively low Ω_{Ar} values located in the surface water of the BIC in western Baffin Bay (also seen in Figure 5.4f). Secondly, we observe a trend in Ω_{Ar} with depth, with deeper waters generally displaying lower Ω_{Ar} values (Figures 5.6g, and 5.8a). The most undersaturated Ω_{Ar} values were observed in BBDW and BBBW (0.36 to 0.59), with other undersaturated Ω_{Ar} values ($\Omega_{Ar} < 1$) observed in the SPMW (Atlantic) layer. The primary drivers of these two trends are evident from Figures 5.8b and 5.8c.

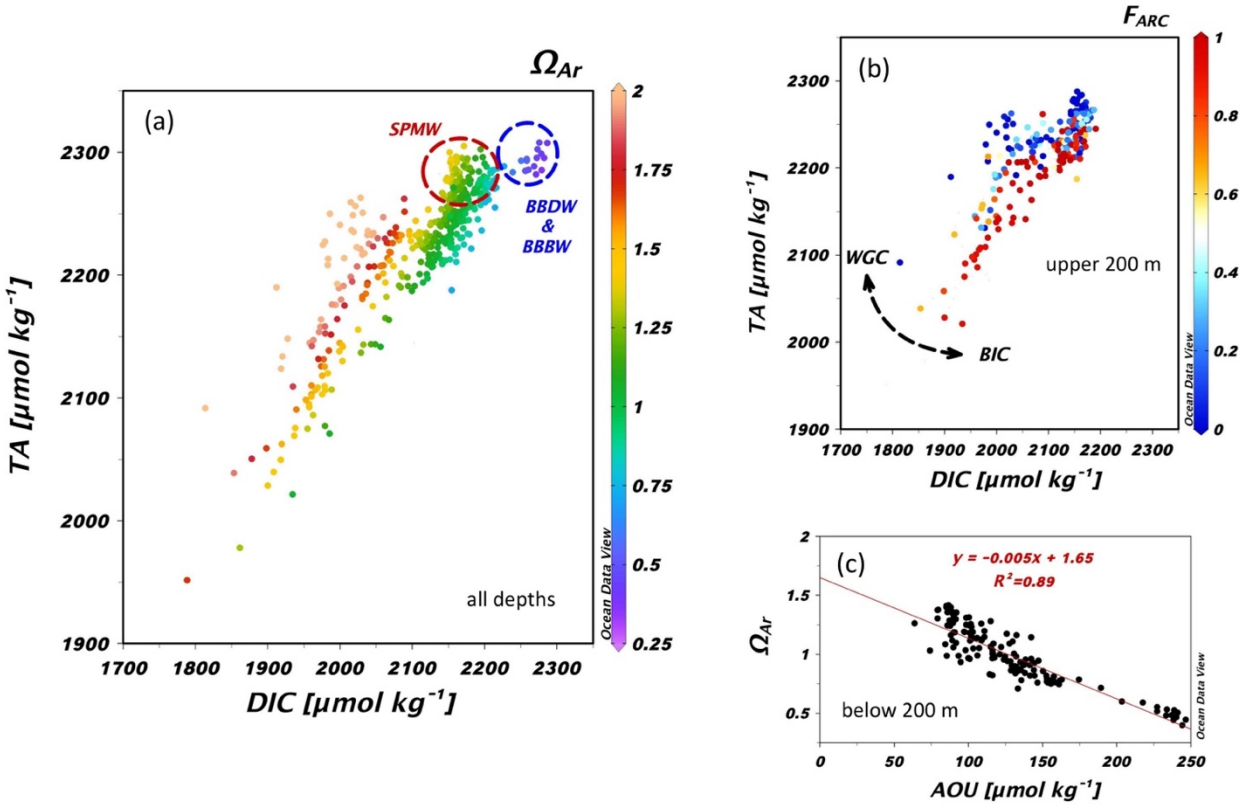

Figure 5.8: Scatterplots of: (a) aragonite saturation state (Ω_{Ar}) versus dissolved inorganic carbon (DIC) and total alkalinity (TA) for all measurements collected during Leg 2 of the 2019 Amundsen expedition; (b) fraction of Arctic water (F_{ARC}) versus DIC and TA for all measurements in the upper 200 m of the water column; and (c) apparent oxygen utilization (AOU) versus Ω_{Ar} for all measurements below 200 m depth. The red circle in (a) indicates Subpolar Mode Water (SPMW), and the blue circle represents Baffin Bay Deep Water (BBDW) and Baffin Bay Bottom Water (BBBW). Dashed arrows in (b) show how measurements in the upper water column are distributed spatially between the WGC and BIC across Baffin Bay.

Different processes and factors affect Ω_{Ar} at different depths in the water column. Figure 5.8b isolates measurements from the upper 200 m of the water column and displays F_{ARC} values in DIC-TA space. In these shallower waters of Baffin Bay there is a strong east-west divide in water masses, because of the presence of the WGC in eastern Baffin Bay, and the BIC to the west. Due to the fact that Arctic waters in the BIC are primarily composed of relatively low salinity Pacific waters, and additional freshwater inputs from sea-ice melt and meteoric waters, they are characterized by a relatively low TA to DIC ratio. This drives lower Ω_{Ar} values in the upper water column of the BIC. In contrast, the upper water column of the WGC is mainly composed of Atlantic waters, with a relatively high TA to DIC ratio and therefore higher Ω_{Ar}. Near surface waters in the major fjord systems of western Greenland displayed the highest Ω_{Ar} values (Figure 5.6g), likely due to strong primary production in this region (Burgers et al., 2020; Jensen et al., 1999; Krawczyk et al., 2021), which lowers DIC without significantly affecting TA.

Below 200 m, SPMW dominates the mid-water column in both western and eastern Baffin Bay. The only other water masses present below 200m are BBDW and BBBW, which are located below 1200 m in the deep central basin of Baffin Bay. We do not observe large variations in TA at depths below 200 m, but we do see a large gradient in DIC (Figure 5.8a). This is consistent with the respiration of organic matter, which releases DIC into the surrounding waters and consumes oxygen (leading to increases in AOU) with minimal changes to TA. Figure 5.8c reinforces the point that organic matter respiration is the main driver of Ω_{Ar} variations below 200 m, by showing a strong negative correlation between AOU and Ω_{Ar} in these waters. The most undersaturated values of Ω_{Ar} are present in BBDW and BBBW, waters with a very long residence time (hundreds of years; Zeidan et al., 2022) and consequent accumulation of respiratory DIC. Within the SPMW layer the lowest Ω_{Ar} and highest AOU are located in western Davis Strait where this water mass exits Baffin Bay after its full counter-clockwise circulation through the region.

5.4.6 Temporal changes in Ω_{Ar} across Davis Strait

Here we examine temporal changes in the distribution of Ω_{Ar} across Davis Strait by comparing measurements (including temperature and salinity) from 1997, 2004 and 2019 (Figure 5.9). We refer to measurements taken in 1997 and 2004 as “historical” data. Measurements across Davis Strait were used for this temporal analysis because it was the only location in Baffin Bay where multiple stations were sampled at an approximately consistent location between our 2019 dataset and historical ones.

Year-to-year variability in the distribution of Arctic waters and SPMW across Davis Strait heavily influences the distribution of Ω_{Ar}. The Ω_{Ar} saturation horizon shoaled between 2004 and 2019, with $\Omega_{Ar} < 1$

present in western Davis Strait at depths between 50 and 200 m in 2019. If these undersaturated waters reach the Baffin Island shelf ecosystem, they could pose a potential threat to calcifying organisms.

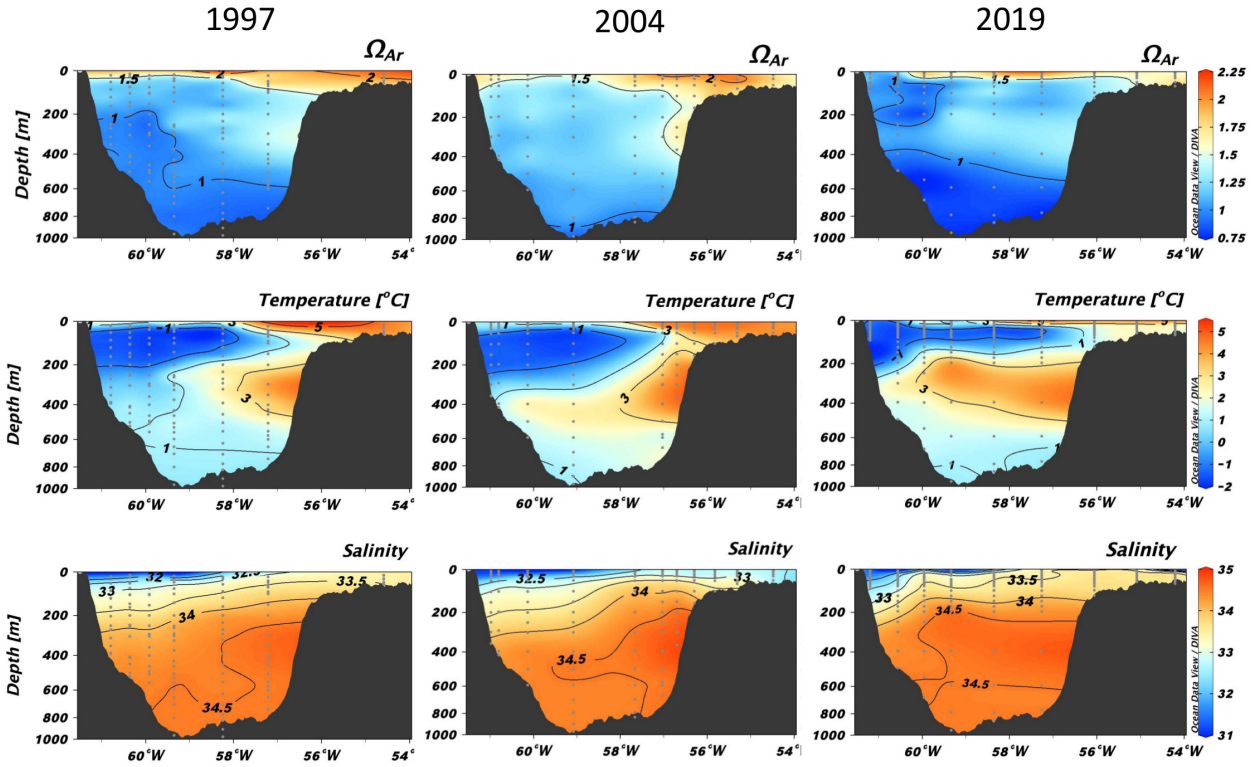

Figure 5.9: Section plots of Ω_{Ar}, seawater temperature (°C), and salinity across Davis Strait in 1997 (7 –10 August), 2004 (23 –28 September), and 2019 (8 –10 July).

We observe a statistically significant decrease in Ω_{Ar} of Arctic waters between the historical data and those from 2019, according to unpaired t-tests (p-values < 0.001; Table 5.3), which coincides with a significant decrease in TA (unpaired t-test, p-value < 0.001) but no significant change in DIC or salinity. A typical mechanism that would lead to decreasing TA would be freshwater inputs, but this would also coincide with observed decreases in salinity. The average salinity of Arctic waters in 2019 did decrease compared to 1997 and 2004, but the change was not statistically significant (Table 5.3). Further studies are required with more data points to determine what is driving decreases in Ω_{Ar} in Arctic waters, and if the trend of decreasing TA we have identified is indeed real over a longer timeseries. We do not observe significant Ω_{Ar} decreases between years for any other water mass present in the Davis Strait transect (Table 5.3). Having measurements spanning two decades, we expected that perhaps an increase in DIC due to increased uptake of atmospheric CO_2 would be present in this temporal analysis, but we did not observe any significant signal of this, in any water mass. Since the physical oceanography of the region is so variable, this likely precludes us from being able to identify an anthropogenic signal, yet.

Table 5.8: Water mass properties (mean ± sd) across Davis Strait in 1997, 2004, and 2019, with the number of observations (n) averaged for each water mass indicated in parentheses. Abbreviations: Arctic water (ARC), Baffin Bay Polar water (BBPW), Sub-Polar Mode water (SPMW).

Measure	Year	ARC	BBPW	SPMW
Ω_{Ar}	1997	1.20 ± 0.05 (17)	1.06 ± 0.08 (10)	1.05 ± 0.15 (40)
	2004	1.31 ± 0.08 (8)	1.27 ± 0.06 (6)	1.23 ± 0.22 (18)
	2019	1.02 ± 0.04 (19)	1.10 ± 0.14 (6)	0.97 ± 0.18 (20)
TA	1997	2242 ± 7 (18)	2246 ± 9 (10)	2276 ± 11 (42)
	2004	2242 ± 11 (8)	2258 ± 11 (6)	2288 ± 14 (18)
	2019	2208 ± 17 (19)	2223 ± 7 (6)	2264 ± 13 (20)
DIC	1997	2137 ± 9 (17)	2157 ± 15 (10)	2183 ± 19 (40)
	2004	2124 ± 19 (8)	2139 ± 5 (6)	2171 ± 27 (20)
	2019	2127 ± 20 (19)	2132 ± 19 (6)	2185 ± 21 (20)
Salinity	1997	33.0 ± 0.2 (24)	33.5 ± 0.1 (10)	34.4 ± 0.2 (44)
	2004	32.8 ± 0.3 (15)	33.5 ± 0.1 (10)	34.4 ± 0.2 (30)
	2019	32.6 ± 0.4 (55)	33.5 ± 0.1 (19)	34.4 ± 0.2 (21)

Although it is not a statistically significant trend, the SPMW layer in Davis Strait also displays a lower mean Ω_{Ar} in 2019 compared to 1997 and 2004 (Table 5.3). The lowest Ω_{Ar} values seen in the SPMW layer each year generally coincide with the relatively cold version of SPMW that exits Baffin Bay at Davis Strait (with approximate properties of $T < 2$ °C and $S > 34.3$). These low saturation states result from physical and biochemical changes to SPMW along its cyclonic flow path around Baffin Bay. SPMW is significantly cooled as it transits north along the west Greenland shelf, and shows a slight decrease in TA from south to north. Additionally, this water mass accumulates DIC from the respiration of organic matter along its flow path (as indicated in Figure 5.6). These processes combined contribute to lowering the Ω_{Ar} of SPMW along its flow path, leading to a gradient in Ω_{Ar} within the SPMW layer across Davis Strait (where SPMW both enters and exits Baffin Bay). This reinforces the trend of decreasing Ω_{Ar} in SPMW that we observed from south to north on the west Greenland shelf, and shows that these waters continue to accumulate respiration products as they are redirected southwards back towards Davis Strait, with the BIC.

We also investigated inter-annual changes in carbon system variables in BBDW and BBBW, using cruise data that accessed the deep central basin of Baffin Bay in 1997 and 2003, as well as our 2019 data (see Figure S5.7 for the historical station locations). We find no significant changes in Ω_{Ar}, DIC, TA and pH between years (see Table S5.1).

5.5 Summary and Conclusions

This work provides an updated analysis of the main biogeochemical drivers influencing trends in Ω_{Ar} throughout Baffin Bay. Spatially, we find that different processes are important in different regions, and at different depths in the bay. Within the upper 200 m, increasing F_{ARC} is the primary driver of decreasing Ω_{Ar}, due to the low TA:DIC ratio of Arctic-outflow waters. At depths below 200 m, respiration of organic matter is the main driver of low Ω_{Ar}. Within the SPMW layer, the amount of respiration tends to increase along the cyclonic flow path of this water mass around Baffin Bay. To examine temporal trends in Ω_{Ar}, we compared "historical" measurements across Davis Strait from the years 1997 and 2004 with our 2019 dataset. We observe a statistically significant decrease in the Ω_{Ar} of Arctic waters between the historical years and 2019, coinciding with a significant decrease in TA, but no significant changes in DIC or salinity. No other water masses across Davis Strait displayed any significant temporal changes in Ω_{Ar}, TA, DIC or salinity. It is likely that the large variability in the physical oceanography of this region precludes us from identifying any anthropogenic ocean acidification signal at this time.

We observe significant F_{ARC} within the BBPW layer on the northern portion of the west Greenland shelf, coinciding with decreases in TA and Ω_{Ar}. Using a passive tracer included in a numerical modeling simulation, we find that periodic changes in wind direction lead to a switch from onshore to offshore Ekman transport in western Baffin Bay, transporting Arctic waters towards central Baffin Bay and ultimately onto the west Greenland shelf. This goes against the conventional view of a persistent cyclonic circulation in Baffin Bay and suggests there is still much to be learned about the physical oceanography of Baffin Bay, its seasonal and interannual variability and how it may be changing.

Freshwater inputs in western Baffin Bay, which result from a combination of Pacific-source halocline waters, sea-ice melt, and meteoric waters, are associated with lower Ω_{Ar} than the freshwater inputs in eastern Baffin Bay, which are assumed to primarily originate from glacial meltwater. Based on salinity-TA linear regression relationships (corrected for the influences of sea-ice related processes; Figure 4.5a), surface waters on the west Greenland shelf have a significantly lower meteoric end-member TA value (390 ± 140 μmol kg^{-1}) compared to surface waters of the BIC in western Baffin Bay (1170 ± 120 μmol kg^{-1}). In contrast, the difference between the $\delta^{18}O$ meteoric end-members of these two regions is relatively small. The low TA freshwater end-member we have derived here agrees well with the limited measurements of glacial meltwater TA that have been reported in recent literature (Hopwood et al., 2020; Meire et al., 2015; Rysgaard et al., 2012).

Literature Cited

Alkire, M. B., Jacobson, A. D., Lehn, G. O., Macdonald, R. W., & Rossi, M. W. (2017). On the geochemical heterogeneity of rivers draining into the straits and channels of the Canadian Arctic Archipelago. *Journal of Geophysical Research: Biogeosciences*, *122*, 2527–2547. https://doi.org/10.1002/2016JG003723

AMAP. (2013). *AMAP Assessment 2013: Arctic Ocean Acidification*. Oslo, Norway: Arctic Monitoring and Assessment Programme (AMAP).

AMAP. (2018). *AMAP Assessment 2018: Arctic Ocean Acidification*. Tromsø, Norway: Arctic Monitoring and Assessment Programme (AMAP).

Amundsen Science Data Collection (2024). CTD data collected by the CCGS Amundsen in the Canadian Arctic. ArcticNet Inc., Québec, Canada. Processed data. Cruise 1902 Release 1. Archived at www.polardata.ca, Canadian Cryospheric Information Network (CCIN), Waterloo, Canada. https://doi.org/10.5884/12713.

Aumont, O., Éthé, C., Lovato, T., Mouchet, A., Nurser, G., Palmiéri, J., et al. (2018). *Tracers in Ocean Paradigm (TOP) – The NEMO passive tracers engine. Notes du Pôle de modélisation de l'Institut Pierre-Simon Laplace (IPSL) (v4.2.0, Number 28)*. Zenodo. https://doi.org/10.5281/zenodo.1471700

Azetsu-Scott, K., Clarke, A., Falkner, K., Hamilton, J., Jones, E. P., Lee, C., et al. (2010). Calcium carbonate saturation states in the waters of the Canadian Arctic Archipelago and the Labrador Sea. *Journal of Geophysical Research: Oceans*, *115*, C11021. https://doi.org/10.1029/2009JC005917

Azetsu-Scott, K., Petrie, B., Yeats, P., & Lee, C. (2012). Composition and fluxes of freshwater through Davis Strait using multiple chemical tracers. *Journal of Geophysical Research*, *117*, C12011. https://doi.org/10.1029/2012JC008172

Bâcle, J., Carmack, E. C., & Ingram, R. G. (2002). Water column structure and circulation under the North Water during spring transition: April-July 1998. *Deep-Sea Research Part II: Topical Studies in Oceanography*, *49*, 4907–4925. https://doi.org/10.1016/S0967-0645(02)00170-4

Ballinger, T. J., Moore, G. W. K., Garcia-Quintana, Y., Myers, P. G., Imrit, A. A., Topál, D., & Meier, W. N. (2022). Abrupt northern Baffin Bay autumn warming and sea-ice loss since the turn of the twenty-first century. *Geophysical Research Letters*, *49*, e2022GL101472. https://doi.org/10.1029/2022GL101472

Bamber, J. L., Tedstone, A. J., King, M. D., Howat, I. M., Enderlin, E. M., van der Broeke, M. R., & Noel, B. (2018). Land Ice Freshwater Budget of the Arctic and North Atlantic Oceans: 1. Data, Methods and Results. *Journal of Geophysical Research: Oceans*, *123*, 1827–1837. https://doi.org/10.1002/2017JC013605

Barnier, B., Madec, G., Penduff, T., Molines, J.-M., Treguier, A.-M., Le Sommer, J., et al. (2006). Impact of partial steps and momentum advection schemes in a global ocean circulation model at eddy-permitting resolution. *Ocean Dynamics*, *56*, 543–567. https://doi.org/10.1007/s10236

Bi, H., Zhang, Z., Wang, Y., Xu, X., Liang, Y., Huang, J., et al. (2019). Baffin Bay sea ice inflow and outflow: 1978-1979 to 2016-2017. *Cryosphere*, *13*, 1025–1042. https://doi.org/10.5194/tc-13-1025-2019

Bouillon, S., Morales Maqueda, M. A., Legat, V., & Fichefet, T. (2009). An elastic–viscous–plastic sea ice model formulated on Arakawa B and C grids. *Ocean Modelling*, *27*(3–4), 174–184. https://doi.org/10.1016/j.ocemod.2009.01.004

Brown, K. A., Williams, W. J., Carmack, E. C., Fiske, G., François, R., McLennan, D., & Peucker-Ehrenbrink, B. (2020). Geochemistry of Small Canadian Arctic Rivers with Diverse Geological and Hydrological Settings. *Journal of Geophysical Research: Biogeosciences*, *125*(1), 1–21. https://doi.org/10.1029/2019JG005414

Burgers, T. M., Miller, L. A., Thomas, H., Else, B. G. T., Gosselin, M., & Papakyriakou, T. (2017). Surface water pCO_2 variations and sea-air CO_2 fluxes during summer in the eastern Canadian Arctic. *Journal of Geophysical Research: Oceans*, *122*(12), 9663–9678. https://doi.org/10.1002/2017JC013250

Burgers, T. M., Tremblay, J.-É., Else, B. G. T., & Papakyriakou, T. N. (2020). Estimates of net community production from multiple approaches surrounding the spring ice-edge bloom in Baffin Bay. *Elementa: Science of the Anthropocene*, *8(1):013*. https://doi.org/10.1525/elementa.013

Burgers, T. M., Miller, L. A., Rysgaard, S., Mortensen, J., Else, B., Tremblay, J.-É., & Papakyriakou, T. (2023). Distinguishing Physical and Biological Controls on the Carbon Dynamics in a High-Arctic Outlet Strait. *Journal of Geophysical Research: Oceans*, *128*, e2022JC019393. https://doi.org/10.1029/2022JC019393

Carlson, D. F., Pasma, J., Jacobsen, M. E., Hansen, M. H., Thomsen, S., Lillethorup, J. P., et al. (2019). Retrieval of Ice Samples Using the Ice Drone. *Frontiers in Earth Science*, *7*(November), 1–14. https://doi.org/10.3389/feart.2019.00287

Carmack, E. C., Yamamoto-Kawai, M., Haine, T. W. N., Bacon, S., Bluhm, B. A., Lique, C., et al. (2016). Freshwater and its role in the Arctic Marine System: Sources, disposition, storage, export, and physical and biogeochemical consequences in the Arctic and global oceans. *Journal of Geophysical Research: Biogeosciences*, *121*, 675–717. https://doi.org/10.1002/2015JG003140

Charette, M. A., Kipp, L. E., Jensen, L. T., Dabrowski, J. S., Whitmore, L. M., Fitzsimmons, J. N., et al. (2020). The Transpolar Drift as a Source of Riverine and Shelf-Derived Trace Elements to the Central Arctic Ocean. *Journal of Geophysical Research: Oceans*, *125*, e2019JC015920. https://doi.org/10.1029/2019JC015920

Cooper, L. W., Whitledge, T. E., Grebmeier, J. M., & Weingartner, T. (1997). The nutrient, salinity, and stable oxygen isotope composition of Bering and Chukchi Seas waters in and near the Bering Strait. *Journal of Geophysical Research: Oceans*, *102*(C6), 12563–12573. https://doi.org/10.1029/97JC00015

Cooper, L. W., McClelland, J. W., Holmes, R. M., Raymond, P. A., Gibson, J. J., Guay, C. K., & Peterson, B. J. (2008). Flow-weighted values of runoff tracers (δ18O, DOC, Ba, alkalinity) from the six largest Arctic rivers. *Geophysical Research Letters*, *35*, L18606. https://doi.org/10.1029/2008GL035007

Courtois, P., Garcia-Quintana, Y., Hu, X., & Myers, P. G. (2020). Kinematic Subduction Rate Of Labrador Sea Water From an Eddy-Permitting Numerical Model. *Journal of Geophysical Research: Oceans*, *125*, e2019JC015475. https://doi.org/10.1029/2019JC015475

Curry, B., Lee, C. M., & Petrie, B. (2011). Volume, Freshwater, and Heat Fluxes through Davis Strait, 2004 – 05. *Journal of Physical Oceanography*, *41*, 429–436. https://doi.org/10.1175/2010JPO4536.1

Curry, B., Lee, C. M., Petrie, B., Moritz, R. E., & Kwok, R. (2014). Multiyear Volume, Liquid Freshwater, and Sea Ice Transports through Davis Strait, 2004–10. *Journal of Physical Oceanography*, *44*(4), 1244–1266. https://doi.org/10.1175/JPO-D-13-0177.1

Dalton, A., Copland, L., Tivy, A., Van Wychen, W., & Cook, A. (2019). Iceberg production and characteristics around the Prince of Wales Icefield, Ellesmere Island, 1997-2015. *Arctic, Antarctic,*

and Alpine Research, *51*(1), 412–427. https://doi.org/10.1080/15230430.2019.1634442

Dalton, A., Van Wychen, W., Copland, L., Gray, L., & Burgess, D. (2022). Seasonal and Multiyear Flow Variability on the Prince of Wales Icefield, Ellesmere Island: 2009–2019. *Journal of Geophysical Research: Earth Surface*, *127*, e2021JF006501. https://doi.org/10.1029/2021JF006501

Dickson, A. G., Sabine, C. L., & Christian, J. R. (Eds.). (2007). *Guide to best practices for ocean CO_2 measurements*. *PICES Special Publication 3*. Sidney, BC: North Pacific Marine Science Organization.

Doney, S. C., Fabry, V. J., Feely, R. A., & Kleypas, J. A. (2009). Ocean Acidification : The Other CO_2 Problem. *Annual Review of Marine Science*, *1*, 169–194. https://doi.org/10.1146/annurev.marine.010908.163834

Escher, J. C. (1985). *Geological map of Greenland, 1:500 000, Sheet 4, Upernavik Isfjord*. https://doi.org/10.22008/FK2/YERETL

Fairbanks, R. (1982). The Origin of Continental Shelf and Slope Water in the New York Bight and Gulf of Maine: Evidence from $H_2{}^{18}O$/ $H_2{}^{16}O$ Ratio Measurements. *Journal of Geophysical Research*, *87*(C8), 5796–5808.

Fichefet, T., & Morales Maqueda, M. A. (1997). Sensitivity of a global sea ice model to the treatment of ice thermodynamics and dynamics. *Journal of Geophysical Research: Oceans*, *102*(C6), 12609–12646.

Fransson, A., Chierici, M., Nomura, D., Granskog, M. A., Kristiansen, S., Martma, T., & Nehrke, G. (2015). Effect of glacial drainage water on the CO_2 system and ocean acidification state in an Arctic tidewater-glacier fjord during two contrasting years. *Journal of Geophysical Research: Oceans*, *120*. https://doi.org/10.1002/2014JC010320

Friedlingstein, P., O'Sullivan, M., Jones, M. W., Andrew, R. M., Bakker, D. C. E., Hauck, J., et al. (2023). Global Carbon Budget 2023. *Earth System Science Data*, *15*, 5301–5369. https://doi.org/10.5194/essd-15-5301-2023

Garde, A. A., & Marker, M. K. (2010). *Geological map of Greenland, 1:500 000, Sheet 3, Kangerlussuaq / Søndre Strømfjord - Nuussuaq, 2nd edition*. https://doi.org/10.22008/FK2/X9U5BF

Gattuso, J.-P., Epitalon, J.-M., Lavigne, H., & Orr, J. (2021). seacarb: seawater carbonate chemistry. R package version 3.3.1. http://CRAN.R-project.org/package=seacarb

Haine, T. W. N., Curry, B., Gerdes, R., Hansen, E., Karcher, M., Lee, C., et al. (2015). Arctic freshwater export: Status, mechanisms, and prospects. *Global and Planetary Change, 125, 13-35*. https://doi.org/10.1016/j.gloplacha.2014.11.013

Holmes, R. M., Aminot, A., Kérouel, R., Hooker, B. A., & Peterson, B. J. (1999). A simple and precise method for measuring ammonium in marine and freshwater ecosystems. *Canadian Journal of Fisheries and Aquatic Sciences*, *56*, 1801–1808. https://doi.org/10.1139/f99-128

Hopwood, M. J., Carroll, D., Dunse, T., Hodson, A., Holding, J. M., Iriarte, J. L., et al. (2020). Review article: How does glacier discharge affect marine biogeochemistry and primary production in the Arctic? *The Cryosphere*, *14*(4), 1347–1383. https://doi.org/10.5194/tc-14-1347-2020

Hu, X., Myers, P. G., & Lu, Y. (2019). Pacific Water pathway in the Arctic Ocean and Beaufort Gyre in two simulations with different horizontal resolutions. *Journal of Geophysical Research: Oceans*, *124*, 6414–6432. https://doi.org/10.1029/2019JC015111

Hunke, E. C., & Dukowicz, J. K. (1997). An Elastic-Viscous-Plastic Model for Sea Ice Dynamics. *Journal*

of Physical Oceanography, *27*(9), 1849–1867.

Jensen, H. M., Pedersen, L., Burmeister, A. D., & Hansen, B. W. (1999). Pelagic primary production during summer along 65 to 72°N off West Greenland. *Polar Biology*, *21*(5), 269–278. https://doi.org/10.1007/s003000050362

Johnson, K. M., Wills, K. D., Butler, D. B., Johnson, W. K., & Wong, C. S. (1993). Coulometric total carbon dioxide analysis for marine studies : maximizing the performance of an automated gas extraction system and coulometric detector. *Marine Chemistry*, *44*(1993), 167–187. https://doi.org/10.1016/0304-4203(93)90201-X

Jones, E. P., Anderson, L. G., & Swift, J. H. (1998). Distribution of Atlantic and Pacific waters in the upper Arctic Ocean : Implications for circulation. *Geophysical Research Letters*, *25*(6), 765–768. https://doi.org/10.1029/98gl00464

Klein, B., LeBlanc, B., Mei, Z. P., Beret, R., Michaud, J., Mundy, C. J., et al. (2002). Phytoplankton biomass, production and potential export in the North Water. *Deep-Sea Research Part II: Topical Studies in Oceanography*, *49*(22–23), 4983–5002. https://doi.org/10.1016/S0967-0645(02)00174-1

Krawczyk, D. W., Kryk, A., Juggins, S., Burmeister, A., Pearce, C., Seidenkrantz, M. S., et al. (2021). Spatio-temporal changes in ocean conditions and primary production in Baffin Bay and the Labrador Sea. *Palaeogeography, Palaeoclimatology, Palaeoecology*, *563*. https://doi.org/10.1016/j.palaeo.2020.110175

Landy, J. C., Ehn, J. K., Babb, D. G., Thériault, N., & Barber, D. G. (2017). Sea ice thickness in the Eastern Canadian Arctic: Hudson Bay Complex & Baffin Bay. *Remote Sensing of Environment*, *200*, 281–294. https://doi.org/10.1016/j.rse.2017.08.019

Lauvset, S. K., Lange, N., Tanhua, T., Bittig, H. C., Olsen, A., Kozyr, A., et al. (2022). GLODAPv2.2022 : the latest version of the global interior ocean biogeochemical data product [Dataset]. *Earth System Science Data*, *14*, 5543–5572. https://doi.org/10.5194/essd-14-5543-2022

Lehmann, N., Kienast, M., Granger, J., Bourbonnais, A., Altabet, M. A., & Tremblay, J.-É. (2019). Remote Western Arctic Nutrients Fuel Remineralization in Deep Baffin Bay. *Global Biogeochemical Cycles*, *33*, 649–667. https://doi.org/10.1029/2018GB006134

Lin, P., Pickart, R. S., Torres, D. J., & Pacini, A. (2018). Evolution of the Freshwater Coastal Current at the Southern Tip of Greenland. *Journal of Physical Oceanography*, *48*(9), 2127–2140. https://doi.org/10.1175/JPO-D-18-0035.1

Lueker, T. J., Dickson, A. G., & Keeling, C. D. (2000). Ocean pCO_2 calculated from dissolved inorganic carbon, alkalinity, and equations for K_1 and K_2: validation based on laboratory measurements of CO_2 in gas and seawater at equilibrium. *Marine Chemistry*, *70*, 105–119.

Madec, G. (2008). *NEMO Ocean engine* (No 27). France: Note du Pôle de Modélisation de l'Institut Pierre-Simon Laplace (IPSL).

Meire, L., Søgaard, D. H., Mortensen, J., Meysman, F. J. R., Soetaert, K., Arendt, K. E., et al. (2015). Glacial meltwater and primary production are drivers of strong CO_2 uptake in fjord and coastal waters adjacent to the Greenland Ice Sheet. *Biogeosciences*, *12*, 2347–2363. https://doi.org/10.5194/bg-12-2347-2015

Melling, H., Agnew, T. A., Falkner, K. K., Greenberg, D. A., Lee, C. M., Münchow, A., et al. (2008). Fresh-water fluxes via pacific and arctic outflows across the Canadian polar shelf. In R. R. Dickson, J. Meincke, & P. Rhines (Eds.), *Arctic-Subarctic Ocean Fluxes: Defining the Role of the Northern Seas in Climate* (pp. 193–247). Springer Netherlands. https://doi.org/10.1007/978-1-4020-6774-7

Mesinger, F., & Arakawa, A. (1976). *Numerical methods used in Atmospheric models* (GARP Publi).

Miller, L. A., Papakyriakou, T. N., Collins, R. E., Deming, J. W., Ehn, J. K., MacDonald, R. W., et al. (2011). Carbon dynamics in sea ice: A winter flux time series. *Journal of Geophysical Research: Oceans*, *116*, C02028. https://doi.org/10.1029/2009JC006058

Mortensen, J., Rysgaard, S., Winding, M. H. S., Arendt, K. E., Lund, H., Stuart-Lee, A. E., & Meire, L. (2022). Multidecadal Water Mass Dynamics on the West Greenland Shelf. *Journal of Geophysical Research: Oceans*, *127*, e2022JC018724. https://doi.org/10.1029/2022JC018724

Mouginot, J., Rignot, E., Bjørk, A. A., van den Broeke, M., Millan, R., Morlighem, M., et al. (2019). Forty-six years of Greenland Ice Sheet mass balance from 1972 to 2018. *Proceedings of the National Academy of Sciences of the United States of America*, *116*(19), 9239–9244. https://doi.org/10.1073/pnas.1904242116

Mucci, A. (1983). The solubility of calcite and aragonite in seawater at various salinities, temperatures, and one atmosphere total pressure. *American Journal of Science*, *283*(7), 780–799. https://doi.org/10.2475/ajs.283.7.780

Myers, P. G. (2023). Pacific Water circulation in Baffin Bay from 1/12 degree NEMO model simulation. *ERA (Education and Research Archive), University of Alberta*. https://doi.org/10.7939/r3-rh6y-9q93

Myers, P. G., & Ribergaard, M. H. (2013). Warming of the Polar Water Layer in Disko Bay and Potential Impact on Jakobshavn Isbrae. *Journal of Physical Oceanography*, *43*(12), 2629–2640. https://doi.org/10.1175/JPO-D-12-051.1

Myers, P. G., Donnelly, C., & Ribergaard, M. H. (2009). Structure and variability of the West Greenland Current in Summer derived from 6 repeat standard sections. *Progress in Oceanography*, *80*(1–2), 93–112. https://doi.org/10.1016/j.pocean.2008.12.003

Orr, J. C., Epitalon, J.-M., Dickson, A. G., & Gattuso, J.-P. (2018). Routine uncertainty propagation for the marine carbon dioxide system. *Marine Chemistry*, *207*, 84–107. https://doi.org/10.1016/j.marchem.2018.10.006

Punshon, S., Azetsu-Scott, K., Sherwood, O., & Edinger, E. N. (2019). Bottom water methane sources along the high latitude eastern Canadian continental shelf and their effects on the marine carbonate system. *Marine Chemistry*, *212*, 83–95. https://doi.org/10.1016/j.marchem.2019.04.004

Randelhoff, A., Oziel, L., Massicotte, P., Bécu, G., Galí, M., Lacour, L., et al. (2019). The evolution of light and vertical mixing across a phytoplankton ice-edge bloom. *Elementa: Science of the Anthropocene*, *7:20*. https://doi.org/10.1525/elementa.357

Rantanen, M., Karpechko, A. Y., Lipponen, A., Nordling, K., Hyvärinen, O., Ruosteenoja, K., et al. (2022). The Arctic has warmed nearly four times faster than the globe since 1979. *Communications Earth and Environment*, *3:168*. https://doi.org/10.1038/s43247-022-00498-3

Rysgaard, S., Glud, R. N., Sejr, M. K., Bendtsen, J., & Christensen, P. B. (2007). Inorganic carbon transport during sea ice growth and decay: A carbon pump in polar seas. *Journal of Geophysical Research*, *112*, C03016. https://doi.org/10.1029/2006JC003572

Rysgaard, S., Mortensen, J., Juul-Pedersen, T., Sørensen, L. L., Lennert, K., Søgaard, D. H., et al. (2012). High air–sea CO_2 uptake rates in nearshore and shelf areas of Southern Greenland: Temporal and spatial variability. *Marine Chemistry*, *128–129*, 26–33. https://doi.org/10.1016/j.marchem.2011.11.002

Rysgaard, S., Boone, W., Carlson, D., Sejr, M. K., Bendtsen, J., Juul-Pedersen, T., et al. (2020). An

updated view on water masses on the pan-West Greenland continental shelf and their link to proglacial fjords. *Journal of Geophysical Research: Oceans*, *125*, e2019JC015564. https://doi.org/10.1029/2019jc015564

Shadwick, E. H., Thomas, H., Gratton, Y., Leong, D., Moore, S. A., Papakyriakou, T., & Prowe, A. E. F. (2011). Export of Pacific carbon through the Arctic Archipelago to the North Atlantic. *Continental Shelf Research*, *31*, 806–816. https://doi.org/10.1016/j.csr.2011.01.014

Shadwick, E. H., Thomas, H., Chierici, M., Else, B., Fransson, A., Michel, C., et al. (2011). Seasonal variability of the inorganic carbon system in the Amundsen Gulf region of the southeastern Beaufort Sea. *Limnology and Oceanography*, *56*(1), 303–322. https://doi.org/10.4319/lo.2011.56.1.0303

Smith, G. C., Roy, F., Mann, P., Dupont, F., Brasnett, B., Lemieux, J.-F., et al. (2004). A new atmospheric dataset for forcing ice–ocean models: Evaluation of reforecasts using the Canadian global deterministic prediction system. *Quarterly Journal of the Royal Meteorological Society*, *140*(680), 881–894.

Sulpis, O., Lauvset, S. K., & Hagens, M. (2020). Current estimates of K_1^* and K_2^* appear inconsistent with measured CO_2 system parameters in cold oceanic regions. *Ocean Science*, *16*(4), 847–862. https://doi.org/10.5194/os-16-847-2020

Tang, C. C. L., Ross, C. K., Yao, T., Petrie, B., DeTracey, B. M., & Dunlap, E. (2004). The circulation, water masses and sea-ice of Baffin Bay. *Progress in Oceanography*, *63*, 183–228. https://doi.org/10.1016/j.pocean.2004.09.005

Wu, Y., Tang, C., & Hannah, C. (2012). The circulation of eastern Canadian seas. *Progress in Oceanography*, *106*, 28–48. https://doi.org/10.1016/j.pocean.2012.06.005

Yamamoto-Kawai, M., Tanaka, N., & Pivovarov, S. (2005). Freshwater and brine behaviors in the Arctic ocean deduced from historical data of $\delta^{18}O$ and alkalinity (1929-2002 A.D.). *Journal of Geophysical Research: Oceans*, *110*, C10003. https://doi.org/10.1029/2004JC002793

Yamamoto-Kawai, M., McLaughlin, F. A., Carmack, E. C., Nishino, S., & Shimada, K. (2008). Freshwater budget of the Canada Basin, Arctic Ocean, from salinity, $\delta^{18}O$, and nutrients. *Journal of Geophysical Research: Oceans*, *113*, C01007. https://doi.org/10.1029/2006JC003858

Yamamoto-Kawai, M., McLaughlin, F. A., Carmack, E. C., Nishino, S., & Shimada, K. (2009). Aragonite undersaturation in the Arctic Ocean: Effects of ocean acidification and sea ice melt. *Science*, *326*, 1098–1100.

Yamamoto-Kawai, M., McLaughlin, F., & Carmack, E. (2013). Ocean acidification in the three oceans surrounding northern North America. *Journal of Geophysical Research: Oceans*, *118*(11), 6274–6284. https://doi.org/10.1002/2013JC009157

Zeidan, S., Walker, J., Else, B. G. T., Miller, L. A., Azetsu-Scott, K., & Walker, B. D. (2022). Using Radiocarbon Measurements of Dissolved Inorganic Carbon to Determine a Revised Residence Time for Deep Baffin Bay. *Frontiers in Marine Science*, *9:845536*. https://doi.org/10.3389/fmars.2022.845536

Supplementary Material

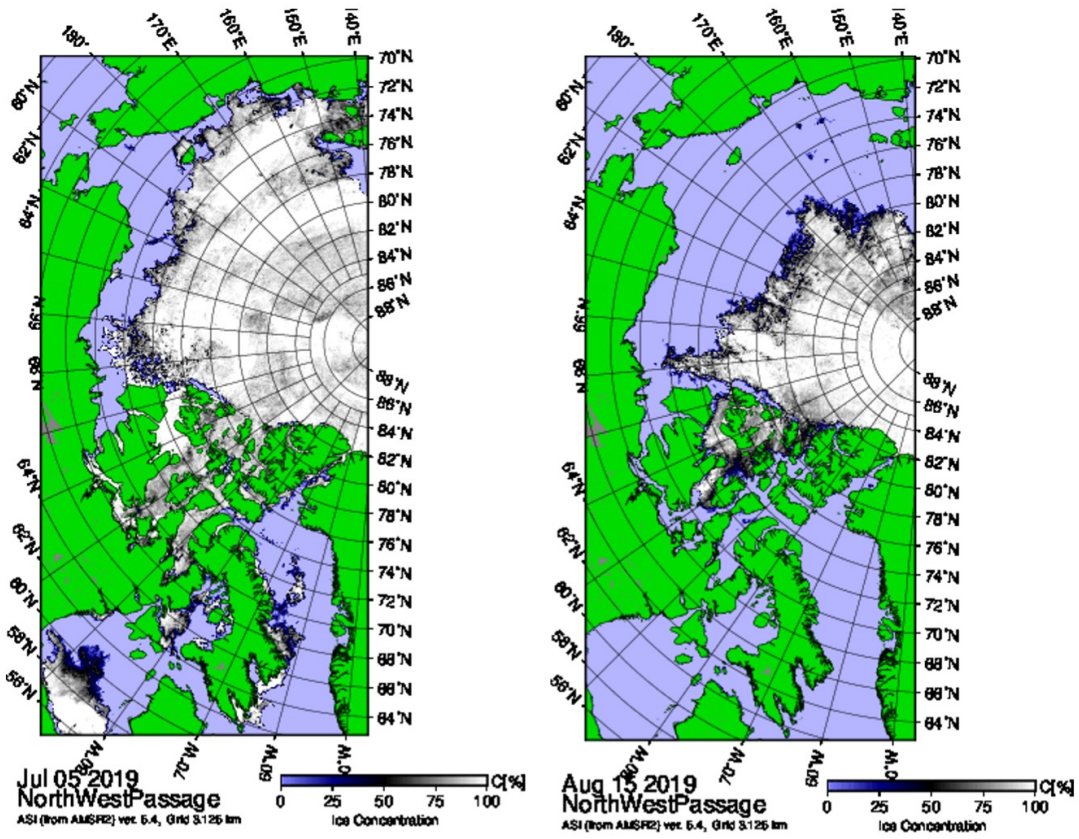

Figure S5.1: Maps of sea-ice concentration measurements by AMSR-E (Spreen et al., 2008) during sampling for this study (5 July to 15 August 2019). These images were downloaded on 18 Aug 2023 from https://seaice.uni-bremen.de/sea-ice-concentration/amsre-amsr2/.

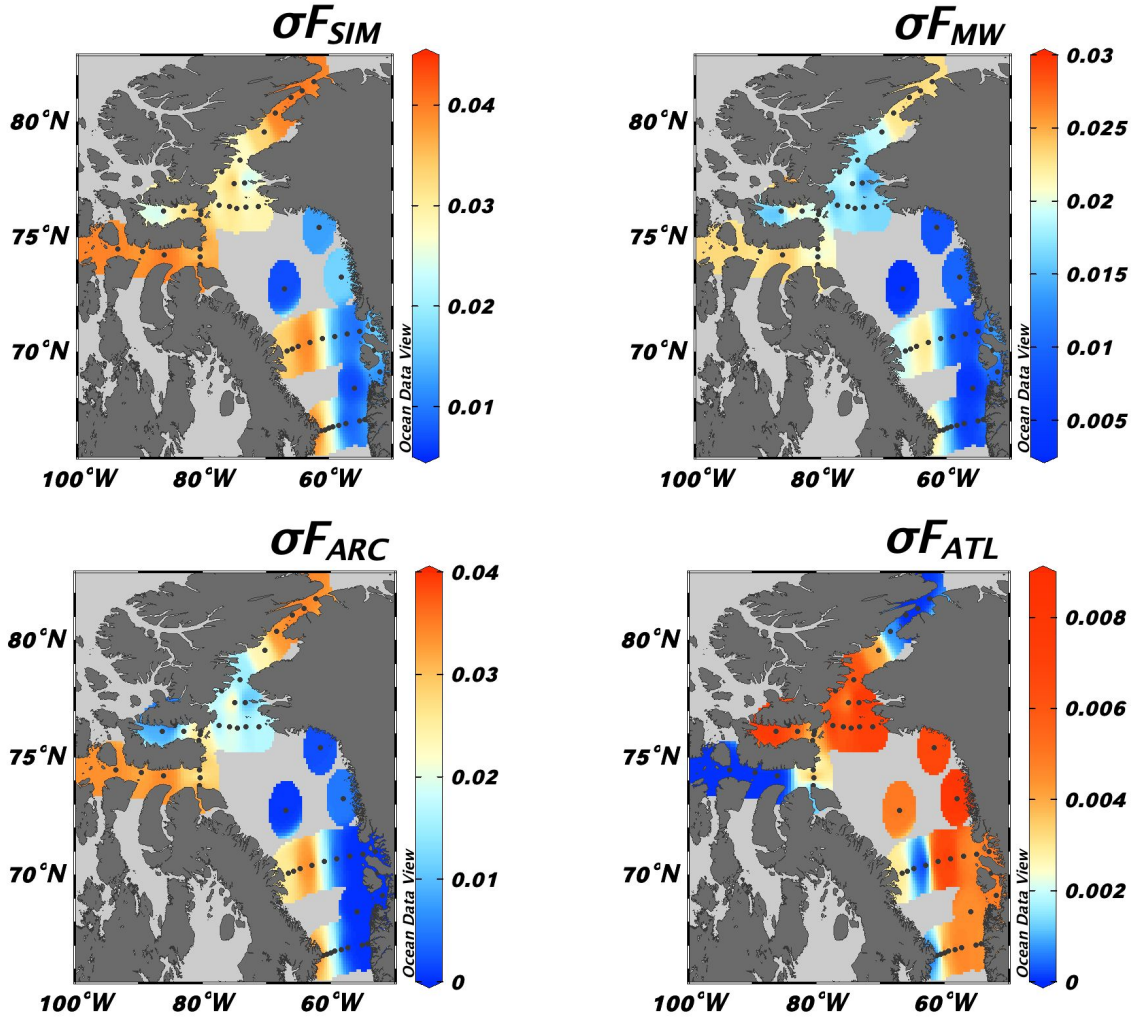

Figure S5.2: Standard deviations (σ) of calculated surface water mass fractions from Monte Carlo uncertainty analysis. Standard deviations are representative of absolute uncertainties of calculated water mass fractions. Abbreviations: F_{SIM}, fraction of sea ice melt; F_{MW}, fraction of meteoric water; F_{ARC}, fraction of Arctic water; F_{ATL}, fraction of Atlantic water.

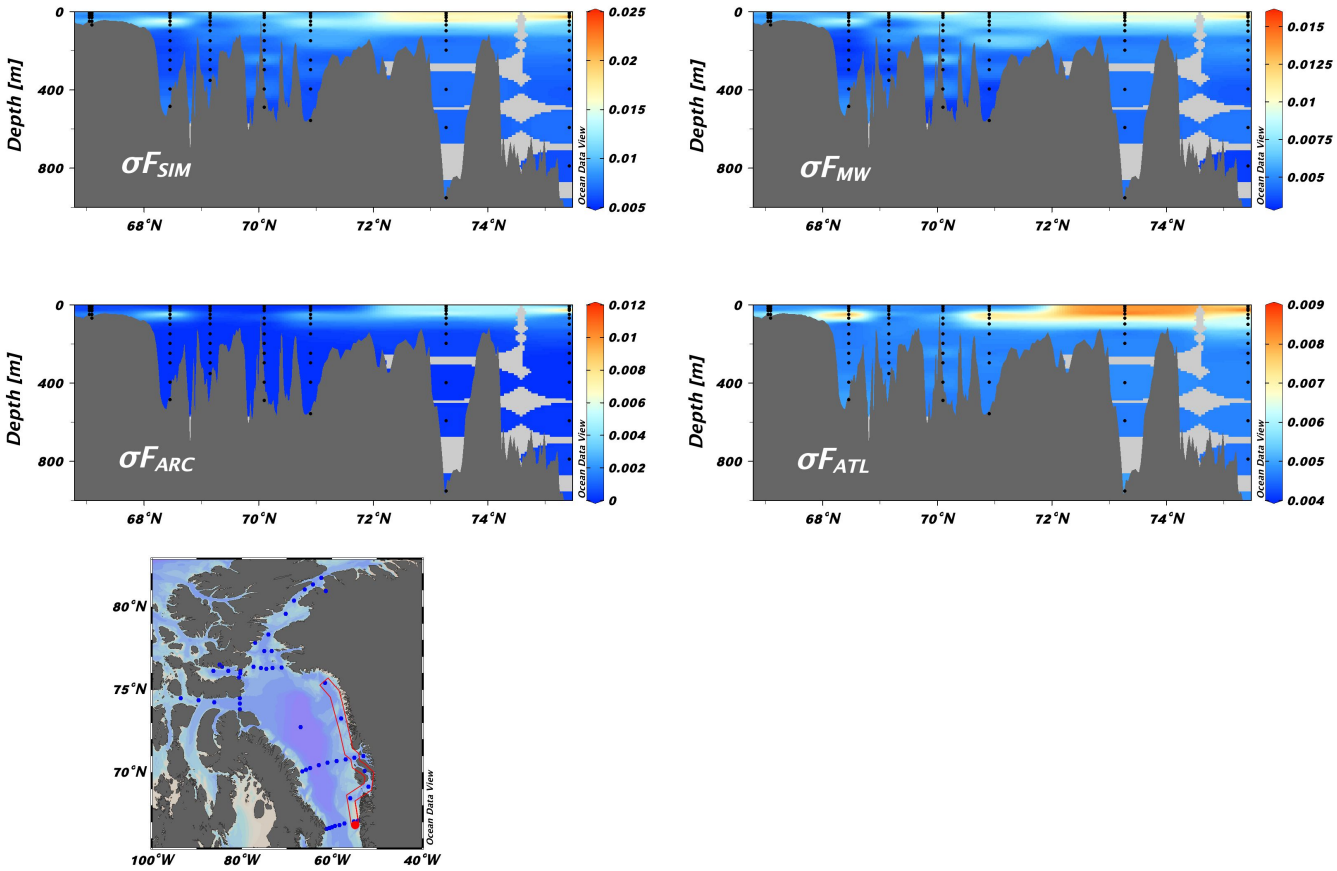

Figure S5.3: Standard deviations (σ) of calculated water mass fractions along the west Greenland shelf section (section outline shown in red in inset map) from Monte Carlo uncertainty analysis. Standard deviations are representative of absolute uncertainties of calculated water mass fractions. Abbreviations: F_{SIM}, fraction of sea ice melt; F_{MW}, fraction of meteoric water; F_{ARC}, fraction of Arctic water; F_{ATL}, fraction of Atlantic water.

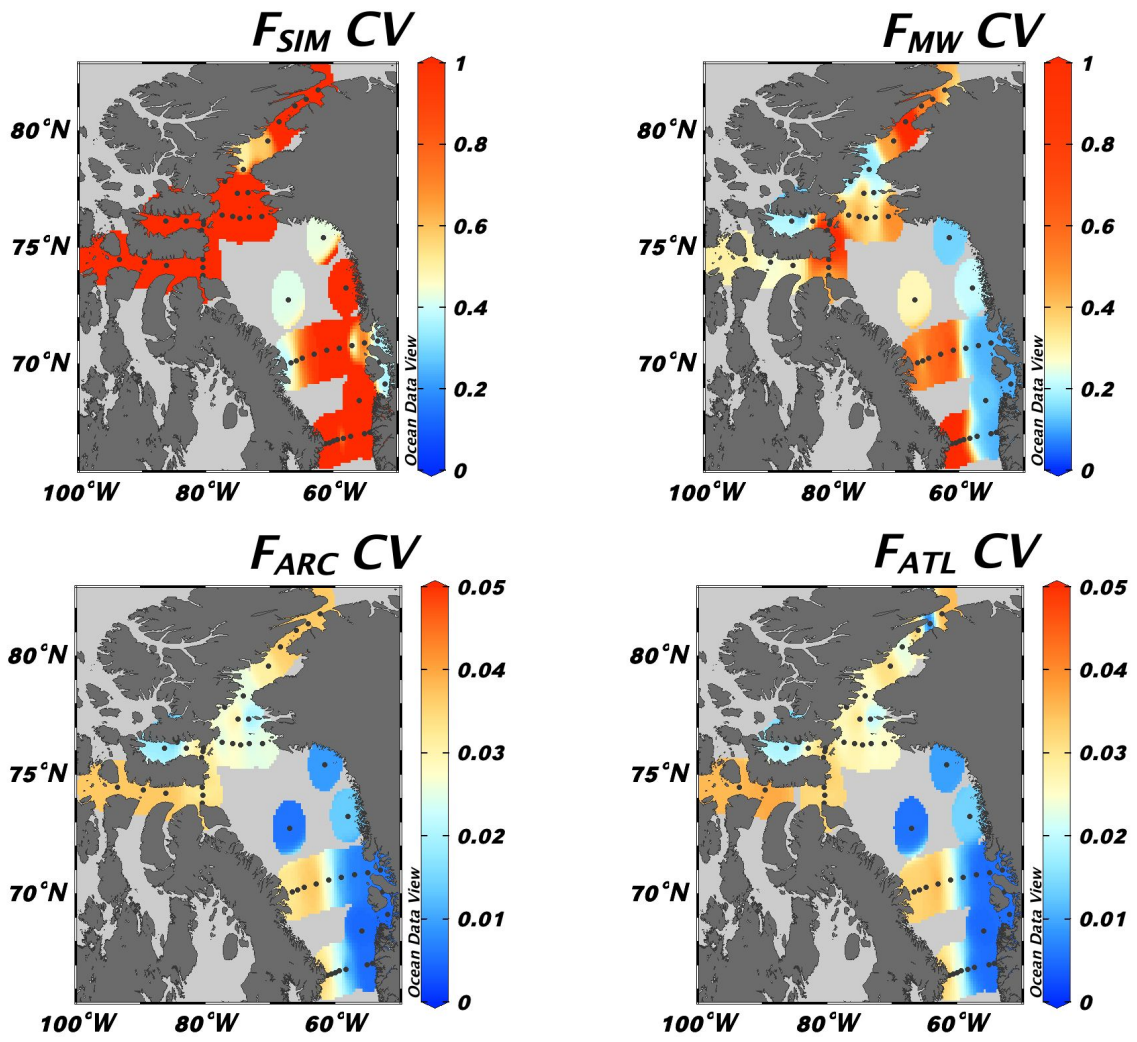

Figure S5.4: Coefficient of variation (CV = standard deviation/mean) of calculated surface water mass fractions from Monte Carlo uncertainty analysis. CVs are representative of relative uncertainties of calculated water mass fractions. Abbreviations: F_{SIM}, fraction of sea ice melt; F_{MW}, fraction of meteoric water; F_{ARC}, fraction of Arctic water; F_{ATL}, fraction of Atlantic water.

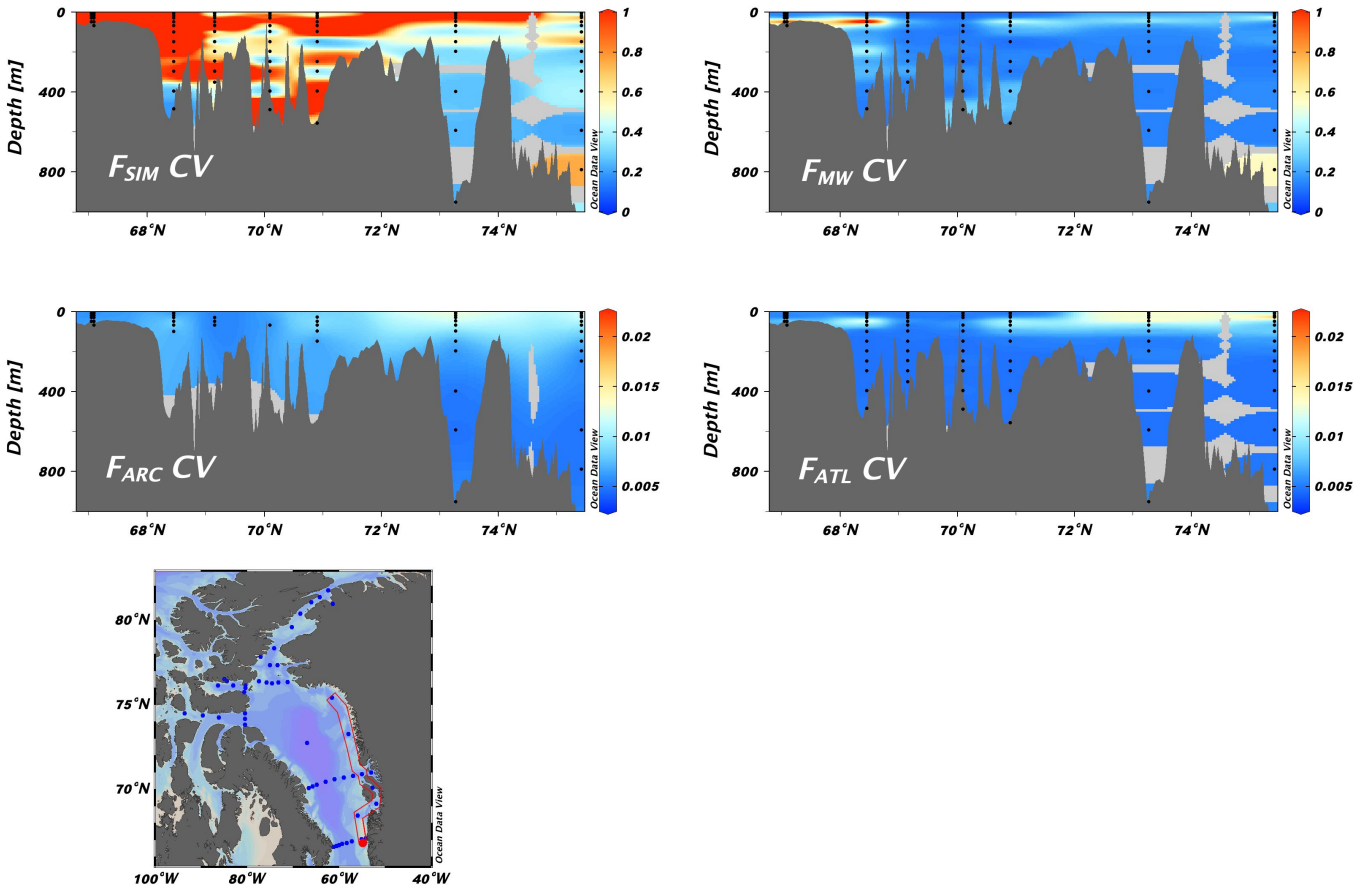

Figure S5.5: Coefficient of variation (CV = standard deviation/mean) of calculated surface water mass fractions along the west Greenland shelf section (section outline shown in red in inset map) from Monte Carlo uncertainty analysis. CVs are representative of relative uncertainties of calculated water mass fractions. Abbreviations: F_{SIM}, fraction of sea ice melt; F_{MW}, fraction of meteoric water; F_{ARC}, fraction of Arctic water; F_{ATL}, fraction of Atlantic water.

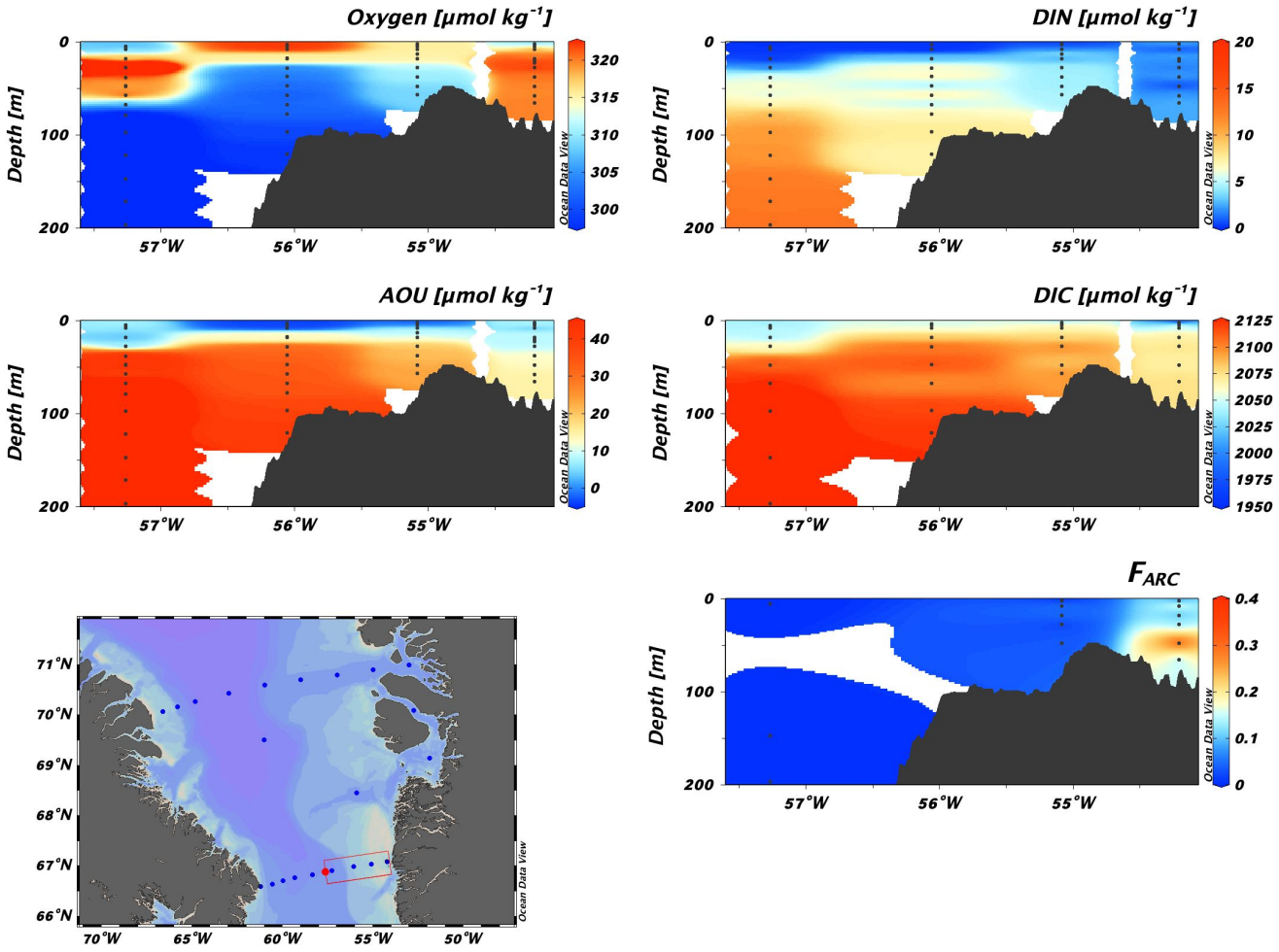

Figure S5.6: Section plots showing concentrations of (a) dissolved oxygen, (b) dissolved inorganic nitrogen (DIN), (c) apparent oxygen utilization (AOU), (d) dissolved inorganic carbon (DIC), and (e) calculated Fraction of Arctic water (F_{ARC}) within the southern West Greenland continental shelf area.

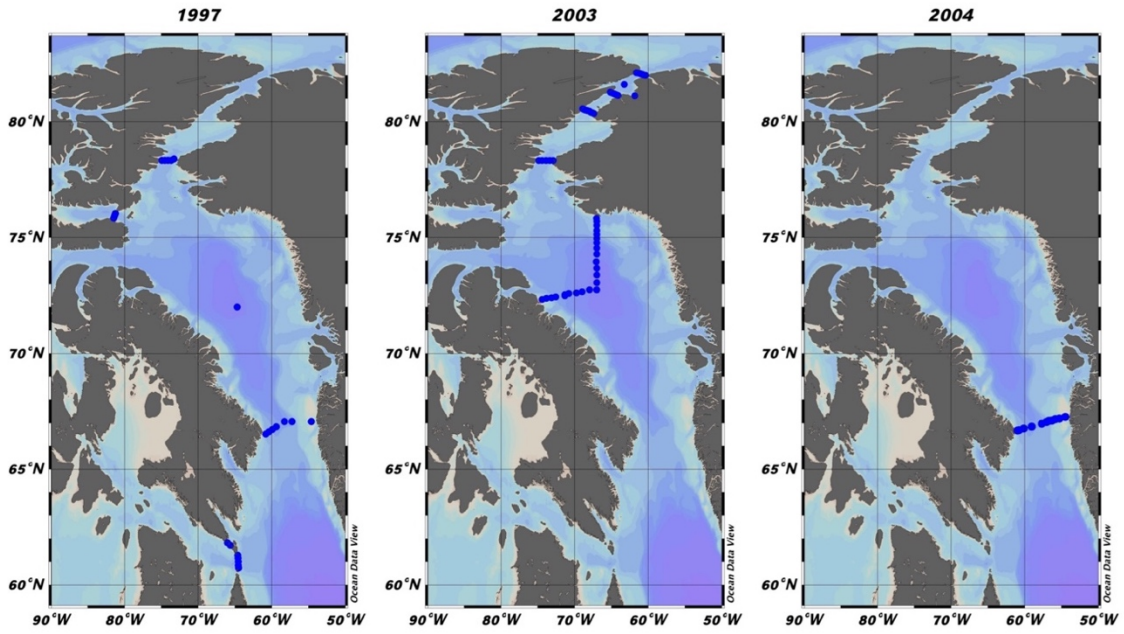

Figure S5.7: Station locations for each dataset downloaded from GLODAP v2.2022 (expocodes 18SN19970803, 32H120030721, and 316N20040922, for 1997, 2003, and 2004, respectively).

Measure	Year	BBDW	BBBW
Ω_{Ar}	1997	0.62 ± 0.12	0.51 ± 0.10
	2004	0.51 ± 0.06	0.44 ± 0.03
	2019	0.53 ± 0.04	0.43 ± 0.04
TA	1997	2297 ± 12	2314 ± 30
	2004	2289 ± 14	2298 ± 7
	2019	2291 ± 7	2294 ± 9
DIC	1997	2247 ± 7	2269 ± 2
	2004	2261 ± 7	2275 ± 3
	2019	2257 ± 10	2273 ± 4
pH	1997	7.79 ± 0.07	7.74 ± 0.09
	2004	7.71 ± 0.06	7.68 ± 0.03
	2019	7.73 ± 0.03	7.66 ± 0.04

Table S5.1: Average inorganic carbon system parameters of Baffin Bay Deep Water (BBDW) and Baffin Bay Bottom Water (BBBW) using station locations that accessed the deep central basin of Baffin Bay in 1997, 2003, and 2019.

Chapter 6 Summary and Conclusions

6.1 Summary of Major Contributions

The research contributions presented in this thesis have built on new and existing datasets to advance our collective understanding of the physical and biological controls on the marine carbon cycle in eastern Canadian Arctic waters, specifically the waterbodies of Baffin Bay and Nares Strait. This is a region that uniquely connects the Pacific, Arctic, and Atlantic Oceans, and is influenced not only by water masses formed in each of these oceans, but also by various freshwater sources. This region is also undergoing significant warming and changes in sea ice distribution and seasonality, and it is therefore important to have up-to-date measurements to see how ongoing climate change is altering the regional environment. Each research chapter of this thesis has made the most of the datasets collected to advance our understanding of the regional marine carbon cycle. Although there is a great deal of detail and many fascinating results of this thesis, I would like to focus specifically on four major contributions of this work.

Major Contribution 1: Rates of net community production (NCP) are found to vary greatly between eastern and western Baffin Bay, mainly due to nutrient availability of the predominant near-surface water mass. In the more productive waters of eastern Baffin Bay, a large portion of NCP (up to 70%) resulted from sub-surface blooms.

The first results chapter of this thesis (Chapter 3) focused on quantifying springtime rates of net community production (NCP) in Baffin Bay. NCP is an important measure as it represents an upper threshold on the amount of organic carbon that may be exported from the surface and sequestered in the deep ocean (i.e., the potential strength of the biological carbon pump). Our NCP estimates revealed a strong contrast between the Arctic and Atlantic water domains of western and eastern Baffin Bay, respectively. Arctic waters flowing southwards off the coast of Baffin Island displayed low NCP rates (< 1 mol C m^{-2}), associated with colder surface water temperatures, persistent sea ice cover, higher freshwater content, and stronger stratification of the upper water column. In contrast, modified Atlantic waters in eastern Baffin Bay (over the West Greenland shelf) displayed high NCP rates (up to 5.7 mol C m^{-2}, with an average value of 3.7 mol C m^{-2}), and were associated with warmer, ice-free surface waters with comparatively deep surface mixed layers (i.e., weaker stratification). Importantly, Atlantic-source waters also provided higher pre-bloom nitrate concentrations than Arctic waters, supplying necessary fuel for the spring bloom. These results demonstrate that the west Greenland continental shelf region in eastern Baffin Bay has a strong biological pump, comparable to that of the productive Barents Sea inflow shelf of the Arctic Ocean (2.3 to 4.2 mol C m^{-2}; Chierici et al., 2019; Codispoti et al., 2013; Fransson et

al., 2001), while the Baffin Island shelf region in western Baffin Bay has a weaker biological pump, mainly due to limited nutrient availability, with strong stratification preventing replenishment of nutrients from deeper waters.

In Chapter 3 we employed three different methods of estimating rates of NCP, with each method quantifying NCP rates over different depth and time scales. This unique combination of methods enabled us to provide detailed information about the progression of the bloom to different depth horizons over time. We determined that the Baffin Bay spring phytoplankton bloom was first initiated under sea-ice cover, up to 15 days prior to ice retreat, and that after waters became fully ice-free a large portion of NCP in eastern Baffin Bay (potentially up to 70%) was driven by primary production occurring below the surface mixed layer, in sub-surface chlorophyll maxima (SCM's). This is an important finding, as remote sensing studies attempt to quantify rates of primary production based on satellite measurements of surface water chlorophyll *a* fluorescence. However, such studies would miss the large portion of primary production that is occurring below the surface waters, in SCM's. We have shown that SCM's in eastern Baffin Bay are a very important feature in contributing to NCP, potentially contributing more than half of the total seasonal NCP in some areas. Based on this, the quantification of total seasonal primary production in eastern Baffin Bay cannot be fully quantified by remote sensing products.

Major Contribution 2: Provided concrete evidence, for the first time, that Siberian river runoff can influence the geochemical characteristics of the waters entering Nares Strait.

Chapter 4 of this thesis provided the first comprehensive investigation of carbon dynamics in Nares Strait, the northernmost outflow channel of the Arctic Ocean, and a major conduit of Arctic-outflow waters into Baffin Bay and ultimately to the North Atlantic. A major objective of this study was to distinguish the impacts of physical (water mass transport/mixing) and biological processes on the observed distribution of dissolved inorganic carbon. In order to achieve this, we first had to characterize the unique properties of each water mass entering Nares Strait from its northern and southern gateways, before inputting these characteristics into a multi-tracer linear mixing model (a method referred to as optimum multi-parameter (OMP) analysis).

In the particular years' dataset that this model was applied to (summer of 2014), we observed a rather unique water mass assembly arriving in Nares Strait from the Arctic Ocean. We showed the first documented evidence of Siberian shelf waters arriving in Nares Strait, carrying with it a high dissolved organic matter signal from Siberian river runoff. The small number of previous investigations that have reported on the water mass properties entering Nares Strait observed a mainly Pacific-origin upper water

column arriving from the Beaufort Sea or Canada Basin (Jackson et al., 2014; Münchow et al., 2007; Steele et al., 2004; de Steur et al., 2013). Therefore, our observations showing the arrival of Siberian shelf waters (Atlantic-origin) in Nares Strait was novel and quite significant, as it provided clear evidence that the water mass assembly in Nares Strait can be variable from year-to-year, driven by surface circulation changes over the central Arctic Ocean. Previous literature had discussed the basis for such variability, noting that the region north of Nares Strait (the Lincoln Sea) acts as a "switchyard", directing either Pacific- or Atlantic-origin surface waters toward the Lincoln Sea and Nares Strait depending on the predominant atmospheric circulation patterns, such as the strength of the Beaufort High, and the location of the Transpolar Drift stream (TPD; Jackson et al., 2014; Newton & Sotirin, 1997; Steele et al., 2004; de Steur et al., 2013). However, the impact of this "switchyard" effect on the waters in Nares Strait, and their biogeochemistry had not been studied before. Our results from Chapter 4 provided the first geochemical dataset in Nares Strait documenting the arrival of Siberian shelf waters, and the resulting biogeochemical processes downstream.

From the results of the OMP analysis we determined that water mass mixing was the dominant control on the inorganic carbon budget in Nares Strait, although a modest phytoplankton bloom in Kane Basin (associated with shoaling bathymetry and upwelling of additional nutrients from deeper waters) also played an important role in decreasing DIC and surface pCO_2. This productivity paved the way for additional uptake of atmospheric CO_2, although overall we found gas exchange played a minor role in the carbon dynamics of the region.

Major Contribution 3: Presented a new conceptual framework describing how the water mass assembly in the Nares Strait-Baffin Bay corridor may be influenced by large-scale circulation over the central Arctic basin, including a testable hypothesis that can guide continuing climate research in this area well into the future.

Another significant contribution to the field of Arctic marine biogeochemistry is provided by the discussion section of Chapter 4. Here we contrasted how the water mass assembly that we observed arriving in northern Nares Strait in 2014 (with Siberian shelf waters present at the surface) was different from those previously documented in the region (surface waters from the Canada Basin), and how these two different water mass assemblies may alter carbon dynamics in the region. Based on our observations, we postulate that it is not only the surface water characteristics that are different between these two water mass assemblies, but also the water layers that are advected towards Nares Strait at intermediate depths (between 50 to 150 m).

The major climate index that controls the surface circulation patterns over the central Arctic Ocean is called the Arctic Oscillation (AO) index. In years when the AO index is negative, the Beaufort Gyre becomes expanded, and the Transpolar Drift stream transports Siberian shelf waters across the central Arctic Ocean towards northern Greenland (and Nares Strait, as we observed in Chapter 4). On the other hand, when the AO index is positive, the Beaufort Gyre is relatively small, and the Transpolar Drift stream is aligned from the Chukchi Sea to northern Greenland (see Figure 4.1b for a schematic of these circulation patterns).

In our discussion section we put forward the hypothesis that under a positive AO index, northern Nares Strait would receive a water mass assembly from the Canada Basin (Pacific sector of the Arctic Ocean). Under this scenario, Nares Strait would be receiving highly stratified, nutrient-depleted surface waters (< 1 μM; Brown et al., 2020), as the Canada Basin in recent years has been subject to perennial stratification (Randelhoff et al., 2020; Brown et al., 2020; Coupel et al., 2015) inhibiting nutrient replenishment from deeper waters year-round. At the same time, the upper halocline layer from the Canada Basin (intermediate water mass centered around 150 m depth), contains high nutrient and carbon concentrations, and has been shown to be corrosive to aragonite ($\Omega_{Ar} < 1$; Brown et al., 2016; Miller et al., 2015; Yamamoto-Kawai et al., 2013). The depth horizon of 150 m for the upper halocline is relatively deep compared to what we witnessed under a negative AO scenario in Chapter 4, and therefore may prohibit nutrient replenishment by vertical mixing within Nares Strait, even over the shallow sill in Kane Basin. Thus, we predict that under a negative AO index primary production in Nares Strait would be limited, due to low nutrient availability, and simultaneously the water column would be more susceptible to ocean acidification due to the undersaturated Ω_{Ar} values of the upper halocline layer from the Canada Basin.

We based our concept of negative AO conditions in Nares Strait on our observations from the summer of 2014 (presented in Chapter 4). In this scenario, the TPD is aligned in a such a way to transport Siberian shelf waters towards Nares Strait, bringing with them high dissolved organic matter concentrations from the influence of Siberian river runoff (also observed by Stedmon et al., 2021), and moderate surface nutrient concentrations (also observed by Charette et al., 2020). Our observations in northern Nares Strait showed modest nitrate concentrations entering from the north (up to 3.5 μmol kg^{-1}; Figure 4.3e). Additionally, under a negative AO scenario we observed a shallower, thinner, and diluted (in terms of peak nutrient and inorganic carbon concentrations) upper halocline layer compared to that in the Canada Basin water mass assembly. The relatively shallow position of this water mass would make it easier for nutrients to be mixed vertically into the euphotic zone, where it may spur additional primary production,

especially in Kane Basin where a shoaling bathymetry promotes upwelling. To summarize, in a negative AO scenario we predict that comparatively more primary production may occur in the surface waters of Nares Strait, and in turn these waters will be less susceptible to ocean acidification due to the lower inorganic carbon concentrations in the upper halocline layer (and the drawdown of surface CO_2 concentrations by primary production).

These ideas about how different AO indices will impact the biogeochemistry in Nares Strait will provide a testable hypothesis for future investigations to either support or disprove.

Major Contribution 4: Provided geochemical evidence of cross-bay mixing in Baffin Bay, which is contrary to the conventionally accepted cyclonic circulation, and appears to play a major role in determining the aragonite saturation state of waters in the upper 200 m over the West Greenland continental shelf.

In Chapter 5 we once again focused on Baffin Bay, to investigate the key processes controlling the variability in aragonite saturation states (Ω_{Ar}), an indicator used to assess the state of ocean acidification in terms of its potential impact to calcifying organisms. This study utilized a geochemical dataset collected during the summer of 2019, with a greater density of sampling stations located over the West Greenland continental shelf compared to previous scientific expeditions onboard the CCGS *Amundsen*. Since this particular sub-region of Baffin Bay had been relatively under-studied in terms of its biogeochemistry, we were particularly interested to examine conditions in this region.

After utilizing geochemical measurements to distinguish Arctic and Atlantic water distributions within Baffin Bay, we were surprised to identify substantial fractions of Arctic-outflow waters (20 to 40%) in the upper water column of the West Greenland shelf region. This contradicts the prevailing view of an overall cyclonic circulation pattern in Baffin Bay, with Arctic-outflow waters flowing southwards in western Baffin Bay, and Atlantic waters flow northwards along the West Greenland shelf in eastern Baffin Bay (Fissel et al., 1982; Bourke et al., 1989; Tang et al., 2004; Curry et al., 2011). To further investigate how Arctic waters may arrive on the West Greenland shelf we employed a numerical modeling simulation with a passive tracer. The model results demonstrated how periodic shifts in wind direction induce a transition from onshore to offshore Ekman transport in western Baffin Bay, transporting Arctic waters towards central Baffin Bay, and ultimately onto the West Greenland shelf. These results potentially demonstrate an important feature of Baffin Bay surface circulation that has not previously been documented in the scientific literature.

In terms of the biogeochemical drivers of Ω_{Ar} in Baffin Bay, the results of Chapter 5 also demonstrated

that an increased presence of Arctic water fractions is the main process leading to decreases in Ω_{Ar} within the upper 200m of the water column in Baffin Bay. At depths greater than 200 m, the primary control on Ω_{Ar} was the respiration of organic matter, which contributes to increased dissolved inorganic carbon concentrations, leading to decreases in Ω_{Ar}.

6.2 Limitations and Recommendations for Future Work

One of the greatest limitations to the research presented in this thesis, which is applicable to all three research chapters, is that the observations we draw conclusions from only represent one specific snapshot in time (and space), and are often representative of the summer open-water season. We are left to hypothesize and make best estimates of what winter conditions were prior to sampling, and what is expected to occur as the summer season progresses and transitions into fall.

Related to this limitation - in Chapter 3 of this thesis we demonstrated how different techniques of estimating surface winter water conditions can lead to large differences in estimates of NCP. In this case, taking periodic measurements in late-winter would greatly improve the accuracy of seasonal NCP estimates. Also in Chapter 3, we concluded that Arctic waters in western Baffin Bay displayed low springtime rates of NCP, and were unlikely to show a large NCP increase further into the summer season due to low near-surface nutrient concentrations and strong stratification of the upper water column. However, at the time of sampling the waters in western Baffin Bay remained ice-covered, or had only recently become ice-free. It is possible that later into the ice-free season strong winds might force upwelling of nutrients along the Baffin Island shelf break, resulting in a stronger bloom than anticipated. Or perhaps sub-surface blooms play a larger role than expected in contributing to summer NCP along the Baffin Island shelf. This is a future research question that could be answered by datasets that currently exist over the Baffin Island shelf, and is a suggestion for a future research paper.

Chapter 4 provided a unique snapshot of the water mass assembly in Nares Strait during the summer of 2014. The discussion section of this chapter provided many hypotheses of how wind pattern changes over the Arctic Ocean basin (associated with different phases of the Arctic Oscillation) might influence the water mass assembly, its nutrient concentrations, and carbon dynamics in Nares Strait. Future studies should employ multi-year datasets within Nares Strait to investigate the variability of its water mass assembly more thoroughly, and provide concrete evidence of any associated changes in stratification, nutrient availability, and carbon dynamics. Although in the past ship-based observations in Nares Strait were not logistically feasible due to heavy sea ice conditions, Nares Strait is becoming more accessible due to the impact of climate change in the region. Scientific research cruises made by CCGS *Amundsen* have now accessed Nares Strait in 2014, 2016, 2019, and 2023. These datasets combined

would provide an excellent starting point for a multi-year investigation of how different phases of the Arctic Oscillation affect the water mass assembly in Nares Strait.

In Chapter 5 our ability to assess decadal changes in the ocean acidification state of Baffin Bay was challenged by sampling locations that changed year-by-year throughout the bay. Although it is beneficial that sampling locations change from year to year to examine new areas, it is also extremely beneficial to maintain measurements at certain key locations year after year in order to assess long term changes. Within Baffin Bay, Davis Strait is a key location where observations have been collected relatively consistently since the late 1990's largely thanks to the efforts of Fisheries and Oceans Canada. Another key long-term sampling location is the east-west transect of stations across the North Water polynya region in northern Baffin Bay, which has been consistently sampled by ArcticNet funded cruises onboard CCGS *Amundsen* since 2005. Continuing the long-term monitoring of these sites into the future will be essential to assessing the progression of ocean acidification in this region.

Another large limitation for the research presented in this thesis is that the physical oceanography of the Nares Strait – Baffin Bay corridor is still not well characterized. Having a good understanding of the regional circulation patterns often provides much needed context for the interpretation of biogeochemical measurements. This limitation was demonstrated clearly in Chapter 5, where we noted substantial Arctic water fractions present over the west Greenland shelf, an area where they were not necessarily expected to be present. In order to understand if changes in the general circulation patterns in Baffin Bay could explain these results, we employed a numerical modeling simulation with a passive tracer, since the limited observation-based studies of physical oceanography of Baffin Bay could not explain these observations. Future mooring deployments in key areas of Baffin Bay and Nares Strait would provide much needed observations of the changing circulation patterns in this region. It would be especially meaningful to have deployments throughout the west Greenland shelf region, with its complex bathymetry, and at the northern gateway to Nares Strait.

There are still many questions and uncertainties relating to the marine carbon cycle in Baffin Bay and Nares Strait. Just to name a few outstanding questions: where exactly is Baffin Bay Polar water formed within Baffin Bay? And do the mechanisms contributing to the formation of this water mass also allow it to act as a significant CO_2 sink within the region? How might we determine what the historical baseline CO_2 sink of Baffin Bay and/or Nares Strait actually was, and how much has it changed due to climate change? Will the biological pump within Baffin Bay and Nares Strait be enhanced due to climate change and a longer ice-free season? Or will it be reduced due to enhanced freshwater inputs, stratification, and resulting nutrient limitation? Answering these questions will require more data, and also likely some

innovations in how we might utilize biogeochemical modeling tools or historical remote sensing measurements to estimate how these natural systems have changed over time.

6.3 Closing comments: A new perspective of Baffin Bay

The research presented in this thesis has highlighted the importance of water mass variability as the prime driver of the marine inorganic carbon system in the Nares Strait-Baffin Bay complex. Previous to this work, researchers were certainly aware that eastern and western Baffin Bay were dominated by two different water mass assemblies, but the key role that the advection of these water masses play in controlling the state of the inorganic carbon system was not always clear. Miller et al. (2002) provided the first observations of full water column inorganic carbon system concentrations in the North Water (NOW) polynya region of northern Baffin Bay, and did identify two differing water mass assemblies of Arctic and Atlantic origin (based on their differing temperature and salinity characteristics), however their observed concentrations of dissolved inorganic carbon and total alkalinity did not differ significantly at their time of sampling in 1998 and 1999. Based on this observation, Miller et al. (2002) stated that the importance of advective transport to the carbon budget of the region was unclear, and that based on their similar inorganic carbon system characteristics these two water mass assemblies likely do not represent a major control on the region's inorganic carbon system (although they did state this analysis may be too simplistic). A later investigation by Azetsu-Scott et al. (2010) provided the first reported values of calcite and aragonite saturation states in the greater Baffin Bay complex, and did observe a clear difference in saturation states between the two water mass assemblies, with Arctic-outflow waters being characterized by lower pH and saturation states compared to Atlantic-source waters.

The research of this thesis has continued to build from these initial investigations, and has shown that the predominant near-surface water mass can affect the marine inorganic system in many ways, from changing temperature and salinity characteristics (which can alter surface pCO_2, and affect rates of air-sea CO_2 exchange), to governing nutrient availability for primary production (affecting the seasonal drawdown of dissolved inorganic carbon in near-surface waters), and modulating the buffering capacity of the waters against ocean acidification. Specifically, in Chapter 3, it was demonstrated how Arctic-outflow waters (primarily of Pacific origin) are relatively nutrient-depleted upon arrival in Baffin Bay compared to Atlantic-source waters, leading to a marked dichotomy in rates of net community production between western and eastern Baffin Bay. Further in Chapter 5, it was demonstrated that the relatively low TA:DIC ratio of Arctic-outflow waters is the main driver of low aragonite saturation states in the upper water column of Baffin Bay, making locations with a high prevalence of Arctic-outflow waters more

susceptible to ongoing ocean acidification. Atlantic-source waters in Baffin Bay displayed a comparatively higher TA:DIC ratio, making these waters more resistant to ocean acidification, at least currently.

A secondary, but very important, outcome of the research in this thesis has been new discoveries about regional circulation patterns based on our measurements of seawater chemistry. For example, Chapter 4 provided the first direct observations of Siberian shelf waters arriving in Nares Strait, carrying with them a higher dissolved organic matter signal and relatively high surface pCO_2 and nutrient concentrations (compared to Pacific-source waters). This represents a novel finding since previous literature had only documented Pacific-source waters arriving in Nares Strait (Jackson et al., 2014; Münchow et al., 2007; Steele et al., 2004; de Steur et al., 2013). This discovery indicates that interannual shifts in atmospheric and surface circulation patterns over the central Arctic Ocean can alter the water mass assemblies advected to the outflow shelves of the Arctic Ocean, and potentially alter regional rates of air-sea exchange, primary production, and the state of ocean acidification in these waterways interannually. Additionally, in Chapter 5 we identified significant fractions of Arctic-outflow waters in the upper water column over the West Greenland shelf in Baffin Bay – a region previously thought to be dominated by Atlantic-source waters arriving via the West Greenland current. These results contradicted the prevailing view of an overall cyclonic circulation pattern within Baffin Bay (Tang et al., 2004; Curry et al., 2011; Münchow et al., 2015). Since there has been a general dearth of physical oceanographic measurements in Baffin Bay in recent years, we turned to the use of a numerical modeling simulation with a passive tracer to investigate potential mechanisms for cross-bay mixing in Baffin Bay. The model results suggest that periodic shifts in wind direction can induce a transition from onshore to offshore Ekman transport along the Baffin Island coastline in western Baffin Bay, periodically transporting Arctic-outflow waters towards the West Greenland shelf. Understanding these circulation patterns is critical for a better predictive understanding of the drivers of marine productivity and ocean acidification regionally, seeing as nutrient concentrations and the state of the inorganic carbon system (e.g. TA:DIC ratios) can change drastically depending on the predominant water mass. Our findings of these novel circulation patterns are based on geochemical measurements, and require future oceanographic investigations to confirm our findings, and to continue investigating knock-on impacts of these circulation changes to marine productivity and the state of ocean acidification in the Baffin Bay system. Ultimately, the research works presented in this thesis have helped to shape a new view of water mass variability, circulation, and the resulting impacts of this variability to the marine carbon cycle of the greater Baffin Bay region.

Literature Cited

Azetsu-Scott, K., Clarke, A., Falkner, K., Hamilton, J., Jones, E. P., Lee, C., et al. (2010). Calcium carbonate saturation states in the waters of the Canadian Arctic Archipelago and the Labrador Sea. *Journal of Geophysical Research: Oceans*, *115*, C11021. https://doi.org/10.1029/2009JC005917

Bourke, R. H., Addison, V. G., & Paquette, R. G. (1989). Oceanography of Nares Strait and northern Baffin Bay in 1986 with emphasis on deep and bottom water formation. *Journal of Geophysical Research*, *94*(C6), 8289. https://doi.org/10.1029/JC094iC06p08289

Brown, K. A., McLaughlin, F., Tortell, P. D., Yamamoto-Kawai, M., & Francois, R. (2016). Sources of dissolved inorganic carbon to the Canada Basin halocline: A multitracer study. *Journal of Geophysical Research: Oceans*, *121*. https://doi.org/10.1002/2015JC011535

Brown, K. A., Holding, J. M., & Carmack, E. C. (2020). Understanding Regional and Seasonal Variability Is Key to Gaining a Pan-Arctic Perspective on Arctic Ocean Freshening. *Frontiers in Marine Science*, *7:606*. https://doi.org/10.3389/fmars.2020.00606

Charette, M. A., Kipp, L. E., Jensen, L. T., Dabrowski, J. S., Whitmore, L. M., Fitzsimmons, J. N., et al. (2020). The Transpolar Drift as a Source of Riverine and Shelf-Derived Trace Elements to the Central Arctic Ocean. *Journal of Geophysical Research: Oceans*, *125*, e2019JC015920. https://doi.org/10.1029/2019JC015920

Chierici, M., Vernet, M., Fransson, A., & Børsheim, K. Y. (2019). Net Community Production and Carbon Exchange From Winter to Summer in the Atlantic Water Inflow to the Arctic Ocean. *Frontiers in Marine Science*, *6*(528). https://doi.org/10.3389/fmars.2019.00528

Codispoti, L. A., Kelly, V., Thessen, A., Matrai, P., Suttles, S., Hill, V., et al. (2013). Synthesis of primary production in the Arctic Ocean: III. Nitrate and phosphate based estimates of net community production. *Progress in Oceanography*, *110*, 126–150. https://doi.org/10.1016/j.pocean.2012.11.006

Coupel, P., Ruiz-Pino, D., Sicre, M. A., Chen, J. F., Lee, S. H., Schiffrine, N., et al. (2015). The impact of freshening on phytoplankton production in the Pacific Arctic Ocean. *Progress in Oceanography*, *131*, 113–125. https://doi.org/10.1016/j.pocean.2014.12.003

Curry, B., Lee, C. M., & Petrie, B. (2011). Volume, Freshwater, and Heat Fluxes through Davis Strait, 2004 – 05. *Journal of Physical Oceanography*, *41*, 429–436. https://doi.org/10.1175/2010JPO4536.1

Fissel, D. B., Lemon, D. D., & Birch, J. R. (1982). Major Features of the Summer Near-Surface Circulation of Western Baffin Bay, 1978 and 1979. *Arctic*, *35*(1), 180–200. https://doi.org/10.14430/arctic2318

Fransson, A., Chierici, M., Anderson, L. G., Bussmann, I., Kattner, G., Peter Jones, E., & Swift, J. H. (2001). The importance of shelf processes for the modification of chemical constituents in the waters of the Eurasian Arctic Ocean: Implication for carbon fluxes. *Continental Shelf Research*, *21*, 225–242. https://doi.org/10.1016/S0278-4343(00)00088-1

Jackson, J. M., Lique, C., Alkire, M., Steele, M., Lee, C. M., Smethie, W. M., & Schlosser, P. (2014). On the waters upstream of Nares Strait, Arctic Ocean, from 1991 to 2012. *Continental Shelf Research*, *73*, 83–96. https://doi.org/10.1016/j.csr.2013.11.025

Miller, L. A., Yager, P. L., Erickson, K. A., Amiel, D., Bâcle, J., Cochran, J. K., et al. (2002). Carbon distributions and fluxes in the North Water, 1998 and 1999. *Deep-Sea Research Part II*, *49*, 5151–5170.

Miller, L. A., Macdonald, R. W., Mclaughlin, F., Mucci, A., Yamamoto-Kawai, M., Giesbrecht, K. E., et al.

(2014). Changes in the marine carbonate system of the western Arctic : patterns in a rescued data set. *Polar Research*, *33*(1), 20577. https://doi.org/10.3402/polar.v33.20577

Münchow, A., Falkner, K. K., & Melling, H. (2007). Spatial continuity of measured seawater and tracer fluxes through Nares Strait, a dynamically wide channel bordering the Canadian Archipelago. *Journal of Marine Research*, *65*, 759–788. https://doi.org/10.1357/002224007784219048

Münchow, A., Falkner, K. K., & Melling, H. (2015). Baffin Island and West Greenland Current Systems in northern Baffin Bay. *Progress in Oceanography*, *132*, 305–317. https://doi.org/10.1016/j.pocean.2014.04.001

Newton, J. L., & Sotirin, B. J. (1997). Boundary undercurrent and water mass changes in the Lincoln Sea. *Journal of Geophysical Research: Oceans*, *102*(C2), 3393–3403. https://doi.org/10.1029/96JC03441

Randelhoff, A., Holding, J., Janout, M., Sejr, M. K., Babin, M., Tremblay, J. É., & Alkire, M. B. (2020). Pan-Arctic Ocean Primary Production Constrained by Turbulent Nitrate Fluxes. *Frontiers in Marine Science*, *7*(150). https://doi.org/10.3389/fmars.2020.00150

Stedmon, C. A., Amon, R. M. W., Bauch, D., Bracher, A., Gonçalves-Araujo, R., Hoppmann, M., et al. (2021). Insights Into Water Mass Origins in the Central Arctic Ocean From In-Situ Dissolved Organic Matter Fluorescence. *Journal of Geophysical Research: Oceans*, *126*, e2021JC017407. https://doi.org/10.1029/2021JC017407

Steele, M., Morison, J., Ermold, W., Rigor, I., & Ortmeyer, M. (2004). Circulation of summer Pacific halocline water in the Arctic Ocean. *Journal of Geophysical Research*, *109*, C02027. https://doi.org/10.1029/2003JC002009

de Steur, L., Steele, M., Hansen, E., Morison, J., Polyakov, I., Olsen, S. M., et al. (2013). Hydrographic changes in the Lincoln Sea in the Arctic Ocean with focus on an upper ocean freshwater anomaly between 2007 and 2010. *Journal of Geophysical Research: Oceans*, *118*, 4699–4715. https://doi.org/10.1002/jgrc.20341

Tang, C. C. L., Ross, C. K., Yao, T., Petrie, B., DeTracey, B. M., & Dunlap, E. (2004). The circulation, water masses and sea-ice of Baffin Bay. *Progress in Oceanography*, *63*, 183–228. https://doi.org/10.1016/j.pocean.2004.09.005

Yamamoto-Kawai, M., McLaughlin, F., & Carmack, E. (2013). Ocean acidification in the three oceans surrounding northern North America. *Journal of Geophysical Research: Oceans*, *118*(11), 6274–6284. https://doi.org/10.1002/2013JC009157

Appendix A: Contributions of Collaborating Authors

Chapter 3: For this chapter, I participated in the GreenEdge research expedition onboard CCGS *Amundsen* during June and July of 2016 to collect the underway pCO_2 and DIC/TA samples. Additional field measurements of underway $\Delta O_2/Ar$ and discrete samples of nutrient concentrations were collected by the team of Jean-Éric Tremblay from Université Laval, primarily by Jonathan Gagnon. I designed the research methodology for this paper, with some assistance from Jean-Éric Tremblay who carried out the calculations of NCP from profile measurements of nitrate concentrations (NCP_N). I carried out the calculations of $NCP_{O2/Ar}$ and NCP_{pCO2} estimates. I conducted the data analyses, made the figures, interpreted the results, and wrote the manuscript. Tim Papakyriakou and Brent Else contributed to the interpretation of the results, provided logistical and financial support for the fieldwork, and also reviewed the manuscript drafts multiple times.

Chapter 4: For this chapter, I participated in the 2014 ArcticNet scientific expedition onboard CCGS *Amundsen* to collect underway pCO_2 and DIC/TA samples. Logistical and financial support for this field work was provided by Tim Papakyriakou, Lisa Miller, Brent Else, and Jean-Éric Tremblay. I designed the research methodology, conducted the analysis, made the figures, interpreted the results, and wrote the manuscript. Søren Rysgaard and John Mortensen provided important insights into the interpretation of the results. All authors greatly helped improve the writing of this paper over several rounds of revisions and editing.

Chapter 5: For this chapter, field work was conducted by the team of Brent Else from the University of Calgary (specifically Shawn Marriott and Sarah Prestie), and by Cara Manning from the University of Connecticut, during the 2019 scientific expedition aboard CCGS *Amundsen*. I provided sampling instructions for the field work to Shawn, Sarah, and Cara. Logistical and financial support for field work was provided by Brent Else, Tim Papakyriakou, Kumiko Azetsu-Scott, Lisa Miller, and Jean-Éric Tremblay. I designed the research methodology for this study. Kumiko Azetsu-Scott provided feedback on the freshwater decomposition methodology. Paul Myers contributed the results from a passive tracer simulation using the NEMO model, and provided Figure 5.7. Wayne Chan assisted me in carrying out a Monte Carlo simulation to assess the uncertainty of the freshwater decomposition methodology. I conducted the data analysis, made the figures, interpreted the results, and wrote the manuscript. All authors helped improve the manuscript over several rounds of revisions and editing.